Collectivity and shape phenomena in extremely neutron deficient ^{11}Cs, ^{11}Ba, and ^{11}Cs studied with the JUROGAM 3 + MARA setup

Kuankuan Zheng

université
PARIS-SACLAY

Collectivity and shape phenomena in extremely neutron deficient ^{119}Cs, ^{119}Ba, and ^{118}Cs studied with the JUROGAM 3 + MARA setup

Phénomènes de collectivité et de formes dans les noyaux ^{119}Cs, ^{119}Ba, et ^{118}Cs extrêmement déficients en neutrons étudiés avec le dispositif JUROGAM 3 + MARA

Thèse de doctorat de l'université Paris-Saclay

École doctorale n°576 Particules, hadrons, énergie et noyau : instrumentation, imagerie, cosmos et simulation (PHENIICS)
Spécialité de doctorat: Structure et réactions nucléaires
Unité de recherche: Université Paris-Saclay, CNRS, IJCLab, 91405, Orsay, France
Référent: Faculté des sciences d'Orsay

Thèse présentée et soutenue à Paris-Saclay, le 15 octobre 2021, par

Kuankuan ZHENG

Composition du jury:

Amel KORICHI Directrice de recherche, CNRS, IJCLab Orsay	Présidente
Philip WALKER Professeur émérite de l'Université de Surrey, UK	Rapporteur & Examinateur
Mark RILEY Professeur de l'Université de Tallahassee, Florida, USA	Rapporteur & Examinateur
Furong XU Professeur de l'Université de Pékin, Beijing, Chine	Examinateur
Daniele MENGONI Professeur de l'Université de Padoue et INFN, Padoue, Italie	Examinateur

Direction de la thèse:

Costel Marian PETRACHE Professeur de l'Université Paris-Saclay et CNRS, Orsay	Directeur de thèse
Minliang LIU Professeur de l'Université de l'Académie Chinoise des Sciences, Lanzhou, Chine	Encadrant

Thèse de doctorat

NNT: 2021UPASP104

To my father

Acknowledgements

My study at the IJCLab, Université Paris-Saclay will soon come to an end and, at the completion of my graduation thesis. I wish to express my sincere appreciation to all those who have offered me invaluable help during the three years of my study here at Orsay, France.

My deepest gratitude is first to professor Costel Petrache, my supervisor, for his systematic teaching and training me in experimental nuclear structure research. He has walked me through all the stages of the writing of this thesis. Without his continuous and enlightening guidance, this thesis would not have been in its present form. It is my great honor to have a supervisor who is so famous in nuclear physics. His personal qualities, like work hard, great passion for research, explorative spirit..., will influence me more in the future. Also, I am very grateful to him for his take care of me, making my life in France become more warm and comfortable.

I also thank all the teachers and professors of nuclear structure group of IMP, Lanzhou, in particular, Minliang Liu, my supervisor, for his generous supports and comments with incomparable patience. He inspired me to study nuclear physics. Also, I would like to thank Guo Song and Bingfeng Lv for their selfless sharing of many data analysis skills used in the present work.

I would like to thank all our collaborators and my IJCLab colleagues. I'm thankful to Alain Astier, Guillaume, Min for their nice and useful suggestions.

I am thankful to the jury members of my PhD defense, Dr. Amel Korichi, Prof. Philip Walker, Prof. Daniele Mengoni, Prof. Furong Xu, and Prof. Mark Riley for having spent their valuable time to evaluate my PhD work and read my thesis, also to give suggestions and comments on my manuscript.

I would like to thank all my friends for their supports and encouragements. I want to thank my roommates Etienne, Marie, Florian, who shared a lot stuff with me during the confinements. I also want to thank my dear friend Miaobo Pan, for her accompany, invariable encouragement, and friendship, which help me to get through hard time, particularly in the last year of my PhD.

I would like to thank the financial support of China Scholarship Council and the IMP nuclear structure group.

Finally, I would like to express my most heartfelt gratitude to my family for their constant spiritual support, concern and selfless love in my student career. Their loving considerations and helps are the source of my strength and the greatest fortune of my life.

Contents

Chapter 1

Introduction

The nucleus is an interacting quantum many-body system that includes two types of components: protons and neutrons. A proton is composed of two up quarks (u) and one down quark (d), while a neutron has one up quark (u) and two down quarks (d). The nuclei can contain nucleons from a few to several hundred. Thus, describing a nuclear system composed of many interacting particles, each one with its internal structure, is a enormous task. There are various theoretical models which approximate this complex many-body system with a simpler one to make it more tractable. Meanwhile, experimentally, gamma spectroscopy and nuclear reaction studies are carried out to get a greater comprehension of the nucleus.

From the theoretical point of view, there are different mathematical models ranging from single particle to collective. The former treats the nucleus as an ensamble of individual particles moving in the mean field potential generated by all particles, like in the shell model [1], while the latter considers the nucleons as moving together, collectively, like in the liquid drop model [1]. During the years, the understanding of the nuclear structure progressed, more and more models have been developped. In one of these models, called the cranking model [1], the individual particles are moving in a rotating mean field [2]. A version of this model has been used to interpret the results observed in the current work. From the experimental point of view, sophisticated devices, like accelerators, detectors, and dedicated electronics, have been developed to produce and detect the radiation and particles emitted by the excited nuclei [3].

The present work is devoted to the spectroscopy of the extremely proton-rich nuclei in the A $\approx$ 120 mass region, in particular ^{119}Cs, ^{118}Cs, and ^{119}Ba. The study of the nuclei in this mass region is interesting because they offer the opportunity to investigate several phenomena, like proton-neutron interaction, evolution of the nuclear deformation towards the middle of the major shells $N, Z = 52 - 82$, direct and β-delayed charged particle emission. In addition to these main topics, we also can study the properties of collective rotation bands from low to very high spin, as well as the existence of multiple isomeric states as predicted in Ref. [4]. During our study, other, unexpected phenomena in this mass region are discovered, like for example shape coexistence and chirality in strongly deformed nuclei.

1.1 Chirality

Chirality is a symmetry property of an object or a system which can be distinguished from its mirror image. In 1893, Lord Kelvin first described the concept of Chirality as follows [5]: *"I call any geometrical figure, or group of points, chiral, and say it has chirality, if its image in a plane mirror, ideally realized, can not be brought to coincide with itself."*

Chirality is a very common phenonenon in nature, being observed in physics, mathematics, biology, and chemistry. There are two typical examples of chiral system: the first one consists of the two human hands, left and right, which have fingers with the same order, but they are not mirror images [6], and the second concerns the handedness of molecules, like two enantiomers of a generic amino acid, which has a non-superposable mirror image [7]. In physics, chirality is one of the most important properties of mass-less particles whose spin direction can be parallel or anti-parallel to the direction of motion.

The chiral symmetry breaking can be static and dynamic. In molecules composed of more than four atoms, the chiral symmetry breaking is in a static regime, and occurs when the positions of two atoms are inverted. The nuclei exhibit the chirality when two conditions are satisfied, axial-asymmetry and dynamic regime: triaxial shape, and rotating around an axis out of the principal planes of intrinsic reference system.

1.1.1 Nuclear chirality

In 1997, S. Frauendorf and J. Meng defined the chirality for a rotating nucleus by means of a aplanar Tilted Axis Cranking solution [8]. It was the first time that chirality was proposed in nuclear physics. The aplanar rotation of a triaxial nucleus is shown in Fig. 1.1, in which the rotation axis defined by the total angular momentum $\vec{I}$ is out of the planes defined by the three principal axes of the triaxial density distribution.

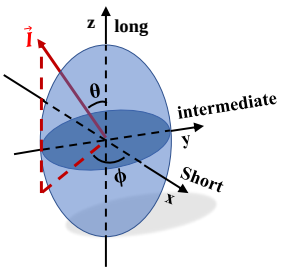

Figure 1.1: Aplanar rotation of a triaxial nucleus. The total angular momentum is $\vec{I}$. x, y, and z show the short, intermediate, and long axes [9].

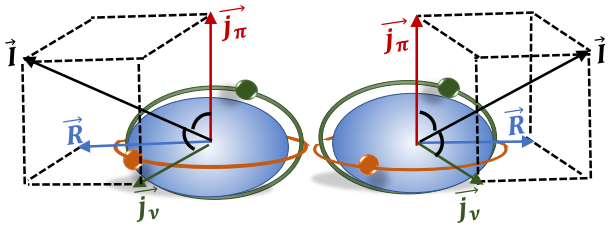

Figure 1.2: Aplanar rotation of a triaxial odd-odd nucleus. $\vec{I}$, $\vec{j}_\upsilon$, $\vec{j}_\pi$, $\vec{R}$ are the total angular momentum, the angular momenta of the neutron, of the proton, and of the core, respectively [10].

The nuclear chirality results from a combination of dynamics induced by rotation, and of geometry induced by the triaxial shape. Chirality is a key fingerprint of nuclear triaxiality. For a spherical or near spherical odd-odd nucleus,

the system is highly symmetric, and existence of mirror images is forbidden quantum mechanically. But a triaxial odd-odd nucleus with three axes of different length, named short, long, and intermediate (see Fig. 1.1), has the chance to spontaneously break the chiral symmetry. In a triaxial nucleus, the nucleons can move in orbits which are perpendicular to each other and to the core. This occurs when the proton Fermi surface lies near the lower part of a high-j subshell, making its angular momentum oriented along the short axis, and the neutron Fermi surface lies in the higher part of a high-j subshell so that its angular momentum is directed along the long axis. In such a case, the interaction energy is minimized as this configuration enables maximum overlap of the valance-particle wavefunctions with that of the triaxial core. Meantime, according to the irrotational flow model [11], the angular momentum of the rotating core get aligned along the intermediate axis as it is the largest, thereby minimizing the rotational energy. These three mutually perpendicular angular momenta can be arranged into a left- and right-handed system (see Fig. 1.2), which differ by intrinsic chirality. The left- and right-handed systems can be transformed from one to the other by the chiral operator of the form $\chi = TR(\pi)$, where $R(\pi)$ corresponds to a rotation of 180°, while T is the time reversal and therefore changes to opposite the directions of the angular momentum vector of the core. When the chiral symmetry is broken in the intrinsic reference system, the restoration of the symmetry in the laboratory reference system gives rise to a pair of nearly-degenerate bands connected by $\Delta I = 1$ transitions and having the same parity which are ”chiral-doublet” bands [8].

The first chiral bands have been observed in ^{134}Pr [12]. Later, K. Starosta and T. Koike studied the odd-odd nuclei in the $A = 130$ mass region, which have $\pi h_{11/2}\nu h_{11/2}$ configurations [13]. Today, a multitude of chiral bands have been observed in the $A \sim 80, 100, 120, 130, 190$ mass regions in all types of nuclei: odd-odd, odd-even, and even-even [14]. Thus, chirality in nuclei is a well established phenomenon. All these experimental studies indicate that chiral symmetry is not confined to a particular configuration in a specific mass region or particular types of nuclei.

One of the most extended sequences of chiral nuclei is that of odd-odd Cs isotopes, from ^{122}Cs to ^{132}Cs [14, 15].

1.1.2 Fingerprints for the chiral bands

Since the prediction of nuclear chirality in 1997, tremendous progresses both the experimental and theoretical fingerprints of chiral bands [14]. The doublet bands must satisfy a set of criteria in order to be recognized as chiral partner bands. In this section, we will introduce these criterias.

I: Energies

The $|I\mathcal{L}\rangle$ and $|I\mathcal{R}\rangle$ orthogonal functions which describe the left- and right-handed states of a near degenerate $\Delta I = 1$ bands system. It is easy to show that the following relations hold [16]:

$$\hat{C}_i|I\mathcal{L}\rangle = |I\mathcal{R}\rangle, \quad \hat{C}_i|I\mathcal{R}\rangle = |I\mathcal{L}\rangle, \tag{1.1}$$

where $\hat{C}_i$ is the chiral transformation. The eigenstates of $\hat{C}_i$ are $|I+\rangle$ and $|I-\rangle$ which satisfy [16, 17]

$$\begin{aligned} |I+\rangle &= \frac{1}{\sqrt{2}}(|I\mathcal{L}\rangle + |I\mathcal{R}\rangle), \quad \hat{C}_i|I+\rangle = +1|I+\rangle, \\ |I-\rangle &= \frac{i}{\sqrt{2}}(|I\mathcal{L}\rangle - |I\mathcal{R}\rangle), \quad \hat{C}_i|I-\rangle = -1|I-\rangle. \end{aligned} \tag{1.2}$$

If the Hamiltonian H is invariant to chiral transformations, then [16]

$$\langle I\mathcal{L}|H|I\mathcal{L}\rangle = \langle I\mathcal{L}|\hat{C}^{+}H\hat{C}_i|I\mathcal{L}\rangle = \langle I\mathcal{R}|H|I\mathcal{R}\rangle \equiv E. \tag{1.3}$$

Because of the different deformation, couplings, and valence nucleon configuration of the two chiral partners, the bands are near degenerate instead of totally degenerate as in Eq. 1.3. Thus, one of the fingerprints for the chiral bands is that they are near degeneracy and have the identical parity, for example the near degenerate $\Delta I = 1$ bands in ^{134}Pr [12]. Normally, one considers that the bands are nearly degenerate when the difference in energy between the chiral partner bands is below 200 keV [16].

The energy staggering parameter $S(I)$ can also serve as a fingerprint for chiral partner bands. It can be extracted from the measured energies as

$$S(I) = \frac{E(I) - E(I-2)}{2I}. \tag{1.4}$$

Usually, at the beginning of the chiral band $S(I)$ exhibits slight odd/even spin staggering, which diminishes when the spin increases, and finally, $S(I)$ takes constant values [16]. Therefore, in the chiral regime, the energy staggering parameter should be almost constant and equal for the states of the same I, in the two bands [16].

II: Electromagnetic transitions

The electromagnetic transition rates in chiral doublet bands obey improtant selection rules. For odd-odd nuclei, with a $\pi h_{11/2} \otimes \upsilon h_{11/2}^{-1}$ configuration coupled to a rigid triaxial rotor with $\gamma = 30^{\circ}$, we can obtain the following approximation of $I \gg 1$ states [17]:

$$\langle I\mathcal{L}|E2|I\mathcal{R}\rangle \approx 0 \quad and \quad \langle I\mathcal{L}|M1|I\mathcal{R}\rangle \approx 0, \tag{1.5}$$

where $E2$ and $M1$ are the electric-quadrupole and the magnetic-dipole operators, respectively. Using the eigenstates from Eq. 1.2, we can obtain [17]

$$\begin{aligned} B(E2 or M1; I'+ \rightarrow I+) &= B(E2 or M1; I'- \rightarrow I-) \\ B(E2 or M1; I'+ \rightarrow I-) &= B(E2 or M1; I'- \rightarrow I+). \end{aligned} \tag{1.6}$$

Thus, we can get the selection rules for both interbands and intrabands with $E2$ and $M1$ transitions, respectively. The selection rules are shown in Fig. 1.3. The thick arrows indicate allowed $E2$ transitions and stronger $M1$ transitions. The thinner arrows indicate the weaker $M1$ transitions. The solid and dashed lines separate the eigenvalues of +1

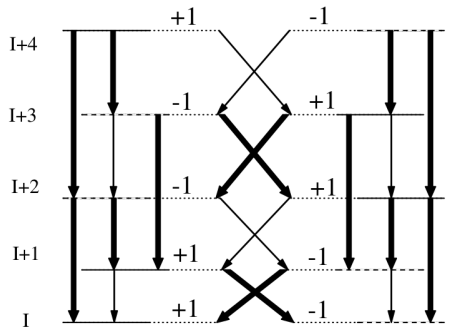

Figure 1.3: Selection rule expected for both interbands and intrabands $E2$ and $M1$ transition in a chiral geometry states. This figure was taken from Ref. [17].

and -1. The properties of electromagnetic transitions therefore can be used for identifying the chiral bands.

In addition, it is found that the $B(M1)$ staggering is sensitive to the triaxiality parameter γ. It depends strongly on the character of the nuclear chirality, i.e., the staggering is week in chiral vibration region and strong in the static regime. For partner bands with near degenerate energy spectra and similar $B(M1)$ and $B(E2)$ transitions, the strong $B(M1)$ staggering can be used as a fingerprint for the static chirality [18]. Ideally, spin alignments, the moment of inertia, the electromagnetic transition probabilities should be equal, but in practice they are very similar for the chiral doublet bands [16].

A. A. Raduta summarized the chirality fingerprints from electromagnetic transitions in Ref. [16] as follow:

a: Almost constant energy difference between partners;

b: Similar intra-band transitions probabilities;

c: Similar single-particle alignments;

d: Attenuated energy staggering;

e: B(M1) staggering (so far observed only in Cs nuclei).

III: Theoretical fingerprints for the chiral bands

The key to form chiral bands in triaxial nuclei is the existence of aplanar total angular momentum. Using wave functions obtained from the particle rotor model, one can calculate the expected values of the total $\langle \hat{I} \rangle$, quasi-

neutron $\langle\hat{j}_{ni}\rangle$, quasi-proton $\langle\hat{j}_{pi}\rangle$, and core $\langle\hat{R}_i\rangle$ angula momenta. The expected values for the three components of the total angular momenta are given as [16, 19]

$$R_i(I) = \sqrt{\langle I|(I_i - j_{pi} - j_{ni})|I\rangle}, \quad j_{pi}(I) = \sqrt{\langle I|j_{pi}^2|I\rangle}, \quad j_{ni}(I) = \sqrt{\langle I|j_{ni}^2|I\rangle}, \tag{1.7}$$

where $i = 1, 2,$ and 3. When chiral-pair bands are realized, the quantities R_i , j_{pi}, and j_{ni} must be very similar for a given I [20]. If those quantities are not very similar, say different by more than 10%, in the two bands, they are not regarded as chiral-pair bands, even if the two bands are nearly degenerate [20].

Thus, A. A. Raduta summarized the theoretical fingerprints of chirality in odd-odd nuclei [16]:

a: Similar expectation values of the squared angular momenta;

b: Similar spin aligned along two perpendicular axes; A near maximal triaxiality;

c: Chirality appears only above a critical rotational frequency;

d: Degeneracy over a limited spin range.

1.1.3 Revolving chiral doublet (RχD)

The simplest chiral configuration is realized in odd-odd nuclei, in which the angular momenta of the odd proton and odd neutron are aligned along perpendicular axes of the intrinsic reference system, in a plane perpendicular to the angular momentum of the core. The chiral regime is best realized when the three-dimensional (3D) geometry of the angular momenta is well balanced, that is when the three angular momentum legs collective angular momentum of the core along one axis and single-particle angular momenta of the active quasiparticles along the two other axes are comparable [21]. Chiral bands have been first identified in odd-odd nuclei with well balanced angular momenta of the active proton and neutron [14], later in odd-even nuclei with less balanced angular momenta of the two protons and one neutron, like in ^{131}Ba [22] and ^{135,137}Nd [23, 24], and recently in the even-even nucleus ^{136}Nd [25], with very good balance of the angular momenta of the two protons and two neutrons present in the configurations of the five observed chiral bands. It is a common feature of all observed cases that both components, protons and neutrons, of this special two-component quantum many-body system play an important role in the formation of the chiral geometry. It raises the question whether the two-componentness is a crucial feature in quantum many-body systems to develop the chirality or not. Very recently we gave an answer to this question, showing that chiral bands can be also be based on configurations with only protons. In an odd-even ^{119}Cs nucleus, the observation for the first time of chiral bands reveals a new type of chirality, called *Revolving Chiral Doublet* ($R\chi D$) bands. The details are discussed in Section 5.2.3.

1.2 Shape coexistence

The phenomenon of shape coexistence may occur in nearly all nuclei and is associated with the fundamental tendency of nuclei to deform which will be discussed in Section 2.2.3 [26]. It is related to the single-particle and collective excitations. In general, in a nucleus with few valence nucleons outside the core, the subtle rearrangement of protons and neutrons around the Fermi surface may create different shapes which can coexist at similar excitation energies. In 1956, the first experimental evidence of spherical-prolate shape coexistence was observed in the ^{16}O isotope [27]. Nuclei with an oblate ground state are far more rare than those with prolate shapes. The oblate shape competes with the prolate shape at low spin only in limited regions of the nuclear chart, around proton-rich Pb [28, 29], Hg [30, 31], and $A \approx 70$ nuclei [32, 33]. At high spin, various types of oblate bands are known[26]: regular dipole bands in the $A \approx 130$ mass region have been interpreted as arising from rotation of oblate nuclei [34], rotational bands evolving from collective prolate to non-collective oblate shapes (terminating states) have been identified in Er nuclei [35], and transition from prolate to oblate shape has been identified in neutron-rich Hf nuclei [36]. Recently, an extremely stable rotational band in ^{137}Nd, extending to $\approx$ 5 MeV above yrast at the highest spin, has been interpreted as collective rotation of a nucleus with oblate shape [37]. Nonetheless, the number of experimentally observed oblate bands is very limited. In particular, no oblate bands have been observed in the strongly-deformed proton-rich $A \approx 120$ mass region nuclei, even though predictions exist since long time, based on calculations employing various interactions [38, 39, 40]. Potential energy surfaces calculated e.g. with the Gogny D1S interaction [41], exhibit coexisting prolate and oblate minima for ^{118}Xe and ^{120}Ba, which are the cores of one of the nuclei of interest in this thesis, ^{119}Cs, which is discussed in Section 5.3.1. The calculated results shown in Figs. 1.4, 1.5, and 1.6, exhabit two minima in the potential energy surface of ^{118}Xe, ^{119}Cs, and ^{120}Ba, for positive and negative quadrupole deformation corresponding to prolate and oblate shapes, respectively. The relative excitation and deformations of the minima depend on the employed single-particle interaction, but in general the oblate minimum has an excitation energy within 1 MeV relative to the ground state, is more narrow and has a smaller deformation than the prolate minimum. The theoretical calculations for odd-even nuclei are more scarce [42, 43]. Aggarwal predicted oblate ground states for ^{115}Cs and ^{117}La [43].

1.2.1 Spectroscopic fingerprints

Kris Heyde and John L. Wood introduced three types of fingerprints in Ref. [26]. The best direct one consists of the diagonal $E2$ matrix elements which require the measurement of γ-ray yields in multistep Coulomb excitation [26]. ^{104}Ru [44] and ^{108}Pd [45] show static and dynamic quadrupole moment data revealing the presence of shape coexistence. The $\langle Q^2 \rangle$ values for the ground and first-excited 0^+ states strongly support shape coexistence in ^{74}Kr and ^{76}Kr [33]. The next best fingerprint consists of the $B(E2)$ values which are widely obtained via lifetime measurements, particularly Doppler line-shape broadening and fast electronic timing, but also via Coulomb excitation [26].

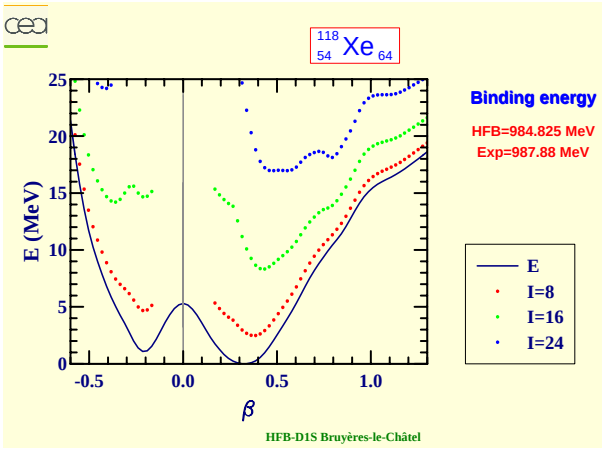

Figure 1.4: Potential energy surface calculated with the Gogny D1S interaction for ^{118}Xe. The figure was taken from Ref. [41].

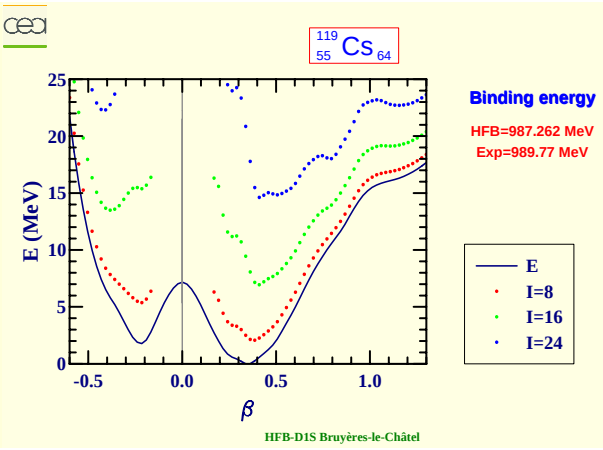

Figure 1.5: The same as in Fig. 1.4, but ^{119}Cs.

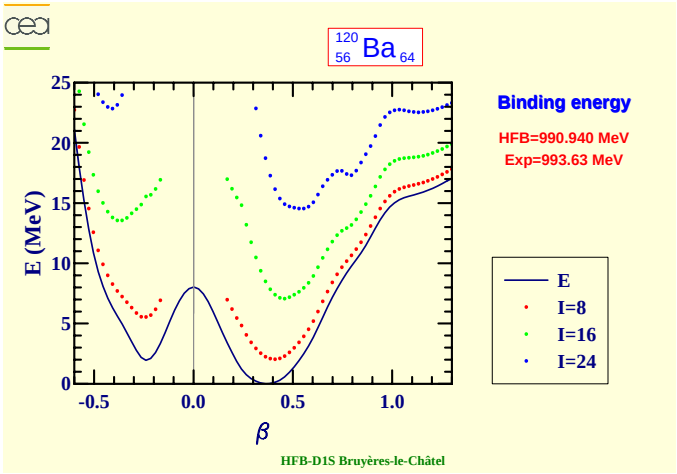

Figure 1.6: The same as in Fig. 1.4, but ^{120}Ba.

However, the $B(E2)$ values do not distinguish between static and dynamic deformation: to achieve it, the relation between the $B_{42} = B(E2 : 4^+ \rightarrow 2^+)/B(E2 : 2^+ \rightarrow 0^+)$ ratio and $B_{20} = B(E2 : 2^+ \rightarrow 0^+)$ is often used [26]. Indirect fingerprints of shape coexistence are strong $E0$ transitions and particle-core coupling patterns [26]. The strength of the $E0$ transitions depend on the mixing of configurations with different mean-square charge radii, while the particle-core coupling patterns may reveal shape coexistence through the presence of both strongly coupled ($\Delta I = 1$) and decoupled ($\Delta I = 2$) spin sequences in the same nucleus. $N = 58$ isotones (such as ^{96}Sr [46] and ^{98}Zr [47]), $N = 60$ isotones (such as ^{98}Sr [48], ^{100}Zr [48], ^{102}Mo [48], and ^{104}Ru [44]), and $N = 90$ isotones (such as ^{152}Sm [48, 49, 50], ^{154}Gd [48, 49, 51], and ^{156}Dy [48, 49, 52]) have strong $E0$ transitions. The systematics of bands built on the lowest $9/2^-$ and $13/2^+$ states in the odd-Tl isotopes (see the Fig. 18 of Ref. [26]) show strongly coupled and decoupled sequences, with small and large B(E2) values, respectively. they can be interpreted as weakly deformed oblate and strongly deformed prolate structures. Similar examples can be found in the odd-Au and $N = 39$ isotones. In addition, there are some hints, such as changes in mean-square radii (isotope and isomer

shifts), changes in masses (two-nucleon separation energies), and changes in pair occupancies (direct nucleon pair-transfer reaction cross sections), which can be used to fingerprint of shape coexistence [26].

1.2.2 Mass regions of shape coexistence

The dominant factor for the appearance of shape coexistence at low energy is a competition between an energy gap and a residual interaction [26]. This competition decreases the energy of configurations involving the promotion of nucleons across the gap [26]. The $Z = 50$ and 82 regions with $N \approx 66$ and 104, respectively, are clear manifestations of the occurrence of the "gap and interaction" mechanism. Meanwhile, the shape coexistence in the $N = 50$, and 82 regions need to be sought for $Z \approx 33, 45$ and $Z \approx 58, 74$, respectively. The consideration of gaps as ingredients of shape coexistence is not limited to only major shell gaps, but also to subshell gaps, offering thus a fairly widely applicable organizing principle. The $N = 20$ (shell), $Z = 16$ (subshell) gaps appear to control the region around ^{32}Mg. In addition, some light nuclei with $N = Z$ also show shape coexistence, such as ^{16}O, ^{40}Ca, and ^{56}Ni [26].

Shape coexistence at the low energy is therefore a relatively widespread phenomenon in different mass regions, and the criteria mentioned above can be a reference for further researches.

1.3 Motivation of this study

The primary motivation is to study the spectroscopy of the extremely proton-rich nuclei in the A $\approx$ 120 mass region with the JUROGAM 3 + MARA setup. The present thesis is only focused on the study of three of the many populated nuclei in the used ^{58}Ni(^{74}Zn,$xpyn$) reaction, that is ^{119}Cs, ^{118}Cs, and ^{119}Ba. For these three nuclei, the specific objectives are:

To study the properties of collective rotation bands from low to very high spin. The observation of such bands will help to determine the evolution of collectivety and triaxiality on the way towards the proton drip-line.

To extract the half-lives of the isomeric states from the analysis of the focal plane spectra tagged by γ rays measured by JUROGAM 3.

To search for shape coexistence at low spin in the proton-rich strongly deformed lanthanides, a phenomenon predicted since long time, but not yet observed.

To search for chiral doublet bands in very neutron defficient lanthanide nuclei.

To interpret the structures of the observed bands based on the analysis of the alignment properties of the bands, on systematics and on particle number conserving cranked shell model calculations.

1.4 Outline of thesis

The organization of the thesis is as follows:

Chapter 1: Few properties of nuclei, chirality and shape coexistence.

Chapter 2: Brief description of relevant basic nuclear models, liquid drop model and shell model.

Chapter 3: Common experimental methods and techniques used in nuclear spectroscopic studies.

Chapter 4: Details of experimental methods and data analysis used in this thesis.

Chapter 5: Experimental results and discussion of ^{119}Cs.

Chapter 6: Experimental results and discussion of ^{119}Ba.

Chapter 7: Experimental results and discussion of ^{118}Cs.

Chapter 8: Conclusions and future work.

Appendix A: Detailed information of JUROGAM 3 detectors.

Appendix B: Résumé en français.

Chapter 2

Theoretical background

In this chapter, some theoretical structure models and specific properties related to the present work will be presented.

2.1 Independent-particle and collective motions in nuclei

2.1.1 Independent-particle motion

In many situations, it is useful to have some schematic nuclear one-body potential for which analytic solutions exist. Two such potentials are the *harmonic oscillator* and the *infinite square well*. When a nucleon moves in a stationary orbit with a fixed angular momentum, its potential energy can be that of the *harmonic oscillator*, which is [1]

$$V(r) = -V_0 + \frac{1}{2}M\omega^2 r^2, \tag{2.1}$$

or of the *infinite square well*, which is [1]

$$V(r) = \begin{cases} -V_0, & r < R \\ \infty, & r < R. \end{cases} \tag{2.2}$$

In spherical coordinates, a wave function $\psi = R(r)Y_{lm}(\theta, \varphi)$, where $R(r)$ describes the radial wave function and Y_{lm} is an eigenfunction of the angular momentum operator l^2:

$$l^2 Y_{lm}(\theta, \varphi) = \hbar^2 l(l+1) Y_{lm}(\theta, \varphi). \tag{2.3}$$

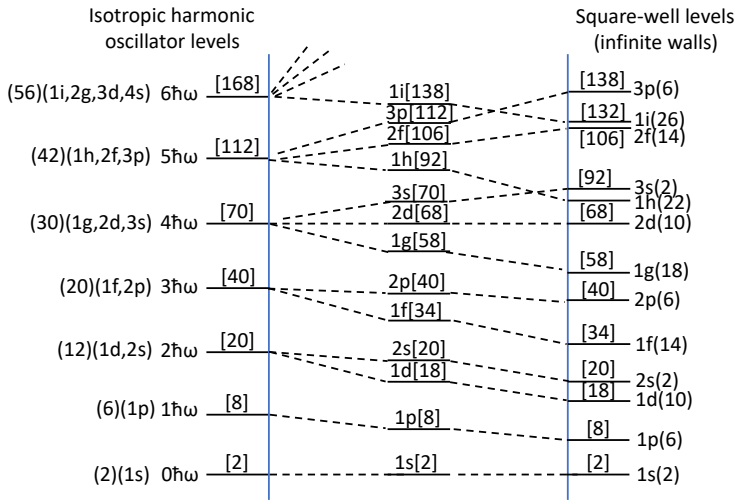

Figure 2.1: The levels of an harmonic oscillator, a square well, and a intermediate potential shape [53].

The Schrödinger equation for the radial wave function is written as [54]

$$\left(-\frac{\hbar^2}{2M}\frac{1}{r}\frac{d^2r}{dr^2}+\frac{\hbar^2 l(l+1)}{2Mr^2}+V(r)-E\right)R(r)=0. \tag{2.4}$$

Introding the harmonic oscillator potentail of Eq. 2.1 into Eq. 2.4, one can obtain the energy eigenvalues [54]

$$E=\hbar\omega\left(N+\frac{3}{2}\right) \tag{2.5}$$

with $N=2(n-1)+l$, where $n=1,2,3,...$, and $l=0,1,2,....$ The degeneracy of the state (n,l) is $D_l=2(2l+1)$. Replacing $V(r)$ of the infinite square-well given by Eq. 2.2 into Eq. 2.4, we obtain the energy eigenvalues [54]

$$\begin{aligned} E(l=0,n=1)&=\frac{\hbar^2}{2MR^2}\pi^2,\\ E(l=0,n=2)&=\frac{\hbar^2}{2MR^2}4\pi^2,\\ E(l\neq 0)&=\frac{\hbar^2}{2MR^2}\xi_{ln}^2. \end{aligned} \tag{2.6}$$

Here, the quantum number n is correlated with the number of nodes of the radial wave function. ξ_{ln} is the root of $j_l(\xi)=0$ (where $j_l(\xi)=\xi^l\left(-\frac{1}{\xi}\frac{d}{d\xi}\right)^l\frac{\sin\xi}{\xi}$ [54]). The energy spectrum is shown in Fig. 2.1, where the left is the calculation for harmonic oscillator potential and the right is for a square-well. The $s,p,d,...$ denote the values of $l=0,1,2,...$ in Fig. 2.1. One can see that the levels for an oscillator potential are evenly spaced and highly degenerate [54]. The degenerates presented in the spectrum of the harmonic oscillator are removed in the spectrum of a square-well, and the states of higher angular momentum move to lower energies [54].

2.1.2 Collective motion of nuclei

The independent-particle model explains many nuclear properties, but fail to accounts for the lager nuclear quadrupole moments and spheroidal shapes which many nuclei have. It is clear that such large effects can only arise from co-ordinated motion of many nucleons, which is the collective motion of nuclei. Many nuclear models have consider the collective motion, where the simplest collective model is the liquid drop model which we will discuss in Section 2.2.1.

2.2 Nuclear models

2.2.1 Liquid drop model

The liquid drop model was proposed by George Gamow in the 1920s and further developed into a complete model by Niels Bohr et al. in the 1930s [55, 56, 57]. It was historically the first model proposed for the explanation of the different properties of the nucleus. The model considers the nucleus as a drop of incompressible fluid of very high density, held together by the nuclear force (resulting from the strong force). While a crude model, the liquid drop model accounts for many properties of the nucleus. One of the basic properties of the nucleus is its binding energy $E_B(N, Z)$, where N and Z are the number of neutrons and protons, respectively. Many attempts were made to reproduce the nuclear binding energy, but the *semi-empirical mass formula* proposed by Weizsäcker and Bethe in the liquid drop model is one of the most successful. The *semi-empirical mass formula* states that the binding energy is [58, 59]:

$$\begin{aligned} E_B &= (Nm_n + Zm_p - m)c^2 \\ &= a_v A - a_s A^{2/3} - a_c \frac{Z^2}{A^{1/3}} - a_a \frac{(N-Z)^2}{A} + \delta(A), \end{aligned} \tag{2.7}$$

where m_n, m_p, m, and $A = N + Z$ indicate the mass of neutron, proton, nucleus, and the mass number, respectively. The five terms have the following physical meaning.

-The first term is related to the volume of the nucleus, being called *volume term*. When an assembly of nucleons of the same size is packed together into the smallest volume, each nucleon at the interior of the nucleus has a certain number of other nucleons in contact with it. The *volume term*, therefore, is proportional to the mass number A.

-The second term is negative, is called the *surface term*, and is proportional to the surface area of the nucleus. It's similar to the liquid surface tension. This term corrects for the previous assumption made, that every nucleon interacts with the same number of other nucleons.

-The third term is the potential energy from each pair of protons, being called the *Coulomb energy*. It is repulsive and reduces the binding energy. The *Coulomb energy* derives from the electrostatic interaction among protons, and

is therefore proportional to Z^2.

-The forth term, called *asymmetry energy* or *Pauli energy*, accounts for the Pauli exclusion principle. It reflects the fact that the nuclear force favors equal numbers of neutrons and protons. Unequal numbers of neutrons and protons imply filling higher energy levels for one type of particles, while leaving lower energy levels vacant for the other type.

-The last term, called *pairing energy*, favors configurations in which two identical fermions are paired. Based on the types of nuclei, it can be rewritten as follows:

$$\delta(A) = \begin{cases} a_p A^{-3/4}, & \text{even-even nuclei} \\ 0, & \text{even-odd, odd-even nuclei} \\ -a_p A^{-3/4}, & \text{odd-odd nuclei.} \end{cases} \tag{2.8}$$

The *pairing energy* accounts for the tendency of protons and neutrons to be coupled in pairs. The five coefficients a_v, a_s, a_c, a_a, and a_p are calculated by fitting to experimentally measured masses of nuclei. The following values are extracted by Wapstra in Ref. [60]: $a_v = 14.1$ MeV, $a_s = 13$ MeV, $a_c = 0.595$ MeV, $a_a = 19$ MeV, and $a_p = 33.5$ MeV.

The liquid drop model successfully predicted the nuclear binding energies and explained nuclear fission [61]. As a collective model, it's particularly useful in describing the macroscopic behaviour of the nucleus. However, the model is not adequate for explaining microscopic properties in nuclei, as for example the *magic numbers*. This led to the development of the nuclear shell model in the coming years.

2.2.2 The shell model

In the 1940s, scientists found that certain nuclei have special properties, for example are more stable, have bigger binding energy, have bigger first excited energy, and have bigger separation energy of one nucleon than its neighbors, when it has certain values of Z or N. These certain values are called *magic numbers* [62]. The seven most widely recognized magic numbers as of 2019 are 2, 8, 20, 28, 50, 82, and 126. The existence of magic numbers implies that the nucleus has a shell structure. Meanwhile, the success of the shell model in the description of the atomic structure led to the development of an analogous model for the atomic nucleus. In 1949, Mayer and Jensen [63, 64] firstly proposed the nuclear shell model to interpret the structure in nuclei. The model assumes that the nucleon move independently in an average potential produced by all nucleons. The structure of the nucleus in terms of energy levels is built following the Pauli exclusion principle which prevents the occupation of the same quantum state by two identical nucleons. The independent motion of the nucleons is quite similar to the motion of electrons

in the atom. The Schrödinger equation can be written as

$$(-\frac{\hbar^2}{2m}\Delta^2 + V(r))\psi_i(r) = \epsilon_i\psi_i(r), \tag{2.9}$$

where $\psi_i(r)$ and ϵ_i are the eigenstates and eigenvalues, respectively. The potential $V(r)$ can have different expressions, as for example the simple harmonic oscillator, the square-well, or the Woods-Saxon potentials. The comparison of these three potentials is shown in Fig. 2.2.

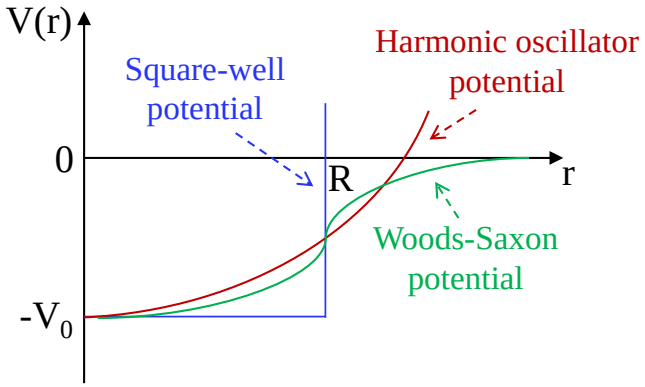

Figure 2.2: Comparison between the harmonic oscillator, the square-well, and the Woods-Saxon potentials. V_0, $R \approx r_0 A^{1/3}$, and r are the depth of the well, nuclear radius, and the distance from the origin, respectively.

For the harmonic oscillator potential, the Hamiltonian is:

$$H = \frac{\hbar^2}{2m}\Delta^2 - \frac{1}{2}m\omega^2 r^2, \tag{2.10}$$

where m and ω are the mass of the particle and the angular frequency of the oscillator. The energy eigenvalues of the Schrödinger equation for one-body harmonic oscillator potential have been given in Eq. 2.5, which shows that the levels with the same principal quantum number N are $2(2l+1)$ degenerate. According to the parity conservation, the parity of each level is defined as:

$$\pi = (-1)^N. \tag{2.11}$$

The harmonic oscillator potential can only reproduce the magic numbers 2, 8, and 20.

A more realistic potential which better reproduces the nuclear properties is the Woods-Saxon potential which is given by [65]

$$V_{WS}(r) = \frac{V_0}{1 + e^{(r-R)/a}}, \tag{2.12}$$

where a represents the skin thickness which describes the diffuseness of the nuclear surface. The typical values

for the parameters are: $V_0 \approx -50$ MeV, $a \approx 0.5$ fm. One can see from Fig. 2.2 that V_{WS} has a flatter edge than the harmonic oscillator potential and its bottom is not as sharp as in the square-well potential. Compared with the harmonic oscillator potential it removes the l degeneracies of the major shells, filling the shells in order with $2(2l+1)$ levels. However, the limitation of the this potential is the same as that of the harmonic oscillator. They only can reproduce the 2, 8 and 20 magic numbers.

In order to break the limitation, the spin-orbit interaction $\vec{l} \cdot \vec{s}$ has been added into the single-particle Hamiltonian by Mayer et al. [63, 64]. The additional term leads to the splitting of the states with the same orbital angular momentum l. The total angular momentum j of a single particle is given by

$$j = l \pm s, \tag{2.13}$$

where the use of the $\pm$ sign depends on whether the orbital angular momentum l is aligned or anti-aligned with respect to the spin s. For a nucleon, which is fermion, the spin $s = \frac{1}{2}$. The total angular momentum j of the split-up levels are therefore expressed by $j = l \pm \frac{1}{2}$. As the opposite to the case of atoms, in nuclei, the level with $j = l + \frac{1}{2}$ is lower than the level with $j = l - \frac{1}{2}$. The splitting energy ΔE is proportional to $2l + 1$. If an orbital angular momentum l has a large value, the next highest oscillator shell may invade the opposite-parity lower level shell, resulting in an *intruder orbital* in the shell. The intruder state plays a significant role in the nuclear shell structure, especially in the shape evolution of transitional nuclei.

The shell model plays a central role in the nuclear physics and it successfully reproduced the magic numbers, the spins and parties of the ground states of most spherical nuclei, energy levels, magnectic moments of ground states, and other properties [53, 66]. However, the shell model with the spin-orbit coupling term is still not sufficiently precise to describe the nuclei which are far away from the closed shells. Thus, some other models have been developed to describe and understand the properties of aspherical nuclei.

2.2.3 The deformed shell model: the Nilsson model

I: Deformation of nuclei

The nucleus is treated as an incompressible liquid drop in the liquid drop model. But the shape surface of the nucleus is not necessarily spherical. We can imagine it to undergo dynamical shape or surface oscillations. In order to investigate these oscillations, we can parametrize the surface in some way. One possibility is to describe it by the length of the radius vector pointing from the origin to the surface [1]

$$R = R(\theta, \phi) = R_0 \left[1 + \alpha_{00} + \sum_{\lambda=1}^{\infty} \sum_{\mu=-\lambda}^{\lambda} \alpha_{\lambda\mu} Y_\lambda^\mu(\theta, \phi) \right], \tag{2.14}$$

where R_0 is the radius of the sphere with the same volume, α_{00} is a factor of nuclear volume conservation, θ and ϕ are polar angles, λ represents different modes of deformation, $Y_\lambda^\mu(\theta,\phi)$ are the spherical harmonics, and $\alpha_{\lambda\mu}$ is the amplitude of the spherical harmonic component. Such a surface is certainly not the most general one, but it is widely used and extremely useful in nuclear structure [1]. It is instructive to look at the shapes of the lowest multipolarity in Eq. 2.14, as displayed in Fig. 2.3.

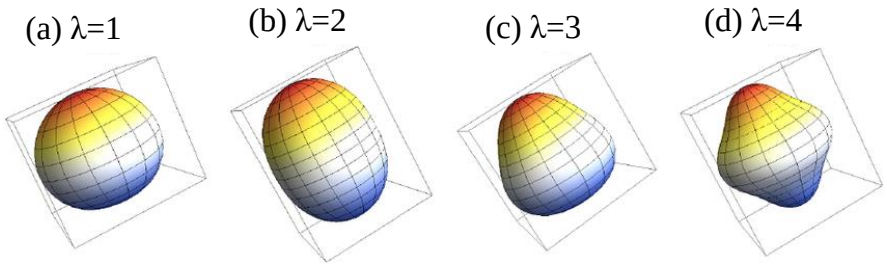

Figure 2.3: Nuclear shapes with dipole ($\lambda = 1$), quadrupole ($\lambda = 2$), octupole ($\lambda = 3$), and hexadecupole ($\lambda = 4$) deformations. Figure was taken from Ref. [67].

The lowest order multipole term, $\lambda = 1$, describes mainly (at least for small deformations) a transition of the whole system. The nuclear shape is shown in Fig. 2.3 (a) which is a sphere. It expresses a shift of the position of the center of mass. This shift can be modified by using the relation between the origin of the coordinate system and the center of mass system. Thus, the term $\lambda = 1$ is equivalent to a translation of the nucleus that should be neglected for nuclear excitations.

The deformations corresponding to $\lambda = 2$ look like ellipsoidal deformations. In this case, three types of shapes, *oblate*, *prolate* (see Fig. 2.3 (b)), and *triaxial*, can exist. Two semi-major axes are equal in the *oblate* and *prolate* shapes, while all axes lengths are different in the *triaxial* shape. It turns out to be the most important mode of excitation of the nucleus, therefore $\lambda = 2$ quadrople deformation will be discussed more details in the next section.

The term $\lambda = 3$ describes the octupole deformations and is associated with pear shape (see Fig. 2.3 (c)). Although the octupole deformation is the principal asymmetric mode of deformation of the nucleus, calculations taking it into account are much more complicated than the calculations for only quadrupole deformations.

The $\lambda = 4$ multipole term corresponds to the hexadecapole deformations. One of the nuclear shapes is shown in Fig. 2.3 (d). Normally, the $\lambda = 4$ and higher order terms are small and are often neglected.

II: Deformation parameters

In the case of quadrupole deformations ($\lambda = 2$), one can have five parameters $\alpha_{\lambda\mu}$. Not all of them describe the shape of the drop. Three determine only the orientation of the drop in space, and correspond to the three *Euler angles* [1]. By a suitable rotation, we can transform to the body-fixed system characterized by three axes 1, 2, 3, which coincide with the principal axes of the mass distribution of the drop. Therefore, the five coefficients $\alpha_{\lambda\mu}$ reduce

to two real independent variables a_{20} and $a_{22} = a_{2-2}$ ($a_{21} = a_{2-1} = 0$), which, together with the three *Euler angles*, give a complete description of the system [1]. The length of the radius vector pointing from the origin to the surface is simplified as

$$R(\theta, \phi) = R_0[1 + \alpha_{20}Y_{20}(\theta, \phi) + \alpha_{22}Y_{22}(\theta, \phi) + \alpha_{22}Y_{2-2}(\theta, \phi)]. \tag{2.15}$$

It is convenient to use the coordinates β ($\beta > 0$) and γ instead of a_{20} and a_{22}, respectively. Their relationships are as follows [1]:

$$\begin{aligned} a_{20} &= \beta \cos\gamma, \\ a_{22} &= \frac{1}{\sqrt{2}}\beta \sin\gamma. \end{aligned} \tag{2.16}$$

β and γ are called Hill-Wheeler coordinates [68].

The nuclear shapes in the (β, γ) plane are shown in Fig. 2.4. One can see that: (i) the nuclear shapes are

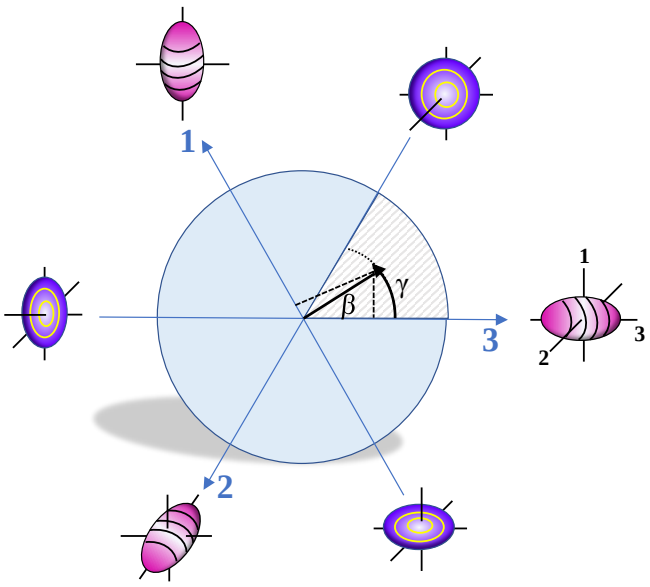

Figure 2.4: Nuclear shapes in the (β, γ) plane. The dashed lines are the projections onto the 1 and 3 axes which are proportional to the increments of δR_1 and δR_3, respectively [1].

prolate spheroids with 3, 1, and 2 axes as axes of symmetry when γ values are $0°$, $120°$, and $240°$; (ii) the nuclear shapes are oblate when γ values are $60°$, $180°$, and $300°$; (iii) the nuclear shapes correspond to triaxial when γ is not multiple of $60°$; (iv) since there are discrete symmetries, the interval $0° < \gamma < 60°$ is sufficient to describe all the $\lambda = 2$ shapes [1]. We can interchange all three axes without changing the shape, which means an in invariance under the point group D_2 [1]. All other points in Fig. 2.4 are thus obtained by suitable exchanges of the different axes; (v) one can calculate the increments of the three semi-axes, δR_1, δR_2, and δR_3, in the intrinsic reference

system as function of β and γ [1]:

$$\begin{aligned}\delta R_1 &= R_0\sqrt{\frac{5}{4\pi}}\beta\cos(\gamma-\frac{2\pi}{3}),\\ \delta R_2 &= R_0\sqrt{\frac{5}{4\pi}}\beta\cos(\gamma+\frac{2\pi}{3}),\\ \delta R_3 &= R_0\sqrt{\frac{5}{4\pi}}\beta\cos(\gamma).\end{aligned} \tag{2.17}$$

However, the parameters β and γ only describe exactly ellipsoidal shape in the limit of small β-values.

III: The Nilsson model

In the usual formulation of the shell model the potential is assumed to be isotropic, but it has been found that nuclei with proton and neutron numbers very different from those corresponding to closed shells have large deformations, as evidenced, e.g., by large quadrupole moments [69]. The deformation of the nuclear field may have a great influence on the motion of the individual nucleons. Thus, Sven Gösta Nilsson firstly proposed a deformed shell model in 1955 [69], which is also often referred to as the Nilsson model. In this model, the anisotropic harmonic oscillator potential is described as an average field. The single-particle Hamiltonian is expressed as [69]

$$H_N = -\frac{\hbar^2}{2m}\Delta+\frac{1}{2}m(\omega_x^2x^2+\omega_y^2y^2+\omega_z^2z^2)+C\boldsymbol{l}\bullet\boldsymbol{s}+Dl^2. \tag{2.18}$$

The first term is the kinetic energy of the particle. The anisotropic harmonic oscillator potential is represented by the second term where ω_x, ω_y, and ω_z are the one-dimensional oscillator frequencies in the x, y, and z directions, respectively. The third term is the same as in the shell model, included to correctly reproduce the magic numbers. C gives the strength of the spin orbit force. The inclusion of the fourth term Dl^2 adds an attractive term to the particles orbiting near the edges of the nucleus. However, for large N quantum numbers, the l^2-term shift is too strong and Nilsson replaced the fourth term with the following expression

$$D(l^2-\langle l^2\rangle_N), \tag{2.19}$$

where $\langle l^2\rangle_N=\frac{1}{2}N(N+3)$ is the expectation values of l^2 averaged over one major shell with quantum number N.

The three frequencies ω_x, ω_y, and ω_z have to be chosen proportional to the inverse of the half axes a_x, a_y, a_z of the ellipsoid [1]:

$$\omega_i=\omega_0\frac{R_0}{a_i},\ (i=x,y,z), \tag{2.20}$$

where R_0 is the nuclear radius of the sphere with the same volume. The condition for volume conservation is, therefore,

$$\omega_0^3=\omega_x\omega_y\omega_z=constant. \tag{2.21}$$

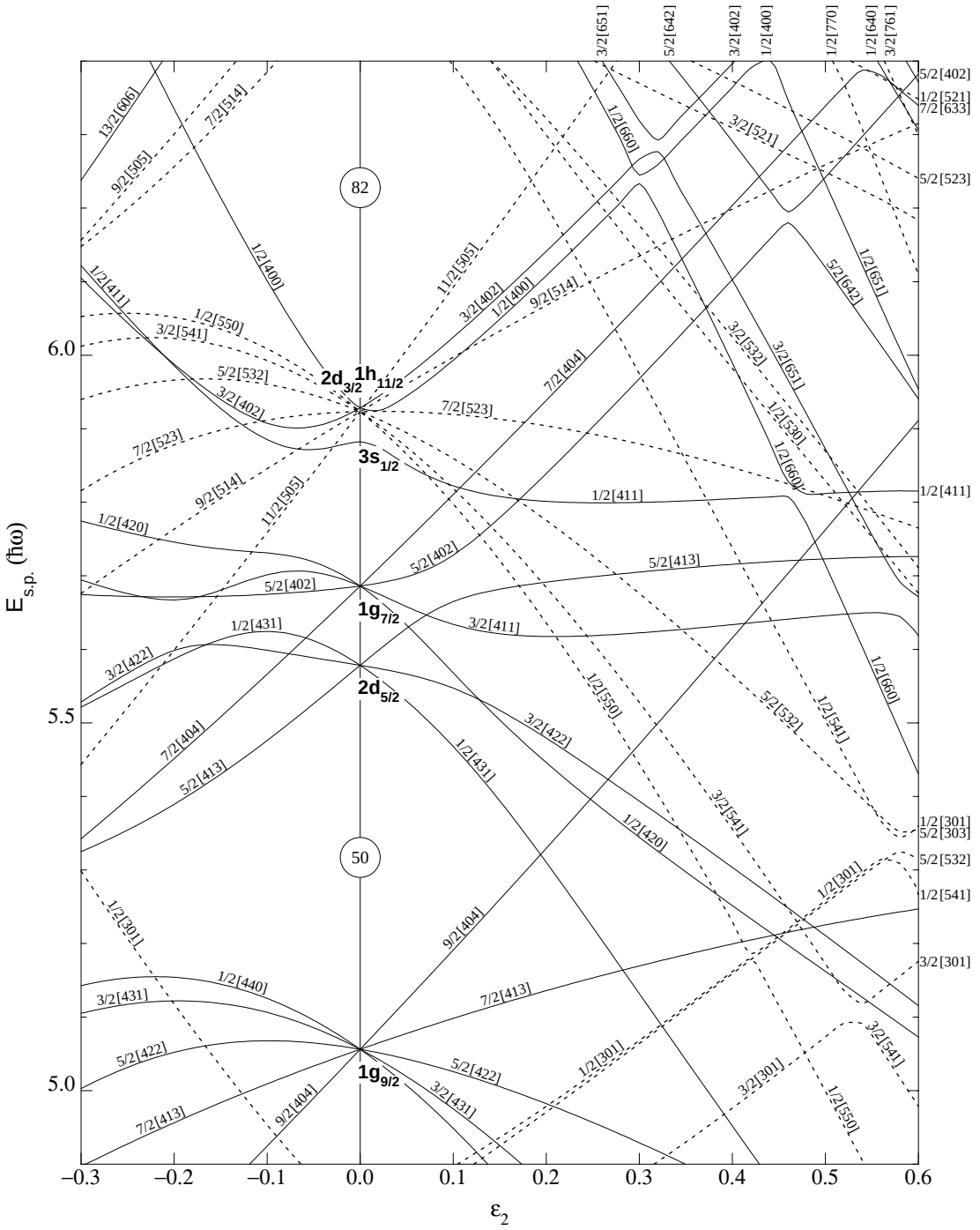

Figure 2.5: Nilsson diagram for neutrons in the $50 \leq N \leq 80$ region showing the single-particle energies as a function of the deformation parameter ϵ_2. The $\epsilon_2 > 0$, $\epsilon_2 = 0$, and $\epsilon_2 < 0$ correspond to the prolate shape, the spherical shape and the prolate shape, respectively.

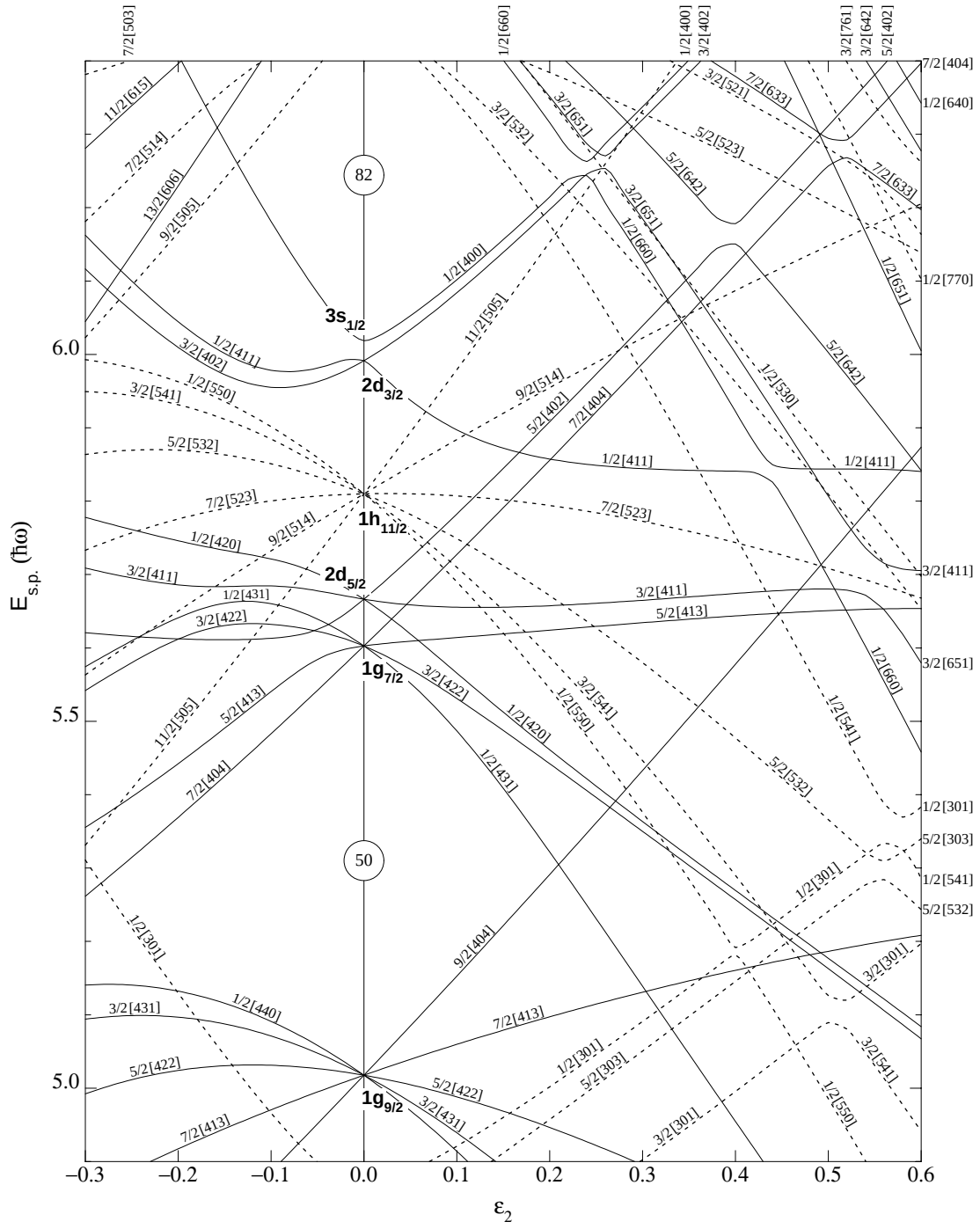

Figure 2.6: Nilsson diagram for protons in the $50 \leq Z \leq 80$ region showing the single-particle energies as a function of the deformation parameter ϵ_2. The $\epsilon_2 > 0$, $\epsilon_2 = 0$, and $\epsilon_2 < 0$ correspond to the prolate shape, the spherical shape and the prolate shape, respectively.

If one only takes into account the anisotropic harmonic oscillator Hamiltonian which is separable in x, y, z, the eigenstates are characterized by the quantum numbers of n_x, n_y, and n_z. The eigenvalues are [54]

$$\epsilon_0(n_x, n_y, n_z) = \hbar\omega_x(n_x + \frac{1}{2}) + \hbar\omega_y(n_y + \frac{1}{2}) + \hbar\omega_z(n_z + \frac{1}{2}). \tag{2.22}$$

In the case of *axially symmetric shapes*, one usually chooses the z-axis as symmetry axis and introduces a deformation parameter δ defined by [1]:

$$\begin{aligned} \omega_\perp^2 = \omega_x^2 = \omega_y^2 &= \omega^2(\delta)(1 + \frac{2}{3}\delta), \\ \omega_z^2 &= \omega^2(\delta)(1 - \frac{4}{3}\delta). \end{aligned} \tag{2.23}$$

δ is the only deformation parameter, since $\omega(\delta)$ is determined in such a way that volume conservation is guaranteed. Up to the quadratic terms in δ, we can get from Eq. 2.21 [54],

$$\omega(\delta) = \omega_0(1 + \frac{2}{3}\delta^2). \tag{2.24}$$

There is a roughly equal relation between the deformation parameters δ and β [69], as follows,

$$\delta \approx \frac{3}{2}\sqrt{\frac{5}{4\pi}}\beta \approx 0.95\beta. \tag{2.25}$$

When the above conditions (Eqs. 2.21 and 2.23) are substituted in Eq. 2.18, the Hamiltonian becomes

$$H_N = \frac{p^2}{2m} + \frac{1}{2}m\omega_0^2 r^2 - m\omega_0^2 r^2\delta^2\frac{4}{3}\sqrt{\frac{\pi}{5}}Y_{20}(\theta, \phi) + C\boldsymbol{l} \bullet \boldsymbol{s} + Dl^2, \tag{2.26}$$

where $r^2 = x^2 + y^2 + z^2$ and Y_{20} is the spherical harmonic. The terms $\boldsymbol{l} \bullet \boldsymbol{s}$ and l^2 are generally written in terms of the $\kappa(= C/2\hbar\omega_0)$ and $\mu(= 2D/C)$ parameters which depend on the type of nucleon and are obtained by fitting the experimental energy levels. In the case of axial symmetry, it is more convenient to use cylindrical coordinates. The eigenvalues are characterized by quantum numbers n_z, n_ρ, m_l, where m_l is the projection of the orbital angular momentum on to the symmetry axis. With [1]

$$N = n_z + 2n_\rho + m_l = n_x + n_y + n_z, \tag{2.27}$$

we can get from Eq. 2.22 [54]

$$\begin{aligned} \epsilon_0(n_z, n_\rho, m_l) &= \hbar\omega_z(n_z + \frac{1}{2}) + \hbar\omega_\perp(2n_\rho + m_l + 1) \\ &\simeq \hbar\omega_0\left[\left(N + \frac{3}{2}\right) + \delta\left(\frac{N}{3} - n_z\right)\right], \end{aligned} \tag{2.28}$$

where N is the principal quantum number of the major oscillator shell, m_l is a good quantum number due to the axial symmetry, n_z is the number of nodes in the wave function in the $z-$direction. Now, if one treats Eq. 2.26 by using the first order perturbation theory [54], we can obtain

$$\begin{aligned} E &= < Nn_z\Lambda\Omega|H_N|Nn_z\Lambda\Omega > \\ &= (N+\frac{3}{2})\hbar\omega_0 + \frac{1}{3}\delta\hbar\omega_0(N-3n_z) - 2\kappa\hbar\Lambda\Sigma - \mu'\hbar\omega_0(\Lambda^2 + 2n_\perp n_z + 2n_z + n_\perp - \frac{N(N+3)}{2}), \end{aligned} \tag{2.29}$$

where Σ, Λ and Ω are the projections of the spin, the orbital angular momentum, and the single-particle angular momentum on the symmetry axis, respectively. Thus, we can get $\Omega = \Sigma \pm \Lambda = \Sigma \pm \frac{1}{2}$.

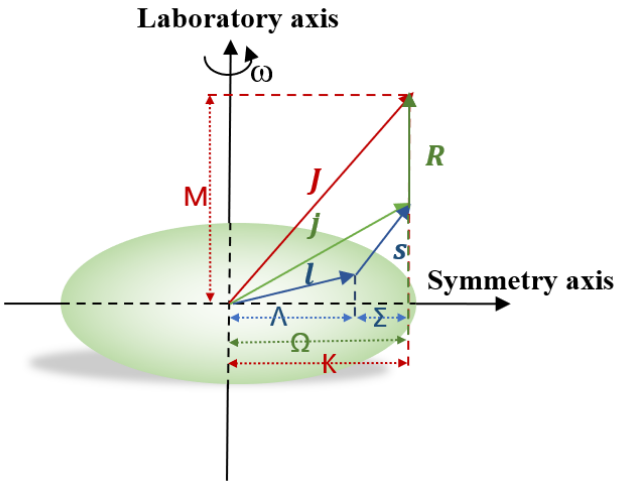

Figure 2.7: Schematic of the quantum numbers describing a deformed nucleus. Λ, Ω, Σ, and K are the projections of the orbital angular momentum l, of the total angular momentum of the particle j, of the spin s, and of the total angular momentum J onto the symmetry axis, respectively. R is the angular momentum of the core and M is the projection of the total angular momentum onto the laboratory axis.

One can solve Eq. 2.26 numerically for protons and neutrons, where the solutions are presented in Figs. 2.5 and 2.6 which are called Nilsson diagrams. The orbitals for protons and neutrons are different which arise due to the isospin dependence of the anisotropic harmonic oscillator. The energy levels in the Nilsson diagrams are often labeled by a set of "asymptotic" quantum numbers [54]

$$\Omega_\pi[Nn_z\Lambda], \tag{2.30}$$

where $\pi = (-1)^l = (-1)^N$ is the parity of the states. All the symbols are clearly shown in the Fig. 2.7. The Nilsson model successfully describes the ground state properties of deformed nuclei. But in order to correctly reproduce their high-spin behaviour, rotation has to be included, which is precisely what is implemented in the cranking model (see Section 2.2.5).

2.2.4 The particle-plus-rotor model

To describe the interplay between the motion of particles and the collective rotation, Bohr and Mottelson proposed to take into account only a few valence particles, which move more or less independently in the deformed well of the core, and to couple them to a collective rotor which stands for the rest of the particles [1]. Thus, the Hamiltonian is decomposed into two terms of intrinisic H_{intr} and collective H_{coll}, as follows [1]:

$$H_{PR} = H_{intr} + H_{coll}, \tag{2.31}$$

where

$$H_{intr} = \sum_{k} \epsilon_k a_k^+ a_k + \frac{1}{4} \sum_{klmn} \bar{v}_{klmn} a_k^+ a_l^+ a_n a_m \tag{2.32}$$

describes a microscopic motion of valence particles or a whole subgroup of particles near the Fermi level. ϵ_k are single-particle energies in the deformed potential, such as Nilsson energies. $\bar{v}$ is the interaction between the valence particles, which is, or can be, neglected in many cases [1]. The collective term H_{coll} describes the rotations of inert nuclei and is decomposed into three terms [1]:

$$H_{coll} = H_{rot} + H_{rec} + H_{Cor}, \tag{2.33}$$

where H_{rot}, H_{rec}, and H_{Cor} indicate the pure rotational operator of the rotor, the recoil energy of the rotor, and the Coriolis interaction, respectively. The total angular momentum is $\boldsymbol{I} = \boldsymbol{R} + \boldsymbol{J}$, where $\boldsymbol{J} = \sum j$ is the angular momentum of the valence nucleons. Thus, these three terms are written as [1]:

$$H_{rot} = \frac{I_1^2}{2\mathscr{I}_1} + \frac{I_1^2}{2\mathscr{I}_2} + \frac{I_3^2}{2\mathscr{I}_3}, \tag{2.34}$$

$$H_{rec} = \sum_{i=1}^{3} \frac{J_i^2}{2\mathscr{I}_i}, \tag{2.35}$$

and

$$H_{Cor} = -\sum_{i=1}^{3} \frac{I_i J_i}{\mathscr{I}_i}, \tag{2.36}$$

where the H_{Cor} couples the degrees of freedom of the valence particles to the degrees of freedom of the rotor [1]. It should be pointed that the total angular momentum operators in the laboratory reference system I_x, I_y, I_z commute with the Hamiltonian H_{PR}. Although the rotational symmetry is violated in the intrinsic reference system (e.g., in the Nilsson Hamiltonian), the model conserves angular momentum for the total system, because the operators I_x, I_y, I_z acts only on the Euler angles and commute with the intrinsic components I_1, I_2, I_3 [1]. However, it must be emphasized that this rotational invariance is achieved only through the introduction of a phenomenological core [1].

The recoil term H_{rec} acts only in the intrinsic reference system, which is often neglected since the intrinsic single-particle energies are adjusted to experimental data [1]. According to the physical situation, the different terms in Eqs. 2.32, 2.34, and 2.36 are of different importance. Therefore, it is useful to consider three limits, strong coupling, week coupling, and decoupling limit, in which one of the terms becomes predominant and which as a consequence can be solved analytically.

I: Strong coupling limit (deformation alignment)

The strong coupling limit is realized when the Coriolis interaction matrix elements are small compared with the level splitting of the single-particle energies in the deformed shell model for different values of Ω [1]. Assuming that the rotor has the 3-axis being the symmetry axis, the projection of the total angular momentum on the symmetry axis $K = \Omega$ (see Fig. 2.8), and the moments of inertia $\mathscr{I}_1 = \mathscr{I}_2 = \mathscr{I}$, the corresponding collective term for rotation of an axially symmetric nucleus is rewritten as [54]

$$\begin{aligned} H_{coll} &= \frac{1}{2\mathscr{I}}[(I_1 - J_1)^2 + (I_2 - J_2)^2] \\ &= \frac{1}{2\mathscr{I}}[(\boldsymbol{I}^2 + (J_1^2 + J_2^2) - I_3^2) + (I_+J_- + I_-J_+)], \end{aligned} \tag{2.37}$$

where $I_\pm = I_1 \pm I_2$ and $J_\pm = J_1 \pm J_2$. The term $(I_+J_- + I_-J_+)$ corresponds classically to the Coriolis and centrifugal forces, which generates a coupling between the particle motion and the collective rotation. For small I it is justified to assume that this term is small and we need therefore to take into account only its diagonal contributions, i.e. the term is treated in first order perturbation theory [54]. This approximation, in which it is assumed that the influence of the rotational motion in the intrinsic reference system of the nucleus can be ignored, is always referred to as the adiabatic approximation or the strong coupling limit [54].

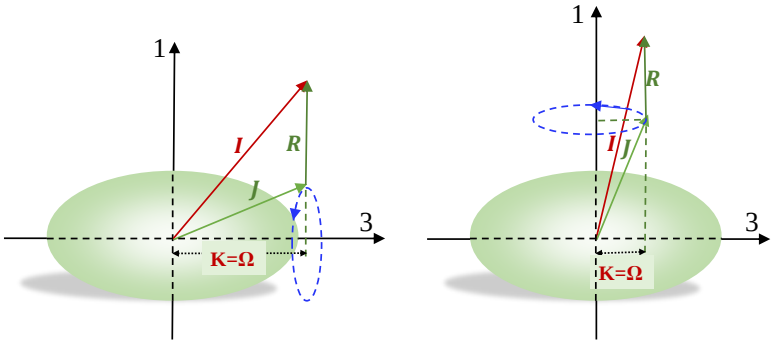

(a) (b)

Figure 2.8: Schematic diagrams of the two extreme coupling schemes: deformation alignment (a) and rotation alignment (b) [54].

In the case of the strong coupling or deformation aligned limit, the projection of the total angular momentum on

the symmetry axis K (see Fig. 2.8(a)) is a good quantum number. The total angular momentum $I = R + J$, where R is the collective angular momentum of the core. The angular momentum J of the valence particles is strongly coupled to the motion of the core, leading to J perpendicular to R: this gives rise to a band $I = K$, $I = K + 1$, $I = K + 2$, ... The total energy is given by [1, 54]

$$E_{IK} = \begin{cases} E_K + \frac{1}{2\mathscr{I}}[I(I+1) - K^2], & K \neq \frac{1}{2}; \\ E_K + \frac{1}{2\mathscr{I}}[I(I+1) - a(-1)^{I+\frac{1}{2}}(I+\frac{1}{2})], & K = \frac{1}{2}, \end{cases} \tag{2.38}$$

where E_K is the quasiparticle energy and a is the decoupling factor which is calculated by [1]

$$a = -\sum_{nj} |C_{nj}|^2 (-1)^{j+\frac{1}{2}}(j + \frac{1}{2}). \tag{2.39}$$

II: Weak coupling limit (no alignment)

The strong coupling approximation breaks down if the Coriolis matrix elements are not longer negligible compared to the energy splitting of the single-particle levels belonging to different K values [1]. In the weak coupling limit, which is realized for very small deformations, the odd particle essentially moves on spherical shell model levels only slightly disturbed by, for example, the quadruple vibrations [1].

III: Decoupling limit (rotational alignment)

In the decoupling limit, the Coriolis force is so strong that the coupling to the deformation of the core may be neglected [1]. The corresponding rotor Hamiltonian H_{coll} is rewritten as [54]

$$H_{coll} = \frac{\hbar}{2\mathscr{I}}(I^2 + J^2 - 2\boldsymbol{I}\cdot\boldsymbol{J}). \tag{2.40}$$

The principle of minimisation of the total energy shows that for a fixed I and for a more or less fixed J, the term $\boldsymbol{I}\cdot\boldsymbol{J}$ tries to align the intrinsic spin J with the total spin I.

The effects of the $\boldsymbol{I}\cdot\boldsymbol{J}$-term are especially important for large J and large I [54]. In the rotation aligned case, the total angular momentum I is parallel to the single-particle angular momentum J (see Fig. 2.8 (b)). This gives rise to the typical $\Delta I = 2$ bands.

2.2.5 Cranking model

One of the most important and widely used models in the study of high-spin states of nuclei is the cranked model [70, 71, 72].

I: Cranking model

The cranking model was firstly proposed by Inglis in 1955, [73, 74], and was further developed by Bengtsson, Frauendorf and Garrett [2, 75, 76]. The basic assumption of the cranking model is: if one introduces a coordinate system which rotates with a certain frequency ω around x-axis, the motion of the nucleon in the rotating system is rather simple when the angular frequency is properly chosen; in particular, the nucleons can be described as independent particles moving in an average potential well which is rotating with the coordinate system [1]. With the coordinates in the laboratory system given by x, y, z and those in the rotating body-fixed system by x', y', z' (see Fig. 2.9), we get [54]

$$\begin{aligned} x' &= x, \\ y' &= y\cos\omega t + z\sin\omega t, \\ z' &= -y\sin\omega t + z\cos\omega t. \end{aligned} \tag{2.41}$$

The single-particle Hamiltonian of the rotating body-fixed system h_ω is defined by [54]:

$$h_\omega = h - \omega j_x, \tag{2.42}$$

where h is the single-particle Hamiltonian in the laboratory system and j_x is the x-component of the single-particle angular momentum. The cranking one-particle Hamiltonian may be summed over all the independent particles of

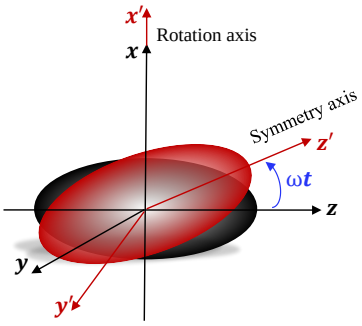

Figure 2.9: The two rotating body-fixed and laboratory systems. The body-fixed system is drawn with the red color and primed letters.

the system to obtain the total cranking Hamiltonian [54],

$$H_\omega = H - \omega J_x, \tag{2.43}$$

where $H_\omega = \sum_{i=1}^{A} h_\omega^i$ and $J_x = \sum_{i=1}^{A} j_x^i$. The Coriolis and centrifugal forces are comprised in the second term of Eq. 2.43. The Coriolis force is responsible for breaking nucleon pairs and aligning their angular momenta along the

rotational axis.

Within the cranking model we must diagonalize H_ω, and the resulting ground state wave function Φ_ω is a Slater determinant. Thus, the total energy in the laboratory system is given by [1]

$$\begin{aligned} E(\omega) &= \langle \Phi_\omega | H | \Phi_\omega \rangle \\ &= \langle \Phi_\omega | H_\omega | \Phi_\omega \rangle + \omega \langle \Phi_\omega | J_\omega | \Phi_\omega \rangle, \end{aligned} \tag{2.44}$$

and the total spin J is expressed as

$$J \approx J_x = \langle \Phi_\omega | j_x | \Phi_\omega \rangle, \quad J \gg 1. \tag{2.45}$$

The energies of the particles are measured in the laboratory system and are calculated as [1]

$$e_i^\omega = \langle \Phi_\omega^i | h | \Phi_\omega^i \rangle, \tag{2.46}$$

where the time-independent wave function, Φ_i^ω, represent the single-particle eigenfunction in the rotating system. When the above conditions (Eqs. 2.45 and 2.46) are substituted in Eq. 2.44, the total energy becomes

$$E(\omega) = \sum_i e_i^\omega + \omega J, \tag{2.47}$$

where e_i^ω are also called single-particle *Rounthians*. The slope of the Rounthian corresponds to the alignments i_x, which is written as

$$i_x = -\frac{de_i^\omega}{d\omega}. \tag{2.48}$$

The cranking model has several advantages. (i) This model provides a completely microscopic description of the rotating nucleus [1]. There is no introduction of redundant variables, therefore, we are able to calculate the rotational inertial parameters microscopically within this model and get a deeper insight into the dynamics of the rotational motion. (ii) The cranking model describes the collective angular momentum as a sum of single-particle angular momenta [1]. Therefore, collective rotation as well as single-particle rotation, and all transitions in between such as decoupling processes, are handled on the same footing. (iii) It corrects for very large angular momenta, where classical arguments apply (even if the quantum mechanical derivation does not work in this limit) [1]. However, this model has also shortcomings. (i) It is basically a nonlinear theory. Only in the limit of small angular momenta can one linearize it using perturbation theory [1]. In general, the calculations are therefore complicated, especially in case where one has several solutions. (ii) The resulting wave functions are not eigenstates of the angular momentum operators. It is therefore not clear a priori how one has to calculate, for example, electromagnetic transition probabilities [1].

II: The symmetries of the Hamiltonian

The diagonalization of the Hamiltonian can be simplified considerably if the physical system is symmetric under specific symmetry operations [70]. Note that the Hamiltonian of Eq. 2.43 is dependent on the rotational frequency ω, and therefore it breaks the time-reversal symmetry, but remains invariant with respect to space inversion (parity invariance), which means that the parity π is a good quantum number. In addition, the cranking Hamiltonian remains invariant in the one-dimensional cranking approximation with respect to a rotation through an angle π around the cranking axis [1, 70]

$$R_x = e^{-i\pi j_x}, \;\; R_x\psi_i = e^{-i\pi j_x}\psi_i. \tag{2.49}$$

The eigenvalues of R_x are [70]

$$r = e^{-i\pi\alpha}, \tag{2.50}$$

where α in the exponent is the signature quantum number. The single-particle orbitals can be classified with respect to the signature quantum number $\alpha_i(r_i)$, which can take the values $\alpha_i = +1/2(r_i = -i)$ and $\alpha_i = -1/2(r_i = +i)$. The total signature $\alpha_{tot}(r_{tot})$ of a system is defined as [70]

$$\alpha_{tot} = \sum_i \alpha_i \; mod \; 2, \quad or \quad r_{tot} = \Pi_i r_i, \tag{2.51}$$

where the sum and the multiplication extend over the occupied proton and neutron orbitals [70].

For a system with an even number of nucleons, the total signature $\alpha_{tot}(r_{tot})$ are [70]

$$\begin{aligned} \alpha_{tot} &= 0 \; (r_{tot} = +1), \quad J = 0, 2, 4..., \\ \alpha_{tot} &= 1 \; (r_{tot} = -1), \quad J = 1, 3, 5..., \end{aligned} \tag{2.52}$$

where J are the total angular momenta. For a system with an odd number of nucleons, they are [70]

$$\begin{aligned} \alpha_{tot} &= +\frac{1}{2} \; (r_{tot} = -i), \quad J = \frac{1}{2}, \frac{5}{2}, \frac{9}{2}..., \\ \alpha_{tot} &= -\frac{1}{2} \; (r_{tot} = +i), \quad J = \frac{3}{2}, \frac{7}{2}, \frac{11}{2}.... \end{aligned} \tag{2.53}$$

This classification of the single-particle states by means of the signature quantum number has proven to be, like parity, an important tool for identifying the nucleon orbitals in the rotating nuclear potential [70].

2.2.6 Nuclear rotation

In the 1950s, a general frame for the description of rotational states in nuclei was set by Bohr and Mottelson. Rotation is a typical motion corresponding to a collective degree of the freedom in nuclei. A collective excitation

is characterised by the coherent movement of a large number of nucleons. Thus, an elementary understanding of collective excitations is often achieved from macroscopic models.

I: The rotating anisotropic harmonic oscillator

Many of the effects observed or expected at high spin can be illustrated by the rotating anisotropic harmonic oscillator potential. The projection of orbital angular momentum l_x can be calculated using the coordinates x, y, z and the momenta p_x, p_y, p_z, that is $l_x = yp_z - zp_y$. The intrinsic spin is neglected, since the potential does not depent on it in the pure oscillator. We thus only consider the orbital angular momentum, which gives the cranking Hamiltonian [1]

$$h_\omega = -\frac{\hbar^2}{2m}\Delta + \frac{1}{2}m(\omega_x^2 x^2 + \omega_y^2 y^2 + \omega_z^2 z^2) - \omega(yp_z - zp_y), \tag{2.54}$$

where the y, z, p_z, and p_y are calculated by Boson creation operators (a_x^+, a_y^+, a_z^+) and annihilation operators (a_x, a_y, a_z) as follows [1]:

$$\begin{aligned} x &= \sqrt{\frac{\hbar}{2m\omega_x}}(a_x + a_x^+), \quad p_x = \frac{\hbar}{i}\sqrt{\frac{\hbar\omega_x}{2\hbar}}(a_x - a_x^+), \\ y &= i\sqrt{\frac{\hbar}{2m\omega_y}}(a_y - a_y^+), \quad p_y = \hbar\sqrt{\frac{\hbar\omega_y}{2\hbar}}(a_y + a_y^+), \\ z &= \sqrt{\frac{\hbar}{2m\omega_z}}(a_z + a_z^+), \quad p_z = \frac{\hbar}{i}\sqrt{\frac{\hbar\omega_z}{2\hbar}}(a_z - a_z^+). \end{aligned} \tag{2.55}$$

Expressed in terms of these operators, h_ω becomes [1]

$$\begin{aligned} h_\omega = &\sum_{i=x,y,z} \hbar\omega_i(a_i^+ a_i + \frac{1}{2}) \\ &- \frac{\hbar\omega}{2\sqrt{\omega_y\omega_z}}[(\omega_y - \omega_z)(a_y^+ a_z^+ + a_y a_z) + (\omega_y + \omega_z)(a_y^+ a_z + a_z^+ a_y)]. \end{aligned} \tag{2.56}$$

The Coriolis operator in Eq. 2.56 has two contributions. The first one creates or annihilates two oscillator quanta, therefore, it couples shells with major quantum numbers N and $N \mp 2$. The second part conserves the total number of quanta, but shifts quanta from the y-direction into the z-direction and vice versa [1].

II: Nuclear moments of inertia

For a rigid body, the moment of inertia is a quantity which determines the torque needed for a desired angular acceleration about a rotation axis. In nuclear physics, the moments of inertia are very useful to understand the rotation of the nucleus. The deformed nuclei can rotate collectively: if the nuclei are axially symmetric, the only possible rotation axis is perpendicular to the symmetry axis. For collective rotation, it is then also possible to define

one moment of inertia, $\mathscr{I}$, leading to the following Hamiltonian [54]

$$H_{rot} = \frac{\boldsymbol{R}^2}{2\mathscr{I}}, \tag{2.57}$$

where the $\boldsymbol{R}$ is the collective angular momentum. For pure collective rotation $\boldsymbol{R}$ is equal to total angular momentum I. Thus the energy can take the form [54]

$$E_I = \frac{\hbar^2}{2\mathscr{I}} I(I+1). \tag{2.58}$$

Some theoretical calculation of the magnitude of $\mathscr{I}$ is discussed in Ref. [77].

The moment of inertia $\mathscr{I}$ are extracted from measured rotational bands, and the experimental values are generally 25-50% of the rigid body values [54].

2.3 Transition probabilities

The ratios of reduced transition probabilities $B(M1)/B(E2)$ are crucial in the intrinsic nuclear structure studies. $B(M1)/B(E2)$ are extracted from the experimental transition energies and intensities, together with the multipole mixing ratio (angular distributions/correlations). It's also possible to obtain them from the measurement of the lifetime of nuclear states. Ratios of reduced transition probabilities are extracted as

$$\frac{B(M1; I \to I-1)}{B(E2; I \to I-2)} = 0.697 \frac{E_\gamma^5(E2)}{E_\gamma^3(M1)} \frac{I_\gamma(M1)}{I_\gamma(E2)} f(\delta), \tag{2.59}$$

where

$$f(\delta) = \frac{1}{1+\delta^2}. \tag{2.60}$$

$I_\gamma(M1)/I_\gamma(E2)$ is the ratio of the intensities of the transitions. δ denotes the mixing ratio ration of the $\Delta I = 1$ transitions. $B(M1)/B(E2)$ ratios are expressed in units of $(\mu_N/eb)^2$ and E_γ in MeV.

Theoretically, the transition probability $\omega(\xi)$ for electromagnetic decay of type ξ is proportional to the reduced transition probability. The factors involved in the proportionality depend on the density of photon states and the normalization of the vector potential. When these factors are included one finds [78]

$$\omega(\xi) = \frac{8\pi(L+1)}{L[(2L+1)!!]^2} \frac{1}{\hbar} \left(\frac{E}{\hbar c}\right)^{2L+1} B(\xi L; I_i \to I_f), \tag{2.61}$$

where L and E are the multipolarities and the γ-rays energies, respectively. The mean lifetime τ_m of the state is then given by $\tau_m^\xi = 1/\omega(\xi)$.

In Table 2.1 [78] are given the values of the transition probabilities for both the Weisskopf and Moszkowski estimates. E and A are the γ-ray energy in MeV and the mass number of nucleus, respectively. One can see that

the transition probability decreases rapidly when L increases.

Table 2.1: Numerical values for the single-particle transition probability (s^{-1}).

Multipole L	Electric	Magnetic (Weisskopf)	Magnetic (Moszkowski)
1	$1.0 * 10^{14} A^{2/3} E^3$	$3.1 * 10^{13} E^3$	$2.9 * 10^{13} E^3$
2	$7.3 * 10^{7} A^{4/3} E^5$	$2.2 * 10^{7} A^{2/3} E^5$	$8.4 * 10^{7} A^{2/3} E^5$
3	$3.4 * 10^{1} A^{2} E^7$	$1.0 * 10^{1} A^{4/3} E^7$	$8.7 * 10^{1} A^{4/3} E^7$
4	$1.1 * 10^{-5} A^{8/3} E^9$	$3.3 * 10^{-6} A^{2} E^9$	$4.8 * 10^{-5} A^{2} E^9$
5	$2.4 * 10^{-12} A^{10/3} E^{11}$	$7.4 * 10^{-13} A^{8/3} E^{11}$	$1.7 * 10^{-11} A^{8/3} E^{11}$
6	$4.0 * 10^{-19} A^{4} E^{13}$	$1.2 * 10^{-19} A^{10/3} E^{13}$	$4.0 * 10^{-18} A^{10/3} E^{13}$

2.3.1 Weisskopf units

For a transition from an excited state I_i to the ground state I_{gs} we find in the electric (EL) and magnetic (ML) case

$$B(EL) = \frac{(1.2)^{2L}}{4\pi}(\frac{3}{L+2})^2 A^{2L/3} \tag{2.62}$$

and

$$B(ML) = \frac{10}{\pi}(1.2)^{2L-2}(\frac{3}{L+3})^2 A^{(2L-2)/3}, \tag{2.63}$$

with the units of $e^2(fm)^{2L}$ and $\mu_N^2(fm)^{2L-2}$, respectively. For lowest values of L, the Weisskopf estimates are expressed as

$$\begin{aligned} B(E1) &= 6.446 * 10^{-4} A^{2/3} e^2 b, \\ B(E2) &= 5.940 * 10^{-6} A^{4/3} e^2 b^2, \\ B(E3) &= 5.940 * 10^{-8} A^{2} e^2 b^3, \\ B(M1) &= 1.790(\frac{e\hbar}{2Mc})^2. \end{aligned} \tag{2.64}$$

Chapter 3

Experimental techniques

One of the important topics in nuclear structure physics is the understanding of the properties of high-spin states. In order to excite the nucleus to high-spin, specific experimental techniques are used to populate the nuclei of interest via proper reaction channels. The excited nuclei, in turn, decay to their ground states though the emission of particles and γ rays. Detection and analysis of these particles and γ rays help to reveal various phenomena. In this chapter, the population of high-spin states, the methods of measurements, and the experimental facilities employed in the present work are presented.

3.1 Population of excited nuclei

There are many different reactions to populate excited nuclei, e.g., inelastic scattering, charge exchange reactions, Coulomb excitation, and fusion-evaporation reaction, which are roughly distinguished by the impact parameter ρ (see Fig. 3.1).

The models of heavy-ion collisions classified by the impact parameter ρ are shown in Fig. 3.1. The overlap between the projectile and the distribution of the nuclear density increases when the impact parameter decreases. The Coulomb scattering is the elastic scattering of charged particles by the Coulomb interaction. It occurs when the impact parameter is large. The fusion-evaporation reaction is a reaction in which two nuclei are combined to form a compound nucleus which in turn evaporates several particles giving rise to the so called residual nuclei. It occurs when the impact parameter is small. The elastic, inelastic, and deep inelastic scattering occur when the impact parameters are in between.

The heavy-ion fusion-evaporation reaction (a heavy-ion is defined as a nucleus with mass number $A > 4$) is one of the most typical and useful to produce high-spin states in nuclei. Details about this reaction are presented in the following section.

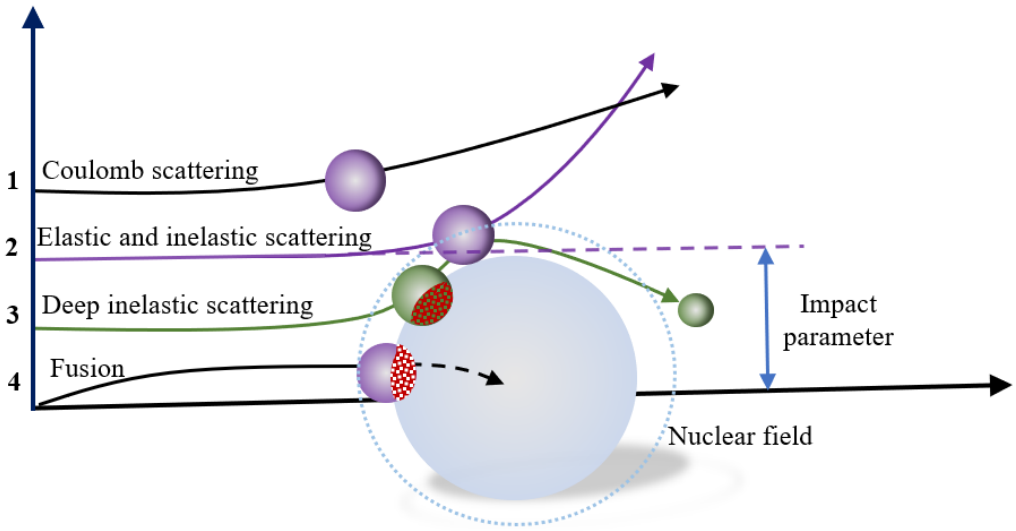

Figure 3.1: The modes of heavy-ion collisions based on the impact parameter.

3.1.1 Heavy-ion fusion-evaporation reactions

The heavy-ion fusion-evaporation reaction is one of the efficacious ways to populate the excited nuclei. To overcome the Coulomb barrier V_c and form a compound nucleus, the minimum beam energy is [79]

$$V_c = 1.44\frac{Z_p Z_t}{R_p + R_t}[MeV], \tag{3.1}$$

where the $R_{p,t} = r_0 A_{p,t}^{1/3}$. The subscript p and t represent projectile and target. $R_{p,t}$ are the radii of nuclei and $Z_{p,t}$ indicate the atomic numbers. A compound nucleus is formed when a projectile bombarding a target, and it rotates rapidly with a high excitation energy E_{exc}, which is expressed as

$$E_{exc} = Q + E_{cm}, \tag{3.2}$$

where

$$Q = E_p + E_t - E_{cn}, \tag{3.3}$$

$$E_{cm} = \frac{m_t}{m_p + m_t}E_{lab}. \tag{3.4}$$

The subscript cn denotes compound nucleus. $E_{p,t,cn}$ and $m_{p,t}$ express the binding energies and masses, respectively. Q-value, E_{cm} and E_{lab} are called the reaction energy, the kinetic energy of the system in the center of the mass and laboratory frames, respectively.

In addition, the maximum angular momentum (l_{max}) transferred in a fusion evaporation reaction can be esti-

mated in the center of mass frame as [80]

$$l^2_{max} = \frac{2\mu R^2}{\hbar^2}(E_{cm} - V_c), \tag{3.5}$$

where μ is the reduced mass, which is given by

$$\mu = \frac{m_p m_t}{m_p + m_t}. \tag{3.6}$$

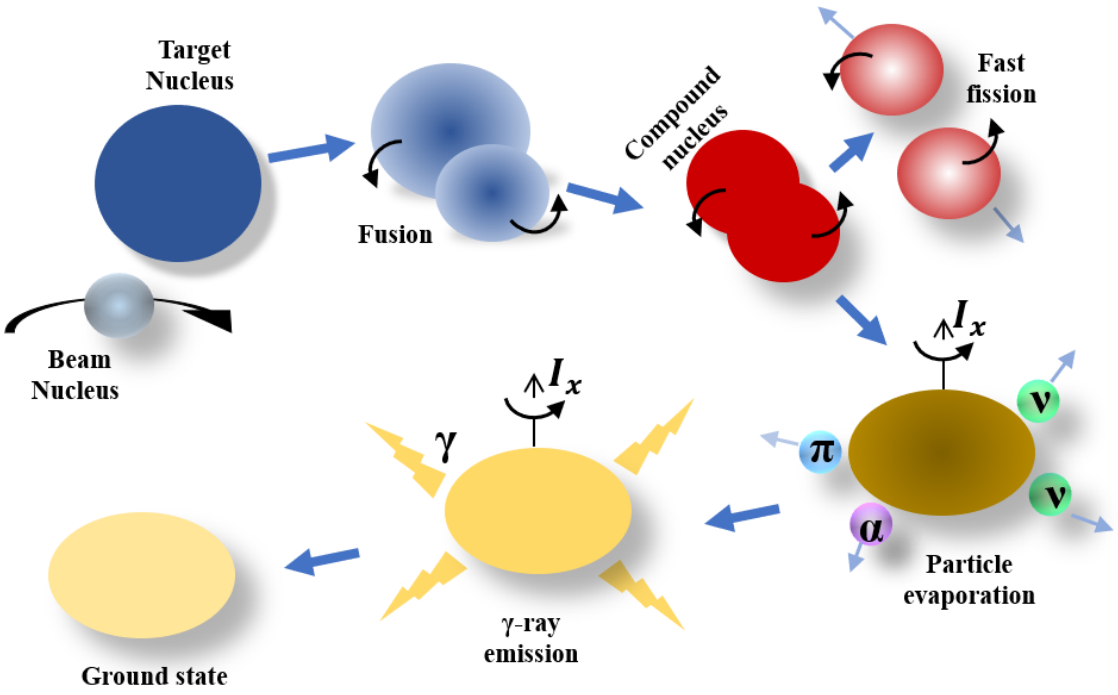

Figure 3.2: The progress of heavy-ion fusion-evaporation reaction.

The process of a heavy-ion fusion evaporation reation from the formation of a compound nucleus to its decay is shown in Fig. 3.2. A compound nucleus with very large angular momentum and high excitation energy is formed when a heavy-ion beam bombards a target nucleus. If the excitation energy of the compound nucleus overcomes the fission barrier, it can split into two nuclei. However, If the compound nucleus does not fission, then the compound hot system will cool down by evaporation of particles, e.g., neutrons, protons, β, and α. Each of the emitted particles carries away 1-2 $\hbar$ of angular momentum and an energy of $\approx$ 8 MeV which are estimated by LISE++ [81]. Finally, the residual nucleus produced after the evaporation of the particles loses the rest of excitation energy and almost all angular momentum via γ-ray emission, until it reaches the ground state. The dominant part of deexcitations of the residual nucleus proceeds by γ-ray emission. Therefore, the γ-ray spectroscopy as an efficient method used to study excited states of nuclei.

3.2 Detection of γ rays

γ rays are uncharged and create no direct ionization or excitation of the material through which they passes. The detection of γ rays is therefore critically dependent on the interaction that transfers all or part of the photon energy to an electron in the absorbing material [82]. Although a large number of possible interaction mechanisms of γ rays in matter are known, only three major types play an important role: *photoelectric effect, Compton scattering*, and *pair production* [3]. The relative importance of these three processes for different absorber materials and γ-ray energies is conveniently illustrated in Fig. 3.3. The line at the right denotes the energy at which Compton scattering and pair production are equally probable as a function of the absorber atomic number. The line at the left represents the energy at which photoelectric effect and Compton scattering are equally probable. Three areas are therefore defined on the plot within which photoelectric effect, Compton scattering, and pair production each predominate. Generally, $E_\gamma <$ 0.3 MeV, 0.3 MeV$< E_\gamma <$ 5 MeV, and $E_\gamma >$ 5 MeV are dominated by the photoelectric effect, Compton scattering, and pair production, respectively. The basic principle of measurement of γ rays in different detectors are similar. When the γ rays enter the detector system, they interact with the material, thereby losing some energy to the atoms in the detector. As a result, the electrons present in the atomic orbits are freed and get collected at the anodes, thereby generating a corresponding current/voltage pulse signal. This signal is amplified and then further processed to reveal the underlying properties associated with the radiation.

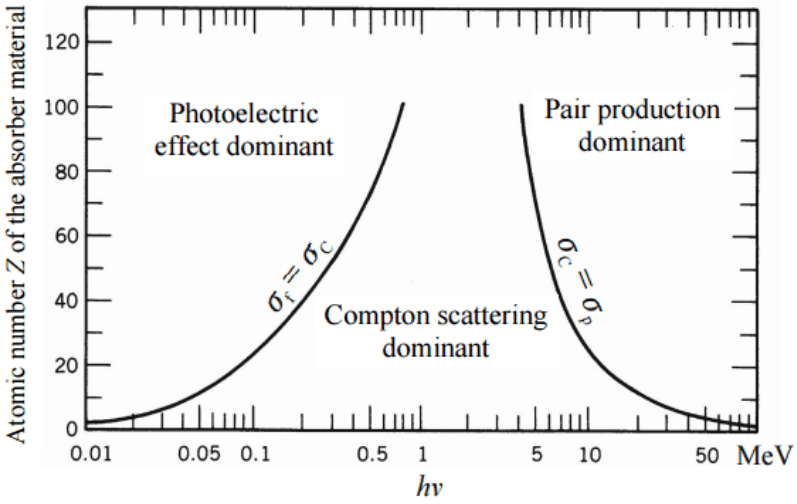

Figure 3.3: The relative importance of the photoelectric effect, Compton scattering, and pair production [82].

3.2.1 Photoelectric effect

In the photoelectric effect, a photon undergoes an interaction with an absorber atom in which the photon completely disappears. In its place, an energetic *photoelectron* is ejected by the atom from one of its bound shells [82]. The energy of an incident γ ray is $h\upsilon$ and the binding energy of the photoelectron is E_b, then the energy of the outgoing

photoelectron is expressed as:

$$E_e = h\upsilon - E_b, \tag{3.7}$$

where the typical binding energies are a few keV for low-Z atoms and tens keV for high-Z materials. Since a free electric cannot absorb a proton and also conserve momentum, the photoelectric effect always occurs on bound electrons with the nucleus absorbing the recoil momentum [3].

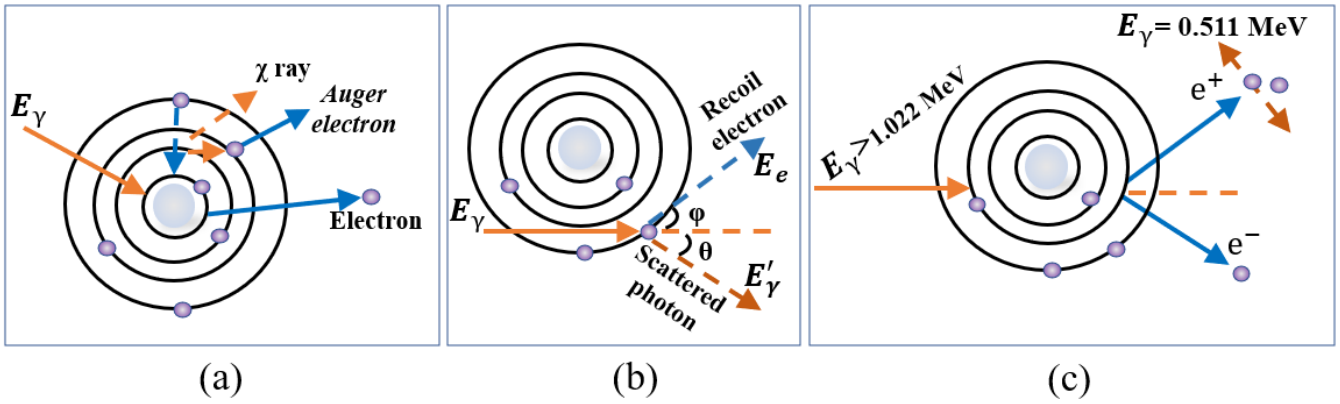

Figure 3.4: The interaction processes of γ ray with matter. (a), (b), and (c) show a process of the photoelectric effect, Compton scattering, and pair production, respectively.

One can see the process of the photoelectric effect in Fig. 3.4 (a). A hole is created in the bound shells of the absorber atom after the electron is ejected. The hole is rapidly filled by capture of a free electron from the medium and/or rearrangement of electrons from other shells of the atoms. Thus, a characteristic X-ray can be generated. In some cases, the emission of an *Auger electron* [83] can substitute for X-ray in carrying away the atomic excitation energy.

The typical photoelectric cross section depends on the incident photon energy. The cross section is relatively small at the energies above the highest electron binding energy of the atom (the K shell), but it increases quickly when the K-shell energy is approached. After this point, since the K-electrons are no longer available for the photoelectric effect, the cross section drops drastically. This drop is called the K-absorption edge. Below this energy, the cross section rises once again and dip as the L, M, levels, etc. are passed. These are called the L-absorption edge, M-absorption edge, etc., respectively [3]. Calculating the cross section for different shells is complicated, but it's rough approximated by [82],

$$\sigma_f \cong constant \times \frac{Z^n}{E_\gamma^{3.5}}, \quad (4 < n < 5), \tag{3.8}$$

Thus, the high-Z materials are preferable for detector fabrication since the dependence of cross section on n of the atomic number Z.

3.2.2 Compton scattering

The process of Compton scattering takes place between the incident photon and an electric in the absorbing atom. The interaction is shown in Fig. 3.4 (b). The incident photon is deflected through an angle θ with respect to its original direction. The photon transfers a portion of its energy to the electron (assumed to be initially at rest), which is called *recoil electron* [82]. The energy transferred to the electron can vary from zero to a large fraction of the γ-ray energy since all angles of scattering are possible. One can assume that the recoil electron is deflected though an angle ϕ with respect to the original direction of the incident photon. The angles θ and ϕ satisfies [84]

$$\cos\theta = 1 - \frac{2}{(1+\gamma)^2\tan^2\phi + 1} \tag{3.9}$$

and

$$\cos\phi = (1+\gamma)\tan\frac{\theta}{2}. \tag{3.10}$$

Based on the energy and momentum conservation, the energy of the scattered photon is defined as [84]:

$$E'_\gamma = \frac{E_\gamma}{1 + \frac{E_\gamma}{m_e c^2}(1-\cos\theta)}, \tag{3.11}$$

where $m_e c^2 = 0.511 MeV$ is the rest-mass energy of the electron. The energy of the recoil electron is given as:

$$E_e = E_\gamma - E'_\gamma = E_\gamma\left[1 - \frac{1}{1 + \frac{E_\gamma}{m_e c^2}(1-\cos\theta)}\right]. \tag{3.12}$$

The energy of the recoil electron is close to zero when the scattering angle θ approaches to zero. In this case, the Compton scattering can be ignored. When the angle θ increases, the energy of the recoil electron increases. It has the maximum energy when the scattering angle reaches to π. In this case, the incident photon is backscattered towards its original direction, while the electron recoils along the incidence direction. This is the so-called "Compton edge" in a γ-ray spectrum, which corresponds to an energy

$$E_e^\pi = E_\gamma\left(\frac{2\frac{E_\gamma}{m_e c^2}}{1 + 2\frac{E_\gamma}{m_e c^2}}\right). \tag{3.13}$$

The cross section for Compton scattering is obtained through integrating the *Klein-Nishina* formula which is given by [85]

$$\frac{d\sigma_c}{d\Omega} = \frac{r_e^2}{2}\left(\frac{E'_\gamma}{E_\gamma}\right)^2\left[\frac{E_\gamma}{E'_\gamma} + \frac{E'_\gamma}{E_\gamma} - 2sin^2\theta cos^2\varphi\right], \tag{3.14}$$

where r_e is the classical electron radius. θ and φ are shown in 3.5 (a), where φ is the angle between the electric vector ($\vec{E}$) of the incident photon and the scattered plane. The cross section as a function of φ is shown in 3.5 (b),

in which the cross section is maximum (minimum) when $\varphi = 90°$ and $270°$ ($0°$ and $180°$).

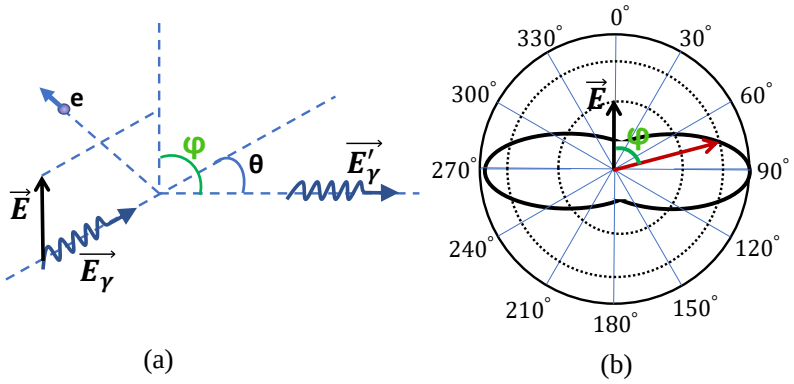

(a) (b)

Figure 3.5: The process (a) and the cross section (b) for the Compton scattering.

3.2.3 Pair production

The third effect shown in Fig. 3.2 (c) is pair production. The process involves the transformation of a photon into an electron-positron pair. Since an energy of the pair $2m_0c^2$ is required to create the pair, the photon must have at least an energy of 1.022 MeV. After their production, both the electron and positron travel through the detector medium loosing their energy. Once the kinetic energy of the positron becomes very low, it will annihilate or combine with an electron in the absorbing medium and emit of two anti-parallel 0.511 MeV γ-rays. Generally, the probabilities of the pair production remain low until the energy of the incident photon reaches several MeV.

3.3 Detectors

While the history of nuclear and elementary particles has seen the development of many different types of detectors, all are based on the same fundamental principle: the transfer of partial or all radiation energy to the detector mass where it is converted into some other form more accessible to human perception.

3.3.1 High-purity germanium detectors

Before the 1960s, the germanium (Ge) detectors had very narrow active volumes due to the high impurity concentration in Ge crystals. A successful progress was made by E. M. Pell [86] and D. V. Freck et al. [87] in 1960, which was introducing Lithium into Ge, and constructed the so called Ge(Li) detectors. This started an era of detecting γ rays through semiconductor crystals. In the late 1970s, high-purity germanium detectors (HPGe) with many advantages

over Ge(Li) became widely used in the high-resolution γ-ray spectroscopy. The commercial production of HPGe detectors almost take the place of Ge(Li) around the 1980s.

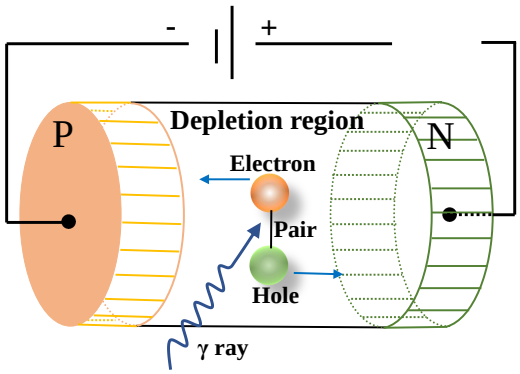

Figure 3.6: Reverse bias of the p-n junction.

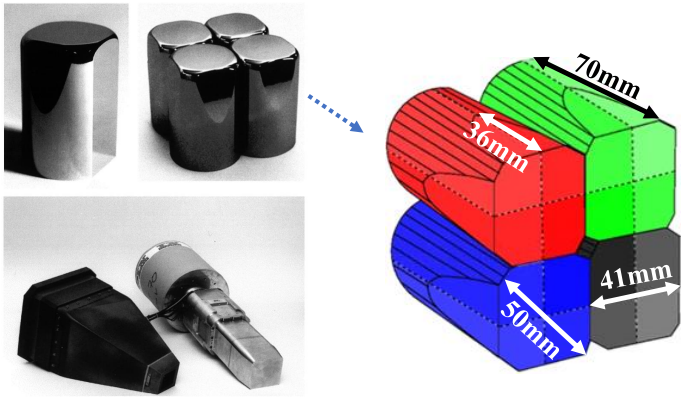

Figure 3.7: The crystal structure of a clover detector [88].

A HPGe detector is generally operated as fully depleted detector. Reverse biasing requires that a positive voltage be applied to the p-n junction, as shown in Fig. 3.6. The depletion region is a region of net zero charge, without free electrons and holes. At the p-n junction, the ”built-in” electric field and the applied electric field are in the same direction. A thicker depletion region is created when these two fields add. The γ-ray interact with the crystal within the depleted zone, producing electron-hole pairs which move towards the detector outer contacts. The produced charge induces a voltage pulse signal in a preamplifier.

For a typical size of a HPGe detector, the time resolution is close to 400 ps [89] which is a poor value compared with scintillation detectors, but with a good quality material, its energy resolution is approaching the Fano limit [90, 91]. The high resolution is widely available for γ-ray energies from a few keV to 10 MeV. There are two major types of HPGe detectors: *planar* and *coaxial*. The former is mainly used to measure the complex low-energy γ

rays in the range of 10 keV to a few hundred keV or X-rays. It achieves the best energy resolution due to low capacitance. Coaxial detectors have a large detection efficiency at high γ-ray energies, and are used to measure γ rays in the range of 10 keV to 10 MeV.

The clover detector consists of four coaxial n-type Ge crystals arranged in the form of a four-leaf clover lodged within the same cryostat. Each crystal is 70 mm long with a tapered front face having 50 mm diameter. The front face has a quasi-squared section obtained by bevelling two adjacent faces with an angle of 7.1° starting at around the half of the crystal length and by cutting the two remaining faces parallel to the crystal axis along its whole length. The Ge-Ge distance is only 0.2 mm. The total active Ge volume is $\sim$ 470 cm^3 and corresponds to 89% of the original Ge volume. The distance between the beveled edges of the crystals and the internal surface of the end-cap is only 3.5 mm. The thickness of the aluminium end-cap is 1.5 mm [88, 92].

The clover detectors are very efficient in measurement of high energy γ rays [88]. As a result, they are employed in many 4π γ-ray arrays, such as EUROBALL [93], GAMMASPHERE [94], JUROGAM 3 [95]. In addition, the interaction of a γ-ray with several crystals can cause time correlated events and if we can add up these time correlated events, then information from the scattered γ-rays which do not escape from the detector system, will be added back to the full energy peak. The clover detectors house four separate crystals, we can use the *addback* to obtain the full energy peaks of the scattered γ-rays. Details of the addback will be discussed in 4.2.5.

3.3.2 Compton suppression shield (BGO detector)

γ rays interact with matter through the three major processes which were introduced in Section 3.2. The dominating contribution to the background in γ-ray spectroscopy comes from the incomplete energy deposition of the incoming γ rays in the detector volume due to the Compton scattering. The Compton scattered γ-rays give rise to a continuum background in the γ-ray spectrum which consequently decreases the peak-to-total (P/T) ratio and also raises the detection limit for low energies. In order to counteract these unwanted effects, we can suppress the Compton scattered γ by surrounding the HPGe detector with a secondary veto detector, which usually is a scintillator. Coincident detection of the escaping photons in a secondary veto detector can serve as a means to reject preferentially those events that only add to the continuum, without affecting the full-energy events. The rejection is carried out by passing the pulses from the HPGe through an electronic gate that is closed if a coincident pulse is detected from the surrounding detector, which is called *anticoincidence mode* [82]. These surrounding detectors and the technique are called ”anti-Compton” detectors and ”Compton suppression spectrometry”, respectively. A process of Compton suppression system is shown in Fig. 3.8.

To be effective, the secondary veto detector must be large enough to intercept most of the escaping photons and should have a good efficiency for their detection. Usually, the large scintillation detectors, e.g., NaI(Tl) and BGO, are employed for meeting these requirements. The BGO detector having the strong advantage of high atomic number,

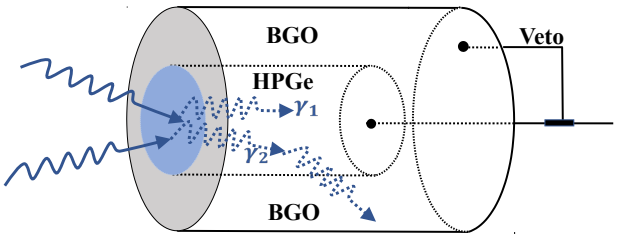

Figure 3.8: The schematic configuration of a BGO anti-Compton shield of a HPGe detector.

high density (7.3 g/cm^3), and excellent timing properties, become the preferred choice. The P/T ratio is around 20% with only the HPGe detector, and it increase to around 50-60% after setting up the anti-Compton shield.

3.4 JUROGAM 3 array

The JUROGAM 3 array has been constructed in the Accelerator Laboratory of the University of Jyväskylä, Finland (JYFL) for in-beam γ-ray sepctroscopy. The layout of JUROGAM 3 is shown in Fig. 3.9. This large γ-ray spectrome-

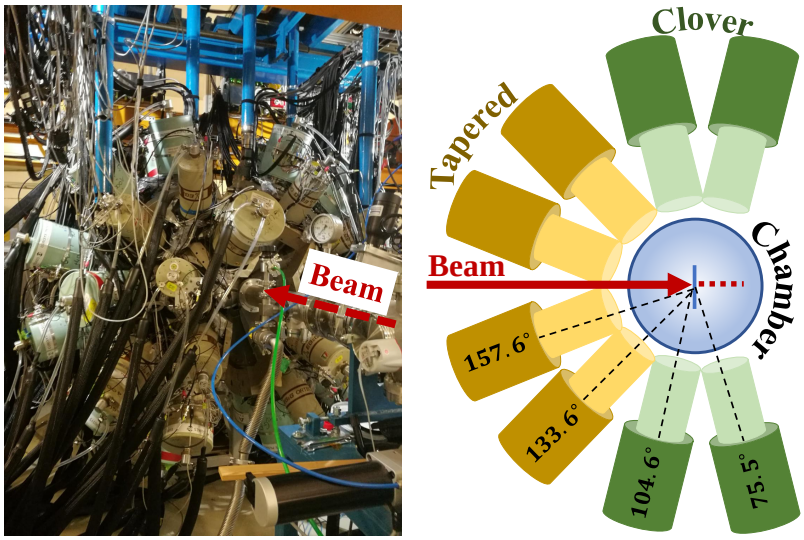

Figure 3.9: The layout of detectors of JUROGAM 3.

ter consists of two types of germanium detectors, tapered single-crystal Phase1 detectors [96] and composite clover detectors [88], which are mounted at the target position. The tapered detectors are placed on two rings at 133.6° (10 detectors) and 157.6° (5 detectors), while the clover detectors are placed on two rings at 75.5° (12 detectors) and 104.5° (12 detectors). In order to improve the P/T ratio, each germanium detector is equipped with a BGO and a collimator. Commonly, a group cosisting a germanium detector, a BGO anti-Compton shield and a collimator is called a detector module. The properties of different generations of the JUROGAM array are given in Table 3.1

where the data is from Ref. [95].

Table 3.1: Properties of the different generations of the JUROGAM arrays.

JUROGAM array	Detector	Configuration	Efficiency[a]	Operating years
JUROGAM I	43 tapered		4.3%	2003-2008
JUROGAM II	15 tapered	24 clover	5.2%	2008-2017
JUROGAM 3	15 tapered	24 clover	5.2%	2019-

[a] For the detection of the 1332-keV γ ray.

3.5 The recoil separator

In the beginning of the 21st century a new recoil separator was constructed at the Accelerator Laboratory of the University of Jyväskylä. The already existing gas-filled recoil separator RITU was designed for studies of heavy elements and has been extensively used for nuclear structure studies near the proton-drip line employing fusion evaporation reactions. However, because in such reactions the difference in magnetic rigidity between reaction products and primary beam is small, this type of recoil separators is not well suited for symmetric or inverse kinematics fusion-evaporation reactions. Meanwhile, the reaction products studied are also restricted to nuclei which can be identified with recognisable decays due to the poor mass-resolving power of the gas-filled separators [97]. The Mass Analysing Recoil Apparatus project (MARA) was conceived to answer to these requirements and to complement the capabilities of the RITU separator [98]. The design and construction of the new recoil mass spectrometer started around year 2004 and was completed in 2015.

A typical separator has the configuration DQQ, where D and Q represent the dipole and quadrupole magnets, respectively. A magnetic dipole is followed by a quadrupole doublet to focus the fusion products into the focal plane. The dipole magnet separates the ions depending on their different magnetic rigidity $B\rho$, where B and ρ are the magnetic field strength and the curvature radius, respectively. $B\rho$ is given by [99]

$$B\rho = \frac{mv}{q_{ave}} = \frac{mv}{(v/v_0)Z^{1/3}} = 0.0227A/Z^{1/3}\ \ Tm, \tag{3.15}$$

where mv is the momentum of the reaction product, $v_0 = \frac{c}{137} = 2.19 \times 10^6$ m/s is the *Bohr velocity* and $q_{ave} = \frac{v}{v_0}Z^{1/3}$ is given by the Thomas-Femi model of the atom. Commonly, Eq. 3.15 is used to roughly estimate the deflection of the separated residues.

3.5.1 The vacuum-mode separator MARA

The ion-optical configuration of the MARA separator is QQQD$_E$D$_M$, where D$_E$ and D$_M$ represent electrostatic deflector with a bending angle of 20° (see Fig. 3.10) and magnetic dipole with a bending angle of 40° (see Fig. 3.10),

respectively. MARA complements the capabilities of the RITU and extends the region of accessible nuclei down to lighter masses. The schematic layout of MARA in floor coordinates is shown in Fig. 3.10, where a quadrupole triplet between the target and the electrostatic deflector is used to create a point-to-point focusing condition over the separator in both directions and to bend horizontally [97]. The combination of electric and magnetic dipoles provides a fixed energy focus for the separated ions with different m/q ratios. The ion-optical configuration and some trajectories with different angles (0 and $\pm$30 mrad horizontally and 0, $\pm$25 and $\pm$50 mrad vertically), energies (0, $\pm$7%) and masses (0, $\pm$1%) are shown in Fig. 3.11 [97]. The MARA performs well and the scattered beam ions entering the focal plane are of small intensity [100].

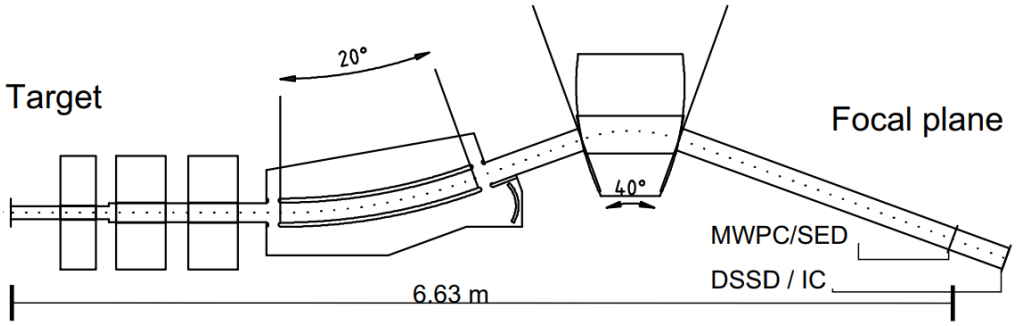

Figure 3.10: The layout of the MARA separator [97].

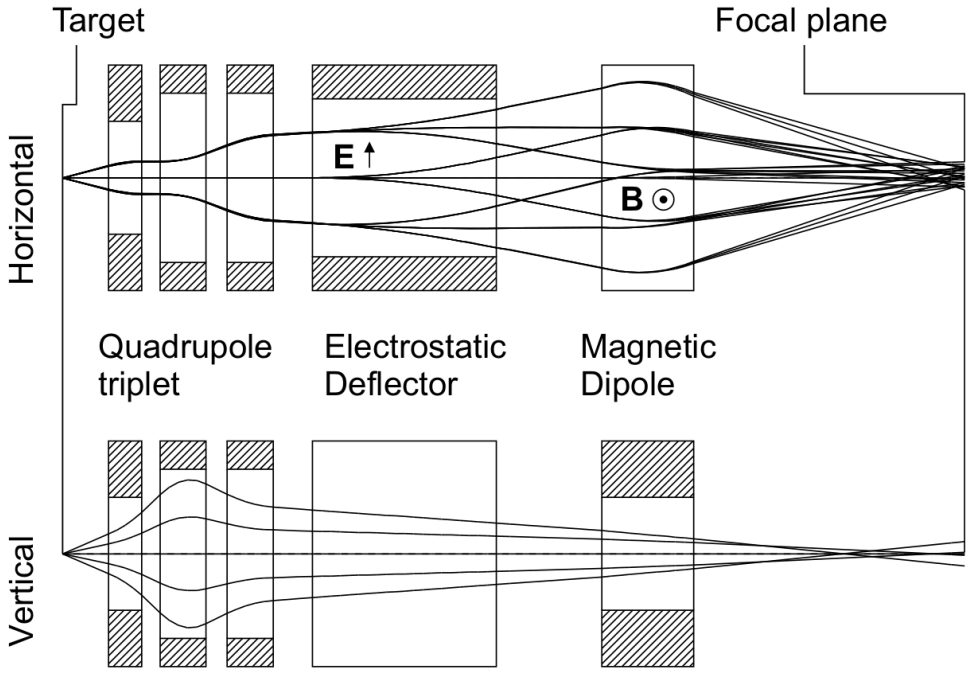

Figure 3.11: Schematic layout of MARA optics in horizontal (top) and vertical (bottom) direction [97].

The relevant parameters and properties of MARA are listed in Table 3.2. MARA is an unique recoil separator

due to its ion-optical configuration QQQD$_E$D$_M$ which makes it less expensive and easier to set-up for experiments [97].

Table 3.2: The properties and parameters of the MARA separator [97, 100].

Configuration	QQQD$_E$D$_M$
Total length along the optical axis	6.85m
Angular acceptance (horizontal, vertical)	$\pm$45 mrad, $\pm$55 mrad
Energy acceptance	-15% to +20%
First order resolving power (2 mm beam spot diameter)	259
Magnification (horizontal, vertical)	-1.55, -4.48
m/q dispersion	8.0 mm/(% in mass)
m/q acceptance	$\pm$4%

3.6 The implantation detection systems

Implantation detection systems coupled with in-flight recoil separators have been one of the most powerful tools available for the study of nuclei far from stability [101]. The implantation detection systems measure the α, β , γ, X-rays, protons, and conversion electrons which are emitted by reaction products.

The transport of the fusion-evaporation reaction products to the focal plane detectors of MARA is as follows. The recoils pass through a multiwire proportional counter (MWPC) before they are implanted into two double-sided silicon strip detectors (DSSD). Each DSSD has an active area of 60 mm $\times$ 40 mm and a thickness of 300 μm with 128 vertical strips on one face and 48 horizontal on the other [102]. The strip pitch is 1 mm in both directions, matching the position resolution of the MWPC and giving a total of 4800 pixels. Reaction products are typically implanted into the DSSD at depths of $\sim$1-10 μm, depending on the target-projectile combination [101]. The MWPC comprises a grid of 20 μm diameter gold coated tungsten wires with 1 mm spacing in 3.5 mbar flowing isobutane gas and provides spatial information on the recoils, which are dispersed across the MARA focal plane according to the ratio of their mass number (A) and charge (q) [102]. It has an aperture of 131 mm (horizontal) $\times$ 50 mm (vertical) [101]. Combining the information on the time of flight of the recoils between the MWPC and the DSSD, with the energy measured in the DSSD, allowed recoils to be distinguished from other implanted ions. Two 500 μm thick silicon detectors are mounted adjacently behind the DSSD to identify light ions that punch through the DSSD. Signals observed in the DSSD without a coincident signal in these silicon detectors or in the MWPC are assumed to be from radioactive decays of implanted nuclei [102]. Five clover detectors are placed around the focal plane point to measure the γ rays.

3.7 Total-Data Read out (TDR)

In the past, recoil decay tagging (RDT) [103] was a very powerful method for the spectroscopy of exotic nuclei [104]. It was employed for many nuclei in the region above Sn which decay by emitting α, β-delayed protons, and direct protons from their isomeric states. RDT is a delayed coincidence technique between the detectors at the target position and the implantation detectors at the focal plane of a spectrometer [104]. However, this method has several shortcomings. (i) Wide gates (over 10 μs) are desirable from the physics perspective, but are precluded by dead time, causing loss of rare ground state emission events from implanted nuclei at the focal plane [104]. (ii) The data written to disk include both good and random data, which must later be separated. This problem gets worse with wider gates [104].

In order to overcome the dead-time limitation, a new data-acquisition, total data readout (TDR), was developed [104]. The TDR method read all the data, timestamp them, and then collect the event fragments together in software in the event builder using spatial and temporal correlations [104]. But the software triggering requires a large amount memory. The most important and valuable feature of the TDR is that it is triggerless and the data is timestamped from a global 100-MHz clock giving a time resolution of 10 ns. The data from TDR are not structured or filtered, apart from the time-ordered, it allows the offline process data more flexible and events reconstructed in real time in the event builder using temporal and spatial associations depend on the physics of the experiment. The schematic diagram of the GREAT TDR system's electronics and data acquisition are shown in Fig. 3.12.

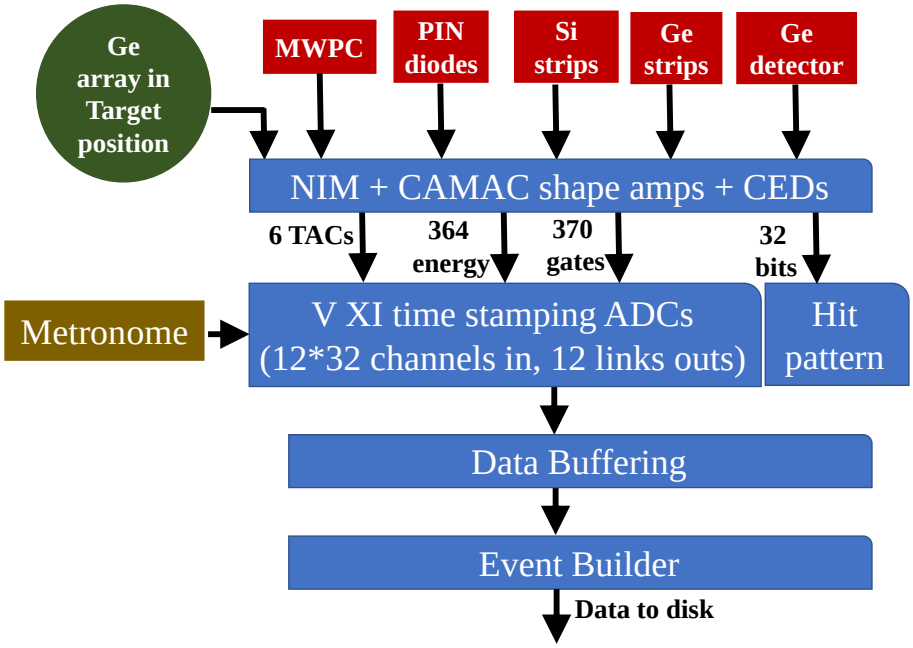

Figure 3.12: The flow chart of the GREAT TDR system's data acquisition [104].

Chapter 4

Experimental details and data analysis

4.1 Experimental details

The experiment was performed at JYFL used the JUROGAM 3 + MARA setup [95, 97, 100]. The compound nucleus ^{122}Ce was produced using the ^{64}Zn ion beam, which was delivered by the Electron cyclotron resonance (ECR) ion source and accelerated by the K130 cyclotron [105] to the final energy of 255 MeV, and it bombarded to a self-supporting enriched ^{58}Ni target with a thikness of 0.75 mg/cm^2. The beam intensity was around 2-3 pnA. The beam time was about 3 days. The excited nuclei of ^{119}Cs, ^{119}Ba, and ^{118}Cs were populated via the 3p, 2p1n, and 3p1n reaction channels with cross sections calculated using HIVAP of 150 mb, 20 mb, 40 mb, respectively.

The fusion-evaporation residues were separated as a function of A/q and identified using the in-flight double-focusing recoil mass separator MARA [97, 100]. At the focal plane a double-mass slit system was used to allow only two charge states of a given mass to be transported to the implantation detector. MARA is a mass separator but it cannot resolve isobars or overlapping evaporation channels involving α-particle evaporation due to the A/q ambiguity. The detail of MARA is introduced in section 3.5.1.

The setting of the implantation detectors is slightly different from that of the GREAT spectrometer. The Time of Flight (ToF) between the MWPC and DSSD was recorded. The ToF and the recoil energy deposited in the DSSD were used to distinguish between fusion recoils and scattered beam. Five clover germanium detectors surrounding the MARA focal-plane detection system were used to detect γ-rays emitted by long-lived isomers and daughters of the β-decay of the implanted recoils. All detector signals were recorded by the triggerless TDR data acquisition system [104], and time stamped by a global 100 MHz clock which allowed to establish both temporal and spatial correlations between recoils and events obtained with the rest of the focal plane and JUROGAM 3 arrays [100, 102].

Prompt γ-rays were detected at the target position using the JUROGAM 3 germanium detector array consisting of 24 Euroball clover [88] and 15 Eurogam Phase I-type [96] escape-suppressed detectors, with an efficiency of $\approx 5\%$ at 1.3 MeV. The clover detectors were arranged symmetrically relative to the direction perpendicular to the

beam (twelve at 75.5° and twelve at 104.5°), while the Phase I detectors were placed at backward angles with respect to the beam direction (five at 157.6° and ten at 133.6°). Details of JUROGAM 3 are given in section 3.4.

4.2 Data analysis

In this experiment, a total of 4×10^{10} prompt γ-ray coincidence events with fold ≥ 3 were detected by the JUROGAM 3 array, and $\approx$ 700 Gb of data spread across $\approx$ 350 files were stored. All the data were recorded by the triggerless TDR data acquisition system and the events were time-stamped using a 100 MHz clock with the time resolution of 10 ns.

In order to achieve the practical purposes, two processes were performed on the huge amount of raw data. First, standard procedures like energy calibrations, efficiency calibration, gain matching, addback process, etc. were performed. Then specific procedures like making matrices in different conditions were performed. Both processes require the use of the GRAIN code [106]. After that, the newly identified bands can be assigned to a certain nucleus, for example ^{119}Cs, ^{118}Cs, ^{120}Ba, ^{119}Ba, ^{118}Ba, using recoil-gated prompt coincidences and the presence of X-rays in the spectra. Following this identification, the analysis of the higher statistics prompt $\gamma\gamma\gamma$ coincidences without recoil gating enabled to construct comprehensive level schemes, with a rich tapestry of band structures interconnected by a multitude of transitions. Fully symmetrized, three-dimensional (E_γ-E_γ-E_γ) cube was analyzed using the RADWARE package [107, 108].

4.2.1 Setting the threshold

Before starting the experiment, an important step is to set the low energy thresholds for detectors. In this experiment, X-rays were important to confirm the assignment of new bands to certain nuclei. The characteristic X-ray energies are 29.8-, 31.0-, 32.2-, and 33.4- keV for Xe, Cs, Ba, and La, respectively [109]. Therefore, the threshold energy of most detectors was set to $\approx$ 25 keV.

4.2.2 Energy calibration and gain matching

To avoid the possible gain drifting along the measurement, it is necessary to calibrate each detector and to gain matching all detectors. Normally, each detector is connected to one or more channels (depending on the type of detectors) of an analog-to-digital converter (ADC) electronic device which transforms proportionally the incident γ-rays energies into digital signals. In order to obtain the corrected energy, the ADC converters are calibrated by some standard radioactive sources whose energy are already known.

In the current experiment, the ADC converters for the detectors of JUROGAM 3 array and the focal plane clover detectors were calibrated by using two standard γ-ray sources of ^{152}Eu and ^{133}Ba. To calibrate the detectors, the

following polynomial expression was used

$$E_\gamma = a + bx + cx^2, \tag{4.1}$$

where E_γ are the energies of γ rays. x is the channel number of the ADC converters which is related to the centroid position of the photopeak. a, b, and c are the fitted parameters of the polynomial used for obtaining the calibrated energy where a is the zero offset, b is associated with the gain of amplifier (or preamplifier), and c is used for adjust the nonlinearity of the detector.

In the present work, the values of the coefficients a, b and c were fitted by using the software GRAIN [106]. The results of Ring 1, Ring 2, Ring 3, and Ring 4 detectors of the JUROGAM 3 array after the calibrations are shown in Fig. 4.1. The DSSD were calibrated by using a combination of ^{239}Pu, ^{241}Am, and ^{244}Cm sources in this work. The

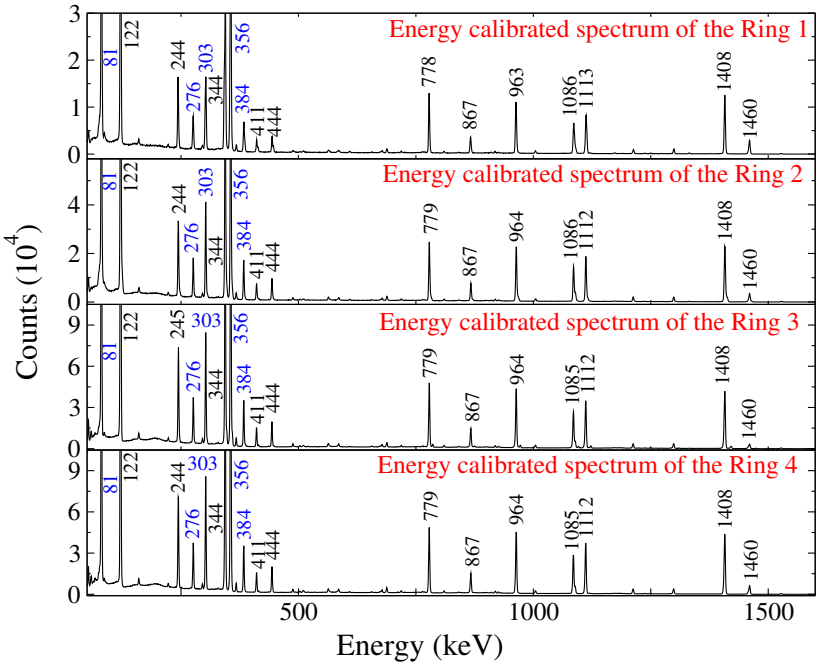

Figure 4.1: The energy calibrated spectra of the 4 rings of the JUROGAM 3 array by using two γ-ray sources ^{152}Eu (black) and ^{133}Ba (blue).

fitted parameters were provided by J. Sarén from JYFL.

4.2.3 Efficiency calibration of the Ge detectors

For accurate determination of the relative intensities of the γ rays, we have to first ascertain the efficiency of the spectrometer as a function of energy. To obtain it, we have to fit the data of standard radioactive sources whose intensities for different γ rays are already known. The efficiency (ϵ) of the detectors can be expressed by the function:

$$ln(\epsilon) = (A + BX - e^{C+DX}), \tag{4.2}$$

The A, B, C, and D are the parameters of the equation used to calculate the efficiency of γ rays. X is given by

$$X = ln\left(\frac{E_\gamma}{E_1}\right). \tag{4.3}$$

E_γ is the γ-ray energy with keV unit and the $E_1 = 511$ keV. In this experiment, the best fits of efficiency curves for the four rings of JUROGAM 3 are shown in Fig. 4.2. Ring 3 and Ring 4 consist of more detectors than other rings, resulting in the high efficiencies. Since a few channels of Ring 4 have strong background, we turned off them during the experiment. Thus, the efficiency of Ring 4 is slightly lower than that of Ring 3. Ring 1 shows the lowest efficiency since it consists of the fewest detectors. The values of the four parameters are given in Table 4.1.

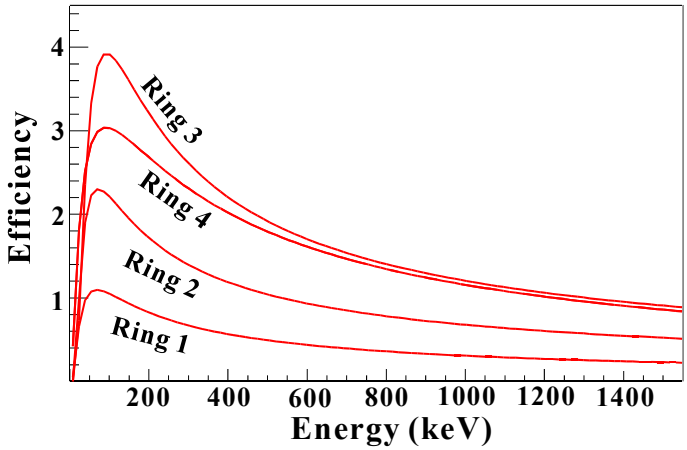

Figure 4.2: The efficiency calibration for 4 rings of JUROGAM 3.

Table 4.1: Efficiency calibration coefficients for the different rings of the JUROGAM 3 array.

Rings	A	B	C	D
Ring 1	-0.527(8)	-0.800(4)	-1.634(32)	-0.808(12)
Ring 2	0.077(3)	-0.660(3)	-3.010(38)	-1.219(19)
Ring 3	0.706(1)	-0.729(2)	-2.673(8)	-1.250(2)
Ring 4	2.000(17)	-1.136(6)	0.356(3)	-0.400(2)

4.2.4 Doppler shift correction

For experiments that use a thin target, the γ rays emitted by the recoiling residues are Doppler-shifted. Thus, a Dopper correction has to be applied to recover the precise γ-ray energies. The shifted γ-ray energy is expressed as [110]:

$$E_\gamma(\theta) = E_\gamma(0)\frac{\sqrt{1-\beta^2}}{1-\beta cos\theta}, \tag{4.4}$$

where θ is the detector angle which is defined with respect to the recoil velocity direction (most are along the beam direction). $E_\gamma(0)$ is the unshifted γ-ray energy. β is the ratio of the recoil velocity (v) and the speed of light (c), $\beta = \frac{v}{c}$.

If $v \ll c$, i.e. $\beta \ll 1$, the effect of the Doppler-shift for the γ-ray energy can be calculated approximately using the following relation:

$$E_\gamma(\theta) = E_\gamma(0)(1 + \beta cos\theta). \tag{4.5}$$

Here, the detectors at 90° show maximum Doppler broadening. In the present experiment, we used a value $\beta = 0.044$ for all γ rays detected in the JUROGAM 3 which resulted in the best resolution for high energy γ rays.

4.2.5 Add-back for the clover detectors

A clover detector consists of four closely mounted Ge crystals. The distances between a crystal and the adjacent crystal are typically 2 mm. When an incident γ ray interacts with one crystal, it can be scattered to the other adjacent crystals or can be completely absorbed in the same crystal. The former is called multiple-fold event, while the latter is called single-fold event. For the multiple-fold events, we use m (2 $\leq$ m $\leq$ 4) to represent the number of crystals which absorb the γ-ray energy.

The clover detector can be operated in two modes: single crystal and add-back mode. The former mode sum up the time uncorrelated events of the four crystals corresponding to events where the full γ-ray energy is deposited in any one of the individual crystals, while the latter mode sum up the time correlated events of the four crystals [111]. The add-back mode corresponds to events where the full γ-ray energies are deposited by single, $m = 2$, $m = 3$, and $m = 4$ multiple-fold events, since it can reconstruct the full γ-ray energy by adding up the individual events that satisfy a certain coincident condition. In the single crystal mode, a full energy peak event can generate m background counts in the spectrum since the energy of the γ-ray can be deposited completely in a single crystal or in m crystals [111]. In the spectrum corresponding to add-back mode, the m background counts are reconstructed to a single full energy peak [111]. Take $m = 2$ fold as a example, where the γ ray is scattered from crystal 1 to crystal 2 with the deposited energies E_1 and E_2, respectively: the full γ-ray energy is $E_{addback} = E_1 + E_2$.

In the add-back mode, the full energy of the incident γ-ray that undergoes scattering(s) after partial energy absorption can get back [111]. Thus the number of events contributing to the full energy peak is equal to the number of under the full energy peak in the spectrum. In the present experiment, we used the add-back mode for all clover detectors in the analysis of the $\gamma\gamma\gamma$ coincidences. In addition, the events with $m = 2$ fold, presenting horizontal and vertical scattering, were used to analyze the electromagnetic character of the γ rays. Details are discussed in the next subsection.

4.2.6 The measurement of γ-ray multipolarity

The raw data are compressed to contain the γ-ray energies, time information, multiplicity, and the γ-ray position (detector identification numbers). In order to analyze γ-ray cincidence relationaships for building the level schemes

and other follow-up works, it is crucial to sort the raw data into histograms under different control conditions based on the events measured at the MARA focal plane. The basic histogram is a one-dimensional histogram, where the x-axis and y-axis are energy (or time) and their corresponding counts. A one-dimensional histogram only shows the energy peaks which have no any coincident relationship with each other. In order to obtain more useful information, the higher dimensional histograms need to be formed by using the higher-fold events [107]. The most used two- and three- dimension histograms of energy are named $E_\gamma - E_\gamma$ matrix and $E_\gamma - E_\gamma - E_\gamma$ cube. The former requires two axes and the latter needs three axes. A 2D matrix and 3D cube can be analyzed by the programs which are from the RADWARE analysis package [107, 108] . In these programs, a single (double) gate can be set on one axis (two axes) on a matrix (cube). As a result, the data are projected on the last energy axis to generate one-dimensional γ-ray spectra which are in coincidence with the γ ray(s) that was (were) selected in the gate.

In the current work, we sorted all raw data by using the GRAIN analysis package [106] which can produce the different 2D matrices with different control conditions on MARA. After sorting using GRAIN, a 3D cube is generated by using the *levit8r* program from the RADWARE analysis package [107, 108]. Based on the matrix and cube, we extracted the γ-ray energies, relative intensities, and their multipolarities to construct the level schemes of ^{119}Cs, ^{118}Cs, ^{119}Ba, and other nuclei not discussed in the present thesis. Normally, before measuring the relative intensities of γ rays, we need to select one strong clean γ ray whose intensity is used to normalize the intensities of all other γ rays. For the measurement of γ-ray multipolarity, there are two methods which can be used: one is based on the Directional Correlation from Oriented states (DCO) ratios (R_{DCO}), and the other exploits the two-point Angular Correlation (anisotropy) ratios R_{ac} [112, 113]. In order to firmly establish the parity of the newly identified bands, linear polarization measurements were performed for a few clean, strong, linking γ-ray transitions by the polarization direction correlation method (PDCO) as described in Ref. [114]. Details of the methods of measuring the R_{DCO}, R_{ac} and PDCO are described in the following.

(I) DCO ratio

The emission probability of a γ ray photon from a nucleus with a certain angular momentum is related to the angle between the photon propagation direction and the orientation of the nucleus. This relationship can be used to obtain the angular correlation function, which is [115, 116, 117]

$$W(\theta) = 1 + A_2 P_2(cos\theta) + A_4 P_4(cos\theta) + ... + A_{2n} P_{2n}(cos\theta), \tag{4.6}$$

where the $W(\theta)$ is the probability of the γ ray having an angle θ relative to the beam direction and $P_{2n}(cos\theta)$ are the *Legendre polynomials*. A_{2n} are the angular distribution coefficients, which are related to the spins of the corresponding states and the multipole of the γ ray. The number n most be smaller than the angular momentum carried by the γ ray.

In the heavy-ion fusion-evaporation reaction, the angular momentum of the compound nucleus is in the plane perpendicular to the beam direction, and is distributed symmetrically. Since the evaporated particles and the emitted γ rays only take away a very small part of the angular momentum, the angular momentum of excited state of the residual nucleus is also perpendicular to the beam deriction. Assuming that γ_1 and γ_2 are detected by detectors 1 and 2 which have angles θ_1 and θ_2 relative to the beam direction, respectively, the DCO ratio is expressed as [112]:

$$R_{DCO} = \frac{W(\theta_2, \theta_1, \varphi)}{W(\theta_1, \theta_2, \varphi)}, \tag{4.7}$$

where φ is the angle between two planes which are formed by γ_1 and γ_2 with the beam direction, respectively. $W(\theta_2, \theta_1, \varphi)$ is proportional to the intensities of the coincident events $I^{\gamma_2}_{\theta_1}(Gate^{\gamma_1}_{\theta_1})$ which means that detector 1 measures γ_1 and detector 2 measures γ_2 at the same time, while $W(\theta_1, \theta_2, \varphi)$ is proportional to the intensities of the coincident events $I^{\gamma_2}_{\theta_2}(Gate^{\gamma_1}_{\theta_1})$ which means that detector 1 measures γ_2 and detector 2 measures γ_1 at the same time. Thus, the corresponding experimental DCO value can be written as [112]:

$$R_{DCO} = \frac{I^{\gamma_2}_{\theta_1}(Gate^{\gamma_1}_{\theta_1})}{I^{\gamma_2}_{\theta_2}(Gate^{\gamma_1}_{\theta_1})}. \tag{4.8}$$

Suming up the events of the detectors placed at forward and backward angles, like θ and $\pi - \theta$, improves the statistics of the spectra. For example one can put the γ rays detected by detectors located at 90° on one axis and those detected at forward-backward angles on the other axis of an asymmetric matrix. In the present work, the detectors of JUROGAM 3 are placed on four rings as shown in Fig. 3.9. In order to extract the DCO ratios from the rings at the different angles, we constructed an asymmetric $E_\gamma - E_\gamma$ matrix where the x-axis has the prompt coincident events filled by the detectors at 157.6°, while the y-axis has the γ rays detected by the detectors at 75.5° and 104.5° which can be treated as the angle $\approx$ 90°. In that case, the DCO ratio is given by

$$R_{DCO} = \frac{I_r\ (157.6^\circ\ \ gated\ \ by\ \ \approx 90^\circ)}{I_r\ (\approx 90^\circ\ \ gated\ \ by\ \ 157.6^\circ)}. \tag{4.9}$$

The values of the DCO ratios are related to the multipolarity of the gating transition, where the typical R_{DCO} values of dipole and quadrupole transitions are around 1.0 and 2.1 when using dipole gating transitions, and the values change to around 0.46 and 1 when gated by quadrupole transitions [23, 118]. Based on the comparisons of the experimental DCO ratios with the DCO ratios of transitions with known multipolarity or with theoretical values, we can determine the multipolarity of the γ-ray transitions.

(II) Augular correlation ratio (R_{ac})

In the calculation of the DCO ratios, we are limited by the statistics of the data of the detectors at 157.6° where only 5 HPGe detectors were placed. As a result, the DCO ratios of some weak γ rays cannot be obtained due to the

low statistics. In addition to the DCO analysis, there is another method that uses the two-point angular correlations ratios (R_{ac}) to measure the γ-ray multipolarities [112, 113]. In this method, the calculation of the R_{ac} value involves the intensity of γ_1 detected by the detectors at θ_1 from a gate on γ_2 detected by all detectors $I^{\gamma_1}_{\theta_1}$, and the intensity of γ_1 detected by the detectors at θ_2 from a gate on γ_2 detected by all detectors $I^{\gamma_1}_{\theta_2}$. The exprimental R_{ac} value is [112, 113]

$$R_{ac} = \frac{I^{\gamma_1}_{\theta_1}\ (gated\ by\ \gamma_2\ at\ all\ angles)}{I^{\gamma_1}_{\theta_2}\ (gated\ by\ \gamma_2\ at\ all\ angles)}. \tag{4.10}$$

Comparing with the matrices used to extract the DCO ratios, the matrices for extracting R_{ac} values have more statistics and are not affected by the multipolarity of the gating γ ray. Thus, we can add spectra gating on $E2$ and $M1$ transitions to improve statistics. Many γ-ray multipolarities are deduced from the R_{ac} values in the present work. The used process is the following: firstly, the raw data were sorted into two asymmetric $E_\gamma - E_\gamma$ matrices where the prompt γ rays recorded by the detectors at the rings at 133.6° + 157.6 ° (or 75.5° + 104.5 °) were put on one axis, whereas on the other axis are put the events detected by all the detectors; secondly, setting a gate on the axis containing the information of all detectors and projecting to the other axis including the 133.6° + 157.6° (or 75.5° + 104.5°) detectors; finally, extracting the intensities of the measured γ ray and calculating the R_{ac} values by using the formula

$$R_{ac} = \frac{I_\gamma(133.6^\circ + 157.6^\circ)}{I_\gamma(75.5^\circ + 104.5^\circ)}. \tag{4.11}$$

Typical R_{ac} values of dipole transitions are around 0.8, while the values for quadrupole transitions are approximately 1.4 [23, 118]. The γ rays with pure dipole and quadrupole characters can be clearly distinguished by comparing with these two values.

(III) PDCO value

Based on the experimental values of R_{DCO} and R_{ac}, the multipolarities of the transitions can be deduced, but their parities still cannot be established. Therefore, we have to perform the linear polarization measurement to determine the electric or magnetic characters of transitions.

For an axially oriented nucleus, the transitions have a linear polarization defined by [119] [120]

$$P(\theta) = \frac{W(\theta, \epsilon = 0^\circ) - W(\theta, \epsilon = 90^\circ)}{W(\theta, \epsilon = 0^\circ) + W(\theta, \epsilon = 90^\circ)}, \tag{4.12}$$

where $W(\theta, \epsilon)$ is given by [119, 121, 122]

$$W(\theta, \epsilon) = \frac{d\Omega}{8\pi} \sum_{\lambda=even} B_\lambda U_\lambda [A_\lambda P_\lambda(cos\theta) + 2A_{2\lambda} P^{(2)}_{2\lambda}(cos\theta) cos2\epsilon], \tag{4.13}$$

where B_λ is the orientation quantity and U_λ is the de-orientation coefficient. A_λ and $A_{2\lambda}$ are the coefficients which

describe the directional and polarizational distribution, respectively. θ is the angle between γ ray and beam direction. ϵ is the angle between the γ-ray electric vector $\vec{E}$ and the reaction plane formed by the beam direction and the γ-ray direction. An example for $\theta = 90^\circ$ (the reason for choosing 90° will be explained later) is shown in Fig. 4.3, where the length of the red lines describe the distributions of scattered γ-rays probabilities with different ϵ.

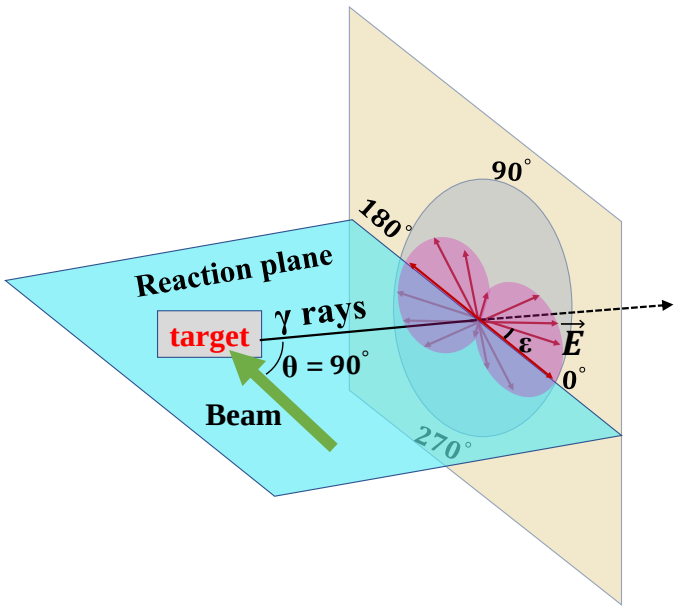

Figure 4.3: The principle of linear polarization measurement.

In the case of $\theta = 90^\circ$, the intensities of the scattered γ rays express the opposite trend for the electric and magnetic transitions in the polarization plane formed by the direction of the γ-ray and its electric vector $\vec{E}$. A pure electric transition shows the highest intensity at $\epsilon = 0^\circ$ which is parallel to the reaction plane, while a pure magnetic transition has the highest intensity at $\epsilon = 90^\circ$ which is perpendicular to the reaction plane. The distribution of the electric vector intensity is shown in Fig. 4.4, where (a) is for the $E1$ and $E2$ transitions and (b) is for the $M1$ transitions.

The variation of the linear polarization intensity $P(\theta)$ with angle θ is displayed in Fig. 4.5. One can see that the value of $P(\theta)$ becomes large when θ is close to 90° (270°) and is small when θ is close to 0° (180°). It even disappears if $\theta = 0^\circ$ or 180°. The intensity value is independent of the γ-ray electromagnetic character. Therefore, many works selected the condition of $\theta = 90^\circ$ to measure the linear polarization. That is the reason why the example in Fig. 4.3 shows the $\theta = 90^\circ$ case.

The clover is a typical detector used to measure the γ-ray linear polarization by using its Compton scattering between the composing crystals. The Compton scattering is very sensitive for the direction of polarization and is suitable for high energy γ rays. The details (including cross section) of Compton scattering have been introduced in the Section 3.2.2. In the present experiment, determining the polarization of the γ ray needs to measure the Compton scattering events perpendicular and parallel to the reaction plane. The events perpendicular to the reaction

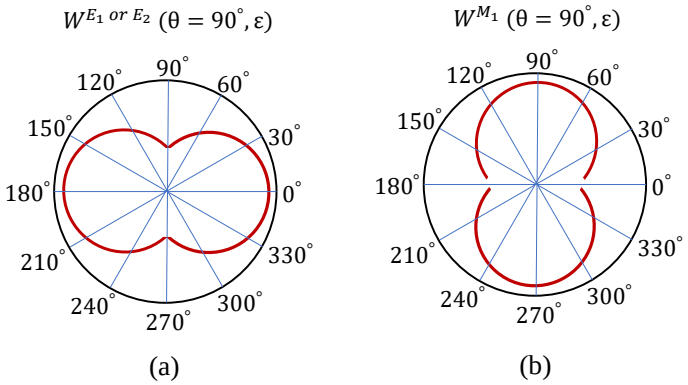

Figure 4.4: The distribution of electric vector intensity for electrical (a) and magnetic (b) transitions

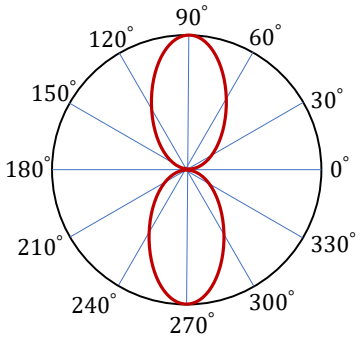

Figure 4.5: The distribution of linear polarization intensity.

plane ($N_\perp$) and parallel to the reaction plane ($N_\parallel$) in a clover detector are shown in Fig. 4.6. The γ-ray linear polarization can be written as function of the asymmetry A [123] [114],

$$A = \frac{aN_\perp - N_\parallel}{aN_\perp + N_\parallel}, \tag{4.14}$$

and the polarization sensitivity $Q(E_\gamma)$ of the detector as $P = A/Q$. In the asymmetry function A, a is a correction coefficient which is determined by using radioactive sources without linear polarization and generally has a value close to 1. This correction is given by

$$a = \frac{N_\parallel(unpolarized)}{N_\perp(unpolarized)}. \tag{4.15}$$

In this experiment, we use the fitting result $a(E_\gamma) = 1.113(7) - 5.4(8) \times 10^{-5} E_\gamma$ [118] to calculate a values. In order to extract the value of asymmetry A, two matrices have to be sorted. One axis recorded the events of parallel or vertical scattering detected by the clover detectors, while the γ rays detected by all detectors were placed on the other axis. Fitting the spectra gated on the latter axis to get the counts of γ rays that have been scattered in the

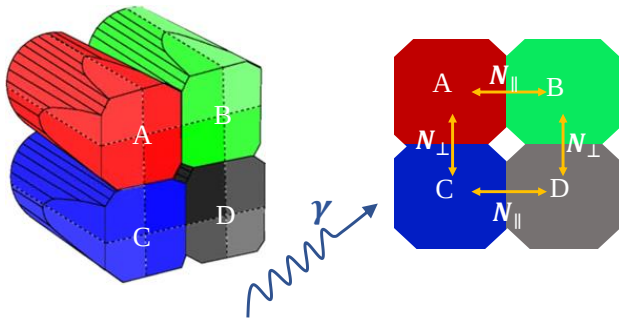

Figure 4.6: The definition of parallel and perpendicular events for clover detectors.

parallel or vertical directions, and correcting the number of counts by using the efficiency mentioned in subsection 4.2.3 leads to the values of $N_{\perp}$ and $N_{\parallel}$. Eventually, the asymmetry A was calculated by applying the correction a of Eq. 4.14. Typically, a positive asymmetry A would imply an electric nature, while a negative asymmetry would imply an the magnetic transition. In the present work, we determined the electromagnetic character of several important transitions.

Chapter 5

Towards complete spectroscopy of ^{119}Cs

This chapter presents the experimental results obtained from the in beam spectroscopic study of the very neutron-deficient nucleus ^{119}Cs. The first observation of chiral bands built on a configuration with only protons in the transient backbending regime and of prolate-oblate shape coexistence of ^{119}Cs are discussed. The structures of known and several new bands are discussed in the framework of the particle number conserving cranked shell model (PNC-CSM).

5.1 Introdution

The recent spectroscopic studies of Cesium nuclei have been focused on chirality, which was observed in a long sequence off odd-odd nuclei from ^{122}Cs to ^{132}Cs. The properties of all chiral bands observed in these nuclei have been collected in Ref. [14]. The investigation of the odd-even Cs nuclei far from stability can help us to understand the evolution of the collective properties in proton rich nuclei [124]. However, the study of the lightest Cs nuclei is confronted with the increasing difficulty to populate high-spin states using fusion-evaporation reactions as a result of the limited choice of projectile-target combinations and the small cross-sections for the evaporation of neutrons close to the proton drip-line. The existing experimental information on high-spin states in very proton-rich nuclei is therefore increasingly scarce towards the proton-drip line. The lightest nucleus with a rich band structure is ^{120}Cs [125]. In the other proton-rich Cs nuclei, such as ^{119}Cs [126] and ^{118}Cs [127], only one to three rotational bands were known before our study, often without interconnecting transitions and unknown excitation energies. This prohibits a detailed comparison between the theoretical calculations employing different interactions and the experimental data, making the understanding of the structure of these nuclei difficult. Fortunately, the magnetic moments and spectroscopic quadrupole moments Q_s have been measured for long-lived isomers close to the ground states of an extended range of Cs nuclei, from ^{118}Cs to ^{145}Cs [128]. These two physical quantities provide important information on the low-lying isomeric states and allow a rough systematic comparison between these nuclei. Taking the Q_s as

an example, based on the two relations of the intrinsic quadrupole moments Q_0 versus spectroscopic quadrupole moments Q_s [128]

$$Q_0 = \frac{(I+1)(2I+3)}{I(2I-1)} Q_s \tag{5.1}$$

and of Q_0 versus the nuclear defromation β [129]

$$Q_0 \simeq \frac{3}{\sqrt{5\pi}} Z r_0^2 A^{2/3} \beta \left(1 + \frac{1}{8}\sqrt{\frac{5}{\pi}}\beta\right), \tag{5.2}$$

we can compare the intrinsic quadrupole moments and deformations of some isomeric states.

Predictions of several isomeric states in nuclei close to the proton drip line have been recently published [4], but only for odd-odd nuclei. However, as coexisting prolate and oblate configurations are predicted in odd-even nuclei, states based on very different deformations and very different orientations of the quasiparticle angular momenta relative to that of the core can exist, and therefore can give rise to isomeric states.

The results on one of the less known ^{119}Cs nucleus will be presented. The latest work of this nucleus was reported by F. Lidén in Ref. [126], where only two floating bands with a limited number of states were observed in experiments with less efficient γ-ray arrays. In this work, new experimental results on ^{119}Cs have been obtained, leading to the extension of the known bands to very high spin and identifying eight new rotational bands. All bands are interconnected by multiple transitions, thus fixing their relative energies. Spins and parities are determined for most of the observed bands. The excitation energies of all observed bands are determined and the configurations of the observed bands are assigned. The several new bands observed in ^{119}Cs lead to one of the most complete level schemes of proton-rich Cs nuclei.

5.2 Experiment results and level scheme

The ^{119}Cs nucleus has been investigated using the ^{58}Ni(^{64}Zn,$3p$)^{119}Cs fusion-evaporation reaction with a beam energy of 255 MeV and the JUROGAM 3+MARA setup [95, 97]. A self-supporting enriched ^{58}Ni foil of 0.75 mg/cm^2 thickness was bombarded by the ^{64}Zn beam delivered by the K130 cyclotron.

A total of 4×10^{10} prompt γ-ray coincidence events with fold ≥ 3 were collected. The experimental information on the γ-ray transitions of ^{119}Cs is given in Table 5.2. Spins and parities of states are based on the measured values of R$_{DCO}$, R$_{ac}$, and A [112, 113, 114] which we introduced in Section 4.2.6. The complete level scheme of ^{119}Cs is shown in three separate figures, one with the negative-parity states (Fig. 5.1), and two with the positive-parity states (Figs. 5.2 and 5.3). A zoom on the low-spin part of the level scheme is also given in Fig. 5.6.

The new bands have been assigned to ^{119}Cs based on the mass 119 measured at the MARA focal plane in coincidence with band transitions and Cs X-rays. Take Band 5 as an example. One can see in Fig. 5.4 (d) that Band 5 is in coincidence with the 31-keV X-rays of Cs, and in Fig. 5.5 that the mass spectrum of Band 5 has the

similar pattern as the mass $A = 119$ spectrum. Combining information on the mass spectra and on X-rays, we could firmly assign Band 5 to ^{119}Cs.

In the present experiment, the focal plane spectra have been used to extract the lifetime of the isomers and of the non-yrast excited levels of the nuclei populated via β-delayed proton emission. The total length of the MARA separator from the target place to the focal plane is around 6.6 meters [97]. The recoils have a velocity of 0.044c (c is the speed of light in vacuum). Thus, the recoils need $t = \frac{6.6m}{0.044c} \approx 500$ ns to arrive at the focal plane. For an isomer with lifetime in the nanosecond range, the decay transitions cannot arrive or arrive with very low statistics to the focal plane to be measured. An isomer with very long lifetime around a second, also cannot be measured due to the too long trigger width which induces huge background. Thus, the JUROGAM 3 + MARA setup is perfect to measure isomers with lifetimes in the range from hundreds of nanoseconds to several tens of microseconds.

5.2.1 Low-lying states

Two long-lived $9/2^+$ and $3/2^+$ isomers were known in ^{119}Cs, with deformations of $\beta = 0.336$ and $\beta = 0.296$, respectively, determined from the measured spectroscopic quadrupole moments [128]. The assigned $9/2^+$, $T_{1/2} = 40.0(2)s$ ground state was not determined experimentally, but based on systematics [130]. In the present work, we assigned the ground state of ^{119}Cs as the long-lived $T_{1/2} = 30.4(1)$ s, β^+-decaying $3/2^+$ state [124]. This is the state with the lowest energy in the level scheme (see Fig. 5.6), which has therefore 0 keV excitation energy. The ground state $3/2^+$ is fixed by the 209-keV $M1/E2$ transition depopulating the $5/2^+$ state of Band 5, and by the four parallel cascades 105-103, 41-103, 96-112 and (32)-112 keV depopulating the $5/2^+$ states of Bands 4 and 5. The spin-parities $(3/2^+)$ and $(1/2^+)$ of the 103- and 112-keV states, respectively, are tentatively assigned based on the angular correlations and the intensity balance of the feeding and depopulating transitions of the two states.

Based on the connecting transitions between all bands, we could establish the relative energy of not only the bands with short-lived band-heads, but also of the two long-lived β^+-decaying $3/2^+$ and $9/2^+$ isomers. The 85.7 keV energy of the $9/2^+$ isomer is established by the connecting transitions between Bands 8 and 6, with Band 6 decaying in turn to Band 4 through the 738.1-keV transition. The 110.2 keV energy of the $11/2^-$ band-head of Band 1 is established by several connecting transitions to Bands 4 and 6. As Band 1 is depopulated by the observed delayed 87.1-keV transition, an unobserved 23.1-keV transition in cascade with the 87.1-keV transition should exist, which defines a state with tentative spin-parity $I^\pi = (7/2^+)$ and energy that can be either 23.1 keV or 87.1 keV. One can exclude the 23.1-keV energy of this $(7/2^+)$ state based on the systematics of low-lying states in the heavier Cs nuclei, and on the long half-life of the $9/2^+$ 85.7-keV isomer which would then have an energy lower than 87.1 keV, and therefore could not decay internally through γ emission. We therefore propose a $(7/2^+)$ state at 87.1(2) keV, which is higher by ≈ 1 keV than the 85.7-keV energy of the β-decaying $9/2^+$ band-head of Band 8. One should note that the energy of the $9/2^+$ band-head is established with an error of ≈ 2 keV, which results from the cumulative

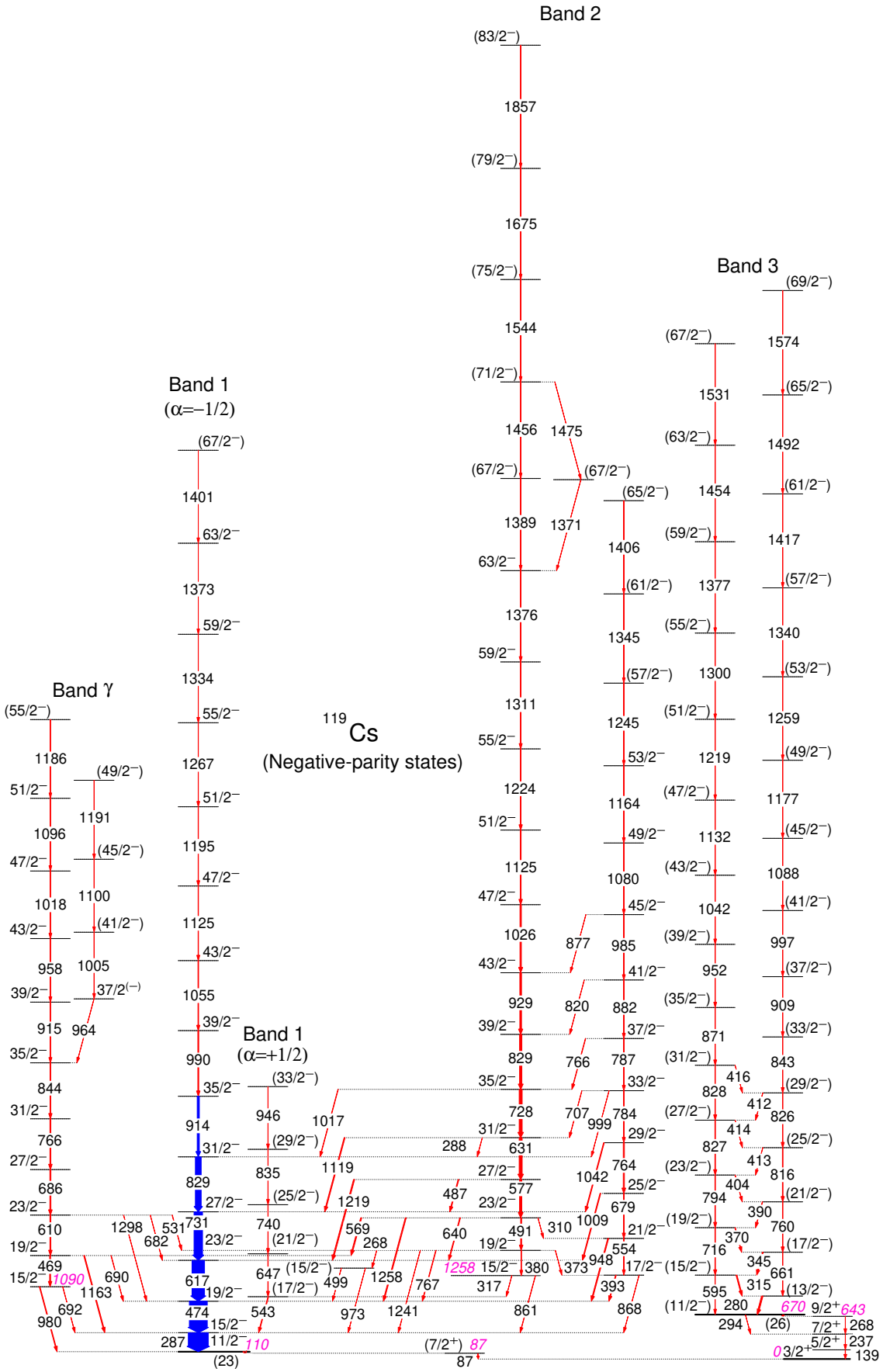

Figure 5.1: Partial level scheme of ^{119}Cs showing the negative-parity bands. The new transitions are indicated in red. The isomeric levels are indicated with thick line. Energies of levels with some relevance are shown in pink italics figures.

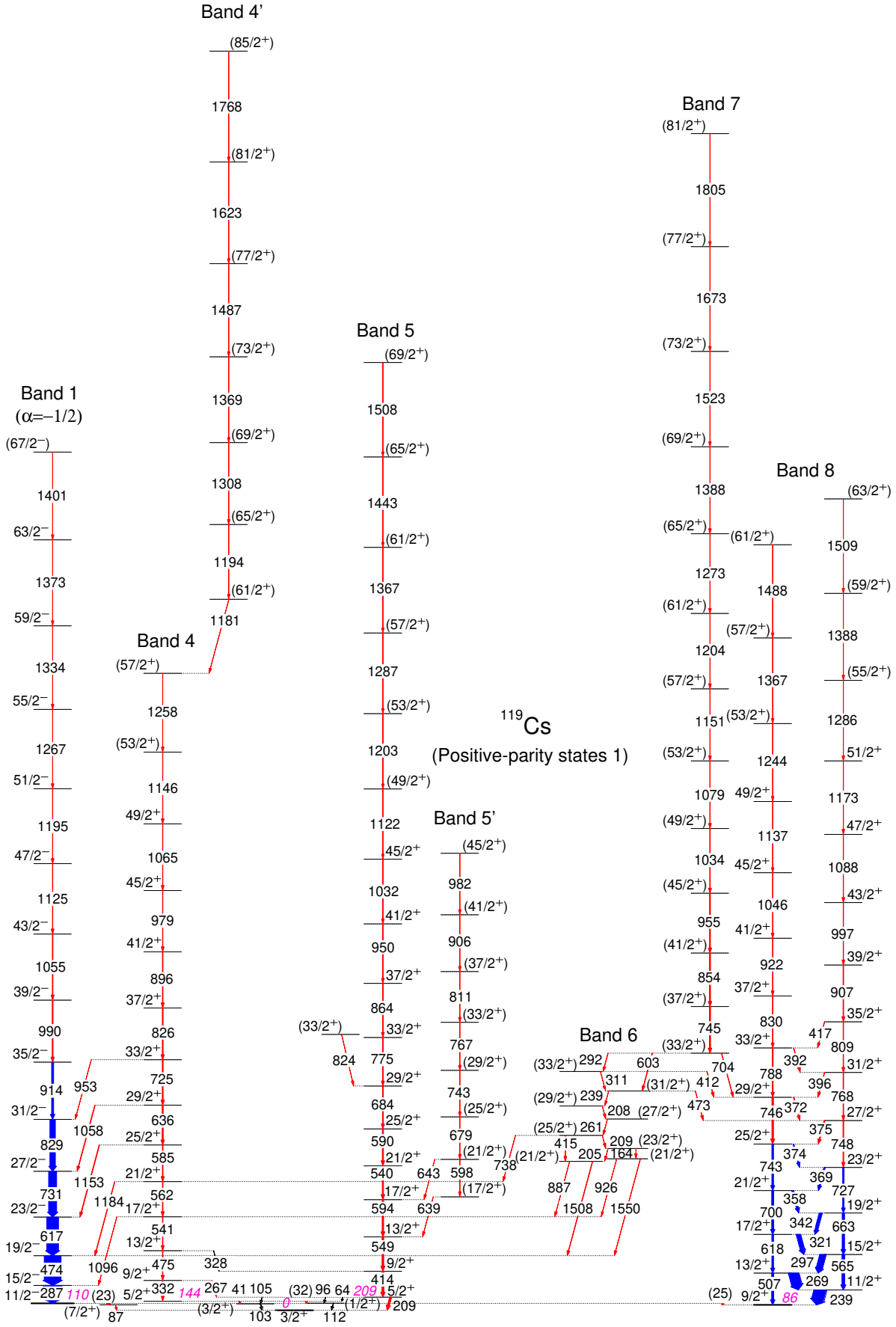

Figure 5.2: Partial level scheme of ^{119}Cs showing the first part of the positive-parity bands. The new transitions are indicated in red. The isomeric levels are indicated with thick line. Energies of levels with some relevance are shown in pink italics figures.

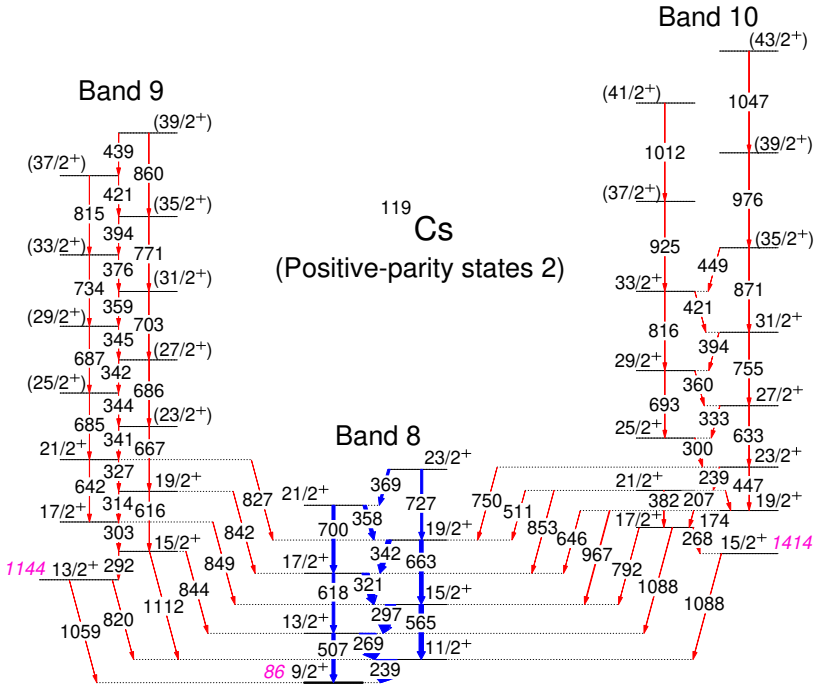

Figure 5.3: Partial level scheme of ^{119}Cs showing the second part of the positive-parity bands. The new transitions are indicated in red. The isomeric levels are indicated with thick line. Energies of levels with some relevance are shown in pink italics figures. The bands continue at higher spins with the transitions listed in Table 5.2 and Fig 5.2.

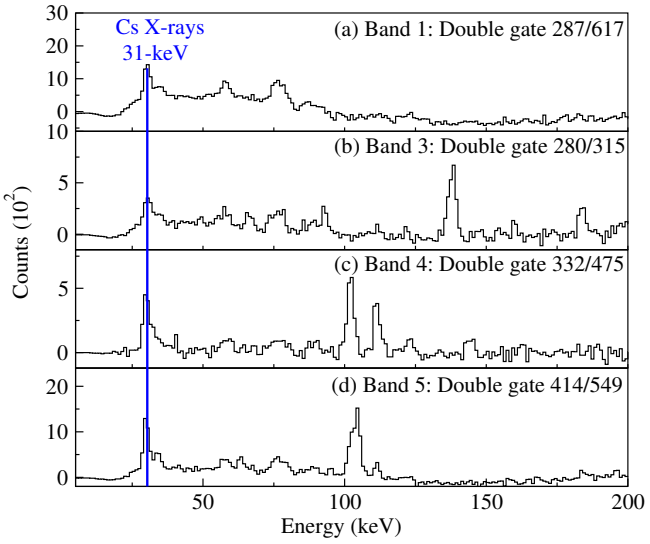

Figure 5.4: Zoom on the low-energy region of the spectra of different bands of ^{119}Cs showing the coincidence with Cs X-rays.

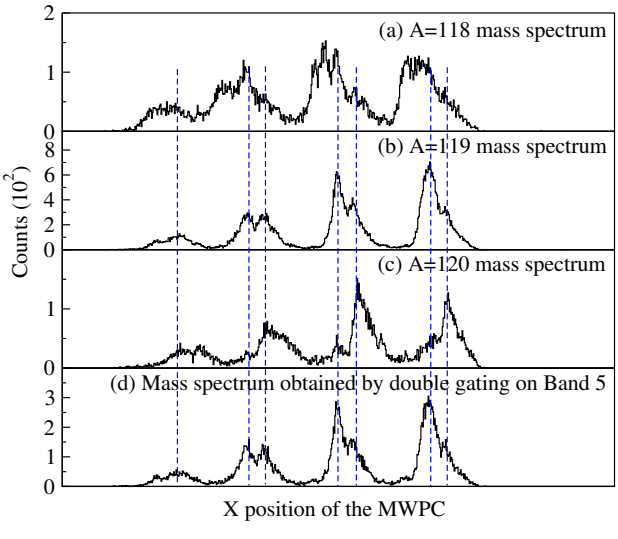

Figure 5.5: Mass spectra for different A measured by the MWPC, obtained by tagging on selected γ rays detected by JUROGAM 3.

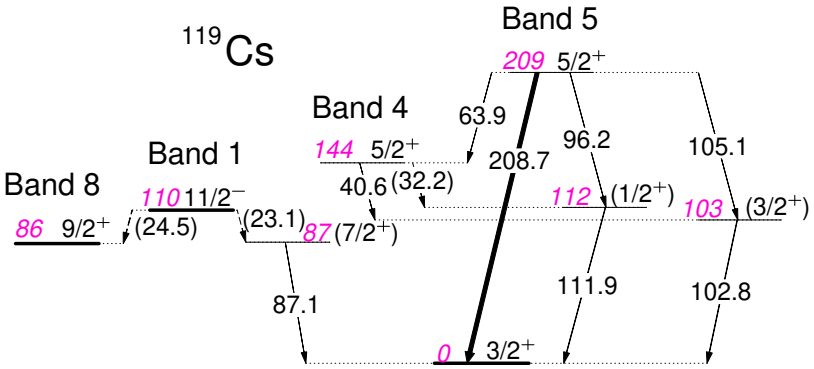

Figure 5.6: Zoom on the low-lying part of the level scheme of ^{119}Cs.

errors of the energies of about 20 transitions on the path from the ground state up to the $33/2^+$ band-head of Band 7 and down to the $9/2^+$ band-head of Band 8. However, we are confident on the estimated energy of 86 keV for the $9/2^+$ band-head of Band 8, because it becomes the lowest excited state which cannot decay internally through γ emission to the $3/2^+$ ground state.

5.2.2 Results of Bands γ, 1, 2, 3, 4, 4′, 5 and 5′

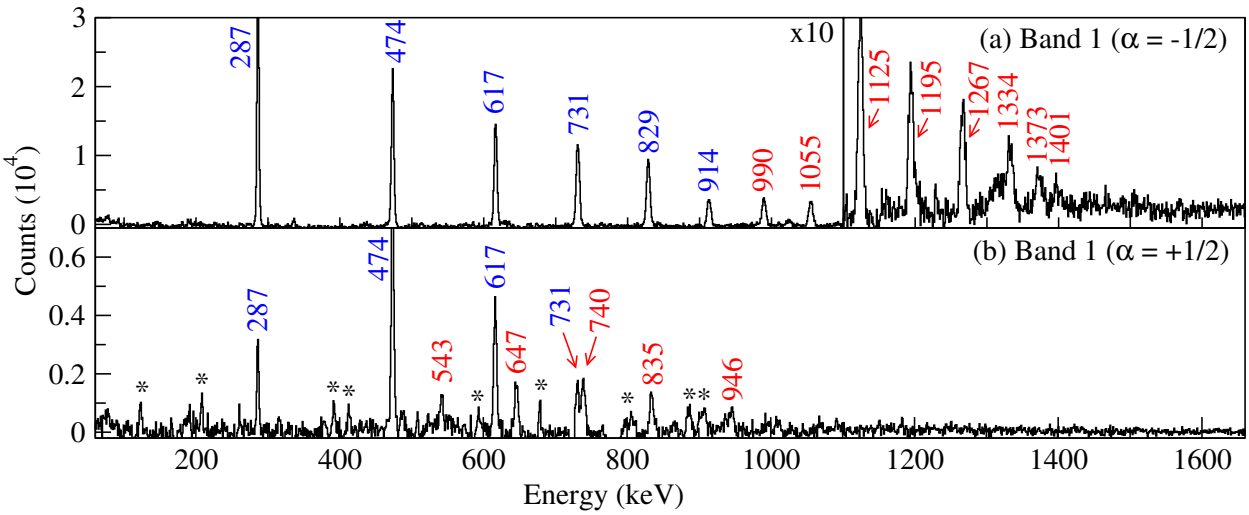

Figure 5.7: Spectra for Band 1 from triple coincidences by double-gating on the 914-, 990-, 1055-, 1125-, 1195-, 1267-, 1373-keV transitions for the $\alpha = -1/2$, on the 287-, 543-, 647-, 740-, 835-keV transitions for the $\alpha = +1/2$. Peak energies for the newly identified transitions are written in red. Transitions from other nuclei (^{116}Xe and ^{119}Ba) are indicated with an asterisk.

Double-gated spectra of Band 1 are given in Fig. 5.7. The known Band 1 is the strongest band in ^{119}Cs and has been extended to very high spin, 67/2, in this work. It decays to the $3/2^+$ ground state via the 87-keV transition and

an unobserved (23)-keV transition. Another unobserved (25)-keV $E1$ transition can also exist between the 110-keV, $11/2^-$ state and the long-lived 86-keV, $9/2^+$ band-head of Band 8. A half-life of $T_{1/2} = 55(5)$ μs was deduced by fitting the time spectrum of the 87-keV γ ray (details are shown in the following). The 55 μs half-life is obviously for the 110-keV state, as the 87-keV $E2$ transition is too fast to generate such a long-living isomer. The tentatively assigned spin and parity $(7/2^+)$ to the 87-keV state is based on systematics. The 110-keV energy of the $11/2^-$ band-head of Band 1 is fixed by five transitions between Bands 4 and 1.

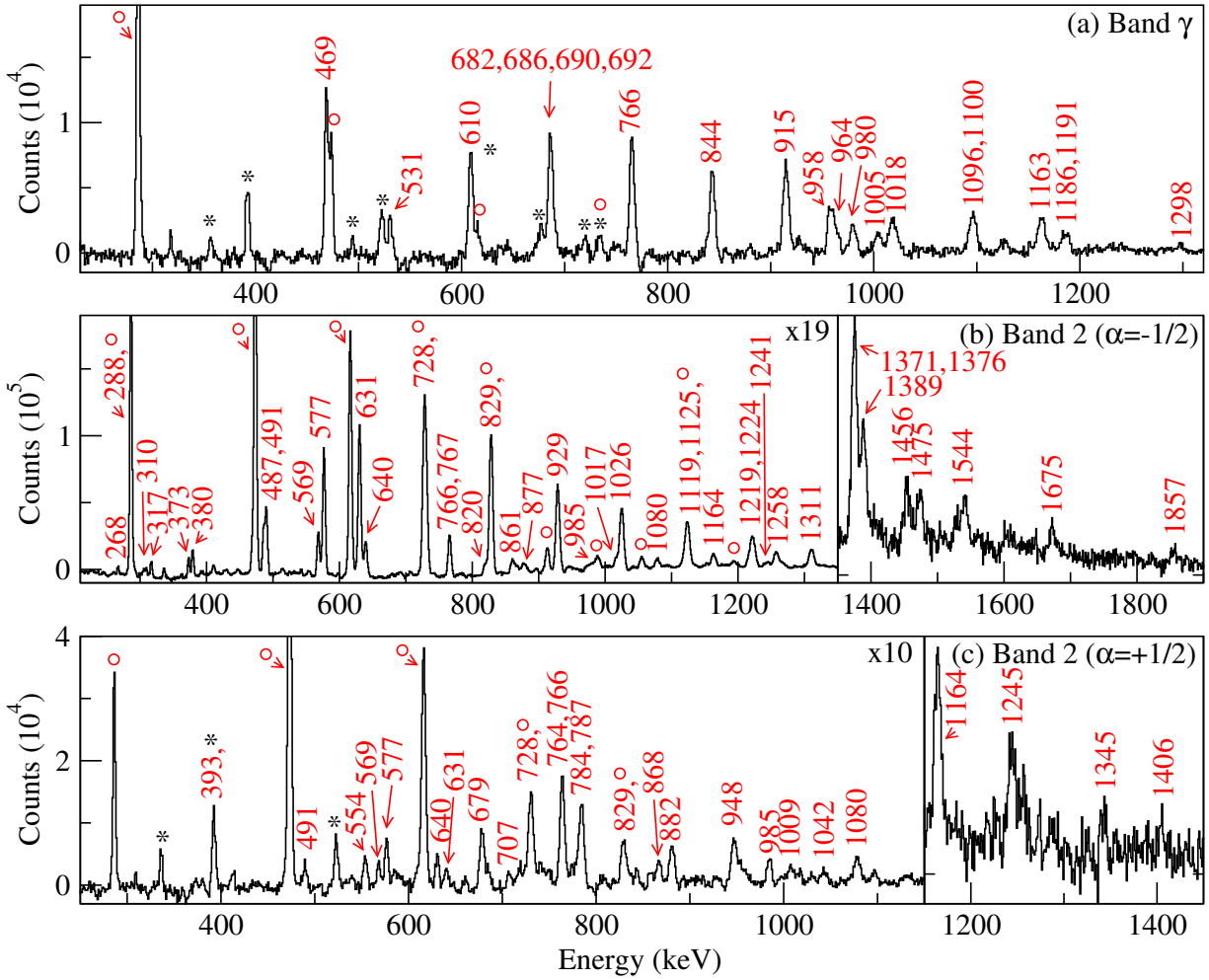

Figure 5.8: Spectra for Bands γ and 2 from triple coincidences by double gating on the lists of 610, 686, 766, 844, 958, 980, 1018, 1163 keV for Band γ, 287, 380, 491, 577, 631, 728, 829, 1026, 1125, 1224, 1311, 1376, 1456, 1544, 1675 keV for Band 2 (α = - 1/2), 287, 554, 679, 787, 868, 882, 948, 985, 1009, 1042, 1080, 1164, 1245 keV for Band 2 (α = + 1/2). Peak energies for the newly identified transitions are written in red. Transitions from other nuclei (^{116}Xe, ^{118}Xe, ^{120}Ba) are indicated with an asterisk, while those from other bands in ^{119}Cs are indicated with a red circle.

A double-gated spectrum of Band γ is shown in Fig. 5.8 (a). Band γ is newly observed and is assigned to ^{119}Cs. It feeds states up to spin $23/2^-$ of Band 1, the $19/2^-$ state of Band 2, and is observed up to spin 55/2. A cascade of three transitions of 1005, 1100 and 1191 keV form a band which decays via the $M1/E2$ 964-keV transition to the

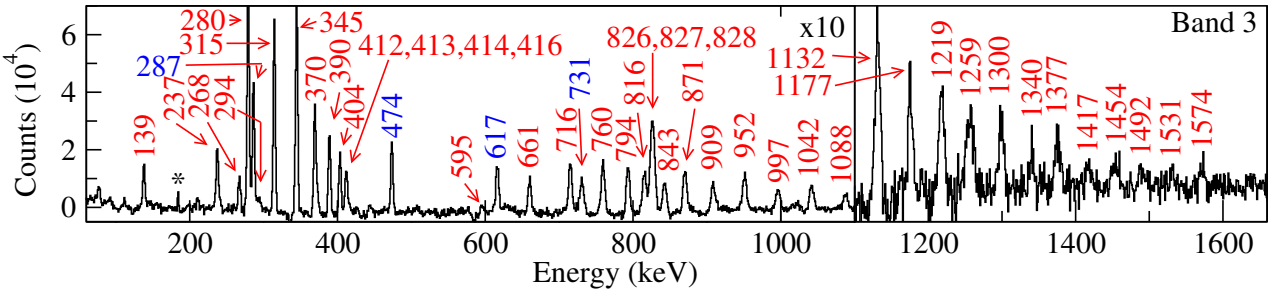

Figure 5.9: Double-gated spectrum for Band 3 of ^{119}Cs. The spectrum was obtained by double gating on 139-, 280-, 315-, 404-, 760-, 816-, 827-, 828-, 843-, 871-, 909-, 952-, 997-, 1042-, 1088-, 1132-, 1177-, 1219-, 1259-, 1340-, 1377-, 1454-keV transitions. Peak energies for the newly identified transitions are written in red. Transitions from other nuclei (^{119}Ba and ^{120}Ba) are indicated with an asterisk, while those from other bands in ^{119}Cs are indicated with a circle.

$35/2^-$ state of Band γ.

Double-gated spectra of Band 2 are shown in Fig. 5.8 (b) and (c). It is newly observed and is assigned to ^{119}Cs based on the connecting transitions between bands. As one can see in Fig. 5.1, Band 2 is composed of two long cascades of $E2$ transitions with opposite signatures, which decay to Band 1 through many $M1/E2$ and $E2$ transitions, and through the 569-keV $E2$ transition to the $19/2^-$ state of Band γ. Several transitions between the signature partners have been identified up to spin $45/2$. The negative parity of the band is firmly established by five $E2$ out-of-band transitions towards Band 1. A $67/2^-$ state with an energy smaller by 18 keV from the state with the same spin of Band 2, which is fed from the $71/2^-$ state and decays to the $63/2^-$ state of Band 2, has been also identified.

A double-gated spectrum of Band 3 is shown in Fig. 5.9. The new Band 3 has been assigned to ^{119}Cs based on the mass 119 measured at the MARA focal plane in coincidence with band transitions and Cs X rays (see Fig. 5.4) measured with JUROGAM 3. The 670-keV energy of the $11/2^-$ band-head is fixed by the cascade of transitions de-exciting the band towards the $3/2^+$ ground state. No transitions towards other low-lying states were observed. The intensity of the 268-, 237-, and 139-keV transitions depopulating the $11/2^-$ band-head is a factor of 16 lower than the intensity of the populating transitions, indicating an isomeric character with a lifetime in the range of tens of nanoseconds. The measured low intensity of the transitions depopulating the $11/2^-$ band-head is due to the emission by in-flight residual nuclei recoiling with a speed $v = 0.044c = 1.3$ cm/ns, mainly out of the focus of JUROGAM 3, and therefore do not directly hitting the collimated and escape-suppressed HPGe detectors. The assigned negative parity to Band 3 is not firmly established, because the 294-keV transition is very weak and the (26)-keV transition to the 643-keV $9/2^+$ state is not observed. It is instead supported by the strongly-coupled character of the band which implies the occupation of a high-Ω orbital.

Double-gated spectra of Bands 4 and 5 are shown in Fig. 5.10. The new Bands 4 and 5 are also assigned to

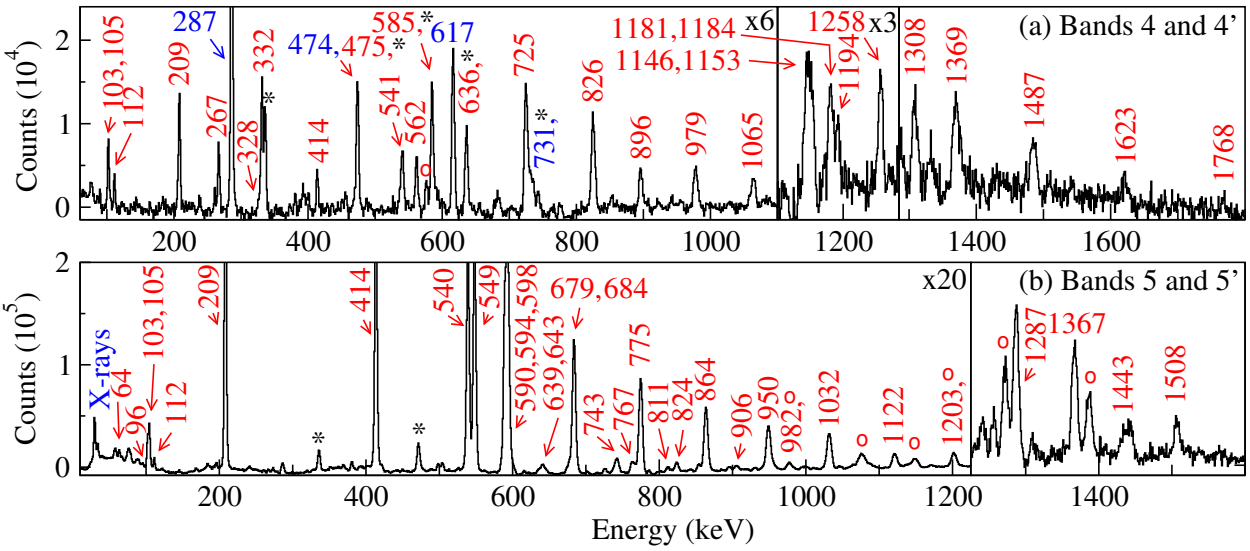

Figure 5.10: Spectra for Bands 4, 4', 5, 5' of ^{119}Cs obtained from triple coincidences by double-gating on selected transitions. The lists of gating transitions for each spectrum are the following: for Bands 4 and 4' 475, 541, 562, 636, 896, 979, 1065, 1146, 1153, 1369, 1487 keV; for Bands 5 and 5' 209, 414, 540, 549, 594, 684, 775, 864, 950 keV. Peak energies for the newly identified transitions are written in red. Transitions from other nuclei (^{116}Xe, ^{119}Ba, ^{120}Ba) are indicated with an asterisk, while those from other bands in ^{119}Cs are indicated with a circle.

^{119}Cs based on the mass 119 measured at the MARA focal plane in coincidence with band transitions and Cs X rays (see Fig. 5.4 (c) and (d)) measured with JUROGAM 3, and subsequently confirmed by the connecting transitions with Band 1, which are not strong enough to allow the extraction of the polarization asymmetry and therefore their electromagnetic character. The assigned positive parity to Band 4 is based on the properties of the band, which, being composed of only one cascade of $E2$ transitions, indicates the occupation of the $\alpha = 1/2$ signature partner of the low-Ω $\pi[420]1/2^+$ orbital.The spins and positive parity of Band 5 are fixed by the connecting $E2$ transitions with Band 4.

A double-gated spectrum of Band 4' is shown in Fig. 5.10 (a). It is composed of six $E2$ transitions which have been observed in coincidence with Band 4. It decays through the 1181-keV transition to the $57/2^+$ state of Band 4. The assigned spins and positive parity to the Band 4 are based on the R_{ac} ratios of the observed transitions which are compatible with $E2$ character.

A double-gated spectrum of Band 5' is shown in Fig. 5.10 (b). It composed of seven $E2$ transitions which have been observed in coincidence with the transitions of Band 5 below spin $17/2^+$. The assigned spins and positive parity to the Band 5 are based on the R_{ac} ratios of the observed transitions which are compatible with $E2$ character.

5.2.3 Bands 6, 7, 8, 9, and 10

A double-gated spectrum of Band 6 is shown in Fig. 5.11 (a). It is newly observed and is assigned to ^{119}Cs based on the connecting transitions between bands. Band 6 is composed of dipole and one crossover quadrupole transitions,

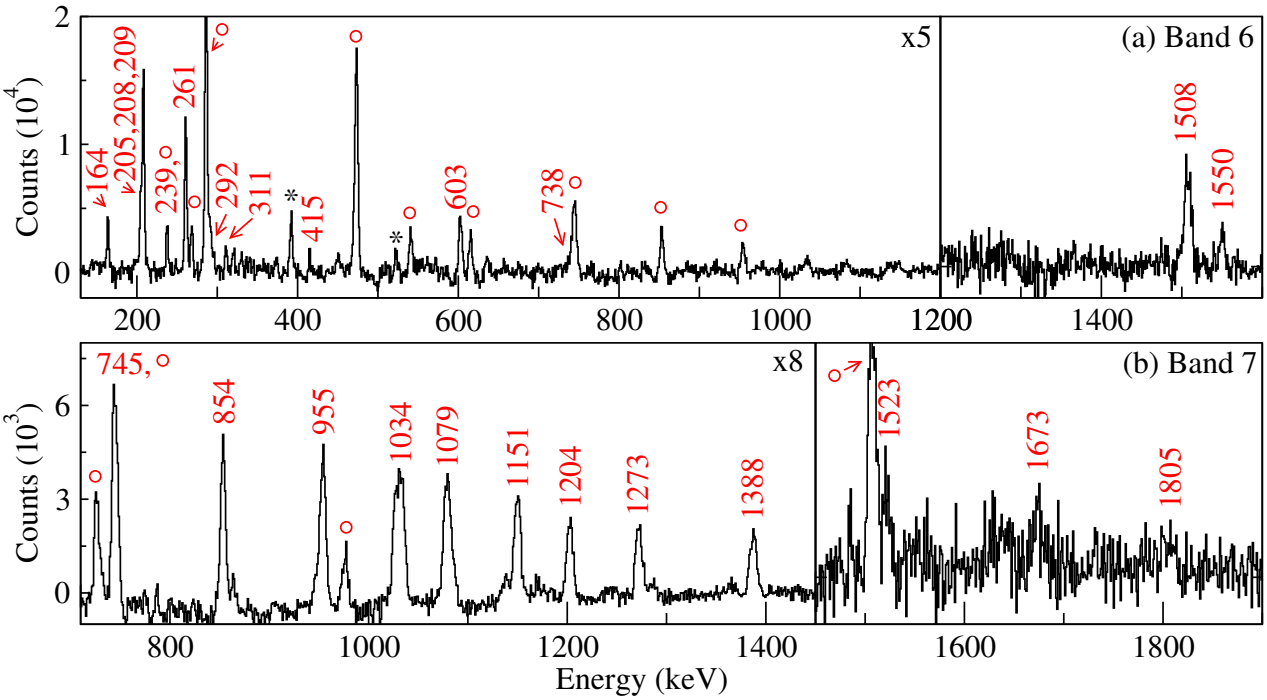

Figure 5.11: Spectra for Bands 6 and 7 of ^{119}Cs obtained from triple coincidences by double-gating on selected transitions. The lists of gating transitions for each spectrum are the following: for Band 6 164, 205, 209, 261, 311, 603, 1508, 1550 keV; for Bands 7 745, 854, 955, 1034, 1151, 1204, 1273, 1388, 1523, 1673 keV. Peak energies for the newly identified transitions are written in red. Transitions from other nuclei (^{116}Xe, ^{119}Ba, ^{120}Ba) are indicated with an asterisk, while those from other bands in ^{119}Cs are indicated with a circle.

and is observed between spin-parity $21/2^+$ and $33/2^+$. It decays to the $19/2^-$ state of Band 1, to the $17/2^+$ and $21/2^+$ states of Band 4, to the $27/2^+$ and $29/2^+$ states of Band 8, and is fed by the 292- and 603-keV $M1/E2$ transitions from the positive-parity Band 7. The positive parity of Band 6 is firmly established by the 738-keV and 887-keV $E2$ transitions towards the $21/2^+$ and $17/2^+$ states of Band 4, respectively.

A double-gated spectrum of Band 7 is shown in Fig. 5.11 (b). The new observed Band 7 is a long cascade of twelve $E2$ transitions, which decays to Bands 6 and 8. The $E2$ character of the 704-keV transition towards the $29/2^+$ state of Band 8 fixes the positive-parity of the band.

A double-gated spectrum of Band 8 is shown in Fig. 5.12 (a). The known Band 8 has been reported up to spin 25/2 in Ref. [126]. In this work, Band 8 has been extended to spin 63/2 and its the lowest lying state is at an excitation energy of 85.7 keV, determined by the connecting transitions to Bands 6 and 7, which in turn are firmly connected with the $3/2^+$ ground state.

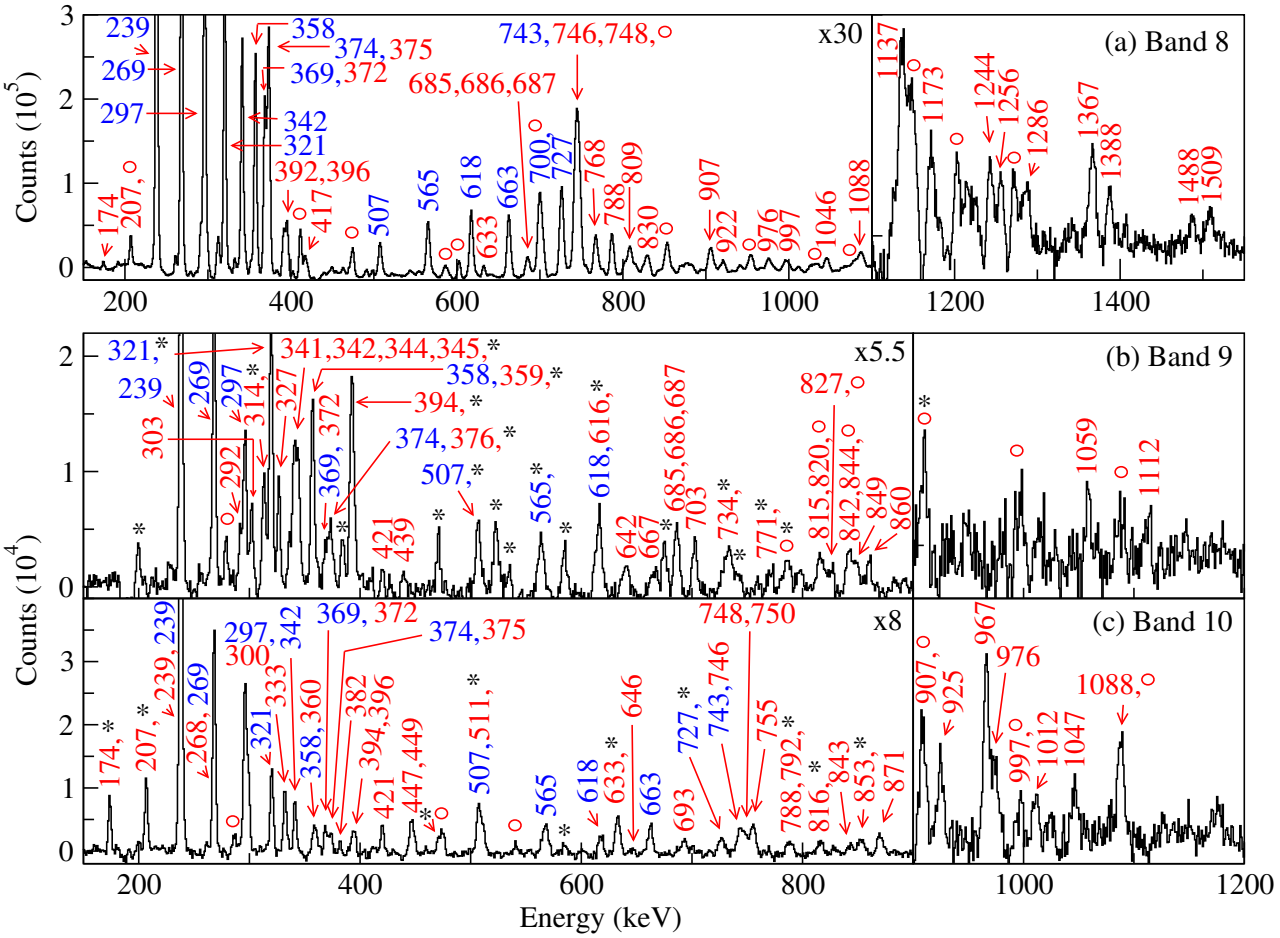

Figure 5.12: Double-gated spectra for bands 8 and 9, and band 10 of ^{119}Cs. The spectra were obtained by double gating on the 239-, 269-, 297-, 321-, 342-, 358-, 369-, 370-, 374-, 507-, 565-, 663-, 700-keV transitions for band 8, on the 292-, 303-, 314-, 327-, 341-, 344-, 376-, 439-, 642-, 685-, 687-, 734-, 771-keV for band 9, and on the 174-, 207-, 268-, 300-, 333-, 360-, 421-, 447-, 755-, 816-, 976-, 1088-keV transitions for band 10. Peak energies are written with blue color for previously known transitions and with red for the newly identified ones. Transitions from other nuclei (^{119}Ba, ^{118}Xe, ^{116}Xe, ^{118}Cs, ^{115}I) are indicated with an asterisk, while those from other bands in ^{119}Cs are indicated with a circle.

A double-gated spectrum of Band 9 is shown in Fig. 5.12 (b). It is newly observed and assigned to ^{119}Cs based on the several connecting transitions between Band 9 and Band 8. Band 9 is observed up to spin 39/2. The positive parity of Band 9 is fixed by the 1112- and 1059-keV $E2$ linking transitions to Band 8.

A double-gated spectrum of Band 10 is shown in Fig. 5.12 (c). Band 10 is observed up to spin 43/2. It is also newly observed and assigned to ^{119}Cs based on the several connecting transitions between Band 10 and Band 8. Among the connecting transitions there are four $E2$ transitions which fix positive parity of Band 10.

5.2.4 The isomeric states of ^{119}Cs

The two long-lived $9/2^+$ and $3/2^+$ isomers with half-lives of $T_{1/2} = 40.0(2)$ s and $T_{1/2} = 30.4(1)$ s in ^{119}Cs [124] cannot be measured in this experiment.

A matrix was constructed of the energies of the delayed γ rays versus the time of the focal plane clover detectors (see Fig. 5.13), which was used to identify and extract the half-lives of the isomeric states. One can see in Fig. 5.13 that the 46-, 53-, 66-, 79-, 87-, and 126-keV transitions are delayed and therefore should depopulate directly or indirectly isomeric states.

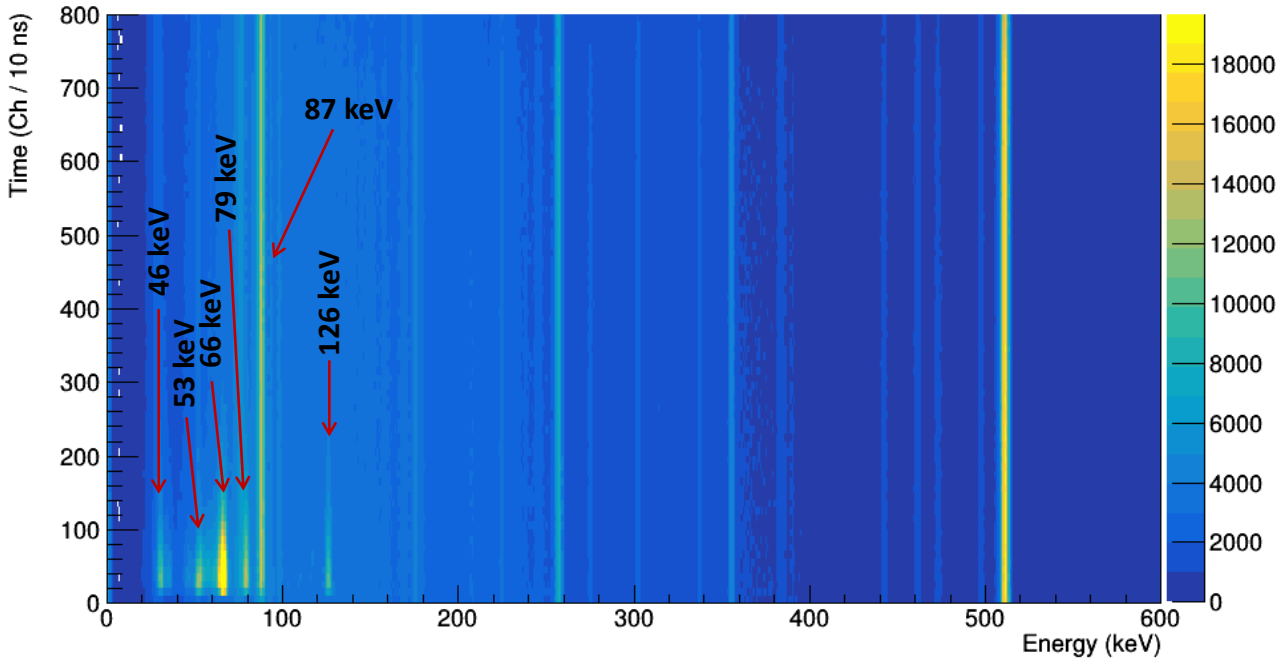

Figure 5.13: E_γ-Time matrix for the clover detectors at the focal plane.

In order to find out to which nuclei these isomeric states belong, the delayed coincidence between prompt transitions detected at the target position and the transitions detected at the MARA focal plane need to be used. We found a delayed coincidence between prompt transitions of Band 1 of ^{119}Cs and the delayed 87-keV transition, as shown in Fig. 5.14. A double-gating spectrum on the 287- and 474-keV transitions of Band 1 detected at the target position clearly shows the delayed 87-keV transition detected at the MARA focal plane in Fig. 5.14 (a). A spectrum of gating on the delayed 87-keV transition detected by the detectors placed around the MARA focal plane clearly shows the strong peaks of Band 1 detected at the target position in Fig. 5.14 (b). The delayed coincidence provide evidence that the 87-keV transition depopulates the $11/2^-$ band head of Band 1 at 110 keV the through an intermediate unobserved (23)-keV transition.

A 511-keV peak is present in the focal plane spectra. The spectrum is a strong background peak and should be flat. However, as one can see in the left panel of Fig. 5.15 the time spectrum of the background 511-keV γ ray has a slight slope. Thus, we fit isomer spectra with two exponentials, one with a fixed lifetime of $\tau = 240$ μs deduced from the fit of the background. Therefore, the formula used to fit time spectrum of the delayed transitions is

$$y = N_0 e^{\frac{-t}{240\mu s}} + N_1 e^{\frac{-t}{\tau}}, \tag{5.3}$$

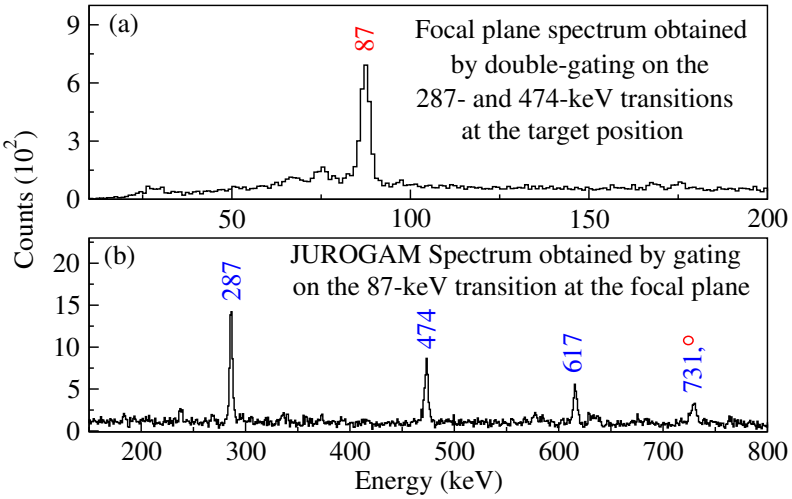

Figure 5.14: Spectra showing the delayed coincidence between transitions of Band 1 detected at the target position and the delayed 87-keV transition detected at the MARA focal plane. The 731-keV peak is wider due to contamination (indicated by a red circle) from the 725-keV transition of Band 4, as well as from the 728-keV transition of Band 2.

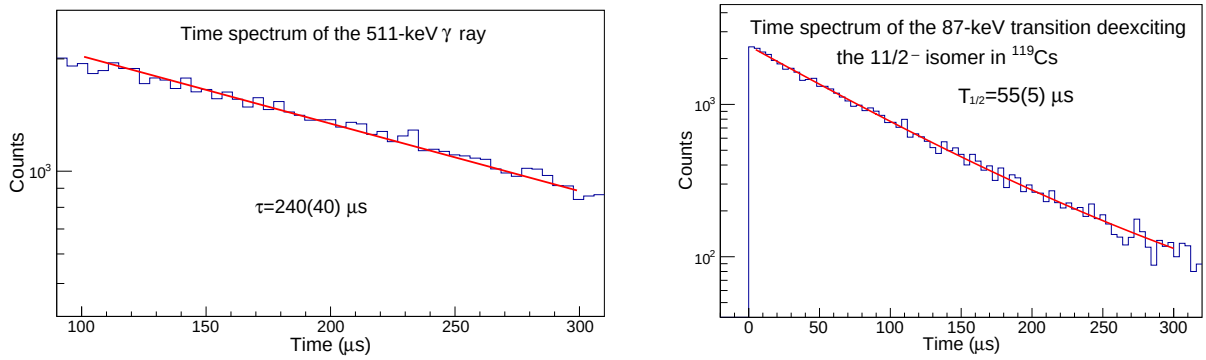

Figure 5.15: (left) Fit of the time spectrum of the 511-keV γ ray. (right) Fit of the time spectrum of the delayed 87-keV transition de-exciting the 11/2$^-$ band-head of Band 1 of ^{119}Cs.

where N_0, N_1 and τ are the fitting parameters. The half-time $T_{1/2}$ is related to the lifetime τ by $T_{1/2} = ln2 * \tau$.

The time spectrum of the 87-keV transition deexciting the 11/2$^-$ isomer in ^{119}Cs is shown in the right panel of Fig. 5.15. The spectrum was obtained from the clover detectors placed at the MARA focal plane, by gating on the 287-keV transition of Band 1 detected with JUROGAM 3 at the target position. The extracted lifetime of the $11/2^-$ state is $T_{1/2} = 55(5)$ μs.

5.3 Discussion

In the present work we investigate the possible configurations of all observed bands using PNC-CSM calculations [131, 132]. The phenomenological Nilsson potential is adopted for the mean field [131], with parameters κ and μ taken from Ref. [72], and effective monopole pairing strengths of 0.8 MeV for protons and 0.6 MeV for neutrons.

This model was recently used to successfully describe the band structure in rare-earth nuclei [132]. We do not discuss the γ band which cannot be described by the PNC-CSM calculations. Single-particle Routhian diagrams as a function of rotational frequency for prolate and oblate deformations which were used to guide the search of the closest quasiparticle orbitals to the proton and neutron Fermi surfaces are shown in Fig. 5.16.

An important issue in the interpretation of the observed bands is the adopted deformation. The calculations have been performed assuming axial symmetric shapes, which for nuclei with limited triaxiality of $\gamma \approx 10^{\circ}$ like ^{119}Cs [133], is a good approximation. The spectroscopic quadrupole moment has been measured for the band-head of Band 8 built on the $\pi[404]9/2^{+}$ orbital and lead to $\varepsilon_2 = 0.32$ ($\beta = 0.34$) [128]. However, the calculated ground-state deformation, like for example using the finite-range droplet model (FRDM) [38], is significantly smaller ($\varepsilon_2 = 0.25, \varepsilon_4 = -0.02, \gamma = 15^{\circ}$), corresponding to an axial deformation of $\varepsilon_2 = 0.23$. We performed calculations for the two deformations and found that the results for the smaller deformation $\varepsilon_2 = 0.23$ are in clear disagreement with the experimental data (see Fig. 5.17). We therefore adopted the $\varepsilon_2 = 0.32$ deformation for all prolate bands, excepting the negative-signature partner of Band 2 for which a slightly smaller deformation of $\varepsilon_2 = 0.30$ leads to a better agreement with the observed crossing at $\hbar\omega \approx 0.3$ MeV (see Fig. 5.32).

Here, two important phenomena, prolate-oblate shape coexistence and the breaking of the chiral symmetry will be presented separately. The former includes Bands 1, 3, 4, and 5, in which the first evidence of prolate-oblate shape coexistence close to the ground state in strongly-deformed proton-rich lanthanide nuclei is observed. The latter includes Bands 8, 9, and 10, in which the first observation of chiral bands built on a configuration with only protons in the transient backbending regime. We called this new type of chiral bands *Revolving Chiral Doublet* ($R\chi D$) bands. All the remaining bands will also be discussed together in a separate section.

5.3.1 Oblate-prolate shape coexistence in the strongly-deformed nucleus ^{119}Cs

Bands 1, 3, 4 and 5 are discussed in this section. As we know, oblate shapes can be induced by large energy gaps, like those at $Z = 56$ and $N = 60$ above $Z, N = 50$ major shells, and favored by the presence close to the Fermi surfaces of high-Ω Nilsson orbitals which have strong driving force towards oblate shape. The proton-rich lanthanide nuclei are among the best cases for oblate ground states, mainly due to the $\pi[505]11/2^{-}$ orbital, which has the steepest slope as a function of quadrupole deformation: when coupled with an oblate core, can give rise to strongly-coupled bands composed of degenerate signature partners which can develop over extended spins ranges, enabling thus the study of their properties. However, no experimental evidence of such low-lying oblate bands in proton-rich lanthanide nuclei has been reported so far.

This missing experimental evidence can be explained by the low barrier between the prolate and oblate minima, and by the strong pairing correlations at low excitation energy, which induce strong mixing and fragmentation of the wave functions, prohibiting thus the development of long rotational cascades. However, in odd-even nuclei, the

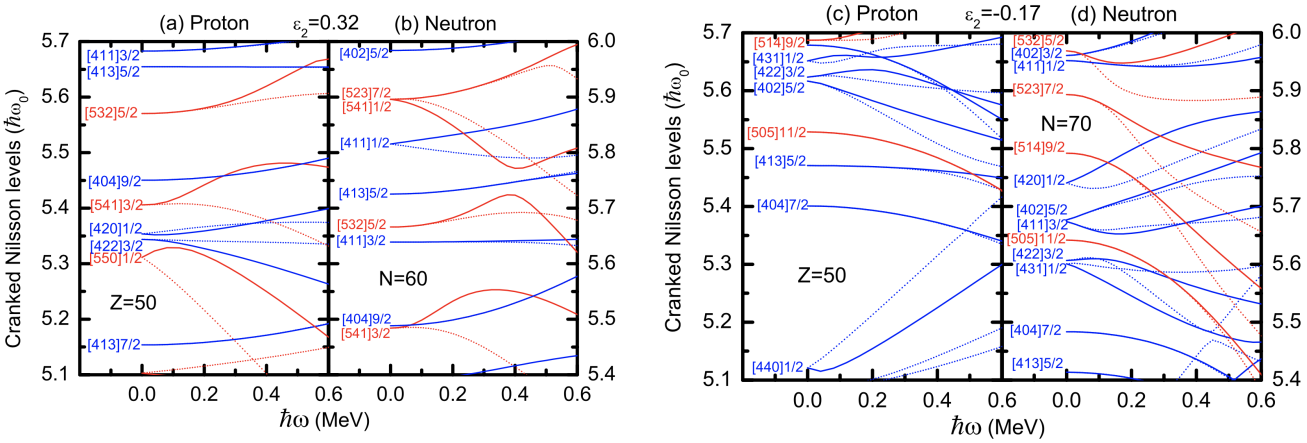

Figure 5.16: Single-particle Routhians located in the vicinity of the Fermi level of ^{119}Cs as a function of rotational frequency for: a) and b) axial prolate deformation of $\varepsilon_2 = 0.32$; c) and d) axial oblate deformation of $\varepsilon_2 = -0.17$. Positive (negative) parity Routhians are shown by blue (red) lines. Solid (dotted) lines are used for signature $\alpha = +1/2$ ($\alpha = -1/2$).

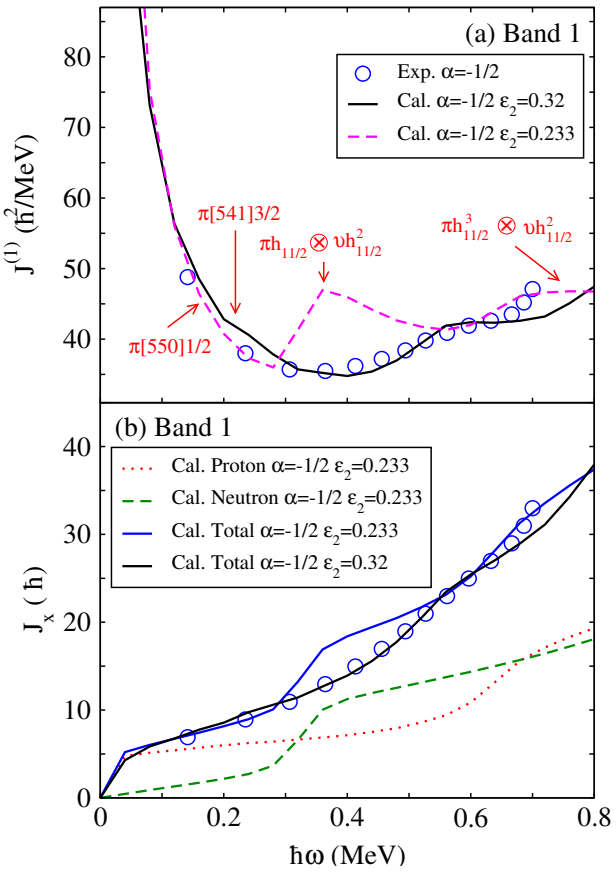

Figure 5.17: (a) Moment of inertia $J^{(1)}$, (b) projection of the angular momentum on the cranking axis J_x for the $\alpha = -1/2$ signature partner of Band 1 calculated using the PNC-CSM model for the two deformations $\varepsilon_2 = 0.23$ and $\varepsilon_2 = 0.32$.

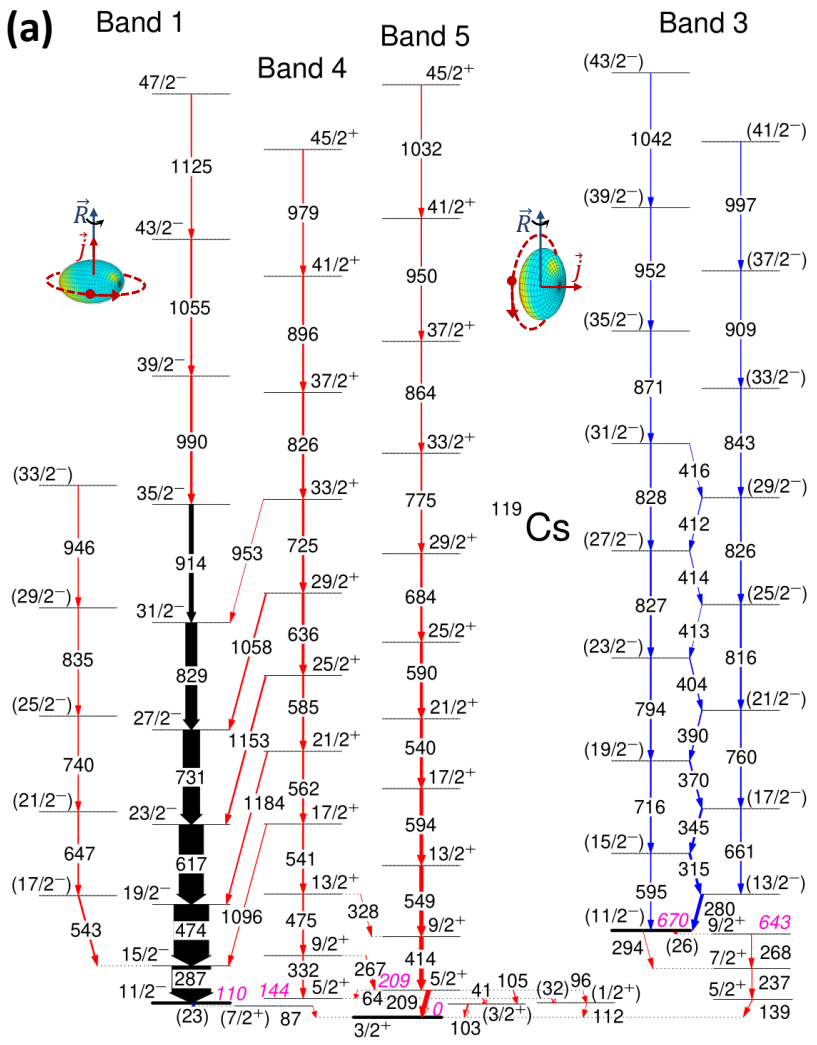

Figure 5.18: Partial level scheme of ^{119}Cs showing the Bands 1, 3, 4 and 5. The prolate shapes assigned to Bands 1, 4, 5 and the oblate shape assigned to Band 3, as well as the orbits and angular momenta of the odd proton are schematically drawn. The new transitions are indicated in red or blue. The isomeric levels are indicated with thick lines. The bands continue at higher spins with the transitions listed in Table 5.2 and Figs. 5.1, 5.2.

angular momentum of the odd nucleon can have very different orientations relative to the core, and can give rise to K isomers, which can facilitate the observation of oblate states [42, 43]. One or two long-lived isomeric states were identified long time ago in Cs nuclei [130], and their magnetic moments and spectroscopic quadrupole moments were measured [134]. All these isomers were assigned to prolate shapes, with deformations increasing towards the drip line. However, the predicted oblate states can have lifetimes too short to allow their identification using isotope separation online methods.

In the present subsection we report the first observation of an oblate negative-parity band in the proton-rich strongly-deformed nucleus ^{119}Cs, the determination of its ground state, the identification of two positive-parity bands, of several low-lying levels, as well as the half-life of the band-head of the prolate band originated from the $\pi h_{11/2}$ configuration.

As for prolate deformation the only high-Ω orbital close to the $Z = 55$ Fermi surface is $[404]9/2^+$ which is assigned to Band 8 (the reason was discussed in Section 5.3.2). The configuration of Band 3 can only be based on the $\pi h_{11/2}[505]11/2^-$ orbital which is close to the Fermi surface for oblate deformation, giving thus confidence in the assigned negative parity. The decay of Band 3 only towards the three $5/2^+$, $7/2^+$ and $9/2^+$ states below the band-head, and the lack of connecting transitions between these states and the other positive-parity states, strongly suggests that these states are also based on oblate shapes, associated to the occupation of the $\pi[413]5/2^+$ and/or $\pi[402]5/2^+$ orbitals close to the Fermi surface for oblate deformation (see Fig. 5.16).

The properties of Band 4 indicate the occupation of a low-Ω orbital with signature $\alpha = 1/2$, most probably $\pi[420]1/2^+$. The PNC-CSM calculation for the $\pi[420]1/2^+(\alpha = 1/2)$ configuration is shown in Fig. 5.19 which is in excellent agreement with Band 4. Fig. 5.19 (b) shows the alignment of a proton pair at ≈ 0.35 MeV/$\hbar$, followed by a more gradual alignment of a pair of neutrons at $\hbar\omega \approx 0.50$ MeV/$\hbar$.

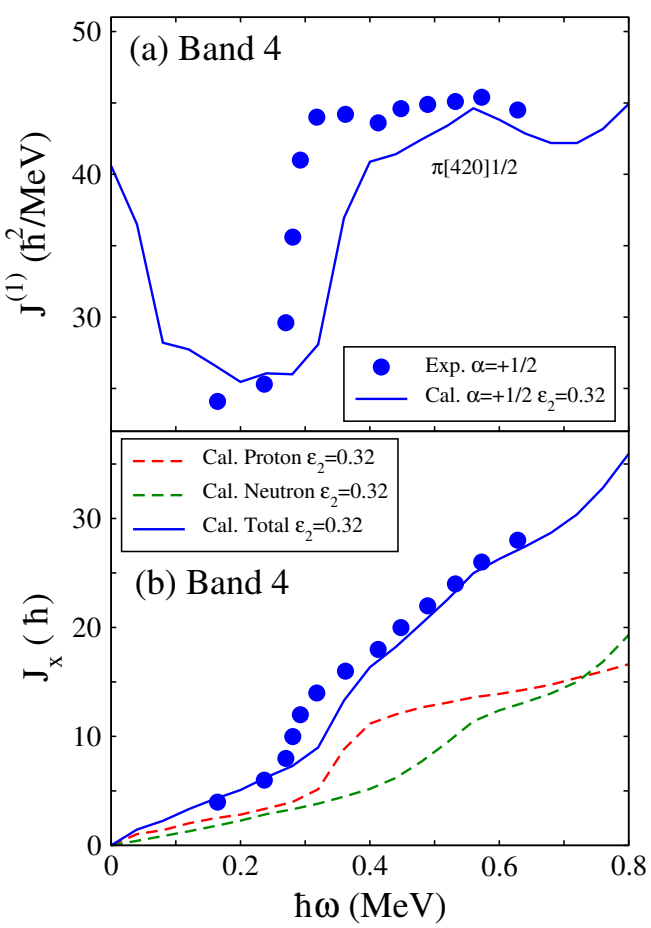

Figure 5.19: (a) Moments of inertia $J^{(1)}$ and (b) projection of the angular momenta on the cranking axis J_x for Band 4.

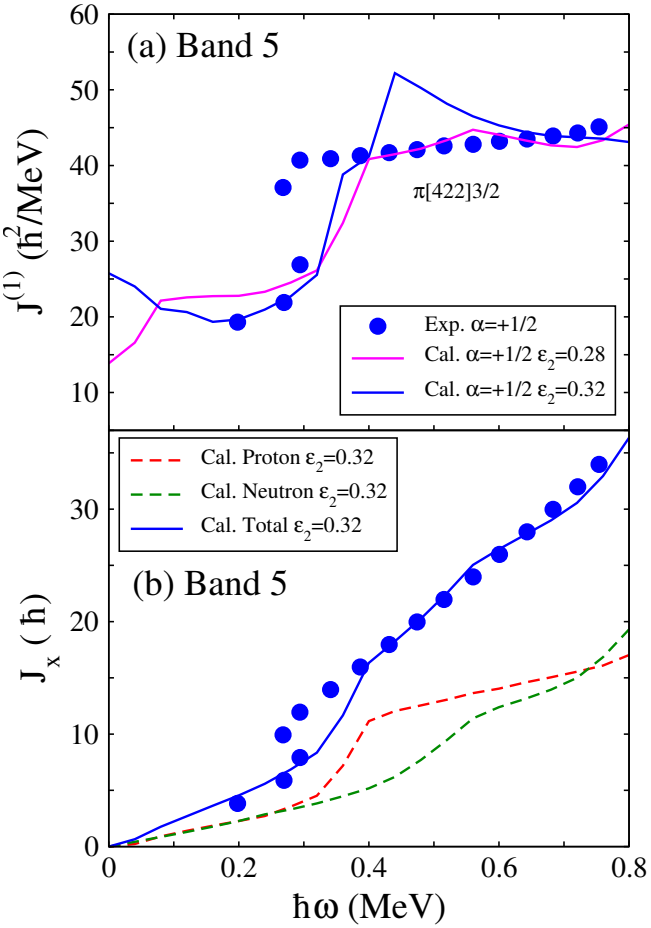

Figure 5.20: (a) Moments of inertia $J^{(1)}$ and (b) projection of the angular momenta on the cranking axis J_x for Band 5.

The spins and positive parity of Band 5 are fixed by the connecting $E2$ transitions with Band 4. The PNC-CSM calculation for the $\pi[422]3/2^+(\alpha = 1/2)$ configuration is shown in the Fig. 5.20 in which we can see excellent

agreement with Band 5. Based on the that good agreement, we assign the $\pi[422]3/2^{+}(\alpha = 1/2)$ configuration to Band 5.

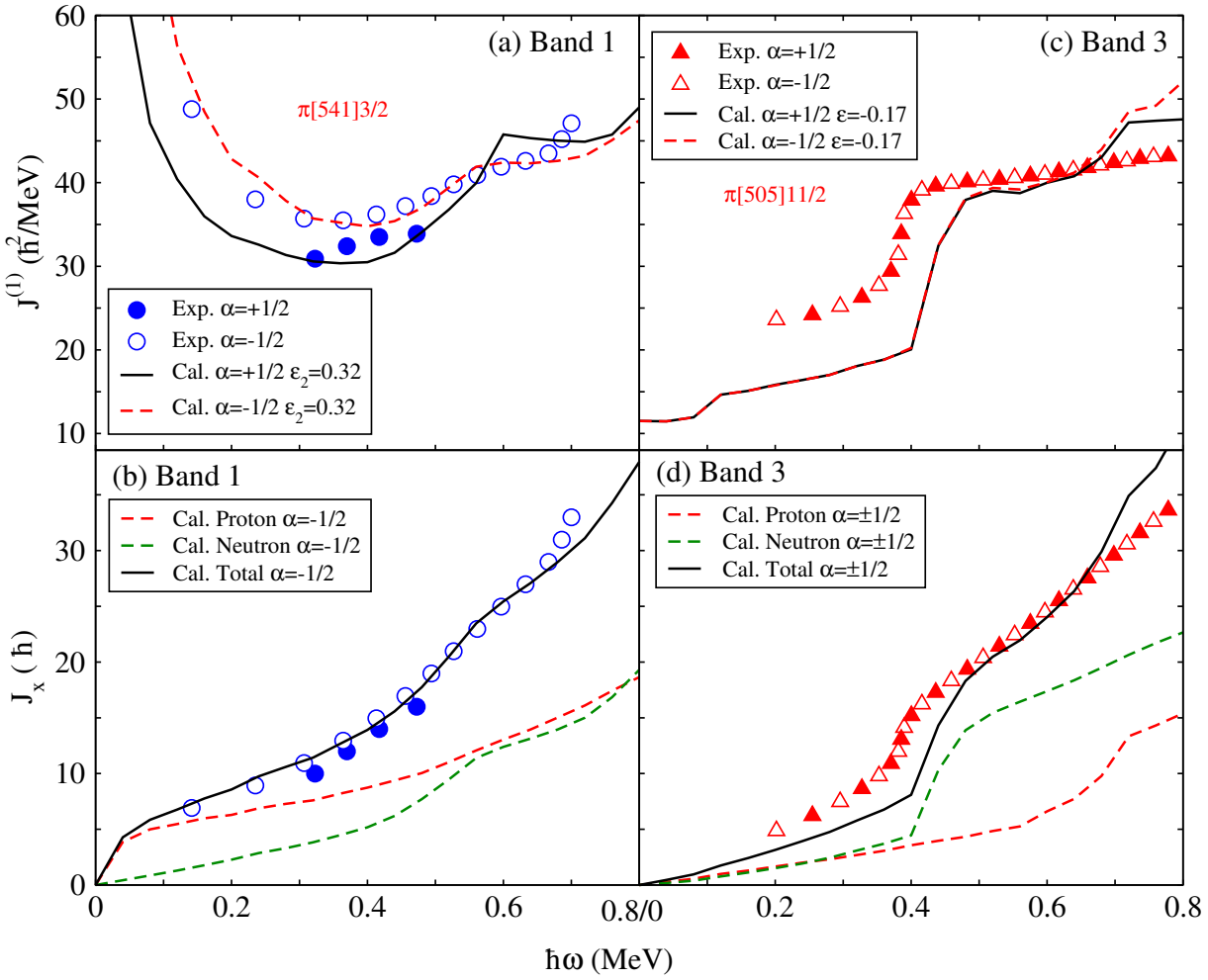

Figure 5.21: (a) and (c) Moments of inertia $J^{(1)}$, (b) and (d) projections of the angular momentum on the cranking axis J_x for Bands 1 and 3 of ^{119}Cs calculated using the PNC-CSM model assuming axially symmetric shapes. The states with signature $\alpha = +1/2$ and $\alpha = -1/2$ are drawn with filled and open symbols, respectively.

Band 1 previously known up to spin $35/2^{-}$ [126], is now extended up to spin $(67/2^{-})$. We also identified a weakly populated band decaying to the $15/2^{-}$ state of Band 1, which we assigned as the unfavored signature partner of Band 1, for which the spin-parity could not be extracted. Based on the calculations described in the following, we assigned it as the unfavored signature partner of Band 1, which lead to tentatively assigned spins as shown in Fig. 5.18.

As one can see in Fig. 5.21, the theoretical moments of inertia $J^{(1)}$ and projection of the total spin on the cranking axis J_x calculated assuming $\varepsilon_2 = 0.32$ for Band 1 and $\varepsilon_2 = -0.17$ for Band 3, respectively, are in good agreement with the experimental values. They show a sharp proton alignment accompanied by a gradual neutron alignment in the favored signature partner of Band 1, together with a reasonable agreement for the unfavored signature partner

with $\alpha = +1/2$. The same good agreement is achieved for Bands 4 and 5 calculated for a deformation of $\varepsilon_2 \approx 0.32$ (see Figs. 5.19 and 5.20), which reveal a sharp proton alignment at $\hbar\omega \approx 0.3$ MeV followed by a more gradual neutron alignment at $\hbar\omega \approx 0.5$ MeV. In addition, a smaller deformation for the positive-parity Bands 4 and 5 can be excluded, since in that case the neutron alignment is calculated sharper than experimentally observed (see in Fig. 5.20).

The negative-parity Band 3 supposed to have an oblate shape does not decay to the other negative-parity bands, which are all consistently interpreted as built on prolate shape. This can be explained by the existence of a barrier between the oblate and prolate minima, which can be as high as 5 MeV [39, 40, 41], but also by a very different orientation of the spin of the odd proton relative to the core which can lead to ΔK forbidden transitions. It also does not decay to the low-lying states populated by transitions from Bands 4 and 5, which are also based on prolate shapes. One can therefore speculate that the decay of Band 3 proceeds towards states built on the same oblate shape, with configurations built on $\pi[413]5/2^+$ and $\pi[402]5/2^+$ orbitals close to the Fermi surface for an oblate deformation of $\varepsilon_2 \approx -0.2$. The missing high-$\Omega$ orbitals close to the $Z = 55$ Fermi surface for a prolate deformation of $\varepsilon_2 \approx 0.3$, which can explain the observed decay of Band 3, is another argument in favor of oblate shapes assigned to Band 3 and to the positive-parity states towards which it decays. These oblate states coexist at low spins with several prolate states associated with the low-Ω orbitals $\pi[422]3/2^+$, $\pi[420]1/2^+$, and $\pi[541]3/2^-$, and on the high-Ω orbital $\pi[404]9/2^+$, which are all close to the Fermi surface for $\varepsilon_2 \approx 0.3$. The experimental observation of low-lying oblate states coexisting with prolate states within a few tens of keV is favored by the large gap above the $Z = 55$ proton Fermi surface for oblate deformation, induced by strongly down-sloping high-Ω orbitals.

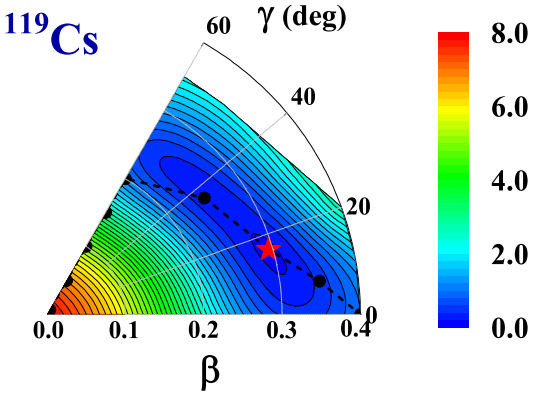

Figure 5.22: The potential energy surface of ^{119}Cs in the β-γ deformation plane for the configuration $\pi h_{11/2}$ calculated by the TAC-CDFT. The energy separation between contour lines is 0.2 MeV. The energy minimum pathway and the position of absolute energy minimum are denoted by black dots and red star, respectively.

The potential energy surface of ^{119}Cs for the $\pi h_{11/2}$ configuration calculated by the tilted axis cranking covariant density functional theory (TAC-CDFT) [135, 136, 137] is shown in Fig. 5.22. The density functional PC-PK1 [138] is used in the particle-hole channel, and it has been successfully used to describe not only the ground-state properties including the nuclear masses [139, 140, 141] and quadrupole moments [142], but also nuclear rotations such as

magnetic and antimagnetic rotations [135, 143, 144, 145], chiral rotations [9], etc. For the particle-particle channel, a finite-range separable pairing force [146] is employed. As one can see from Fig. 5.22, the potential energy surface exhibits a minimum around $\beta \approx 0.3$ and is very soft in the γ direction. The energy minimum pathway demonstrates that the oblate shape is favored for β smaller than 0.2 corresponding to the observed Band 3, and the prolate shape becomes favored for larger β values, corresponding to Band 1. These features support the coexistence of prolate and oblate minima, however without a separating barrier between them. Note that beyond-mean-field correlations induced by the rotational symmetry restoration and the shape fluctuation, which are missing in the present calculations, would play a role in the shape coexistence. Further investigations by the five dimensional collective Hamiltonian approach [147, 148] could be very interesting.

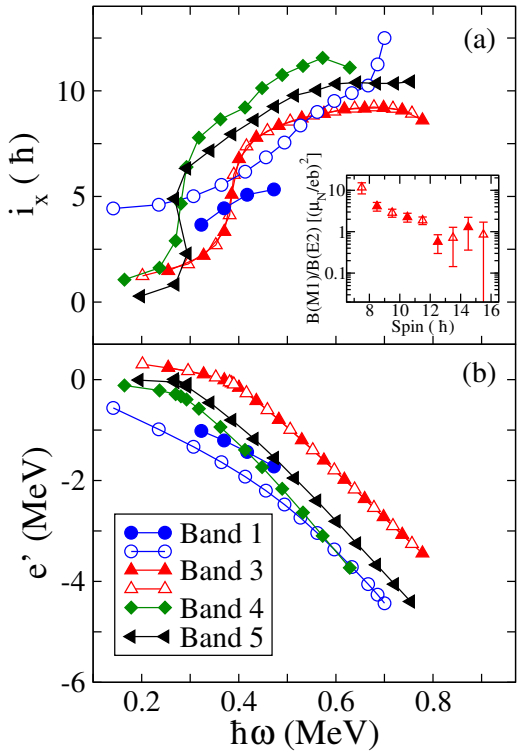

Figure 5.23: (a) Single-particle angular momenta i_x and $B(M1)/B(E2)$ values, as well as (b) Routhians e' of Bands 1, 3, 4, and 5 of ^{119}Cs. The Harris parameters are $J_0 = 17\hbar^2$MeV^{-1} and $J_0 = 25\hbar^4$MeV^{-3}. The K values are 1.5, 5.5, 0.5, and 1.5 for Bands 1, 3, 4, and 5, respectively. The states with signature $\alpha = +1/2$ and $\alpha = -1/2$ are drawn with filled and open symbols, respectively.

The experimental quasiparticle alignments and Routhians of Bands 1, 3, 4, 5 are shown in Fig. 5.23. $B(M1)/B(E2)$ ratios of reduced transition probabilities of Band 3 is also shown in Fig. 5.23. They offer a view on the different alignment properties and relative excitation of the bands.

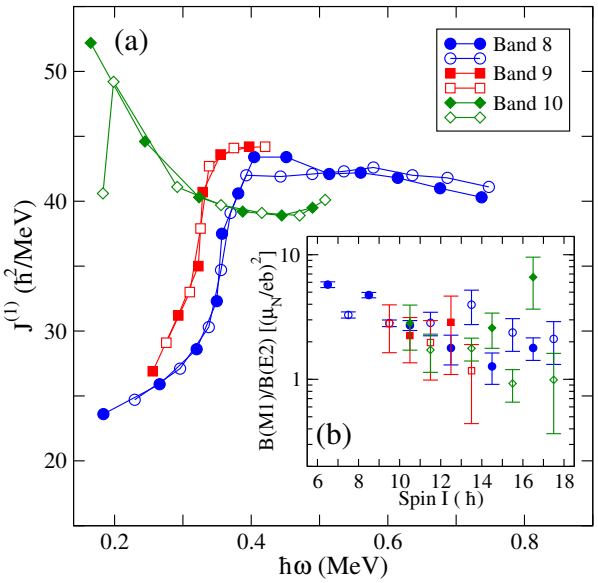

Figure 5.24: (a) Moments of inertia $J^{(1)}$ and (b) B(M1)/B(E2) ratios of Bands 8, 9 and 10 of ^{119}Cs. A K-value equal to 4.5 has been used. The states with signature $\alpha = +1/2$ and $\alpha = -1/2$ are drawn with filled and open symbols, respectively.

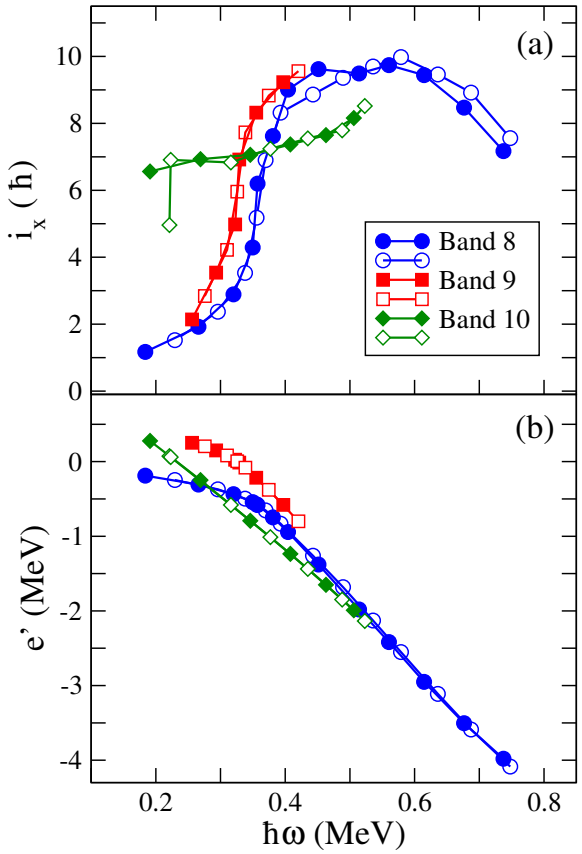

Figure 5.25: (a) Single-particle angular momenta i_x and (b) Routhians e' of Bands 8, 9 and 10 of ^{119}Cs. The Harris parameters are $J_0 = 17\ \hbar^2$MeV^{-1} and $J_1 = 25\ \hbar^4$MeV^{-3}. The K values are 4.5 for Bands 8 and 9, and 0.5 for Band 10. The states with signature $\alpha = +1/2$ and $\alpha = -1/2$ are drawn with filled and open symbols, respectively.

5.3.2 Proton based revolving chiral bands in ^{119}Cs

In this section, Bands 8, 9, and 10 will de discussed. We can see in Fig. 5.2 that the newly observed states in ^{119}Cs lead to the extension of Band 8 to much higher spin than previously known [126], well above the backbending region. The kinematic moments of inertia $J^{(1)}$ and $B(M1)/B(E2)$ ratios of Bands 8, 9 and 10 are shown in Fig. 5.24, in which Bands 8 and 9 are nearly degenerate and have similar moments of inertia. The aligned single-particle angular momenta are shown in Fig. 5.25. One can see the similar patterns of Bands 8 and 9, which exhibit crossings with three-quasiparticle configurations at rotational frequencies of 0.32 and 0.37 MeV, respectively. The gain of angular momentum is $\approx$ 8 $\hbar$, indicating the alignment of a pair of $h_{11/2}$ particles, and the negligible contribution of the strongly-coupled $[404]9/2^+$ proton orbital. Band 10 has a completely different pattern, with a lower aligned angular momentum of $\approx$ 6 $\hbar$, which increases steadily up to $\approx$ 9 $\hbar$ over the observed frequency range, while the moments of inertia (MoI) decreases from $\approx$ 53 $\hbar^2$MeV^{-1} at low frequency to $\approx$ 40 $\hbar^2$MeV^{-1} at the top of the band. This clearly indicates a different configuration of Band 10 from that of Bands 8 and 9.

The deformation of the different configurations was first calculated using the tilted axis cranking covariant density functional theory (TAC-CDFT) [135, 143] with pairing correlations [137, 145, 149], employing the density functional PC-PK1 in the ph channel [138] and a separable force in the pp channel [146]. The results for Bands 8 and 9 are shown in Fig. 5.26. Convergence was obtained for only limited frequency regions due to the mean field nature of the model. The calculated quadrupole deformation of the $\pi g_{9/2}^{-1}$ configuration $\beta = 0.36$ is in agreement with the measured value of $\beta = 0.336$ [128], and decreases slightly to 0.35 and 0.33 in the configurations with two more protons and two more neutrons, respectively. A stable moderate triaxiality $\gamma \approx 12^\circ$ is calculated for all one-, three-, and five-quasiparticle configurations shown in Fig. 5.26.

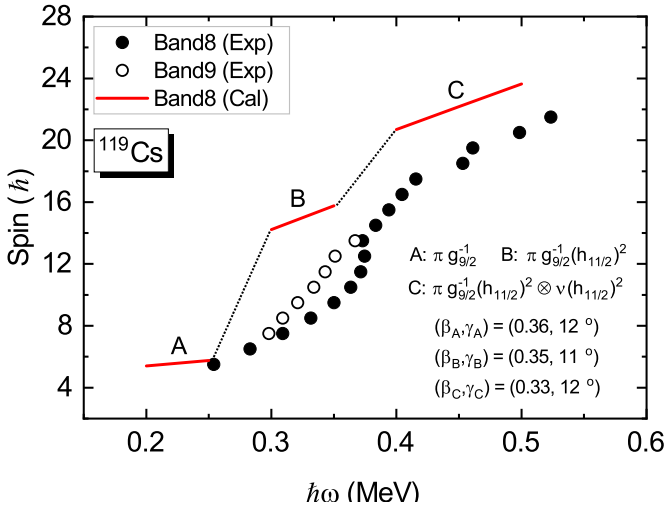

Figure 5.26: Comparison between the experimental spin versus rotational frequency and the TAC-CDFT calculations for Bands 8 and 9 of ^{119}Cs. The states with signature $\alpha = +1/2$ and $\alpha = -1/2$ are drawn with filled and open symbols, respectively.

In order to investigate the possible configurations of Band 8, we performed calculations using the PNC-CSM

as in Fig. 5.27. The agreement with the experiment is excellent. The calculated angular momentum alignment J_x for the $\pi[404]9/2^+$ configuration of Band 8, and its decomposition in proton and neutron contributions, indicate that the backbending is due to the alignment of a pair of $h_{11/2}$ protons at a frequency of ≈ 0.35 MeV/$\hbar$, followed by the more gradual alignment of a pair of neutrons at ≈ 0.5 MeV/$\hbar$. The orbitals in the $N = 4$ shell only provide a gradual increase of the angular momenta. As for the contribution from the $\pi[404]9/2^+$ orbital, it keeps nearly constant with rotational frequency, which means that this orbital keeps aligned along the long axis.

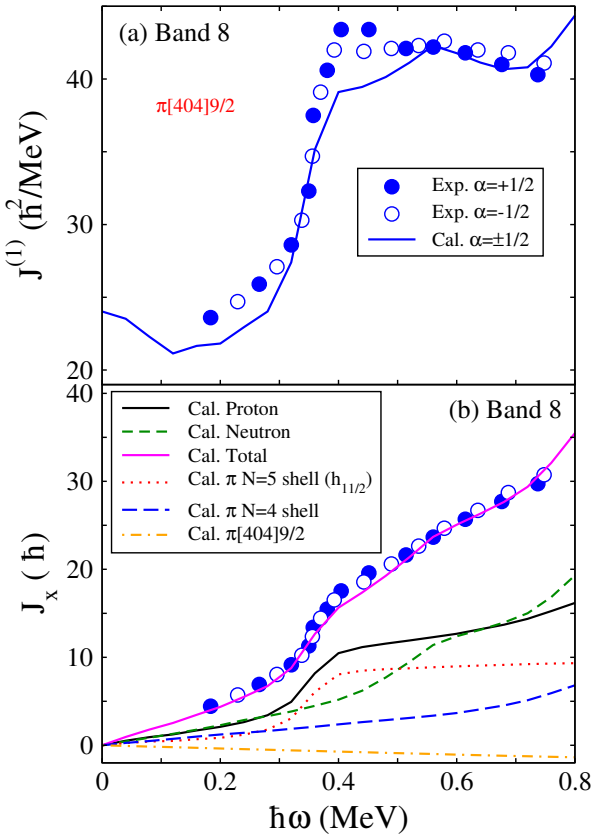

Figure 5.27: (a) Moment of inertia $J^{(1)}$, (b) projection of the angular momentum on the cranking axis J_x for Band 8 of ^{119}Cs calculated using the PNC-CSM model. The states with signature $\alpha = +1/2$ and $\alpha = -1/2$ are drawn with filled and open symbols, respectively.

The calculations of moments of inertia $J^{(1)}$ and projection of the angular momenta on the cranking axis J_x for Band 10 are shown in Fig. 5.28. The agreement with the experiment is excellent. As one can see in Fig. 5.29, one diagonal and two off-diagonal (interference) terms (see Eqs. 11 and 12 in Ref. [132]) of the orbitals in the $N = 5$ shell contribute to the backbending. Band 10 has a MoI with similar pattern to that of the decoupled band built on the $11/2^-$ state [126], which is based on the $\pi[541]3/2^+$ orbital. Its positive parity and the near degeneracy of their signature partners indicate the presence of two nucleons in opposite parity high-Ω orbitals, which induce an alignment in agreement with experiment only for neutrons. We therefore assign the three-quasiparticle configuration $\pi[541]3/2(\alpha = +1/2) \otimes \nu^2[413]5/2[523]5/2$ to Band 10.

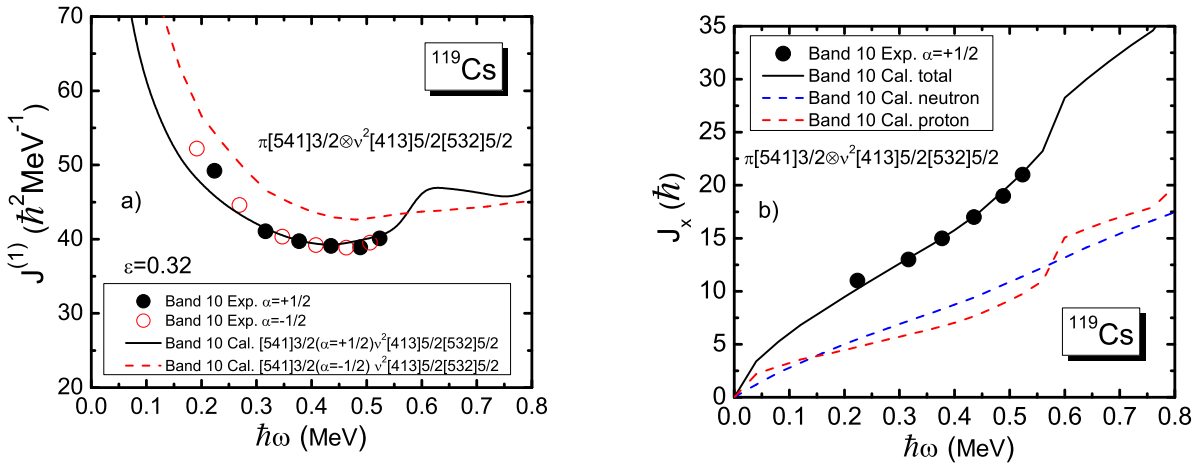

Figure 5.28: Moments of inertia $J^{(1)}$ and projection of the angular momenta on the cranking axis J_x for Band 10 of ^{119}Cs. The states with signature $\alpha = +1/2$ and $\alpha = -1/2$ are drawn with filled and open symbols, respectively.

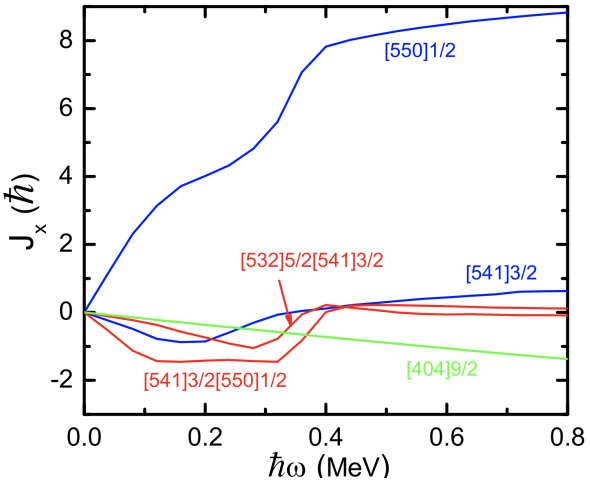

Figure 5.29: Calculated diagonal and off-diagonal contributions to J_x from from the $N = 5$ orbitals calculated with PNC-CSM for the $\pi g_{9/2}[404]9/2^+$ configuration assigned to Bands 8 and 9 of ^{119}Cs.

The similar alignment patterns and $B(M1)/B(E2)$ ratios of the reduced transition probabilities of Bands 8 and 9 suggest identical single-particle configurations (see Figs. 5.24 and 5.26). The single-particle alignment of Band 9 is higher by $\approx 2\hbar$ than that of Band 8 just above the band-head, which suggests an interpretation as γ-band. The slightly different rotational frequencies of the backbends observed in Bands 8 and 9 can be due to slightly different MoIs induced by different directions of the rotation axes in the two bands. The properties of Band 9 are in agreement with a chiral interpretation of the γ-band built on the $\pi[404]9/2^+ \otimes \pi h^2_{11/2}$ configuration. However, in order to adopt this interpretation, one must exclude other possible configurations.

The smaller crossing frequency in Band 9 than in Band 8 can also be attributed to the possible smaller deformation of Band 9. Such a hypothesis was proposed for a band with similar properties observed in the even-even ^{118}Xe nucleus [150], which can be considered as the core of ^{119}Cs. The band in ^{118}Xe was interpreted as the γ-band

which evolves at high spin through the alignment of a pair of neutrons, which, being located in the middle of the $h_{11/2}$ sub-shell, would have a driving force towards smaller deformation and could reduce the crossing frequency. We checked this alternative scenario by PNC-CSM calculations which are shown in Fig. 5.30, where one can see

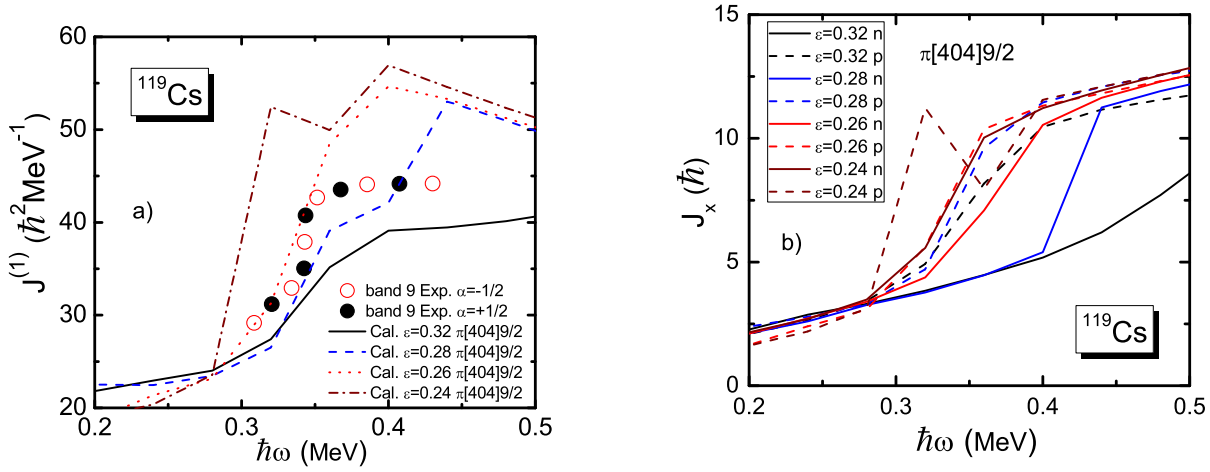

Figure 5.30: Moments of inertia $J^{(1)}$ and projection of the angular momenta on the cranking axis J_x for Band 9 of ^{119}Cs for different deformations. The states with signature $\alpha = +1/2$ and $\alpha = -1/2$ are drawn with filled and open symbols, respectively.

that for smaller deformations than that of Band 8 ($\varepsilon_2 \approx 0.32$), the experimental moment of inertia is not well reproduced: for $\varepsilon_2 \approx 0.28$ the neutron alignment is significantly delayed relative to that of protons and gives rise to an unobserved jump at $\hbar\omega \approx 0.40$ MeV, while for lower deformations $J^{(1)}$ is largely overestimated. We can therefore discard the smaller deformation and the corresponding neutron alignment for Band 9.

Another possible configuration of Band 9 can be $\pi[422]3/2^+$, which is close to the Fermi surface and can give rise to a band with nearly degenerate signature partners. However, there are three important arguments contrary to this interpretation: $i)$ Band 9 decays only to Band 8 and not to another band built on the close-lying [420]1/2$^+$ orbital, with which the [422]3/2$^+$ is strongly mixed; $ii)$ the observed two signatures of Band 9 are degenerate at the bottom of the band, which is in contradiction with the calculations; $iii)$ the mixing of the high-Ω [404]9/2$^+$ configuration with other close-lying low-Ω positive-parity states like [420]1/2$^+$ and [422]3/2$^+$ is expected to be low.

One can therefore conclude that Band 9 is built on the same three-proton configuration as Band 8 in the backbending region, one in the high-Ω [404]9/2$^+$ orbital and two in low-Ω $h_{11/2}$ orbitals. The nearly orthogonal geometry of the angular momenta of the involved high-Ω and low-Ω orbitals, the similar alignment patterns and $B(M1)/B(E2)$ ratios of reduced transition probabilities, strongly suggest the chiral nature of Bands 8 and 9.

The collective motion which gives rise to Bands 8 and 9 in ^{119}Cs can therefore be 3D rotation and have chiral character. For an odd-even ^{119}Cs nucleus, the observation for the first time of chiral bands in this nucleus reveal a new type of chirality, which we can call ”electric chirality”, which is based on a configuration involving only protons, one in the strongly-coupled $\pi g_{9/2}[404]9/2^+$ orbital, and the two others in $\pi h_{11/2}$ orbitals. Strongly coupled bands

based on high-Ω Nilsson orbitals are known in nuclei with odd number of protons (Rh, Ag, Sb) or odd number of neutrons (Nd, Sm, Gd, Dy) [124], but were all observed below the backbending region, where the configuration involves only one quasiparticle, and the 3D chiral geometry cannot be realized because one of the three angular momentum legs is missing. The new chiral bands in ^{119}Cs are instead observed in the backbending region induced by the alignment of two $h^{11/2}$ protons, having thus a three-proton configuration. The total angular momenta of the bands results from two $h_{11/2}$ protons revolving from the short to the intermediate axis of the triaxial core, and a strongly coupled $g_{9/2}$ proton sticked along the long axis. The direction of the total angular momentum moves in 3D, giving rise to chiral bands that can be called $R\chi D$ (*Revolving Chiral Doublet*) bands.

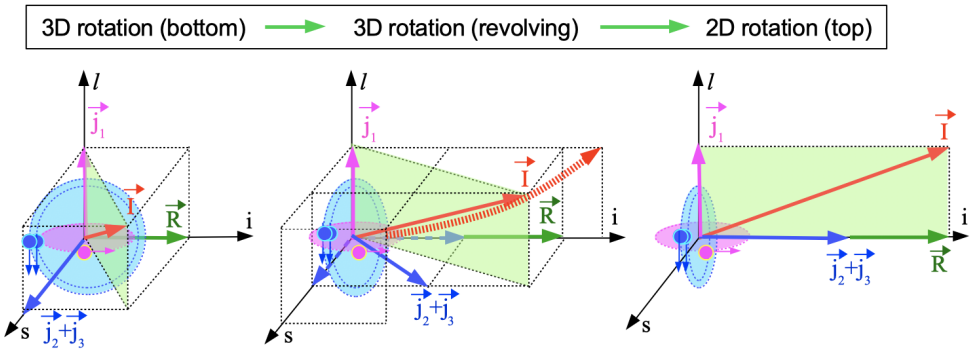

Figure 5.31: Sketch of the coupling of angular momenta in Bands 8 and 9 of ^{119}Cs. The angular momenta of the strongly-coupled proton $\vec{j}_1$, of the two $h_{11/2}$ protons $\vec{j}_2 + \vec{j}_3$ revolving from the short to the intermediate axis, and of the core $\vec{R}$ along the intermediate axis, couple to the total spin $\vec{I}$ out of the principal planes, which consequently revolves in 3D towards the intermediate axis in the backbending region, finally ending in the long-intermediate plane. The nearly degenerate Bands 8 and 9 correspond to the drawn angular momenta and their mirror images in the $s-l$ plane, obtained by inverting the core angular momentum $\vec{R}$.

A schematic figure showing the geometry of the angular momenta is given in Fig. 5.31. The two $h_{11/2}$ protons placed on low-Ω orbitals at the bottom of the $h_{11/2}$ sub-shell have the angular momenta aligned along the short axis at the bottom of the band. With increasing spin, their angular momenta revolve from the short to the intermediate axis. The total spin I revolves in 3D from the short-long ($s-l$) plane at the bottom of band to the intermediate-long ($i-l$) plane at the top of the band. The chiral regime extends over a wide spin range, ending when the angular momenta of the two $h_{11/2}$ protons are nearly completely aligned along the intermediate axis of collective rotation. Due to the triaxiality of the core, the broken chiral symmetry induces two degenerate doublet bands with total angular momenta which are mirror images of each-other in the $s-l$ plane.

The proposed chiral bands of ^{119}Cs are particularly interesting because they are observed in a strongly deformed nucleus ($\varepsilon \approx 0.30$), with moderate triaxiality ($\gamma \approx 10-15°$), as predicted by the TAC-CDFT calculations shown in Fig. 5.26. The triaxiality being moderate, the PNC-CSM works well. In fact, all ten bands observed in ^{119}Cs are qualitatively well reproduced assuming axial symmetry, supporting that the triaxiality is rather weak as it is predicted. However, even this moderate triaxiality brakes the chiral symmetry and gives rise to nearly degenerate doublet bands. The strong deformation also induces a large mixing between the one-quasiparticle and three-quasiparticle

configurations in the backbending region, opening a window on the geometry of the angular momenta in a transient regime, and giving thus the opportunity to observe the two $h_{11/2}$ protons during their alignment.

It should be pointed that the new type of chirality was first proposed in the ^{119}Cs which are particularly interesting because they are observed in a strongly deformed nucleus with moderate triaxiality.

5.3.3 The other bands in ^{119}Cs

In this setion, we assign configurations to the Bands 2, 4', 5', 6, and 7 which are not discussed previously. As

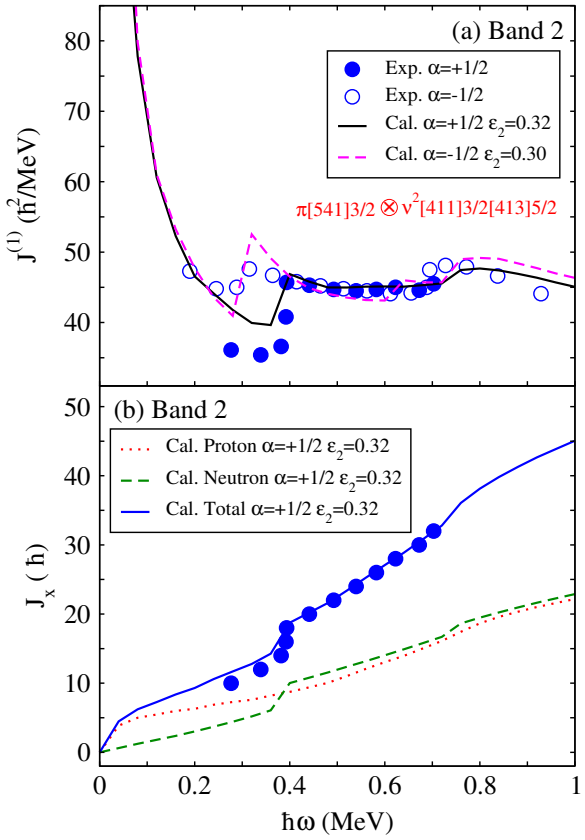

Figure 5.32: (a) Moment of inertia $J^{(1)}$, (b) projection of the angular momentum on the cranking axis J_x for Band 2 of ^{119}Cs calculated using the PNC-CSM model. The states with signature $\alpha = +1/2$ and $\alpha = -1/2$ are drawn with filled and open symbols, respectively.

one can see in Fig. 5.32, the configuration assigned to Band 2 is similar to that of Band 1, $\pi[541]3/2^-$, which is crossed at $\hbar\omega \approx 0.3$ MeV for the negative-signature partner and at $\hbar\omega \approx 0.4$ MeV for the positive-signature partner by a three-quasiparticle configuration involving two additional neutrons placed in positive-parity orbitals, leading to a $\pi[541]3/2 - \otimes\nu[411]3/2^+[413]5/2^+$ configuration at high spin. For the $\alpha = 1/2$ signature partner, the calculated second alignment at $\hbar\omega \approx 0.7$ MeV induced by neutrons has not been observed experimentally (see Fig. 5.32 (b)).

Band 4' which feeds the top of Band 4, exhibits a higher MOI and J_x than Band 4, indicating the presence of additional nucleons in its configuration. The best agreement is obtained for the $\pi([420]1/2^+[550]1/2^-[541]3/2^-) \otimes$

$\nu^2([541]1/2^-[532]5/2^-)$ configuration (see Fig. 5.33).

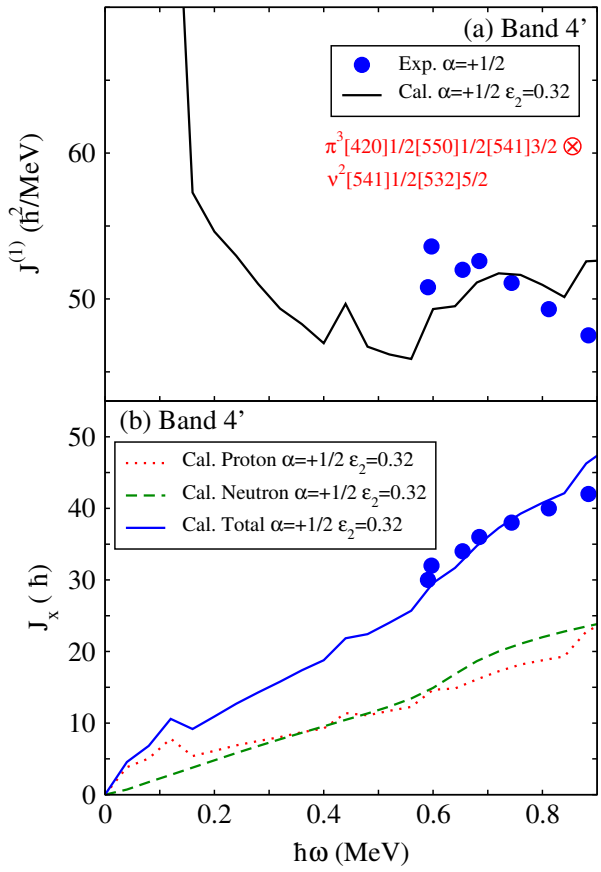

Figure 5.33: (a) Moment of inertia $J^{(1)}$, (b) projection of the angular momentum on the cranking axis J_x for Band 4′ of ^{119}Cs calculated using the PNC-CSM model. The states with signature $\alpha = +1/2$ and $\alpha = -1/2$ are drawn with filled and open symbols, respectively.

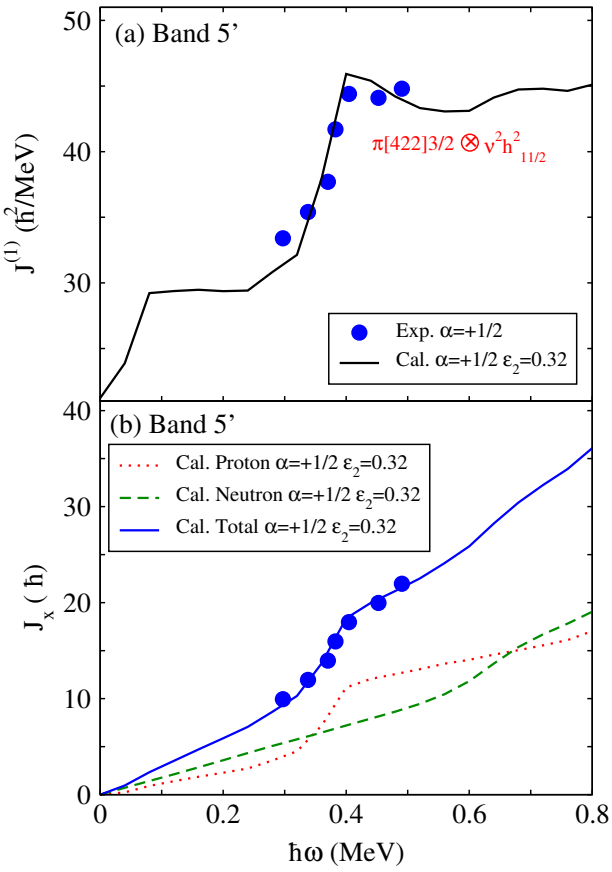

Figure 5.34: (a) Moment of inertia $J^{(1)}$, (b) projection of the angular momentum on the cranking axis J_x for Band 5′ of ^{119}Cs calculated using the PNC-CSM model. The states with signature $\alpha = +1/2$ and $\alpha = -1/2$ are drawn with filled and open symbols, respectively.

Band 5' decays to the $13/2^+$ and $17/2^+$ states of Band 5. It should have a three-quasiparticle configuration, most probably with one proton placed on the same positive-parity orbital $\pi[422]3/2^+$ as in the case of Band 5. The moment of inertia $J^{(1)}$ and projection of the angular momentum on the cranking axis J_x as function of frequency are shown in Fig. 5.34. The first alignment is observed at a frequency of $\hbar\omega \approx 0.30$ MeV which is higher than $\hbar\omega \approx 0.26$ MeV observed in Bands 4 and 5. It should therefore be induced by neutrons which, for a deformation of $\varepsilon_2 \approx 0.32$, align later than $h_{11/2}$ protons. We therefore assign the $\pi[422]3/2^+ \otimes \nu h^2_{11/2}([532]5/2^-[523]7/2^-)$ configuration to Band 5', which is in excellent agreement with the experimental results.

Band 6, composed of dipole and cross-over $E2$ transitions, is populated by transitions from Band 7 and mainly decays to Band 1. One would expect to have involved the $\pi[541]3/2^-$ orbital on which Band 1 is built, and also orbitals present in the five-quasiparticle configuration of Band 7 (see discussion below), in particular the positive-

parity neutron orbital $\nu[413]5/2^+$. A configuration involving such low- and high-Ω orbitals can lead to rotation around a tilted axis and give rise to a dipole band like Band 6. However, one cannot expect a very good agreement of the PNC-SCM calculations performed in the present work and the experimental data, because of the adopted axial symmetric shapes and principal axis rotation in PNC-CSM. We performed anyhow calculations for the $\pi[541]3/2^- \otimes \nu^2[413]5/2^+[532]5/2^-$ configuration and compared it with the experimental Band 6 in Fig. 5.35. One can see that there is a qualitative agreement for the configuration involving the $\pi[541]3/2^-$ ($\alpha = -1/2$) orbital. One can therefore speculate that Band 6 is based on a configuration with one proton in the $\pi[541]3/2^-$ ($\alpha = -1/2$) orbital, and two neutrons in orbitals with positive- and negative-parity. Tilted axis cranking calculations are more adequate for the description of dipole bands and can validate this configuration assignment.

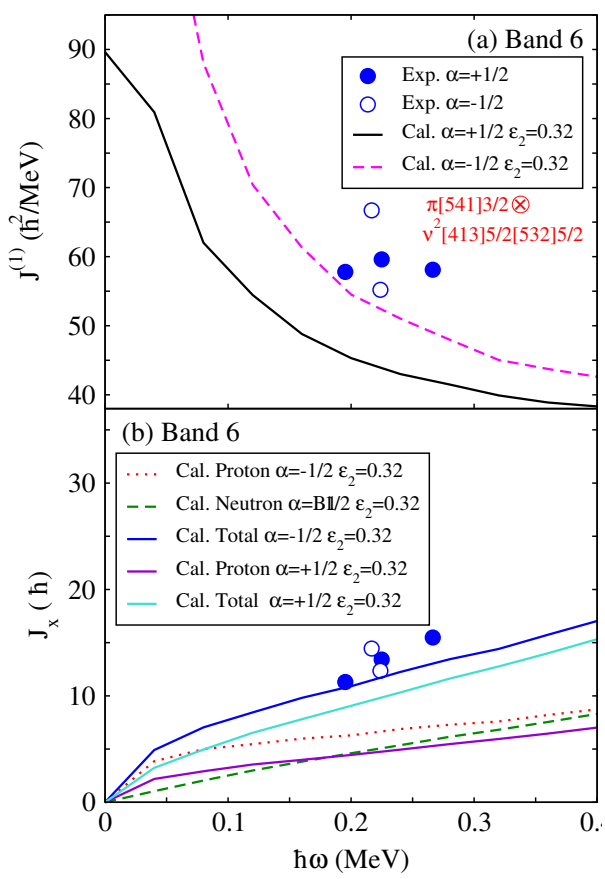

Figure 5.35: (a) Moment of inertia $J^{(1)}$, (b) projection of the angular momentum on the cranking axis J_x for Band 6 of ^{119}Cs calculated using the PNC-CSM model. The states with signature $\alpha = +1/2$ and $\alpha = -1/2$ are drawn with filled and open symbols, respectively.

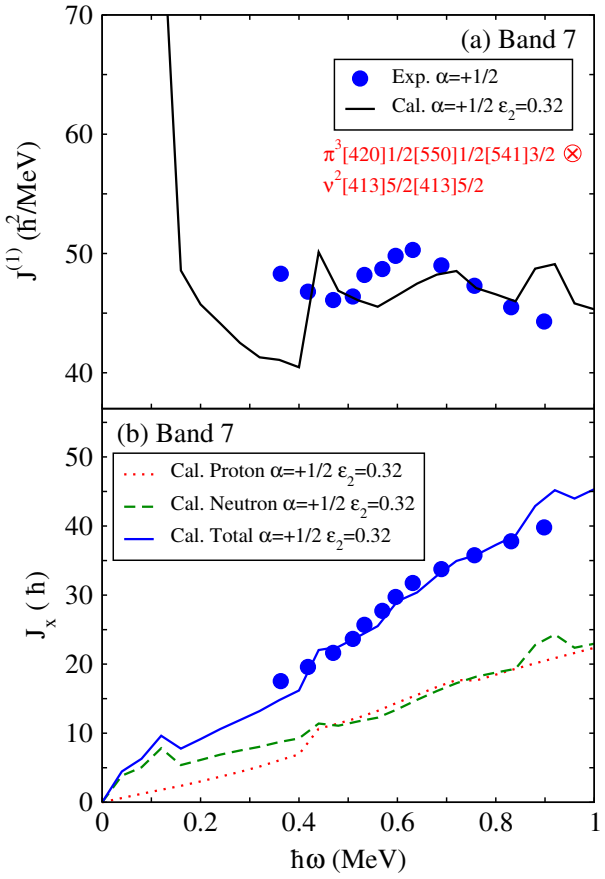

Figure 5.36: (a) Moment of inertia $J^{(1)}$, (b) projection of the angular momentum on the cranking axis J_x for Band 7 of ^{119}Cs calculated using the PNC-CSM model. The states with signature $\alpha = +1/2$ and $\alpha = -1/2$ are drawn with filled and open symbols, respectively.

Band 7 is a very long sequence of electric quadrupole transitions, which develops in the spin range from $33/2$ to $81/2$, and decays to positive-parity states of Bands 6 and 8. We assigned it the five-quasiparticle configuration

$\pi^3[550]1/2^-[541]3/2^-[420]1/2^+ \otimes \nu^2[413]5/2^+[413]5/2^+$, which is in good agreement with the experimental data (see Fig. 5.36). The decay to Band 6 is explained by the presence of $\pi h_{11/2}$ orbitals in the two bands, whereas the decay to Band 8 can be understood by the accidental mixing between the $33/2^+$ states of the two bands.

5.4 Summary of results on ^{119}Cs

This chapter reported new results on ^{119}Cs, including two known bands and eight newly observed bands. The assigned configurations and adopted deformations of all bands are listed in Table 5.1.

Table 5.1: Assigned Nilsson configurations, parity π, and deformations ε_2 to the bands of ^{119}Cs based on PNC-CSM calculations. The configurations include the orbitals occupied at the band-head, as well as those occupied after alignments and crossings at higher spin.

Band	Configuration	1^{st} crossing ($\hbar\omega$)	2^{nd} crossing ($\hbar\omega$)	π	ε_2
1	$\pi[541]3/2^-$	$\nu^2 h_{11/2}$ (0.45)	$\nu^2(g_{7/2}, d_{5/2})$ (0.70)	$-$	0.32
2	$\pi[541]3/2^-(\alpha = 1/2)$	$\nu^2(g_{7/2}, d_{5/2})$ (0.36)		$-$	0.32
2	$\pi[541]3/2^-(\alpha = -1/2)$	$\nu^2(g_{7/2}, d_{5/2})$ (0.30)	$\nu^2(g_{7/2}, d_{5/2})$ (0.70)	$-$	0.30
3	$\pi[505]11/2^-$	$\nu^2 h_{11/2}$ (0.38)		$-$	-0.17
4	$\pi[420]1/2^+(\alpha = 1/2)$	$\pi^2 h_{11/2}$ (0.26)	$\nu^2 h_{11/2}$ (0.40)	+	0.32
4'	$\pi[420]1/2^+(\alpha = 1/2) \otimes \pi^2(h_{11/2}) \otimes \nu^2(h_{11/2})$			+	0.32
5	$\pi[422]3/2^+(\alpha = 1/2)$	$\pi^2 h_{11/2}$ (0.26)	$\nu^2 h_{11/2}$ (0.50)	+	0.32
5'	$\pi[422]3/2^+(\alpha = 1/2) \otimes \nu^2 h_{11/2}$			+	0.32
6	$\pi[541]3/2^- \otimes \nu^2(h_{11/2} g_{7/2})$			+	0.32
7	$\pi[420]1/2^+(\alpha = 1/2) \otimes \pi^2 h_{11/2} \otimes \nu^2(g_{7/2}, d_{5/2})$			+	0.32
8	$\pi[404]9/2^+$	$\pi^2 h_{11/2}$ (0.36)		+	0.32
9	$\pi[404]9/2^+$	$\pi^2 h_{11/2}$ (0.30)		+	0.32
10	$\pi[541]3/2^- \otimes \nu^2(h_{11/2} g_{7/2})$			+	0.32

All resulting from the same high statistics experiment, contribute to the realization of one of the most complete level schemes from low to high spin in proton-rich cerium nuclei. The band configurations are discussed within the PNC-CMS formalism, which nicely describe the band patterns, as well as the the contribution of protons and neutrons to the observed alignments. The multitude of rotational bands identified in ^{119}Cs represents the largest set of collective excitations built on one-quasiparticle configurations observed in a proton-rich nucleus of the $A \sim 120$ mass region. The present results constitute an unique set of spectroscopic information which can be used to test state-of-the-art theoretical models aiming to describe strongly-deformed proton-rich lanthanide nuclei.

Table 5.2: Experimental information including the γ-ray energies E_γ, energies of the initial levels E_i, relative intensities I_γ, anisotropies R_{DCO} and/or R_{ac}, parameter a_2, parameter a_4, polarization asymmetries A, mixing ratios δ, multipolarities, and the spin-parity assignments to the observed states in ^{119}Cs. The transitions listed with increasing energy are grouped in bands.

E_γ (keV)[a]	E_i (keV)	I_γ (keV)[b]	R^c_{DCO}	R^d_{ac}	a_2	a_4	A	δ	Mult.	$J^\pi_i \rightarrow J^\pi_f$
469.4	1559.8	46(11)	1.0(3)[e]				0.03(1)		$E2$	$19/2^- \rightarrow 15/2^-$
609.9	2169.5	45(7)	0.9(2)[e]				0.15(8)		$E2$	$23/2^- \rightarrow 19/2^-$
686.3	2855.8	51(12)	0.9(3)[e]				0.2(1)		$E2$	$27/2^- \rightarrow 23/2^-$
765.6	3621.4	46(12)	1.2(3)[e]				0.03(2)		$E2$	$31/2^- \rightarrow 27/2^-$
843.8	4465.2	35(9)	1.1(2)[e]				0.07(6)		$E2$	$35/2^- \rightarrow 31/2^-$
915.2	5380.4	19(6)	1.0(2)[e]						$E2$	$39/2^- \rightarrow 35/2^-$
958.0	6338.4	14(5)	1.1(3)[e]						$E2$	$43/2^- \rightarrow 39/2^-$
964.3	5429.5	7(3)	0.7(5)[e]	0.9(3)					$(M1/E2)$	$37/2^{(-)} \rightarrow 35/2^-$
1004.7	6434.2	5(4)		1.5(5)					$(E2)$	$(41/2^-) \rightarrow 37/2^{(-)}$
1018.4	7356.8	12(5)	0.9(2)[e]						$E2$	$47/2^- \rightarrow 43/2^-$
1096.4	8453.2	9(4)	1.0(4)[e]						$E2$	$51/2^- \rightarrow 47/2^-$
1099.7	7533.9	4(3)							$(E2)$	$(45/2^-) \rightarrow 41/2^{(-)}$
1186.3	9639.5	5(2)		1.3(3)					$(E2)$	$(55/2^-) \rightarrow 51/2^-$
1191.0	8724.9	3(3)							$(E2)$	$(49/2^-) \rightarrow (45/2^-)$
Band $\gamma \rightarrow$ Band 1										
682.0	2169.5	11(3)		1.3(6)					$(M1/E2)$	$23/2^- \rightarrow 23/2^-$
689.5	1559.8	15(5)							$(M1/E2)$	$19/2^- \rightarrow 19/2^-$
692.3	1089.9	11(5)							$(M1/E2)$	$15/2^- \rightarrow 15/2^-$
979.9	1089.9	35(25)		1.6(4)					$E2$	$15/2^- \rightarrow 11/2^-$
1163.4	1559.8	43(14)		1.5(5)					$E2$	$19/2^- \rightarrow 15/2^-$
1297.6	2169.5	9(2)		1.4(4)					$E2$	$23/2^- \rightarrow 19/2^-$
Band $\gamma \rightarrow$ Band 2										
531.0	2169.5	15(3)		1.4(5)					$E2$	$23/2^- \rightarrow 19/2^-$
Band 1										
286.7	396.9	1000	1.00(6)[e]				0.11(2)		$E2$	$15/2^- \rightarrow 11/2^-$
473.9	870.7	887(19)	1.00(9)[e]				0.12(4)		$E2$	$19/2^- \rightarrow 15/2^-$
542.6	939.5	33(10)							$(M1/E2)$	$(17/2^-) \rightarrow 15/2^-$
616.8	1487.5	623(25)	1.1(1)[e]				0.12(4)		$E2$	$23/2^- \rightarrow 19/2^-$
646.6	1586.1	18(7)							$(E2)$	$(21/2^-) \rightarrow (17/2^-)$
740.1	2326.2	13(6)							$(E2)$	$(25/2^-) \rightarrow (21/2^-)$
731.4	2218.9	425(30)	1.11(7)[e]				0.12(4)		$E2$	$27/2^- \rightarrow 23/2^-$
828.5	3047.4	290(15)	1.03(6)[e]				0.08(3)		$E2$	$31/2^- \rightarrow 27/2^-$
835.0	3161.2	11(6)							$(E2)$	$(29/2^-) \rightarrow (25/2^-)$
913.6	3961.0	106(8)	0.99(5)[e]				0.07(2)		$E2$	$35/2^- \rightarrow 31/2^-$
945.7	4106.9	10(6)							$(E2)$	$(33/2^-) \rightarrow (29/2^-)$
989.9	4950.9	44(4)	0.90(8)[e]				0.07(4)		$E2$	$39/2^- \rightarrow 35/2^-$
1055.2	6006.1	31(3)	1.0(2)[e]						$E2$	$43/2^- \rightarrow 39/2^-$
1124.5	7130.6	18(2)	1.0(4)[e]						$E2$	$47/2^- \rightarrow 43/2^-$
1194.7	8325.3	15(2)	1.0(4)[e]						$E2$	$51/2^- \rightarrow 47/2^-$
1266.5	9591.8	10(2)	1.0(4)[e]						$E2$	$55/2^- \rightarrow 51/2^-$
1333.7	10925.5	7(2)		1.5(3)					$E2$	$59/2^- \rightarrow 55/2^-$
1372.6	12298.1	4(1)		1.3(3)					$E2$	$63/2^- \rightarrow 59/2^-$
1401.0	13699.1	1(1)							$(E2)$	$(67/2^-) \rightarrow 63/2^-$
Band 1 $\rightarrow$ 7/2$^+$ $\rightarrow$ Ground state										
(23.1)	110.2								$(M2)$	$11/2^- \rightarrow (7/2^+)$
87.1	87.1								$(E2)$	$(7/2^+) \rightarrow 3/2^+$
Band 1 $\rightarrow$ Band 8										
(24.5)	110.2								$(E1)$	$11/2^- \rightarrow 9/2^+$

Table 5.2 $(Continued.)$

E_γ (keV)[a]	E_i (keV)	I_γ (keV)[b]	R^c_{DCO}	R^d_{ac}	a_2	a_4	A	δ	Mult.	$J^\pi_i \rightarrow J^\pi_f$
Band 2										
310.0	2128.4	4(1)							$(M1/E2)$	$23/2^- \rightarrow 21/2^-$
373.4	1637.7	10(2)		1.1(4)					$(M1/E2)$	$19/2^- \rightarrow 17/2^-$
380.2	1637.7	19(4)	1.0(2)[e]	1.3(2)					$E2$	$19/2^- \rightarrow 15/2^-$
490.9	2128.4	48(3)	1.0(2)[e]				0.10(5)		$E2$	$23/2^- \rightarrow 19/2^-$
553.7	1818.1	13(3)	0.9(2)[e]						$E2$	$21/2^- \rightarrow 17/2^-$
577.3	2705.7	112(9)	1.0(1)[e]	1.5(2)			0.13(3)		$E2$	$27/2^- \rightarrow 23/2^-$
630.9	3336.8	150(15)	1.2(2)[e]				0.10(3)		$E2$	$31/2^- \rightarrow 27/2^-$
678.5	2496.7	27(4)	1.2(2)[e]				0.2(1)		$E2$	$25/2^- \rightarrow 21/2^-$
707.4	4044.9	8(3)		0.8(3)					$M1/E2$	$33/2^- \rightarrow 31/2^-$
728.1	4064.9	149(46)	0.9(1)[e]				0.11(5)		$E2$	$35/2^- \rightarrow 31/2^-$
764.0	3260.8	56(20)	1.1(3)[e]				0.19(8)		$E2$	$29/2^- \rightarrow 25/2^-$
766.4	4831.7	20(11)		0.9(3)					$M1/E2$	$37/2^- \rightarrow 35/2^-$
784.2	4044.9	20(10)	1.0(4)[e]						$E2$	$33/2^- \rightarrow 29/2^-$
787.2	4831.7	19(10)	1.0(4)[e]						$E2$	$37/2^- \rightarrow 33/2^-$
820.3	5714.1	7(4)							$(M1/E2)$	$41/2^- \rightarrow 39/2^-$
828.8	4893.7	114(14)	1.2(3)[e]				0.17(9)		$E2$	$39/2^- \rightarrow 35/2^-$
877.2	6699.5	4(2)							$(M1/E2)$	$45/2^- \rightarrow 43/2^-$
882.4	5714.1	13(6)	0.9(2)[e]						$E2$	$41/2^- \rightarrow 37/2^-$
929.3	5823.0	84(10)	1.2(4)[e]				0.18(11)		$E2$	$43/2^- \rightarrow 39/2^-$
985.1	6699.5	11(4)	1.0(3)[e]						$E2$	$45/2^- \rightarrow 41/2^-$
1026.1	6849.1	69(10)	1.1(3)[e]				0.09(5)		$E2$	$47/2^- \rightarrow 43/2^-$
1079.5	7779.0	10(4)	0.9(3)[e]						$E2$	$49/2^- \rightarrow 45/2^-$
1124.8	7973.9	43(10)	0.9(3)[e]						$E2$	$51/2^- \rightarrow 47/2^-$
1164.4	8943.4	8(4)	1.0(5)[e]						$E2$	$53/2^- \rightarrow 49/2^-$
1223.9	9197.8	33(8)	0.9(3)[e]						$E2$	$55/2^- \rightarrow 51/2^-$
1245.2	10188.6	5(3)		1.4(3)					$(E2)$	$(57/2^-) \rightarrow 53/2^-$
1311.0	10508.8	22(6)	1.0(3)[e]						$E2$	$59/2^- \rightarrow 55/2^-$
1345.0	11533.6	2.1(9)		1.5(6)					$(E2)$	$(61/2^-) \rightarrow 57/2^-$
1371.0	13256.2	3(2)		1.4(4)					$(E2)$	$(67/2^-) \rightarrow 63/2^-$
1376.4	11885.2	18(5)	1.0(3)[e]						$E2$	$63/2^- \rightarrow 59/2^-$
1389.1	13274.3	11(4)		1.3(3)					$(E2)$	$(67/2^-) \rightarrow (63/2^-)$
1405.8	12939.4	2(2)		1.5(6)					$(E2)$	$(65/2^-) \rightarrow (61/2^-)$
1455.5	14729.8	4(2)		1.4(4)					$(E2)$	$(71/2^-) \rightarrow (67/2^-)$
1474.5	14729.8	3(2)		1.5(5)					$(E2)$	$(71/2^-) \rightarrow (67/2^-)$
1543.7	16273.5	3(2)		1.4(5)					$(E2)$	$(75/2^-) \rightarrow (71/2^-)$
1674.7	17948.2	2(1)		1.3(6)					$(E2)$	$(79/2^-) \rightarrow (75/2^-)$
1857.4	19805.6	<2							$(E2)$	$(83/2^-) \rightarrow (79/2^-)$
Band 2 $\rightarrow$ Band γ										
568.8	2128.4	53(7)		1.3(2)					$E2$	$23/2^- \rightarrow 19/2^-$
Band 2 $\rightarrow$ (15/2$^-$)										
267.5	1637.7	7(5)							$(E2)$	$19/2^- \rightarrow (15/2^-)$
Band 2 $\rightarrow$ Band 1										
288.4	3336.8	6(3)							$(M1/E2)$	$31/2^- \rightarrow 31/2^-$
317.3	1257.8	4.2(10)							$(M1/E2)$	$15/2^- \rightarrow (17/2^-)$
393.4	1264.2	5(2)							$(M1/E2)$	$17/2^- \rightarrow 19/2^-$
486.6	2705.7	44(7)		1.4(2)					$M1/E2$	$27/2^- \rightarrow 27/2^-$
640.4	2128.4	35(5)		1.3(4)					$M1/E2$	$23/2^- \rightarrow 23/2^-$
766.7	1637.7	24(3)		1.4(4)					$M1/E2$	$19/2^- \rightarrow 19/2^-$
861.2	1257.8	15(1)		1.4(3)					$M1/E2$	$15/2^- \rightarrow 15/2^-$
867.8	1264.2	8(2)		0.8(3)					$M1/E2$	$17/2^- \rightarrow 15/2^-$
947.5	1818.1	47(10)		0.8(1)					$M1/E2$	$21/2^- \rightarrow 19/2^-$
998.5	4044.9	2(1)							$(M1/E2)$	$33/2^- \rightarrow 31/2^-$

Table 5.2 (*Continued.*)

E_γ (keV)[a]	E_i (keV)	I_γ (keV)[b]	R^c_{DCO}	R^d_{ac}	a_2	a_4	A	δ	Mult.	$J^\pi_i \rightarrow J^\pi_f$
1009.2	2496.7	39(13)		0.6(3)					$M1/E2$	$25/2^- \rightarrow 23/2^-$
1017.4	4064.9	20(8)		1.6(6)					$E2$	$35/2^- \rightarrow 31/2^-$
1042.0	3260.8	36(8)		0.7(5)					$M1/E2$	$29/2^- \rightarrow 27/2^-$
1118.5	3336.8	47(10)		1.6(4)					$E2$	$31/2^- \rightarrow 27/2^-$
1218.5	2705.7	55(10)		1.3(3)					$E2$	$27/2^- \rightarrow 23/2^-$
1241.2	1637.7	10(5)							$(E2)$	$19/2^- \rightarrow 15/2^-$
1258.0	2128.4	48(8)		1.3(5)					$(E2)$	$23/2^- \rightarrow 19/2^-$
(15/2$^-$) $\rightarrow$ Band 1										
498.9	1370.1	2(1)								$(15/2^-) \rightarrow 19/2^-$
973.4	1370.1	5(2)								$(15/2^-) \rightarrow 15/2^-$
Band 3										
279.6	949.4	68(4)	0.52(8)[e]				-0.09(3)		$M1/E2$	$(13/2^-) \rightarrow (11/2^-)$
315.2	1264.6	51(5)	1.2(2)[f]		-0.14(14)	0.08(27)	-0.06(2)	0.10(15)	$M1/E2$	$(15/2^-) \rightarrow (13/2^-)$
345.1	1609.8	40(5)	1.2(2)[f]		-0.06(11)	0.08(21)	-0.10(4)	0.10(10)	$M1/E2$	$(17/2^-) \rightarrow (15/2^-)$
370.1	1980.0	28(4)	1.1(2)[f]		0.01(16)	0.06(30)		0.15(15)	$M1/E2$	$(19/2^-) \rightarrow (17/2^-)$
389.9	2369.6	18(3)	1.0(2)[f]		-0.09(14)	0.21(27)	-0.06(4)	0.10(20)	$M1/E2$	$(21/2^-) \rightarrow (19/2^-)$
403.6	2773.6	15(2)	1.1(2)[f]		0.05(3)	0.11(6)		0.20(15)	$M1/E2$	$(23/2^-) \rightarrow (21/2^-)$
411.7	4011.9	8(2)		0.7(2)					$M1/E2$	$(29/2^-) \rightarrow (27/2^-)$
412.5	3185.8	5(2)		0.9(2)					$M1/E2$	$(25/2^-) \rightarrow (23/2^-)$
414.4	3600.8	5(3)		0.7(2)					$M1/E2$	$(27/2^-) \rightarrow (25/2^-)$
416.2	4428.3	5(3)		0.8(2)					$M1/E2$	$(31/2^-) \rightarrow (29/2^-)$
595.1	1264.6	7(2)		1.3(3)					$E2$	$(15/2^-) \rightarrow (11/2^-)$
660.6	1609.8	20(4)	1.9(5)[f]				0.08(4)		$E2$	$(17/2^-) \rightarrow (13/2^-)$
715.5	1980.0	24(4)	2.1(6)[f]				0.09(4)		$E2$	$(19/2^-) \rightarrow (15/2^-)$
759.5	2369.6	23(4)	2.2(3)[f]				0.09(4)		$E2$	$(21/2^-) \rightarrow (17/2^-)$
793.8	2773.6	25(4)	1.0(2)[e]				0.04(2)		$E2$	$(23/2^-) \rightarrow (19/2^-)$
816.2	3185.8	30(5)	0.9(2)[e]				0.07(5)		$E2$	$(25/2^-) \rightarrow (21/2^-)$
826.1	4011.9	22(15)	1.2(3)[e]						$E2$	$(29/2^-) \rightarrow (25/2^-)$
827.2	3600.8	28(17)		1.4(3)					$E2$	$(27/2^-) \rightarrow (23/2^-)$
827.5	4428.3	21(15)		1.4(3)					$E2$	$(31/2^-) \rightarrow (27/2^-)$
843.4	4855.3	16(3)	1.0(3)[e]						$E2$	$(33/2^-) \rightarrow (29/2^-)$
870.6	5298.9	16(4)	1.0(2)[e]						$E2$	$(35/2^-) \rightarrow (31/2^-)$
908.7	5764.0	10(2)	0.9(2)[e]						$E2$	$(37/2^-) \rightarrow (33/2^-)$
952.0	6250.9	13(4)	1.1(4)[e]						$E2$	$(39/2^-) \rightarrow (35/2^-)$
997.1	6761.0	7(2)	0.9(3)[e]						$E2$	$(41/2^-) \rightarrow (37/2^-)$
1042.1	7293.0	10(3)	1.1(5)[e]						$E2$	$(43/2^-) \rightarrow (39/2^-)$
1088.2	7849.3	7(2)	1.1(4)[e]						$E2$	$(45/2^-) \rightarrow (41/2^-)$
1132.2	8425.2	9(3)		1.4(4)					$E2$	$(47/2^-) \rightarrow (43/2^-)$
1176.9	9026.2	6(2)		1.3(3)					$(E2)$	$(49/2^-) \rightarrow (45/2^-)$
1218.6	9643.8	4(2)		1.3(4)					$(E2)$	$(51/2^-) \rightarrow (47/2^-)$
1258.8	10285.0	4(2)		1.5(4)					$(E2)$	$(53/2^-) \rightarrow (49/2^-)$
1299.7	10943.5	3(1)		1.3(3)					$(E2)$	$(55/2^-) \rightarrow (51/2^-)$
1340.4	11625.4	2.0(8)		1.5(5)					$(E2)$	$(57/2^-) \rightarrow (53/2^-)$
1377.4	12320.9	1.9(9)		1.2(4)					$(E2)$	$(59/2^-) \rightarrow (55/2^-)$
1416.5	13041.9	1.1(6)		1.3(5)					$(E2)$	$(61/2^-) \rightarrow (57/2^-)$
1454.3	13775.2	1.6(9)		1.4(7)					$(E2)$	$(63/2^-) \rightarrow (59/2^-)$
1492.0	14533.9	$<$1							$(E2)$	$(65/2^-) \rightarrow (61/2^-)$
1531.0	15306.2	$<$2							$(E2)$	$(67/2^-) \rightarrow (63/2^-)$
1574.0	16107.9	$<$1							$(E2)$	$(69/2^-) \rightarrow (65/2^-)$
Band 3$\rightarrow$ Band populated by Band 3										
(26.4)	669.8								$(E1)$	$11/2^- \rightarrow 9/2^+$
294.2	669.8	2(1)							$(M2)$	$11/2^- \rightarrow 7/2^+$
Band populated by Band 3										
138.6	138.6	4(2)	0.8(2)[f]	0.72(8)					$M1/E2$	$5/2^+ \rightarrow 3/2^+$
237.0	375.6	5(1)	0.5(1)[e]	0.69(7)					$M1/E2$	$7/2^+ \rightarrow 5/2^+$
267.8	643.3	4(2)	0.9(2)[f]	1.0(2)					$M1/E2$	$9/2^+ \rightarrow 7/2^+$
Band 4										
331.8	475.9	19(5)	1.0(1)[e]						$E2$	$9/2^+ \rightarrow 5/2^+$
475.2	951.1	26(10)	1.1(1)[e]						$E2$	$13/2^+ \rightarrow 9/2^+$
541.0	1492.5	28(5)	0.9(2)[e]						$E2$	$17/2^+ \rightarrow 13/2^+$
562.3	2054.8	31(5)	1.0(1)[e]				0.11(4)		$E2$	$21/2^+ \rightarrow 17/2^+$
585.3	2640.1	36(6)	1.1(2)[e]				0.2(2)		$E2$	$25/2^+ \rightarrow 21/2^+$
636.3	3276.4	55(10)	1.0(1)[e]				0.04(2)		$E2$	$29/2^+ \rightarrow 25/2^+$

Table 5.2 (*Continued.*)

E_γ (keV)[a]	E_i (keV)	I_γ (keV)[b]	R$^c_{DCO}$	R$^d_{ac}$	a_2	a_4	A	δ	Mult.	$J^\pi_i \rightarrow J^\pi_f$
724.8	4001.2	47(9)	1.0(2)[e]				0.03(2)		$E2$	$33/2^+ \rightarrow 29/2^+$
826.1	4827.3	43(9)	0.9(2)[e]				0.2(1)		$E2$	$37/2^+ \rightarrow 33/2^+$
896.2	5723.5	31(7)	0.9(2)[e]						$E2$	$41/2^+ \rightarrow 37/2^+$
979.0	6702.5	18(5)	1.1(2)[e]						$E2$	$45/2^+ \rightarrow 41/2^+$
1064.5	7767.0	16(4)	0.8(2)[e]						$E2$	$49/2^+ \rightarrow 45/2^+$
1145.8	8912.8	15(4)	0.9(4)[e]						$(E2)$	$(53/2^+) \rightarrow 49/2^+$
1257.5	10170.3	10(4)	1.0(4)[e]						$(E2)$	$(57/2^+) \rightarrow (53/2^+)$
Band 4 → Band 1										
952.8	4001.2	4(2)							$(E1)$	$33/2^+ \rightarrow 31/2^-$
1058.1	3276.4	28(5)	0.5(2)[e]		-0.21(22)	0.25(47)	0.09(7)	0.00(25)	$E1$	$29/2^+ \rightarrow 27/2^-$
1095.6	1492.5	8.2(30)	0.6(1)[e]		-0.17(35)	0.19(67)	0.1(1)	0.05(25)	$(E1)$	$17/2^+ \rightarrow 15/2^-$
1152.5	2640.1	30(5)	0.5(1)[e]		-0.53(11)	0.16(22)	0.09(6)	-0.15(25)	$E1$	$25/2^+ \rightarrow 23/2^-$
1184.2	2054.8	22(3)	0.6(2)[e]		-0.28(20)	0.09(38)	0.1(1)	0.00(10)	$(E1)$	$21/2^+ \rightarrow 19/2^-$
Band 4 → Band 5										
267.2	475.9	7(2)		1.4(4)					$E2$	$9/2^+ \rightarrow 5/2^+$
328.0	951.1	3(2)							$(E2)$	$13/2^+ \rightarrow 9/2^+$
Band 4′										
1194.1	12545.8	5(3)		1.2(5)					$(E2)$	$(65/2^+) \rightarrow (61/2^+)$
1308.2	13854.0	3(2)		1.3(5)					$(E2)$	$(69/2^+) \rightarrow (65/2^+)$
1369.4	15223.4	3(2)		1.3(4)					$(E2)$	$(73/2^+) \rightarrow (69/2^+)$
1487.1	16710.5	2(1)		1.7(5)					$(E2)$	$(77/2^+) \rightarrow (73/2^+)$
1623.4	18333.9	<1							$(E2)$	$(81/2^+) \rightarrow (77/2^+)$
1768.3	20102.2	<1							$(E2)$	$(85/2^+) \rightarrow (81/2^+)$
Band 4′ → Band 4										
1181.4	11351.7	9(4)		1.2(6)					$(E2)$	$(61/2^+) \rightarrow (57/2^+)$
Band 5										
414.1	622.8	102(20)	0.9(1)[e]				0.08(2)		$E2$	$9/2^+ \rightarrow 5/2^+$
548.6	1171.4	88(30)	1.2(1)[e]				0.003(2)		$E2$	$13/2^+ \rightarrow 9/2^+$
594.0	1765.4	77(16)	1.0(2)[e]				0.06(4)		$E2$	$17/2^+ \rightarrow 13/2^+$
539.7	2305.1	65(9)	1.0(2)[e]				0.05(3)		$E2$	$21/2^+ \rightarrow 17/2^+$
590.1	2895.2	61(12)	1.00(8)[e]				0.00(1)		$E2$	$25/2^+ \rightarrow 21/2^+$
684.3	3579.5	40(7)	1.06(9)[e]						$E2$	$29/2^+ \rightarrow 25/2^+$
775.2	4354.7	29(4)	1.2(2)[e]						$E2$	$33/2^+ \rightarrow 29/2^+$
824.4	4403.9	3(2)		1.2(4)					$(E2)$	$(33/2^+) \rightarrow 29/2^+$
864.1	5218.8	20(5)	1.0(2)[e]						$E2$	$37/2^+ \rightarrow 33/2^+$
949.7	6168.5	14(4)	1.1(3)[e]						$E2$	$41/2^+ \rightarrow 37/2^+$
1032.3	7200.8	10(3)	1.0(3)[e]						$E2$	$45/2^+ \rightarrow 41/2^+$
1121.9	8322.7	5(2)		1.5(4)					$(E2)$	$(49/2^+) \rightarrow 45/2^+$
1202.5	9525.2	5(2)		1.3(3)					$(E2)$	$(53/2^+) \rightarrow (49/2^+)$
1287.3	10812.5	3(1)		1.4(6)					$(E2)$	$(57/2^+) \rightarrow (53/2^+)$
1367.3	12179.8	2(1)		1.4(7)					$(E2)$	$(61/2^+) \rightarrow (57/2^+)$
1443.3	13623.1	0.8(5)							$(E2)$	$(65/2^+) \rightarrow (61/2^+)$
1508.0	15131.1	0.8(5)							$(E2)$	$(69/2^+) \rightarrow (65/2^+)$
Band 5 → Ground state										
208.7	208.7	96(18)		0.80(9)	-0.29(4)	0.24(7)	-0.001(1)	0.10(20)	$M1/E2$	$5/2^+ \rightarrow 3/2^+$
Band 4 and Band 5 → 3/2$^+$ or 1/2$^+$ → Ground state										
(32.2)	144.1								$(E2)$	$5/2^+ \rightarrow (1/2^+)$
40.6	144.1	1.2(6)							$(M1/E2)$	$5/2^+ \rightarrow (3/2^+)$
96.2	208.7	0.7(3)							$(E2)$	$5/2^+ \rightarrow (1/2^+)$
102.8	102.8	12(6)	0.5(2)[e]	0.7(2)					$M1/E2$	$(3/2^+) \rightarrow 3/2^+$
105.1	208.7	7(3)						-	$(M1/E2)$	$5/2^+ \rightarrow (3/2^+)$
111.9	111.9	6(3)		0.8(2)					$M1/E2$	$(1/2^+) \rightarrow 3/2^+$
Band 5 → Band 4										
63.9	208.7	1(1)							$(M1/E2)$	$5/2^+ \rightarrow 5/2^+$
Band 5′										
598.0	2408.4	5(3)							$(E2)$	$(a21/2^+) \rightarrow 17/2^+$
678.6	3087.1	9(2)	1.1(4)[e]	1.3(3)					$E2$	$(25/2^+) \rightarrow (21/2^+)$
743.0	3830.1	6(2)		1.5(5)					$(E2)$	$(29/2^+) \rightarrow (25/2^+)$
766.9	4597.0	6(3)		1.4(5)					$(E2)$	$(33/2^+) \rightarrow (29/2^+)$
810.5	5407.5	3(1)		1.5(4)					$(E2)$	$(37/2^+) \rightarrow (33/2^+)$
906.3	6313.8	2(1)		1.5(7)					$(E2)$	$(41/2^+) \rightarrow (37/2^+)$
982.2	7296.0	2(1)		1.5(7)					$(E2)$	$(45/2^+) \rightarrow (41/2^+)$

Table 5.2 (*Continued.*)

E_γ (keV)[a]	E_i (keV)	I_γ (keV)[b]	R^c_{DCO}	R^d_{ac}	a_2	a_4	A	δ	Mult.	$J^\pi_i \rightarrow J^\pi_f$
Band 5′ → Band 5										
638.9	1810.3	5(3)		1.4(7)					$(E2)$	$(17/2^+) \rightarrow 13/2^+$
643.1	2408.4	4(3)		1.4(5)					$(E2)$	$(21/2^+) \rightarrow 17/2^+$
Band 6										
205.3	2583.9	11(5)		0.8(2)	-0.78(24)	0.14(44)	-0.13(13)	-0.35(25)	$M1/E2$	$(23/2^+) \rightarrow (21/2^+)$
207.5	3261.7	10(6)		0.7(2)					$M1/E2$	$(29/2^+) \rightarrow (27/2^+)$
208.9	2792.9	11(6)		0.8(2)					$M1/E2$	$(25/2^{+)} \rightarrow (23/2^+)$
238.9	3500.6	6(5)		0.8(1)					$M1/E2$	$(31/2^+) \rightarrow (29/2^+)$
261.3	3054.2	11(5)		0.8(1)					$M1/E2$	$(27/2^+) \rightarrow (25/2^+)$
311.2	3811.8	8(2)		0.8(2)					$M1/E2$	$(33/2^+) \rightarrow (31/2^+)$
415.0	2792.9	9(4)		1.4(4)					$E2$	$(25/2^+) \rightarrow (21/2^+)$
Band 6 → (21/2$^+$)										
164.3	2583.9	7(3)		0.8(1)					$M1/E2$	$(23/2^+) \rightarrow (21/2^+)$
(21/2$^+$) → Band 1 and Band 4										
926.0	2420.2	3(2)							$(E2)$	$(21/2^+) \rightarrow 17/2^+$
1549.5	2420.2	14(5)		0.9(2)			0.02(2)		$E1$	$(21/2^+) \rightarrow 19/2^-$
Band 6 → Band 1										
1508.0	2378.2	23(5)		0.8(2)			0.10(9)		$(E1)$	$(21/2^+) \rightarrow 19/2^-$
Band 6 → Band 4										
738.1	2792.9	10(5)		1.3(2)			0.13(12)		$E2$	$(25/2^+) \rightarrow 21/2^+$
886.5	2378.2	7(4)		1.4(4)					$E2$	$(21/2^+) \rightarrow 17/2^+$
926.0	2420.2	3(2)							$(E2)$	$(21/2^+) \rightarrow 17/2^+$
Band 6 → Band 8										
412.0	3811.8	25(6)		1.6(3)					$E2$	$(33/2^+) \rightarrow 29/2^+$
472.9	3500.6	14(10)		1.3(3)			0.06(6)		$E2$	$(31/2^+) \rightarrow 27/2^+$
Band 7										
744.8	4848.9	60(15)	1.1(1)[e]				0.05(2)		$E2$	$(37/2^+) \rightarrow (33/2^+)$
854.0	5702.8	59(12)	0.92(9)[e]						$E2$	$(41/2^+) \rightarrow (37/2^+)$
954.8	6657.6	47(10)	0.91(7)[e]				0.13(7)		$E2$	$(45/2^+) \rightarrow (41/2^+)$
1033.5	7691.1	28(6)	1.1(1)[e]				0.12(11)		$E2$	$(49/2^+) \rightarrow (45/2^+)$
1078.9	8770.0	21(5)	0.9(1)[e]						$E2$	$(53/2^+) \rightarrow (49/2^+)$
1150.6	9920.6	14(4)	0.9(2)[e]						$E2$	$(57/2^+) \rightarrow (53/2^+)$
1203.7	11124.3	11(4)	1.0(2)[e]						$E2$	$(61/2^+) \rightarrow (57/2^+)$
1272.6	12396.9	9(4)	0.9(4)[e]						$E2$	$(65/2^+) \rightarrow (61/2^+)$
1388.4	13785.3	7(4)	1.0(3)[e]						$E2$	$(69/2^+) \rightarrow (65/2^+)$
1522.5	15307.8	1.4(9)		1.3(3)					$E2$	$(73/2^+) \rightarrow (69/2^+)$
1672.7	16980.5	<1							$(E2)$	$((77/2^+) \rightarrow (73/2^+)$
1805.4	18785.9	<1							$(E2)$	$(81/2^+) \rightarrow (77/2^+)$
Band 7 → Band 6										
292.0	4104.0	19(5)		1.3(1)			-0.07(6)		$(M1/E2)$	$(33/2^+) \rightarrow (33/2^+)$
603.3	4104.0	23(6)	0.5(2)[e]						$M1/E2$	$(33/2^+) \rightarrow (31/2^+)$
Band 7 → Band 8										
704.4	4104.0	19(4)	1.1(3)[e]						$(E2)$	$(33/2^+) \rightarrow 29/2^+$
Band 8										
238.6	324.3	636(21)	1.02(5)[f]		-0.33(13)	0.18(25)	-0.04(1)	-0.05(30)	$M1/E2$	$11/2^+ \rightarrow 9/2^+$
268.6	592.9	530(12)	1.04(5)[f]		-0.32(14)	0.16(27)	-0.04(1)	-0.05(25)	$M1/E2$	$13/2^+ \rightarrow 11/2^+$
296.5	889.5	326(10)	1.06(5)[f]		-0.28(13)	0.19(25)	-0.02(1)	0.00(20)	$M1/E2$	$15/2^+ \rightarrow 13/2^+$
320.8	1210.4	230(8)	1.04(5)[f]		-0.26(14)	0.13(27)	-0.08(2)	0.10(25)	$M1/E2$	$17/2^+ \rightarrow 15/2^+$
341.9	1552.7	163(9)	1.06(6)[f]		-0.28(14)	0.08(26)	-0.07(2)	0.00(10)	$M1/E2$	$19/2^+ \rightarrow 17/2^+$
357.7	1910.5	113(8)	1.04(7)[f]		-0.20(17)	0.10(32)	-0.04(2)	-0.05(20)	$M1/E2$	$21/2^+ \rightarrow 19/2^+$
369.4	2279.6	75(13)		0.78(9)	-0.33(18)	0.09(35)	-0.03(3)	-0.05(20)	$M1/E2$	$23/2^+ \rightarrow 21/2^+$
371.9	3399.8	34(7)		0.81(9)			-0.04(3)		$M1/E2$	$29/2^+ \rightarrow 27/2^+$
373.7	2653.4	52(10)		0.90(8)			-0.01(1)		$M1/E2$	$25/2^+ \rightarrow 23/2^+$
375.0	3027.9	47(10)		0.88(8)					$M1/E2$	$27/2^+ \rightarrow 25/2^+$
391.6	4187.4	25(3)	0.9(2)[f]						$M1/E2$	$33/2^+ \rightarrow 31/2^+$
396.3	3796.1	22(5)	1.1(2)[f]						$M1/E2$	$31/2^+ \rightarrow 29/2^+$
417.2	4604.8	15(5)		0.7(2)					$M1/E2$	$35/2^+ \rightarrow 33/2^+$
507.4	592.9	109(5)	1.0(2)[e]				0.11(3)		$E2$	$13/2^+ \rightarrow 9/2^+$
565.2	889.5	150(7)	1.0(2)[e]				0.09(3)		$E2$	$15/2^+ \rightarrow 11/2^+$
617.8	1210.4	89(3)	0.8(2)[e]				0.13(4)		$E2$	$17/2^+ \rightarrow 13/2^+$
663.2	1552.7	126(3)	1.2(2)[e]				0.12(4)		$E2$	$19/2^+ \rightarrow 15/2^+$
700.3	1910.5	104(6)	1.0(2)[e]				0.14(5)		$E2$	$21/2^+ \rightarrow 17/2^+$
726.9	2279.6	72(9)	1.0(2)[e]				0.11(4)		$E2$	$23/2^+ \rightarrow 19/2^+$

Table 5.2 (*Continued.*)

E_γ (keV)[a]	E_i (keV)	I_γ (keV)[b]	R^c_{DCO}	R^d_{ac}	a_2	a_4	A	δ	Mult.	$J^\pi_i \rightarrow J^\pi_f$
743.0	2653.4	86(16)	1.0(2)[e]				0.15(7)		$E2$	$25/2^+ \rightarrow 21/2^+$
746.3	3399.8	83(16)	1.2(4)[e]				0.12(6)		$E2$	$29/2^+ \rightarrow 25/2^+$
748.3	3027.9	36(8)	0.8(3)[e]				0.09(7)		$E2$	$27/2^+ \rightarrow 23/2^+$
768.2	3796.1	27(5)	0.9(2)[e]						$E2$	$31/2^+ \rightarrow 27/2^+$
787.5	4187.4	48(8)	0.9(2)[e]						$E2$	$33/2^+ \rightarrow 29/2^+$
808.8	4604.8	23(4)		1.2(2)					$E2$	$35/2^+ \rightarrow 31/2^+$
830.0	5017.4	23(4)		1.4(2)					$E2$	$37/2^+ \rightarrow 33/2^+$
906.6	5511.4	30(6)		1.2(2)					$E2$	$39/2^+ \rightarrow 35/2^+$
921.8	5939.2	14(3)		1.2(2)					$E2$	$41/2^+ \rightarrow 37/2^+$
997.3	6508.7	17(4)		1.3(3)					$E2$	$43/2^+ \rightarrow 39/2^+$
1046.1	6985.3	8(2)		1.3(3)					$E2$	$45/2^+ \rightarrow 41/2^+$
1088.2	7596.9	15(6)		1.4(3)					$E2$	$47/2^+ \rightarrow 43/2^+$
1136.7	8122.0	5(2)		1.4(3)					$E2$	$49/2^+ \rightarrow 45/2^+$
1173.4	8770.3	11(3)		1.4(3)					$E2$	$51/2^+ \rightarrow 47/2^+$
1244.2	9366.2	1.8(8)		1.5(5)					$(E2)$	$(53/2^+) \rightarrow 49/2^+$
1286.3	10056.6	7(2)		1.3(5)					$(E2)$	$(55/2^+) \rightarrow 51/2^+$
1367.0	10733.2	1.9(8)		1.6(5)					$(E2)$	$(57/2^+) \rightarrow (53/2^+)$
1388.0	11444.6	5(2)		1.8(9)					$(E2)$	$(59/2^+) \rightarrow (55/2^+)$
1488.2	12221.4	0.6(3)							$(E2)$	$(61/2^+) \rightarrow (57/2^+)$
1508.7	12953.3	3(2)		1.7(9)					$(E2)$	$(63/2^+) \rightarrow (59/2^+)$
Band 9										
292.2	1436.3	9(2)		0.8(2)	-0.27(6)	-0.01(5).	-0.05(5)	0.40(10)	$M1/E2$	$15/2^+ \rightarrow 13/2^+$
302.6	1738.8	11(2)	1.0(2)[f]		-0.22(5)	0.01(9)	-0.03(3)	0.00(10)	$M1/E2$	$17/2^+ \rightarrow 15/2^+$
314.0	2053.5	11(2)	1.0(1)[f]		-0.27(3)	-0.10(6)	-0.05(3)	0.00(20)	$M1/E2$	$19/2^+ \rightarrow 17/2^+$
327.0	2380.0	7(2)	1.1(3)[f]		-0.23(6).	-0.09(12)	-0.05(4)	0.00(10)	$M1/E2$	$21/2^+ \rightarrow 19/2^+$
340.9	2720.3	5(2)							$(M1/E2)$	$(23/2^+) \rightarrow 21/2^+$
341.5	3406.2	3(1)							$(M1/E2)$	$(27/2^+) \rightarrow (25/2^+)$
344.4	3065.0	5(2)							$(M1/E2)$	$(25/2^+) \rightarrow (23/2^+)$
344.8	3751.6	1.3(8)							$(M1/E2)$	$(29/2^+) \rightarrow (27/2^+)$
359.1	4109.8	<1							$(M1/E2)$	$(31/2^+) \rightarrow (29/2^+)$
376.3	4486.0	<1							$(M1/E2)$	$(33/2^+) \rightarrow (31/2^+)$
393.5	4880.3	<1							$(M1/E2)$	$(35/2^+) \rightarrow (33/2^+)$
421.1	5301.1	<1							$(M1/E2)$	$(37/2^+) \rightarrow (35/2^+)$
439.1	5740.7	<1							$(M1/E2)$	$(39/2^+) \rightarrow (37/2^+)$
616.3	2052.5	8(3)		1.4(5)					$(E2)$	$19/2^+ \rightarrow 15/2^+$
641.6	2380.0	6(2)		1.3(6)					$(E2)$	$21/2^+ \rightarrow 17/2^+$
667.1	2720.3	6(2)		1.4(5)					$(E2)$	$(23/2^+) \rightarrow 19/2^+$
685.3	3065.0	4(2)		1.5(9)					$(E2)$	$(25/2^+) \rightarrow 21/2^+$
685.6	3406.2	6(3)		1.5(9)					$(E2)$	$(27/2^+) \rightarrow (23/2^+)$
687.2	3751.6	3(2)		1.5(9)					$(E2)$	$(29/2^+) \rightarrow (25/2^+)$
702.7	4109.8	<6							$(E2)$	$(31/2^+) \rightarrow (27/2^+)$
734.2	4486.0	<3							$(E2)$	$(33/2^+) \rightarrow (29/2^+)$
771.3	4880.3	<6							$(E2)$	$(35/2^+) \rightarrow (31/2^+)$
814.8	5301.1	<3							$(E2)$	$(37/2^+) \rightarrow (33/2^+)$
860.4	5740.7	<6							$(E2)$	$(39/2^+) \rightarrow (35/2^+)$
Band 9 $\rightarrow$ Band 8										
819.5	1144.2	4(2)							$(M1/E2)$	$13/2^+ \rightarrow 11/2^+$
826.8	2380.0	4(2)							$(M1/E2)$	$21/2^+ \rightarrow 19/2^+$
841.5	2052.5	5(3)		0.7(5)					$M1/E2$	$19/2^+ \rightarrow 17/2^+$
843.5	1436.3	11(2)		0.9(2)					$M1/E2$	$15/2^+ \rightarrow 13/2^+$
849.1	1738.8	10(3)		1.0(5)					$(M1/E2)$	$17/2^+ \rightarrow 15/2^+$
1058.9	1144.2	5(2)							$(E2)$	$13/2^+ \rightarrow 9/2^+$
1111.9	1436.3	7(4)							$(E2)$	$15/2^+ \rightarrow 11/2^+$
Band 10										
174.4	1856.0	9(2)	0.9(4)[f]	0.7(2)			-0.02(1)		$M1/E2$	$19/2^+ \rightarrow 17/2^+$
207.1	2063.0	9(2)	1.0(3)[f]		-0.12(3)	0.02(4)	-0.01(1)	0.10(10)	$M1/E2$	$21/2^+ \rightarrow 19/2^+$
238.9	2302.2	12(4)		0.8(3)			-0.08(5)		$M1/E2$	$23/2^+ \rightarrow 21/2^+$
268.0	1681.3	<11		1.0(4)					$(M1/E2)$	$17/2^+ \rightarrow 15/2^+$
299.8	2602.0	10(2)	0.9(3)[f]		-0.53(52)	-0.24(96)	-0.05(4)	-0.15(40)	$M1/E2$	$25/2^+ \rightarrow 23/2^+$
332.7	2934.9	5.3(8)	1.0(3)[f]		-0.23(8)	-0.09(16)	-0.10(5)	0.00(10)	$M1/E2$	$27/2^+ \rightarrow 25/2^+$
359.9	3294.9	3.3(8)	1.0(2)[f]				-0.16(14)		$M1/E2$	$29/2^+ \rightarrow 27/2^+$
382.3	2063.0	1.9(7)							$(E2)$	$21/2^+ \rightarrow 17/2^+$

Table 5.2 $(Continued.)$

E_γ (keV)[a]	E_i (keV)	I_γ (keV)[b]	R^c_{DCO}	R^d_{ac}	a_2	a_4	A	δ	Mult.	$J^\pi_i \rightarrow J^\pi_f$
394.3	3690.1	3.3(9)							$(M1/E2)$	$31/2^+ \rightarrow 29/2^+$
420.8	4111.1	5(2)		0.7(2)					$M1/E2$	$33/2^+ \rightarrow 31/2^+$
446.8	2302.2	6.4(6)	1.0(2)[e]	1.4(4)					$E2$	$23/2^+ \rightarrow 19/2^+$
449.0	4560.8	1.9(9)							$(M1/E2)$	$35/2^+ \rightarrow 33/2^+$
632.8	2934.9	5.6(8)	0.9(2)[e]	1.3(4)					$E2$	$27/2^+ \rightarrow 23/2^+$
693.0	3294.9	3.0(6)		1.2(4)					$(E2)$	$29/2^+ \rightarrow 25/2^+$
755.2	3690.1	10(2)	1.1(3)[e]						$E2$	$31/2^+ \rightarrow 27/2^+$
816.2	4111.1	2.3(7)							$(E2)$	$33/2^+ \rightarrow 29/2^+$
870.7	4560.8	7(3)		1.4(5)					$(E2)$	$(35/2^+) \rightarrow 31/2^+$
925.2	5036.3	5(2)		1.4(4)					$(E2)$	$(37/2^+) \rightarrow 33/2^+$
975.5	5536.3	6(2)		1.3(4)					$(E2)$	$(39/2^+) \rightarrow (35/2^+)$
1012.0	6048.3	3(2)							$(E2)$	$(41/2^+) \rightarrow (37/2^+)$
1047.0	6583.3	4(2)							$(E2)$	$(43/2^+) \rightarrow (39/2^+)$
Band 10 $\rightarrow$ Band 8										
511.0	2063.0	1.3(8)							$(M1/E2)$	$21/2^+ \rightarrow 19/2^+$
646.2	1856.0	2.3(8)							$(M1/E2)$	$19/2^+ \rightarrow 17/2^+$
750.0	2302.2	$<$1							$E2$	$23/2^+ \rightarrow 19/2^+$
791.6	1681.3	2.9(6)							$(M1/E2)$	$17/2^+ \rightarrow 15/2^+$
852.7	2063.0	7.7(9)							$(E2)$	$21/2^+ \rightarrow 17/2^+$
966.6	1856.0	24(3)	1.9(7)[f]	1.3(3)			0.05(3)		$(E2)$	$19/2^+ \rightarrow 15/2^+$
1088.4	1413.6	$<$15							$(E2)$	$15/2^+ \rightarrow 11/2^+$
1088.4	1681.3	12(5)		1.4(3)					$E2$	$17/2^+ \rightarrow 13/2^+$

[a]The error on the transition energies is 0.3 keV for transitions below 500 keV, 0.7 keV for transitions between 500 and 1000 keV, and 1.0 keV for transitions above 1000 keV. The error on the transition transition energies is 1.0 keV for the transition inthesities less 5.
[b]Relative intensities corrected for efficiency, normalized to the intensity of the 286.7 keV ($15/2^- \rightarrow 11/2^-$ of Band 1) transition [126]. The transition intensities were obtained from a combination of total projection and gated spectra.
[c]R_{DCO} has been deduced from an asymmetric $\gamma - \gamma$ coincidence matrix sorted with the detectors at 157.6° on one axis, and detectors at $\approx$ 90° on the other axis. The tentative spin-parity of the states are given in parentheses.
[d]R_{ac} has been deduced from two asymmetric $\gamma - \gamma$ coincidence matrices sorted with the detectors at 133.6° and 157.6° on one axis, and detectors at $\approx$ 90° on the other axis. The tentative spin-parity of the states are given in parentheses.
[e] DCO ratio from spectrum gated on stretched quadrupole transition.
[f] DCO ratio from spectrum gated on stretched dipole transition.

Chapter 6

Neutron excitations in ^{119}Ba

This chapter presents the experimental results obtained from the in beam spectroscopic study of the very neutron-deficient nucleus ^{119}Ba.

6.1 Introduction

The barium nuclei with $66 \leq N \leq 82$ have been well studied with in-beam γ-ray spectroscopy and heavy-ion fusion-evaporation reactions [151]. Their quadrupole deformation increase gradually from ^{138}Ba to ^{122}Ba [124] and a variety of structural features have been observed [151], for example, the opposite shape-driving force of the nucleons in the $h_{11/2}$ orbital strongly contribute the nuclear shape at low rotation frequency [151, 152], the competing rotation alignments of $\pi h_{11/2}$ and $\upsilon h_{11/2}$ is observed at high frequency [151, 153, 154], and the quasi-particle excitations replace the collective excitations resulting in band termination in the higher frequency regime [155, 151, 156].

Similar to cesium nuclei, the study of the lightest barium nuclei is also confronted with the increasing difficulty to populate high-spin states using fusion-evaporation reactions, due to the limited choice of projectile-target combinations and the small cross-sections for the evaporation of neutrons close to the proton drip-line. The lightest odd-even ^{117,119}Ba nuclei with known rotational bands have been studied using the high-efficiency γ-detector array GAMMASPHERE [94] coupled with the recoil mass separator FMA [157] employing the ^{58}Ni(^{64}Zn,$2pxn$) fusion-evaporation reactions [151, 156], while ^{121}Ba has been studied using the γ-detector array NORDBALL consisting of 15 Compton-suppressed Ge detectors and ancillary detectors for neutrons and protons employing the ^{92}Mo(^{32}S,$p2n$) reaction [158]. Two or three rotational bands have been observed in these odd-even Ba nuclei.

The present work is devoted to the study of ^{119}Ba, in which two bands based on opposite-parity orbitals are known [156]. We identified a new positive-parity band and several low-lying states. We measured the half-live of the $5/2^-$ band-head of the $\nu h_{11/2}$ band, and changed the high-spin part of the known α = +1/2 signature partner of the band built on the $\nu g_{7/2}[413]5/2^+$ orbital. We also assigned configurations of the observed bands based on

PNC-CSM calculations.

6.2 Experiment results and level scheme

The experimental data were obtained from the same high-statistics experiment performed with the γ-ray detector array JUROGAM 3 [95] coupled with the recoil mass separator MARA [97] but employing the ^{58}Ni(^{64}Zn,$2pn$)^{119}Ba reaction. Experimental details have been discussed in Section 4.1.

The level scheme including the previously known and the newly observed bands, as well as a zoom on the low-lying levels are shown in Figs. 6.1 and 6.2, respectively. Double-gated spectra obtained from prompt $\gamma\gamma\gamma$ coincidences showing the newly identified transitions are shown in Figs. 6.3 and 6.4. The complete experimental information on the γ-ray transitions of ^{119}Ba is given in Table. 6.2. Spins and parities of states are based on the measured values of R$_{DCO}$, R$_{ac}$, and A [112, 113, 114]. The assignment of the bands to ^{119}Ba is based on the coincidence of the prompt $\gamma\gamma$ coincidences with recoiling evaporation residues with mass 119 detected at the MARA focal plane, and with the 32 keV K_α X-rays of barium nuclides detected in prompt coincidence with the in-band transitions measured with JUROGAM 3 array at the target position.

Band 2 was previously assigned to ^{119}Ba in Ref. [156], in which the states at the bottom of the band were not understood, and the spin-parity of the ground state could not be firmly assigned. However, based on the systematics of the positive-parity bands in odd-even Ba nuclei, a spin-parity $5/2^+$ was proposed for the state depopulated by the 53-keV transition, which is confirmed by the present work and adopted as band-head of Band 2. We also report evidence of a new band, that we label Band 3, which decays via the 92- and 239-keV transitions to the same $3/2^+$ lowest level to which also Bands 1 and 2 decays. The spin and parity $I^\pi = 3/2^+$ of this lowest level fed by all observed bands are fixed by the angular correlations of the four feeding transitions from Bands 2 and 3, which have spins and parities assigned based on systematics and on the existence of several interconnecting transitions. We assign it as the band-head of Band 3 and the ground state of ^{119}Ba, which is in agreement with the previous assignment [124]. As discussed in the following, the configurations assigned to Bands 2 and 3, $\nu g_{7/2}[413]5/2^+$ and $\nu d_{5/2}[411]3/2^+$, respectively, are also in agreement with the adopted $5/2^+$ and $3/2^+$ band-heads of the two bands.

Band 1, previously assigned to ^{119}Ba in Ref. [156], is confirmed up to $55/2^-$. The 1266-keV transition observed in Ref. [156] and placed on the side of Band 1, is now placed on top of the $55/2^-$ state and becomes the highest transition of Band 1 (see Fig. 6.1).The transitions above the $55/2^-$ state reported in Ref. [156] are not observed in the present data set even though the statistics is sufficient for their observation (see the spectrum shown in Fig. 6.4 (a)). It was known that the state fed by the 60-keV transition has an isomeric character, because no prompt transitions depopulating it were observed. This state was assigned as the band-head, and a spin-parity $I^\pi = 5/2^-$ was assigned based on the systematics of the observed bands in odd-even Ba nuclei [156]. We searched for delayed transitions detected at the MARA focal plane in coincidence with the prompt transitions of Band 1 measured at the

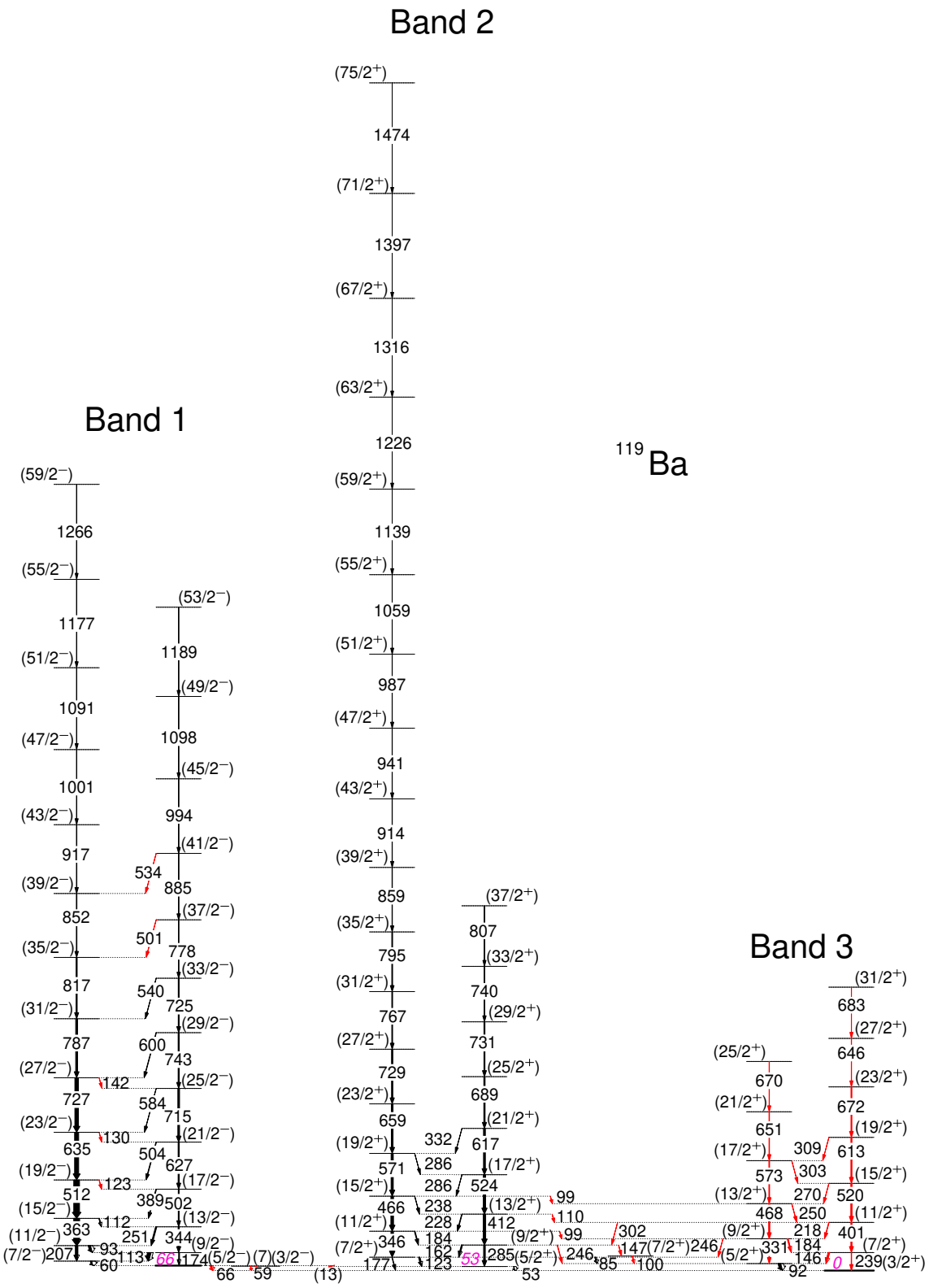

Figure 6.1: Level scheme of ^{119}Ba. The new transitions are indicated with red, the band-head energies of the three bands are indicated in pink, the isomeric and tentative levels are indicated with thick and dashed lines, respectively. The arrow widths are proportional the transition intensities.

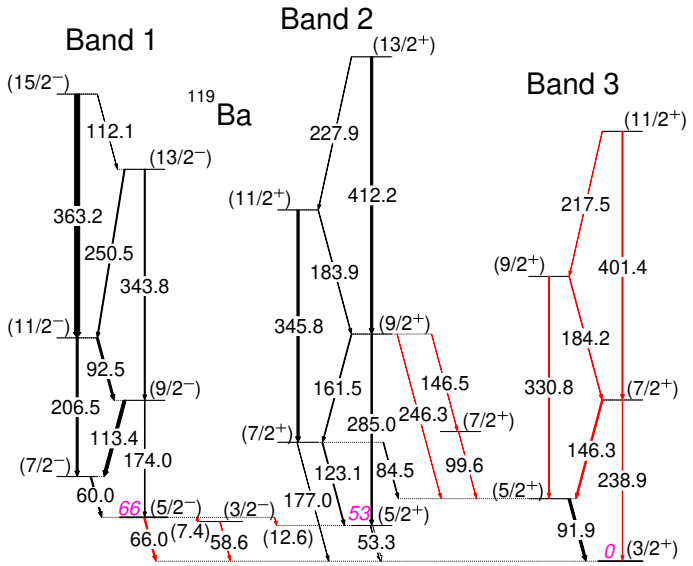

Figure 6.2: The same as in Fig. 6.1, but showing a zoom on the low-spin part of the level scheme.

target position, and succeeded to identify three delayed transitions with energies 53, 59 and 66 keV, which are not in mutual coincidence and therefore can be placed in parallel below the $5/2^-$ isomer. We could not perform angular correlation analysis of the events measured at the MARA focal plane. Therefore, the electromagnetic character of these transitions could not be established experimentally, but only tentatively assigned.

Two out-of-band transitions are observed from the states of Band 2 towards states of Band 3. The negative-signature partner of Band 2 is confirmed up to spin 75/2 (see Figs. 6.1 and 6.4). The previously reported 361- and 364-keV transitions between the signature partner cascades, as well as the highest 1578-keV transition in the negative-signature partner [156], are not observed in the present experiment. The α = +1/2 signature partner of Band 2 is confirmed up to spin 29/2, on top of which two transitions of 740 and 807 keV are placed. The previously reported 796-, 897- and 997-keV transitions in Ref.[156] are not confirmed. The presence of the 796- and 897-keV transitions in the spectra of Ref. [156] are most probably due to contamination from ^{115}I, a well populated nucleus via the $\alpha 3p$ reaction channel in the used reaction, and having a band with transitions of 411, 517, 622, 729, 797, 850, and 894 keV. The presence of the 997-keV transition is probably due to the contamination from ^{116}Xe, a well populated nucleus via the $\alpha 2p$ reaction channel in the used reaction, and having the 524- and 616-keV transitions in the ground-state band, and the 998-keV transition in a Band 3 decaying to the ground-state band [124]. The absence of these transitions in the high-spin part of the positive-signature partner of Band 2 has important consequences: as will be discussed in the following section, it solves the problem of very different alignments in the signature partners of Band 2 reported in Ref. [156].

Band 3 has been identified starting from the 85- and 92-keV transitions previously reported in Ref. [156] and placed in parallel to the other transitions depopulating the $7/2^+$ state of Band 2, but only after inverting their order.

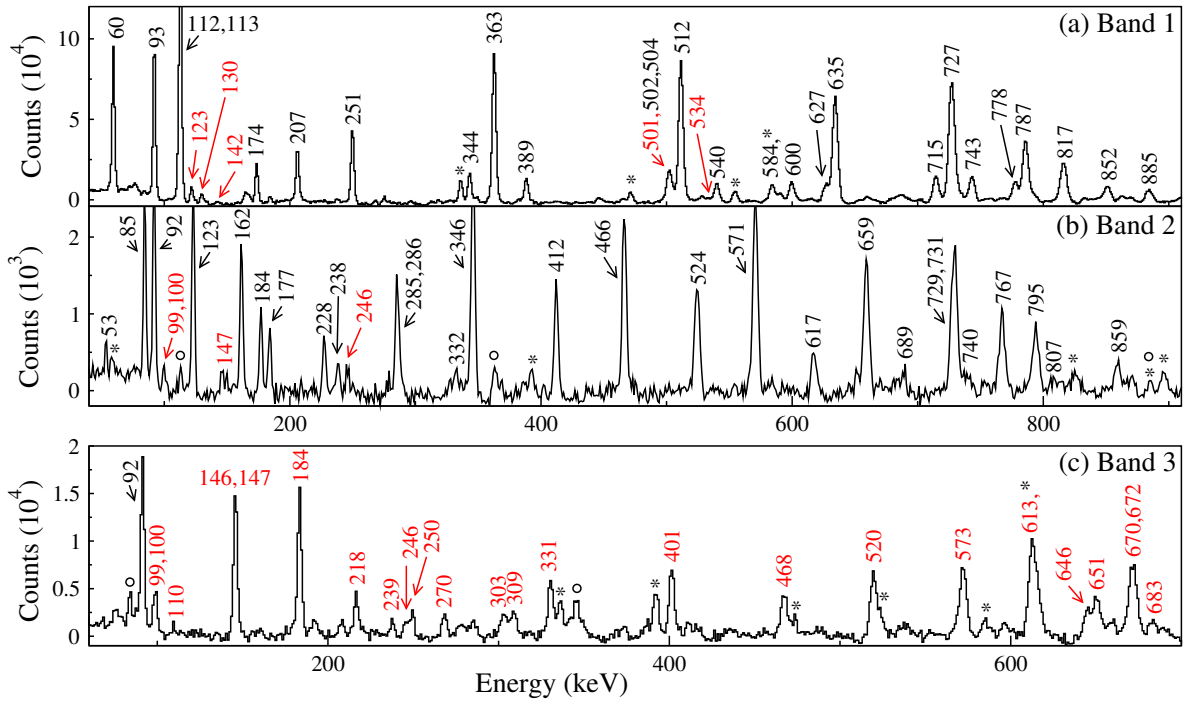

Figure 6.3: Double-gated spectra showing the low and medium energy range for Bands 1, 2 and 3. Peak energies for the newly identified transitions are written in red. Transitions from other nuclei (^{115}I, ^{116}Xe, ^{118}Cs, ^{118}Xe, ^{119}Cs, ^{120}Ba) are indicated with an asterisk, while those from other bands in ^{119}Ba are indicated with a circle. The spectra have been obtained as follows: the spectrum of Band 1 is the sum of the double-gated spectra obtained by gating on all combinations of the 93-, 113-, 207-, 344-, 363-, 502-, 512-, 627-, 635-keV γ rays; the spectrum of Band 2 is the sum of the double-gated spectra obtained by gating on the 85- and 92-, 346- and 466-, 571- and 659-, 617- and 689-keV γ rays; the spectrum of Band 3 is the sum of the double-gated spectra obtained by gating on all combinations of the 92-, 146-, 218-, 331-, 401-, 468-, 520-, 651-keV γ rays.

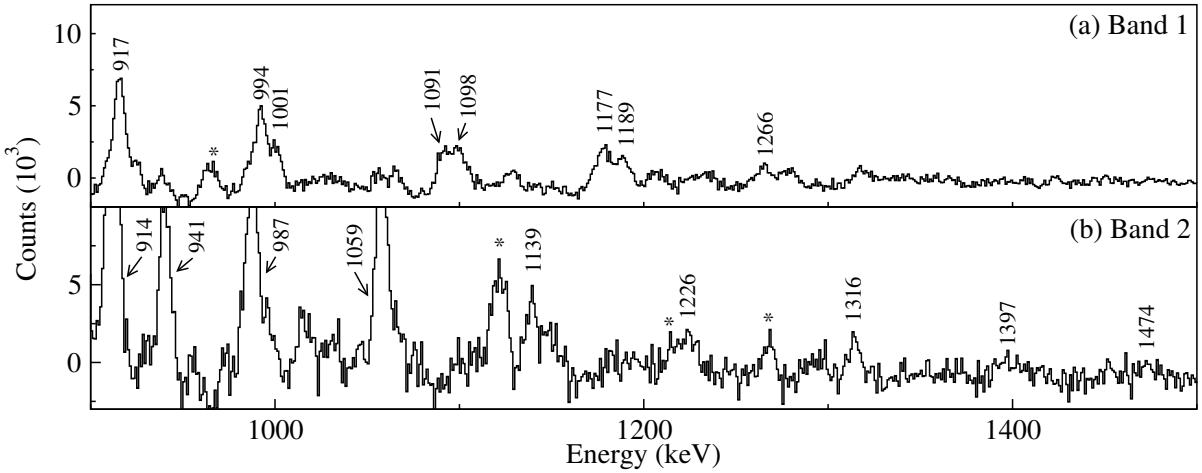

Figure 6.4: The same as in Fig. 6.3 but showing the high-energy range for Bands 1 and 2 of ^{119}Ba.

The 85-keV transition is now a connecting transition between Band 2 to the new Band 3, while the 92-keV transition becomes the lowest dipole transition in Band 3, which is built on the $3/2^+$ ground state. Band 3 is composed of two rotational cascades of $E2$ transitions connected by $M1/E2$ transitions. Their spins and positive parity are fixed by the 92-keV $M1/E2$ and 239-keV $E2$ transitions towards the $3/2^+$ band-head. Two out-of-band transitions have been identified towards states of Band 2. The connecting transitions in both directions between Bands 2 and 3 indicate strong mixing between the states with identical spin, which differ in energy by only a few tens of keV.

6.2.1 The 5/2$^-$ isomer

The spectra obtained from prompt-delayed coincidences of γ-rays detected by JUROGAM 3 and the detectors at the MARA focal plane are shown in Fig. 6.5, where (a) is the focal-plane spectrum, and (b), (c), and (d) are JUROGAM 3 spectra. The delayed 53-, 59-, 66-keV transitions detected at the MARA focal plane are observed when gating on the 113-keV prompt transitions of Band 1 detected at the target position, and the strong peaks of Band 1 detected at the target position are clearly shown when gating on the delayed transitions. The relative intensities of the decay transition can be extracted from the focal-plane spectrum (see Fig. 6.5 (a)), which is 0.72(6), 0.09(3), and 0.19(4) for 66-, 59-, and 53-keV transitions. The delayed coincidence provides evidence that the 53- and 59-keV transitions depopulate the 5/2$^-$ isomer through the intermediate unobserved (13)- and (7)-keV transitions from the 66-keV band-head of Band 1. We can put three parallel cascades, 7-59, 13-53 and 66 keV, below the 5/2$^-$ isomer to connect the Bands 1 and 3. Thus, the 66-keV transition depopulates the 66-keV band-head of Band 1 to the ground state. One can see in Fig. 6.5 (a) that the 66-keV transition is the strongest among the three delayed transitions. Thus, we only select the time spectrum of the delayed 66-keV transition for the fit. In order to increase the statistics of the time spectrum we summed the time spectra produced by gating on the 93-, 113-, 207-, and 363-keV transitions detected with JUROGAM 3. The time spectrum of the delayed 66-keV transition, measured at the MARA focal plane, and produced by using different gates on the transition of detected by JUROGAM 3 are shown in the right panel of Fig. 6.5. We extracted a half-life of $T_{1/2} = 0.36(2)$ μs from the fit of the time spectrum of the 66-keV transition. In fact, we can get similar half-lives but with larger errors from the time spectra of the 53- and 59-keV transitions.

However, the order of the 7- and 59-keV transitions, and of the 13- and 53-keV transitions cannot be determined due to the lower energy thresholds of the present experiment. Thus, calculating all the possibilities and comparing them with the extracted half-life are necessary. The details will be presented in the following.

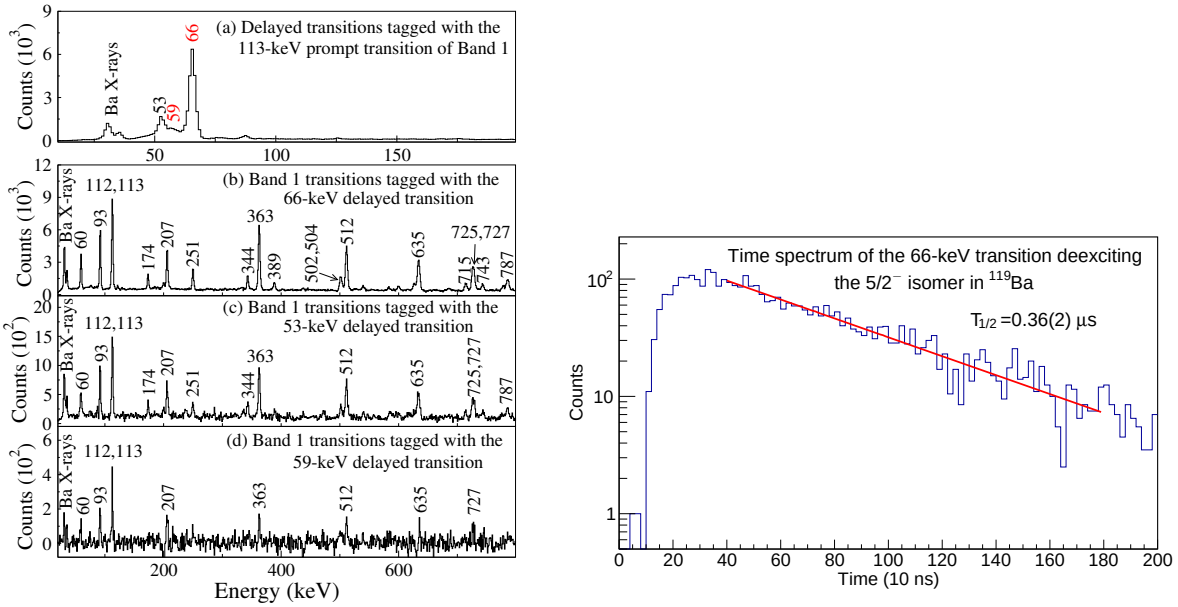

Figure 6.5: (left) Prompt-delayed coincidence spectra for Band 1 of ^{119}Ba. Peak energies for the newly identified transitions are written in red. (right) Fit of the time spectrum of the delayed 66-keV transition de-exciting the $5/2^-$ band-head of Band 1 of ^{119}Ba.

6.3 Discussion

6.3.1 Alignment analysis

The single-particle alignments i_x for the bands of ^{119}Ba are shown in Fig. 6.6, which exhibit a large signature splitting between the signature partners of Band 1, and nearly zero signature splitting between the partners in Bands 2 and 3. The signature partners of the negative-parity Band 1 built on the $\nu h_{11/2}[541]3/2^-$ orbital exhibit alignments at a rotational frequency of $\hbar\omega \approx 0.35$ MeV. The alignment is due to $h_{11/2}$ protons, because the first $h_{11/2}$ neutron alignment predicted to occur at $\hbar\omega \approx 0.4$ MeV is blocked. The alignment in the positive-parity Band 2 occurs at a similar rotational frequency of $\hbar\omega \approx 0.35$ MeV, and is higher by $\approx 1\hbar$ than that observed in Band 3, which is sharper, suggesting a lower deformation of Band 3 relative to that of Band 2. As Bands 2 and 3 are assigned to the $\nu d_{5/2}[413]5/2^+$ and $\nu g_{7/2}[411]3/2^+$ configurations (see the following section), respectively, one would expect a higher alignment in Band 3, which is in contrast with the experimental alignment which is smaller than in Band 2. However, as the two configurations assigned to Bands 2 and 3 are strongly mixed, the K-values are difficult to define. An intermediate $K = 2$ value would lead to very similar alignments of the two bands. A second alignment is observed in Band 2 at $\hbar\omega \approx 0.46$ MeV, which was interpreted in Ref. [156] as due to $h_{11/2}$ neutrons. As the $\alpha = 1/2$ signature partner in Fig. 6.6 is populated up to a lower spin than the $\alpha = -1/2$ one, it is not clear if the alignment at $\hbar\omega \approx 0.46$ MeV is also present in the $\alpha = 1/2$ signature partner.

The alignments in the negative-parity and positive-parity bands of light odd-even Ba nuclei from ^{117}Ba to ^{123}Ba

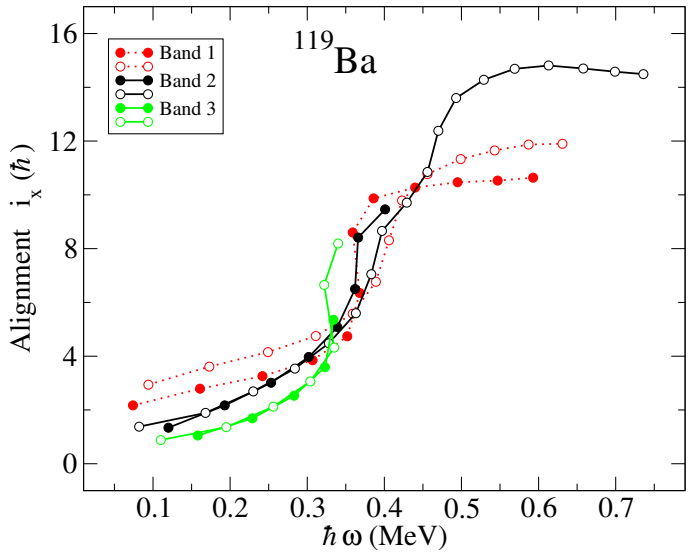

Figure 6.6: Single-particle alignments i_x for the bands of ^{119}Ba. The Harris parameters are $J_0 = 17\ \hbar^2$MeV^{-1} and $J_0 = 25\ \hbar^4$MeV^{-3}. The K values are 2.5, 2.5, and 1.5 for Bands 1, 2, and 3, respectively. The states with signature $\alpha = +1/2$ and $\alpha = -1/2$ are drawn with filled and open symbols, respectively. The positive-parity and negative-parity bands are drawn with continuous and dotted lines, respectively.

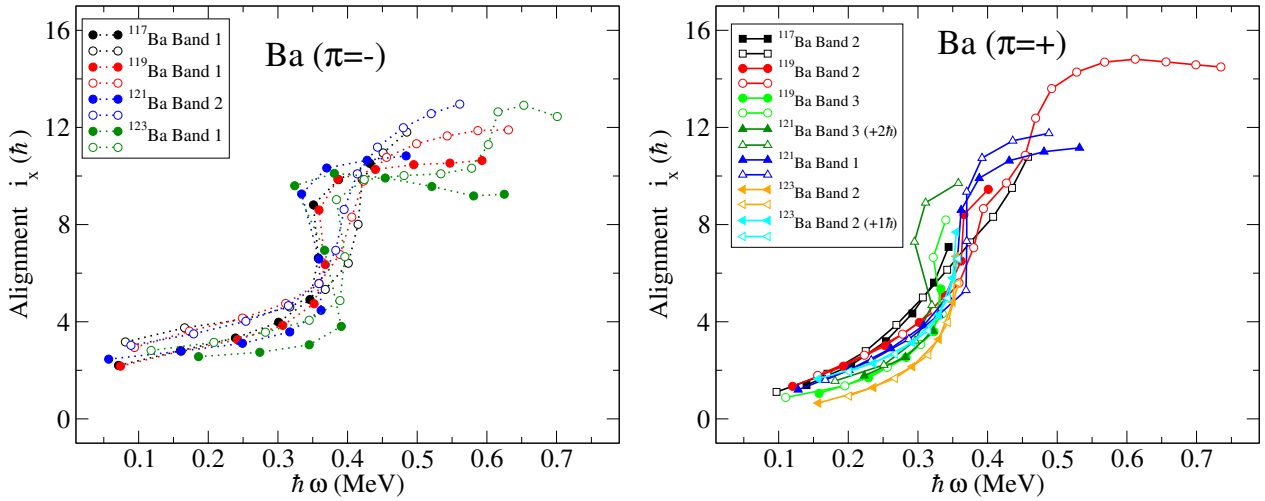

Figure 6.7: Single-particle alignments i_x for the negative-parity (left) and positive-parity (right) bands of ^{117,119,121,123}Ba. The K value is 2.5 for all negative-parity bands. For the figure of positive-parity bands, the K values are 1.5 for Bands 3 of ^{119,121}Ba, and 2.5 for the other bands. The Harris parameters are $J_0 = 17\ \hbar^2$MeV^{-1} and $J_1 = 25\ \hbar^4$MeV^{-3}. The states with signature $\alpha = +1/2$ and $\alpha = -1/2$ are drawn with filled and open symbols, respectively. The positive-parity and negative-parity bands are drawn with continuous and dotted lines, respectively.

are shown in Fig. 6.7. One can see the evolution of the alignments in the negative-parity bands, where the alignment of the α = -1/2 signature partners are sharper than that of the α = +1/2 signature partners and this sharpness increases with the neutron number. Only in the negative-parity signature of Band 1 in ^{123}Ba a second alignment at $\hbar\omega \approx 0.6$ MeV has been observed. For the positive-parity bands we had to change the spins by two and one units in ^{121}Ba and ^{123}Ba, respectively, to get a gradual change of the alignment with increasing neutron number. One can

observe similar alignment frequencies for all bands excepting Bands 3 of ^{119}Ba and ^{121}Ba, in which the alignments are also sharper. In ^{119}Ba the negative-signature partner of Band 3 was observed after the second alignment up to high spin. In ^{117}Ba, the alignment of the negative-signature partner of Band 2 is more gradual, and no second alignment was observed.

6.3.2 PNC-CSM calculations

The possible configurations and alignment properties of the observed bands have been investigated through PNC-CSM calculations, in which the phenomenological Nilsson potential is adopted for the mean field [131], with parameters κ and μ taken from Ref. [72], and effective monopole paring strengths of 0.8 MeV for protons and 0.6 MeV for neutrons. In the present analysis we compared the calculated moments of inertia $J^{(1)}$ and the projection of the angular momentum J_x on the cranking axis with the experimental values. Single-quasiparticle neutron Routhian diagrams as function of rotational frequency for prolate and oblate deformations are shown in Fig. 6.8. They were used to guide the search of the closest quasiparticle orbitals to the proton and neutron Fermi surfaces.

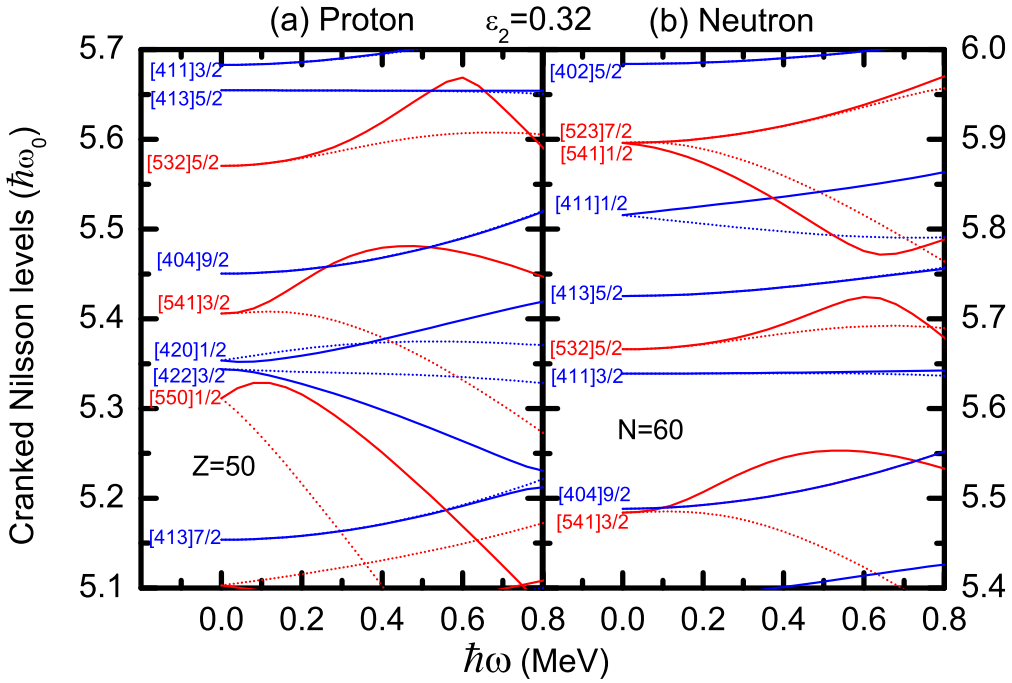

Figure 6.8: Single-particle Routhians located in the vicinity of the Fermi level of ^{119}Ba as a function of rotational frequency for axial prolate deformation of ε_2 = 0.32: (a) protons and (b) neutrons. Positive (negative) parity Routhians are shown by blue (red) lines. Solid (dotted) lines are used for signature α = +1/2 (α = -1/2).

The calculations were performed for an axial quadrupole deformation of $\varepsilon_2 = 0.32$, assumed to be equal to that resulting from the measured spectroscopic quadrupole moment of the neighboring ^{121}Ba nucleus [159, 160], but higher by about 20% than those resulting from total Routhian surface (TRS) calculations ($\varepsilon_2 = 0.27$)[151, 156, 158].

In order to find the deformation which best describes Band 1, we calculated the assigned $\nu[532]5/2^-$ config-

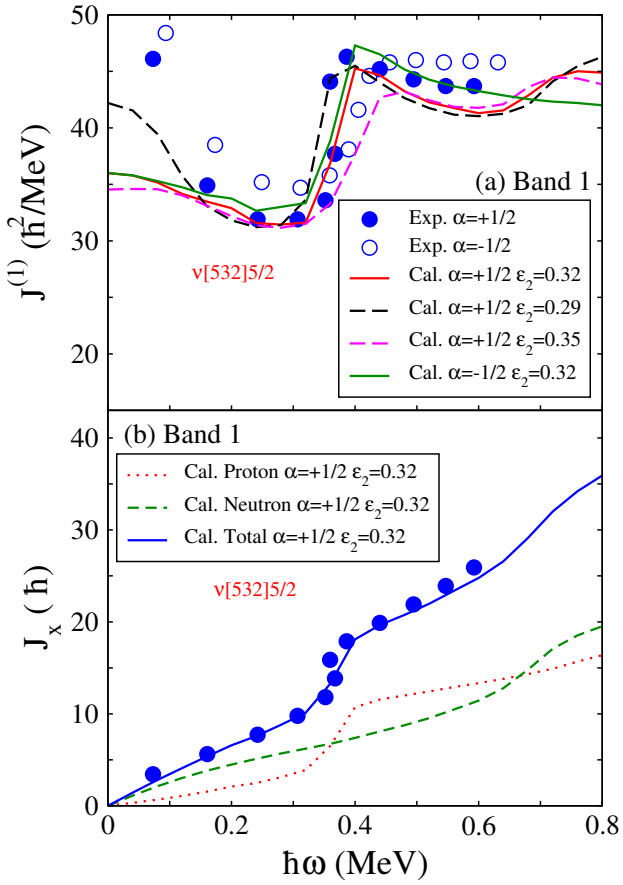

Figure 6.9: (a) Moment of inertia $J^{(1)}$, experimental and calculated for three different deformations, (b) projection of the angular momentum on the cranking axis J_x for Band 1 of ^{119}Ba calculated using the PNC-CSM model for deformation $\varepsilon_2 = 0.32$. The states with signature $\alpha = +1/2$ and $\alpha = -1/2$ are drawn with filled and open symbols, respectively.

uration for different deformations of $\varepsilon_2 = 0.29, 0.32, 0.35$ (see Fig. 6.9). The calculated moments of inertia for a deformation of $\varepsilon_2 = 0.32$ lead to a good agreement for both signature partners. However, the alignments have a slightly different pattern in the two signature partners, being sharper and at lower rotational frequency in the $\alpha = 1/2$ partner. As one can see in Fig. 6.9, this can be induced by slightly different deformations, $\varepsilon_2 = 0.29$ for the $\alpha = 1/2$ partner and $\varepsilon_2 = 0.35$ for the $\alpha = -1/2$ partner, as expected, because a higher deformation induces higher crossing frequency. The larger deformation induced by the $\alpha = -1/2$ signature partner is also expected, since its Routhian has a larger slope and therefore a larger deformation driving force (see Fig. 6.8). The frequency of the observed up-bending at $\hbar\omega \approx 0.4$ MeV is well reproduced by the calculations, being induced by the alignment of $h_{11/2}$ protons. A second level crossing is predicted for the $\alpha = 1/2$ partner at $\hbar\omega \approx 0.7$ MeV, which is induced by $h_{11/2}$ neutrons, but is beyond the observed frequency range of Band 1 and therefore not confirmed. On the other hand, there is no second level crossing predicted for the $\alpha = -1/2$ partner.

Bands 2 and 3 are more difficult to reproduce by the present PNC-CSM calculations, mainly due to the mixing

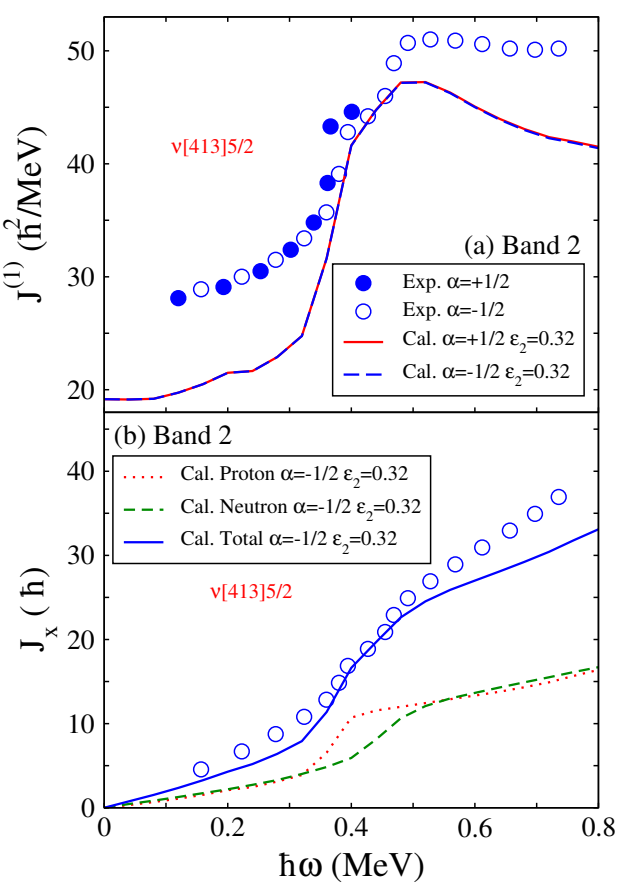

Figure 6.10: (a) Moment of inertia $J^{(1)}$, experimental and calculated for three different deformations, (b) projection of the angular momentum on the cranking axis J_x for Band 2 of ^{119}Ba calculated using the PNC-CSM model for deformation $\varepsilon_2 = 0.32$. The states with signature $\alpha = +1/2$ and $\alpha = -1/2$ are drawn with filled and open symbols, respectively.

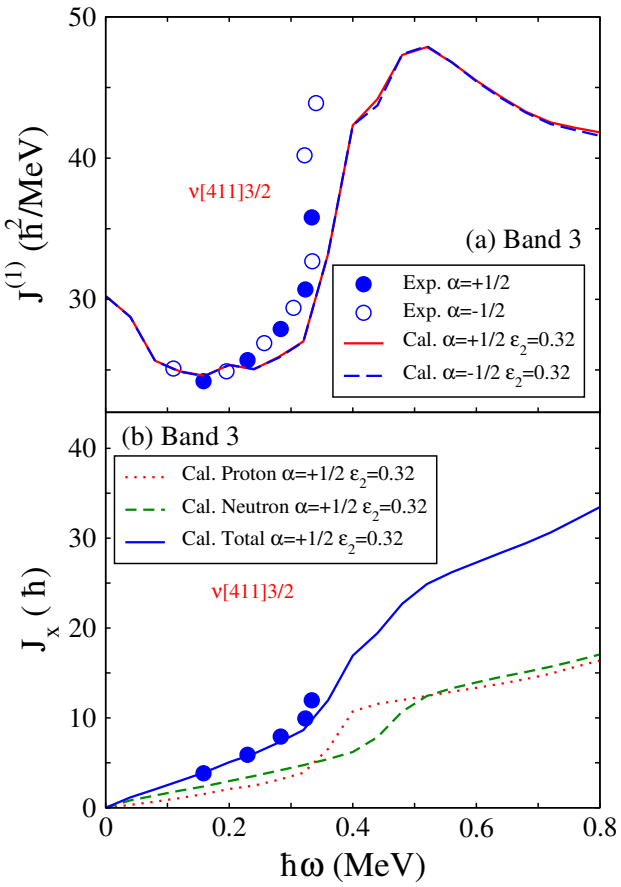

Figure 6.11: (a) Moment of inertia $J^{(1)}$, experimental and calculated for three different deformations, (b) projection of the angular momentum on the cranking axis J_x for Band 3 of ^{119}Ba calculated using the PNC-CSM model for deformation $\varepsilon_2 = 0.32$. The states with signature $\alpha = +1/2$ and $\alpha = -1/2$ are drawn with filled and open symbols, respectively.

between the two bands at low rotational frequency. It has been previously recognized that the configuration of the known positive-parity bands in Ba nuclei changes from $\nu g_{7/2}[402]5/2^+$ in ^{123}Ba to $\nu d_{5/2}[413]5/2^+$ in ^{121}Ba, in agreement with spectroscopic quadrupole moments measurements [159, 160]. The spectroscopic quadrupole moments of ^{117,119}Ba are not known experimentally. The $\nu d_{5/2}[413]5/2^+$ configuration assignment was based on TRS and cranked shell model calculations, which predict lower quadrupole deformations of $\varepsilon_2 = 0.27$. However, even with the higher adopted deformation in the present calculations $\varepsilon_2 = 0.32$, the $\nu d_{5/2}[413]5/2^+$ configuration assignment to the corresponding bands in ^{121,119}Ba remained unchanged, confirming the conclusion concerning the change of configuration from $\nu g_{7/2}[402]5/2^+$ in ^{123}Ba to $\nu d_{5/2}[413]5/2^+$ in the lighter ^{117,119,121}Ba nuclei. One can therefore exclude the $\nu[402]5/2^+$ configuration for Bands 2 and 3, because it is far away from the Fermi surface (see Fig. 6.8). The $\nu[411]1/2^+$ orbital is closer to the Fermi surface, but it has very large signature splitting, and therefore is inconsistent with the data. There remains only two positive-parity orbitals which are close to the Fermi

surface and have small enough signature splitting in the low frequency region in agreement with the observed Bands 2 and 3: $\nu[411]3/2^+$ and $\nu[413]5/2^+$.

The two signature partners of Band 2 are quite similar up to the first up-bending observed at $\hbar\omega \approx 0.35$ MeV (see Fig. 6.6), which, based on the PNC-CSM calculations, is attributed to $h_{11/2}$ protons. The $\alpha = 1/2$ signature partner, which is observed up to much higher spin than the $\alpha = -1/2$ one, exhibits a second alignment at $\hbar\omega \approx 0.45$ MeV. As one can see in Fig. 6.10, the frequency of the first up-bending induced by the $h_{11/2}$ protons is well reproduced, but the calculated $J^{(1)}$ is smaller than the experimental one. The frequency of the second alignment due to the $h_{11/2}$ neutrons is also well reproduced. However, the behavior of the $\alpha = -1/2$ partner of Band 2 above the second alignment is not well reproduced: both the $J^{(1)}$ and J_x are smaller than the experimental values. The moment of inertia $J^{(1)}$ at low frequency is also overestimated by the present calculations. The calculated values can be changed by changing deformation, however, this will also lead to a change of the crossing frequency. In the present calculation, about a 7$\hbar^2$/MeV change of $J^{(1)}$ is needed to reproduce the experimental data. Such a change cannot be obtained by just changing the deformations and pairing strengths without changing the crossing frequency.

As one can see in Fig. 6.11, Band 3 is well reproduced by the $\nu[411]3/2^+$ configuration, except for the slightly higher calculated frequency of the up-bending induced by the alignment of $h_{11/2}$ protons.

6.3.3 The $5/2^-$ isomer

In order to qualitatively account for the half-life of the $5/2^-$ isomer, we analyzed the Weisskopf estimates of the partial half-lives associated with the depopulation of the $5/2^-$ isomer via the two cascades 7 - 59 keV, 13 - 53 keV, and the parallel 66-keV ($5/2^- \rightarrow 3/2^+$) $E1$ transition. The Weisskopf estimates for more than one depopulating transition are given by [161]

$$\frac{1}{T^w_{1/2}} = \sum_k \left(\frac{I_\gamma(1+\alpha_k)}{T^w_k} \right), \tag{6.1}$$

where k is the number of the decay transitions, and α_k, I_k, and T^w_k are the electron conversion coefficient, the relative intensity, and the calculated lifetime by Weisskopf estimates of the k-th transition. Because we cannot measure the 7- and 13-keV transitions due to their too low energy, their relative intensities are calculated by intensity balance based on the relative intensities of the 59- and 53-keV transitions. The electron conversion coefficient can be calculated following the procedure of the website [162]. The T^w_k value can be calculated using the formula from the Table 2.1. By assuming a 10^{-6} hindrance for the $E1$ transitions and no hindrance for the $M1/E2$ transitions, and examining all combinations of multipolarities, parities and order of the transitions in the two cascades, the calculated results are shown in Table 6.1, where the closest values to the measured ones $T_{1/2} = 0.38(20)$ μs and $T_{1/2} = 0.58(20)$ μs are shown in blue color. We chose the case that the 7- and 13-keV transitions have $M1/E2$ and $E1$ characters, and are placed on top of the 59- and 53-keV transitions, respectively, as in the level scheme of Fig. 6.1. In such a scenario, a 53-keV transition is also known as the lowest transition in Band 2 [156], being observed

Table 6.1: The Weisskopf estimates for the $5/2^-$ isomer with different order of the transitions in the depopulating cascades.

Energy (keV)	Spin and parity[a]	Conversion coefficients[b]	Half-life (μs)
5/2$^-$ level depopulated by the 66.0-, 7.4-, 12.6-keV transitions.			
7.4 and 12.6	3/2$^+$ and 3/2$^+$	4.61 and 6.04	2.47
7.4 and 12.6	3/2$^+$ and 3/2$^-$	4.61 and 1.264	0.11
7.4 and 12.6	3/2$^-$ and 3/2$^+$	0.985 and 6.04	0.58
7.4 and 12.6	3/2$^-$ and 3/2$^-$	0.985 and 1.264	0.04
5/2$^-$ level depopulated by the 66.0-, 58.6-, 12.6-keV transitions.			
58.6 and 12.6	3/2$^+$ and 3/2$^+$	0.985 and 6.04	1.98
58.6 and 12.6	3/2$^+$ and 3/2$^-$	0.985 and 1.264	0.05
58.6 and 12.6	3/2$^-$ and 3/2$^+$	4.61 and 6.04	0.0005
58.6 and 12.6	3/2$^-$ and 3/2$^-$	4.61 and 1.264	0.0004
5/2$^-$ level depopulated by the 66.0-, 7.4-, 53.4-keV transitions.			
7.4 and 53.4	3/2$^+$ and 3/2$^+$	4.61 and 1.264	1.45
7.4 and 53.4	3/2$^+$ and 3/2$^-$	4.61 and 6.04	0.0003
7.4 and 53.4	3/2$^-$ and 3/2$^+$	0.985 and 1.264	0.38
7.4 and 53.4	3/2$^-$ and 3/2$^-$	0.985 and 6.04	0.0003
5/2$^-$ level depopulated by the 66.0-, 58.6-, 53.4-keV transitions.			
58.6 and 53.4	3/2$^+$ and 3/2$^+$	0.985 and 1.264	1.15
58.6 and 53.4	3/2$^+$ and 3/2$^-$	0.985 and 6.04	0.0003
58.6 and 53.4	3/2$^-$ and 3/2$^+$	4.61 and 1.264	0.0004
58.6 and 53.4	3/2$^-$ and 3/2$^-$	4.61 and 6.04	0.0002

[a]: The first (second) value corresponds to the first (second) value of "Energy (keV)" column.
[b]: The first (second) value corresponds to the 58.6-keV (53.4-keV) transition.

in prompt coincidence at the target position. We therefore conclude that the 53-keV transitions observed both at the MARA focal plane in delayed coincidence with transitions of Band 1 measured at the target position, and at the target position in prompt coincidence with transitions of Band 2, are in fact the same transition depopulating the $5/2^+$ band-head of Band 2, which is fed by the prompt 123- and 285-keV transitions of Band 2 and by the delayed 13-keV transition from the isomeric band-head of Band 1. The $5/2^-$ band-head of Band 1 decays therefore to the $3/2^+$ ground state via the cascade 7 - 59 keV and the 66-keV transition, as well as to the band-head of Band 2 via the 13-keV transition.

Table 6.2: Experimental information including the γ-ray energies E_γ, energies of the initial levels E_i, relative intensities I_γ, anisotropies R_{DCO} and/or R_{ac}, parameters a_2 and a_4, polarization asymmetries A_p, mixing ratios $\delta(M1/E2)$, multipolarities, and spin-parity assignments to the observed states in ^{119}Ba. The transitions listed with increasing energy are grouped in bands.

E_γ (keV)[a]	E_i (keV)	I_γ^b	R_{DCO}^c	R_{ac}^d	a_2	a_4	A_p	δ	Mult.	$J_i^\pi \rightarrow J_f^\pi$
Band 1										
60.0	126.0	60(18)	1.0(1))[f]		-0.84(3)	0.46(5)		-1.8(4) or -0.3(4)	$M1/E2$	$(7/2^-) \rightarrow)5/2^-)$
92.5	332.2	104(8)	0.40(7)[e]		-0.70(4)	0.43(8)		-2.5(3) or -0.3(5)	$M1/E2$	$(11/2^-) \rightarrow (9/2^-)$
112.1	695.4	18(5)	0.41(5)[e]						$M1/E2$	$(15/2^-) \rightarrow (13/2^-)$
113.4	239.5	150(50)	0.53(6)[e]		-0.66(6)	0.37(5)		-2.6(6) or -0.2(4)	$M1/E2$	$(9/2^-) \rightarrow (7/2^{-)}$
122.6	1207.2	8(4)		0.9(2)					$M1/E2$	$(19/2^-) \rightarrow (17/2^-)$
130.2	1842.0	3(1)							$(M1/E2)$	$(23/2^-) \rightarrow (21/2^-)$
142.3	2568.9	2(1)							$(M1/E2)$	$(27/2^-) \rightarrow (25/2^-)$
174.0	239.5	30(10)	1.9(9)[f]		0.14(10)	-0.29(19)			$E2$	$(9/2^-) \rightarrow (5/2^-)$
206.5	332.2	100	0.93(7)[e]		0.29(3)	-0.19(5)	0.13(4)		$E2$	$(11/2^-) \rightarrow (7/2^-)$
250.5	583.0	50(10)	0.9(1)[f]		-0.68(8)	0.18(14)	-0.02(1)		$M1/E2$	$(13/2^-) \rightarrow (11/2^-)$
343.8	583.0	50(10)	2.2(3)[f]		0.33(5)	-0.02(7)	0.06(2)		$E2$	$(13/2^-) \rightarrow (9/2^-)$
363.2	695.4	250(50)	1.9(3)[f]		0.15(3)	-0.12(5)	0.08(2)		$E2$	$(15/2^-) \rightarrow (11/2^-)$
388.8	1084.5	30(10)		0.7(2)					$M1/E2$	$(17/2^-) \rightarrow (15/2^-)$
500.5	4673.1	6(4)							$(M1/E2)$	$(37/2^-) \rightarrow (35/2^-)$
501.7	1084.5	40(10)	0.95(9)[e]						$E2$	$(17/2^-) \rightarrow (13/2^-)$
504.1	1711.6	24(8)		0.7(2)					$M1/E2$	$(21/2^-) \rightarrow (19/2^-)$
511.8	1207.2	250(50)	1.0(1)[e]		0.11(9)	0.01(17)	0.14(4)		$E2$	$(19/2^-) \rightarrow (15/2^-)$
534.0	5558.1	3(1)							$(M1/E2)$	$(41/2^-) \rightarrow (39/2^-)$
539.8	3895.0	9(5)		0.9(1)					$M1/E2$	$(33/2^-) \rightarrow (31/2^-)$
584.0	2426.5	9(3)		0.5(3)					$M1/E2$	$(25/2^-) \rightarrow (23/2^-)$
600.4	3169.7	18(6)		0.6(2)					$M1/E2$	$(29/2^-) \rightarrow (27/2^-)$
627.2	1711.6	50(30)	1.1(2)[e]		0.03(14)	-0.07(26)			$E2$	$(21/2^-) \rightarrow (17/2^-)$
634.8	1842.0	180(40)	1.2(2)[e]		0.08(15)	0.10(27)	0.11(3)		$E2$	$(23/2^-) \rightarrow (19/2^-)$
715.0	2426.5	80(30)	1.3(2)[e]		0.02(14)	0.03(27)	0.08(4)		$E2$	$(25/2^-) \rightarrow (21/2^-)$
725.3	3895.0	40(20)		1.3(3)					$E2$	$(33/2^-) \rightarrow (29/2^-)$
726.9	2568.9	160(40)	1.0(2)[e]	1.3(1)	0.19(17)	-0.01(31)	0.13(4)		$E2$	$(27/2^-) \rightarrow ((23/2^-)$
743.4	3169.7	50(30)	1.0(2)[e]		0.06(19)	0.04(34)			$E2$	$(29/2^-) \rightarrow (25/2^-)$
778.1	4673.1	20(10)		1.5(3)					$E2$	$(37/2^-) \rightarrow (33/2^-)$
786.5	3355.4	83(20)	1.0(1)[e]						$E2$	$(31/2^-) \rightarrow (27/2^-)$
816.7	4172.1	50(10)	1.0(1)[e]						$E2$	$(35/2^-) \rightarrow (31/2^-)$
851.6	5023.7	24(7)	1.0(2)[e]						$E2$	$(39/2^-) \rightarrow (35/2^-)$
885.1	5558.1	20(10)		1.5(4)					$E2$	$(41/2^-) \rightarrow (37/2^-)$
916.6	5940.3	20(10)		1.3(2)					$E2$	$(43/2^-) \rightarrow (39/2^-)$
993.6	6551.7	19(10)		1.3(3)					$E2$	$(45/2^-) \rightarrow (41/2^-)$
1000.7	6941.0	9(3)		1.4(3)					$E2$	$(47/2^-) \rightarrow (43/2^-)$
1090.9	8031.9	6(3)		1.4(3)					$E2$	$(51/2^-) \rightarrow (47/2^-)$
1097.6	7649.3	10(6)		1.3(4)					$E2$	$(49/2^-) \rightarrow (45/2^-)$
1177.4	9209.3	6(2)		1.2(4)					$E2$	$(55/2^-) \rightarrow (51/2^-)$
1188.9	8838.2	8(5)		1.6(5)					$E2$	$(53/2^-) \rightarrow (49/2^-)$
1265.7	10475.0	4(2)							$(E2)$	$(59/2^-) \rightarrow (55/2^-)$
Band 1 $\rightarrow$ Ground state										
(7.4)	66.0								$(M1/E2)$	$(5/2^-) \rightarrow (3/2^-)$
58.6	58.6	10(4)							$(E1)$	$(3/2^-) \rightarrow (3/2^+)$
66.0	66.0	75(10)							$(E1)$	$(5/2^-) \rightarrow (3/2^+)$
Band 1 $\rightarrow$ Band 2										
(12.6)	66.0								$(E1)$	$(5/2^-) \rightarrow (5/2^+)$
Band 2										
123.1	176.5	45(9)	0.48(6)[e]		-0.91(17)	0.37(31)		-1.6(2) or -0.4(4)	$M1/E2$	$(7/2^{+)} \rightarrow (5/2^+)$
161.5	338.2	40(10)	1.2(1)[f]		-0.72(12)	0.40(23)	-0.14(5)	-2.3(2) or -0.3(5)	$M1/E2$	$(9/2^+) \rightarrow (7/2^+)$
183.9	522.3	30(10)	1.01(9)[f]		-0.69(12)	0.33(21)	-0.02(1)	-2.5(5) or -0.2(3)	$M1/E2$	$(11/2^+) \rightarrow (9/2^+)$
227.9	750.4	20(10)	0.53(9)[e]				-0.11(5)		$M1/E2$	$(13/2^+) \rightarrow (11/2^+)$
238.2	988.7	11(5)		0.8(1)					$M1/E2$	$(15/2^+) \rightarrow (13/2^+)$
285.0	338.2	70(30)	0.94(9)[e]				0.13(5)		$E2$	$(9/2^+) \rightarrow (5/2^+)$
285.5	1559.4	4(3)							$(M1/E2)$	$(19/2^+) \rightarrow (17/2^+)$
285.9	1274.7	5(4)							$(M1/E2)$	$(17/2^+) \rightarrow (15/2^+)$

Table 6.2 $(Continued.)$

E_γ (keV)[a]	E_i (keV)	I_γ^b	R_{DCO}^c	R_{ac}^d	a_2	a_4	A_p	δ	Mult.	$J_i^\pi \rightarrow J_f^\pi$
332.2	1892.1	3(3)							$(M1/E2)$	$(21/2^+) \rightarrow (19/2^+)$
345.8	522.3	110(40)	0.86(7)[e]		0.15(3)	-0.25(5)	0.06(2)		$E2$	$(11/2^+) \rightarrow (7/2^+)$
412.2	750.4	110(40)	0.94(9)[e]		0.15(10)	-0.32(18)	0.15(8)		$E2$	$(13/2^+) \rightarrow (9/2^+)$
466.4	988.7	120(40)	1.01(6)[e]		-0.06(15)	-0.30(28)	0.06(2)		$E2$	$(15/2^+) \rightarrow (11/2^+)$
524.3	1274.7	100(50)	1.18(9)[e]		-0.03(7)	-0.17(12)	0.15(7)		$E2$	$(17/2^+) \rightarrow (13/2^+)$
570.7	1559.4	100(40)	1.0(1)[e]		0.15(10)	-0.01(10)	0.09(4)		$E2$	$(19/2^+) \rightarrow (15/2^+)$
617.4	1892.1	80(40)		1.3(2)	0.22(8)	0.02(14)	0.11(6)		$E2$	$(21/2^+) \rightarrow (17/2^+)$
659.2	2218.6	80(40)	1.2(2)[e]		0.24(16)	0.06(29)	0.18(9)		$E2$	$(23/2^+) \rightarrow (19/2^+)$
688.7	2580.8	60(30)		1.3(2)	0.11(27)	-0.02(49)	0.11(9)		$E2$	$(25/2^+) \rightarrow (21/2^+)$
728.7	2947.3	60(30)	1.3(3)[e]						$E2$	$(27/2^+) \rightarrow (23/2^+)$
731.4	3312.2	45(20)	1.1(3)[e]						$E2$	$(29/2^+) \rightarrow (25/2^+)$
767.2	3714.5	35(20)		1.6(5)					$E2$	$(31/2^+) \rightarrow (27/2^+)$
740.0	4052.2	15(8)		1.4(4)					$E2$	$(33/2^+) \rightarrow (29/2^+)$
794.8	4509.3	35(20)		1.6(4)					$E2$	$(35/2^+) \rightarrow (31/2^+)$
807.0	4859.2	8(4)		1.2(5)					$E2$	$(37/2^+) \rightarrow (33/2^+)$
859.1	5368.4	16(9)		1.3(2)					$E2$	$(39/2^+) \rightarrow (35/2^+)$
913.9	6282.3	11(7)		1.5(5)					$E2$	$(43/2^+) \rightarrow (39/2^+)$
941.3	7223.6	10(7)		1.4(6)					$E2$	$(47/2^+) \rightarrow (43/2^+)$
987.0	8210.6	9(5)		1.4(3)					$E2$	$(51/2^+) \rightarrow (47/2^+)$
1059.3	9269.9	7(4)		1.3(4)					$E2$	$(55/2^+) \rightarrow (51/2^+)$
1139.4	10409.3	4(2)							$E2$	$(59/2^+) \rightarrow (55/2^+)$
1225.6	11634.9	2(1)							$E2$	$(63/2^+) \rightarrow (59/2^+)$
1315.8	12950.7	1(1)							$E2$	$(67/2^+) \rightarrow (63/2^+)$
1397.0	14347.7	<1							$E2$	$(71/2^+) \rightarrow (67/2^+)$
1473.9	15821.6	<1							$E2$	$(75/2^+) \rightarrow (71/2^+)$
Band 2 → Band 3										
53.3	53.3	20(10)		0.7(1)					$M1/E2$	$(5/2^+) \rightarrow (3/2^+)$
84.5	176.5	32(6)	0.5(1)[e]		-0.73(13)	0.64(25)		-2.2(9) or -0.2(4)	$M1/E2$	$(7/2^+) \rightarrow (5/2^+)$
99.2	988.7	3(2)							$(M1/E2)$	$(15/2^+) \rightarrow (13/2^+)$
99.3	522.3	5(4)							$(M1/E2)$	$(11/2^+) \rightarrow (9/2^+)$
109.9	750.4	4(2)							$(M1/E2)$	$(13/2^+) \rightarrow (11/2^+)$
177.0	176.5	17(3)		1.2(3)					$E2$	$(7/2^+) \rightarrow (3/2^+)$
246.3	338.2	16(7)		1.4(4)					$E2$	$(9/2^+) \rightarrow (5/2^+)$
Band 2 → 7/2$^+$										
146.5	338.2	12(5)		0.9(2)					$M1/E2$	$(9/2^+) \rightarrow (7/2^+)$
7/2$^+$ → Band 3										
99.6	191.5	12(5)		0.5(2)					$M1/E2$	$(7/2^+) \rightarrow (5/2^+)$
Band 3										
91.9	91.9	120(60)	0.5(1)[e]		-0.73(15)	0.66(27)		-2.0(10) or -0.2(5)	$M1/E2$	$(5/2^+) \rightarrow (3/2^+)$
146.3	238.4	56(20)	0.5(1)[e]		-0.72(4)	0.32(6)	-0.02(1)	-2.2(8) or -0.2(3)	$M1/E2$	$(7/2^+) \rightarrow (5/2^+)$
184.2	422.6	34(8)	1.3(3)[f]		-0.47(5)	0.46(6)	-0.16(9)	-3.8(6) or -0.1(5)	$M1/E2$	$(9/2^+) \rightarrow (7/2^+)$
217.5	639.9	18(7)		0.8(2)					$M1/E2$	$(11/2^+) \rightarrow (9/2^+)$
238.9	238.4	17(9)	1.0(2)[e]						$E2$	$(7/2^+) \rightarrow (3/2^+)$
249.8	890.2	9(4)		1.0(4)					$M1/E2$	$(13/2^+) \rightarrow (11/2^+)$
269.6	1159.8	7(4)							$(M1/E2)$	$(15/2^+) \rightarrow (13/2^+)$
302.5	1462.7	4(2)							$(M1/E2)$	$(17/2^+) \rightarrow (15/2^+)$
309.1	1772.3	<2							$(M1/E2)$	$(19/2^+) \rightarrow (17/2^+)$
330.8	422.6	31(6)	2.1(4)[f]		-0.08(28)	-0.22(53)			$E2$	$(9/2^+) \rightarrow (5/2^+)$
401.4	639.9	50(13)	2.0(4)[f]		-0.07(23)	-0.33(43)	0.02(1)		$E2$	$(11/2^+) \rightarrow 7(/2^+)$
467.7	890.2	50(20)	1.7(3)[f]		0.02(21)	0.02(40)	0.04(2)		$E2$	$(13/2^+) \rightarrow (9/2^+)$
520.0	1159.8	50(30)	0.9(3)[e]		0.02(31)	0.05(58)	0.09(4)		$E2$	$(15/2^+) \rightarrow (11/2^+)$
572.6	1462.7	30(15)		1.2(3)	0.16(28)	0.21(52)			$E2$	$(17/2^+) \rightarrow (13/2^+)$
612.5	1772.3	47(20)	1.2(2)[e]		0.25(30)	0.35(55)	0.02(2)		$E2$	$(19/2^+) \rightarrow (15/2^+)$
645.8	3090.4	11(5)		1.3(3)					$E2$	$(27/2^+) \rightarrow (23/2^+)$
650.8	2113.5	20(10)		1.4(3)					$E2$	$(21/2^+) \rightarrow (17/2^+)$
670.2	2783.7	12(6)		1.6(5)					$E2$	$(25/2^+) \rightarrow (21/2^+)$
672.3	2444.6	40(18)	1.0(2)[e]	1.4(2)					$E2$	$(23/2^+) \rightarrow (19/2^+)$
683.0	3773.4	7(3)		1.3(5)					$E2$	$(31/2^+) \rightarrow (27/2^+)$
Band 3 → Band 2										
245.9	422.6	6(3)							$(M1/E2)$	$(9/2^+) \rightarrow (7/2^+)$
302.2	639.9	5(2)							$(M1/E2)$	$(11/2^+) \rightarrow (9/2^+)$

[a] The error on the transition energies is 0.3 keV for transitions below 500 keV, 0.7 keV for transitions between 500 and 1000 keV, and 1.0 keV for transitions above 1000 keV. The error on the transition transition energies is 1.0 keV for the transition intesities less 5.

[b] Relative intensities corrected for efficiency, normalized to the intensity of the 206.5 keV, $11/2^- \rightarrow 7/2^-$ transition of Band 1. The transition intensities were obtained from a combination of total projection and gated spectra.

[c] R_{DCO} has been deduced from an asymmetric $\gamma\gamma$ coincidence matrix sorted with the detectors at 157.6° on one axis, and the detectors at ≈ 90° on the other axis. The tentative spin-parity of the states are given in parentheses.

[d] R_{ac} has been deduced from two asymmetric $\gamma\gamma$ coincidence matrices sorted with the detectors at 133.6° and 157.6° on one axis, and the detectors at ≈ 90° on the other axis. The tentative spin-parity of the states are given in parentheses.

[e] DCO ratio from spectrum gated on stretched quadrupole transition.

[f] DCO ratio from spectrum gated on stretched dipole transition.

Chapter 7

Rich band structure in the odd-odd ^{118}Cs nucleus

This chapter presents the experimental results obtained from the in beam spectroscopic study of the very neutron-deficient nucleus ^{118}Cs.

7.1 Introduction

The low-lying states of Cs nuclei have been studied over many years, also exploiting the high yields of radioactive beams of Cs isotopes at ISOL facilities [163, 164]. Two long-lived isomers have been identified in ^{118}Cs, one with half-life $T_{1/2} = 14(2)$ s and low spin $I = 2$, and the other with half-life $T_{1/2}$= 17(3) s and high spin $I = (6, 7, 8)$ [128, 164]. The bands with the unpaired *proton* placed in the $h_{11/2}$ orbital will exhibit $h_{11/2}$ neutron alignments, while the bands with the unpaired *neutron* placed in the $h_{11/2}$ orbital will exhibit $h_{11/2}$ proton alignments at different rotational frequencies. A detailed discussion of the alignment processes in Cs nuclei as arising from total Routhian surface calculations can be found in Ref. [126]. In odd-odd nuclei one can have both types of bands and therefore one can conclude which deformation should be adopted. This is the case in ^{120}Cs [125], in which the band with the unpaired proton in the $\pi g_{9/2}$ orbital exhibits the $h_{11/2}$ proton alignment at $\hbar\omega \approx 0.35$ MeV (band 3), while the band with the unpaired neutron in the $\nu d_{5/2}$ orbital exhibits the $h_{11/2}$ neutron alignment at $\hbar\omega \geq 0.45$ MeV (band 4).

The calculations of odd-odd nuclei are more demanding because of the multiple band structures resulting from the numerous combinations of the low-lying proton and neutron contributing configurations observed in the adjacent odd-even nuclei, which often lead to isomeric band-heads. Such calculations, employing the configuration-constrained potential-energy-surface (PES) model [165], predict the possible isomeric band heads in odd-odd lanthanide nuclei [4]. Six to ten isomers are predicted in the light Cs nuclei, with energies up to a few hundreds keV.

Eight isomers have been calculated in ^{118}Cs, with four configurations obtained by coupling a proton in the $d_{5/2}$, $g_{7/2}$, $g_{9/2}$ and $h_{11/2}$ orbitals to a neutron in the $h_{11/2}$ orbital, each one with two possible spin-parity assignments resulting from the Galagher-Moszkowski (GM) coupling rule [166]. If the spins of the two contributing proton and neutron orbitals in the GM doublets are very different, the electromagnetic transitions between the bands based on GM states with low and high spins can be strongly hindered, leading to long-lived isomers, called spin isomers [167], which can decay internally through delayed γ-ray emission or β decay. In all light odd-odd Cs nuclei only one or two long-lived β-decaying isomers are known, with half-lives of several seconds [124]. However, as predicted in Ref. [4], several other isomeric states with possible shorter half-lives can exist and decay internally through γ-ray emission, but are not known because no experiments involving suitable setups were performed yet. We therefore undertook a systematic search for low-lying isomers with half-lives measurable using recoil mass spectrometers equipped with efficient detection systems both at the entrance and at the focal plane, with the aim to verify the reliability of the theoretical predictions towards and beyond the proton drip line.

We have discussed the odd-even nuclei ^{119}Cs and ^{119}Ba, in which extended sets of single-quasiparticle proton and neutron excitations have been established. In both nuclei we identified low-lying isomers, with half-lives of $T_{1/2} = 0.36(2)$ μs and $T_{1/2} = 55(5)$ μs for the $5/2^-$ and $11/2^-$ band heads of the bands based on neutron and proton $h_{11/2}$ orbitals in ^{119}Ba and ^{119}Cs, respectively. In this chapter, we will discuss the odd-odd ^{118}Cs nucleus, in which the low-lying proton-neutron configurations result from the coupling of the single-quasiparticle configurations observed in the adjacent neighbors with an odd number of protons or neutrons.

In the previous work, only a couple of bands built on top of the 10^+ state were shown due to the limitation of the spectroscopic information [127]. In the current work, several new rotational bands and long-lived isomers have been identified. We reported ten new bands in ^{118}Cs, as well as other low-lying states, which leads to the largest set of proton-neutron excitations of odd-odd cesium nuclei close to the proton drip-line. For the isomeric states in the $\pi h_{11/2} \otimes \nu h_{11/2}$ band, the 8^+ band-head is a short-lived isomer with a half-life in the nanosecond range, while the 7^+ state below it is a long-lived isomer with a half-life of $T_{1/2} = 0.55(6)$ μs. Two other long-lived isomers have been identified: a 66-keV transition detected at the MARA focal plane depopulates one of them, indicating a half-life in the microsecond range, while no depopulating transitions have been identified for the other, indicating a much longer half-life. We assigned the configurations of the observed bands based on the analysis of the alignment properties of the bands, on systematics and particle number conserving cranked shell model (PNC-CSM) calculations [131, 132].

7.2 Experiment results

The presently reported experimental data have been obtained in the same high-statistics experiment performed with JUROGAM 3 + MARA [95, 97], but using the ^{58}Ni(^{64}Zn,$3p1n$)^{118}Cs reaction. Experimental details have been discussed in Section 4.1.

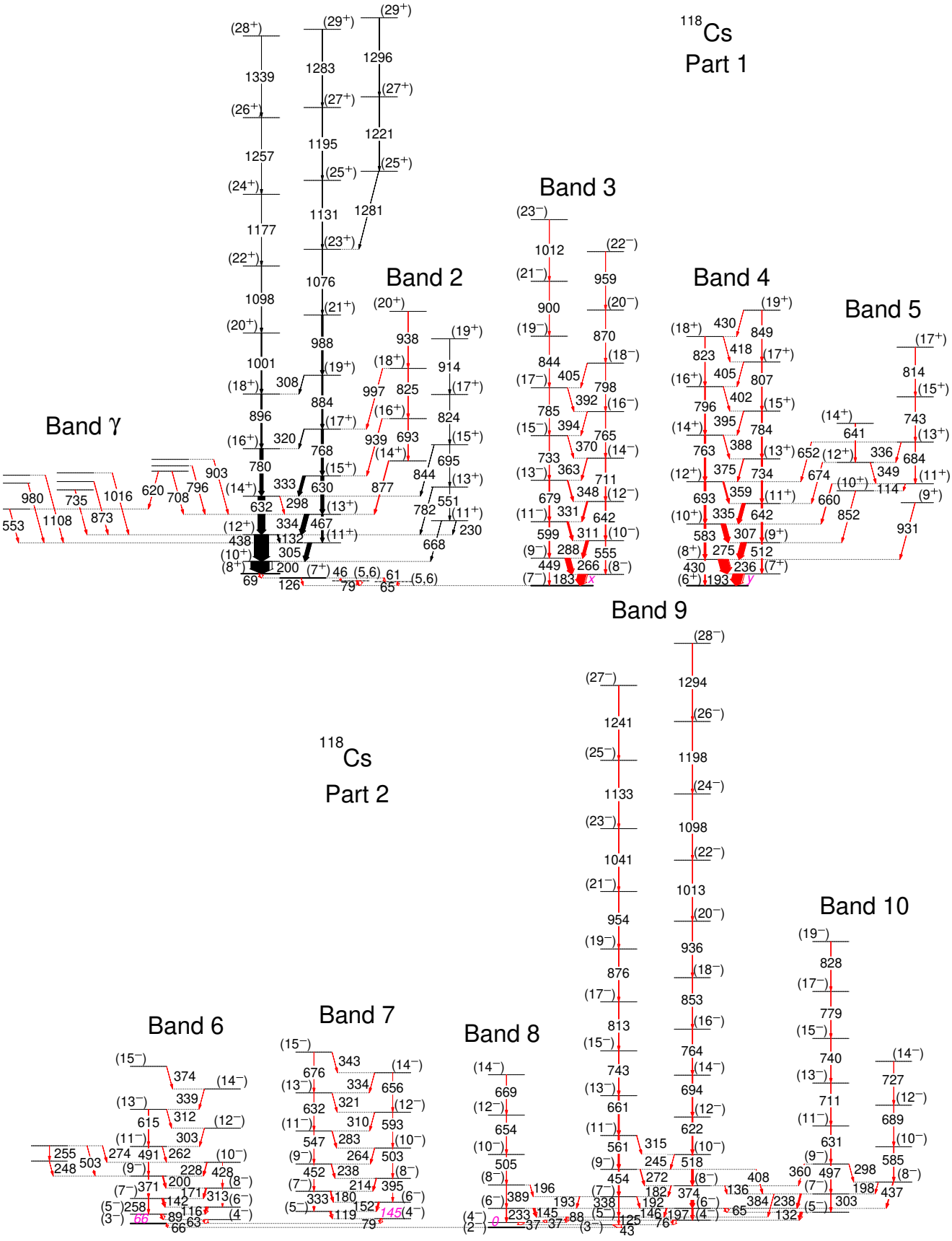

Figure 7.1: The level scheme of ^{118}Cs showing the previously known and the presently reported bands. The new transitions are indicated with red color. The isomeric levels are indicated with thick lines. The proposed energies of the band heads are indicate in pink color.

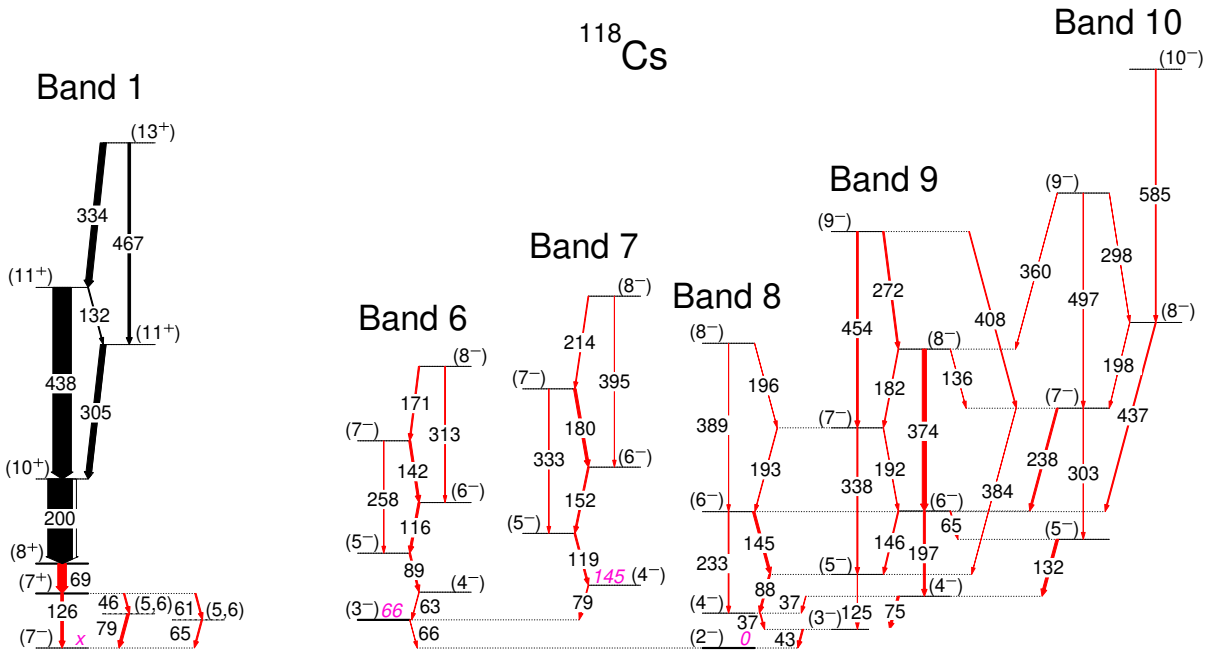

Figure 7.2: Zoom on the low-lying states of the level scheme of ^{118}Cs shown in Fig. 7.1.

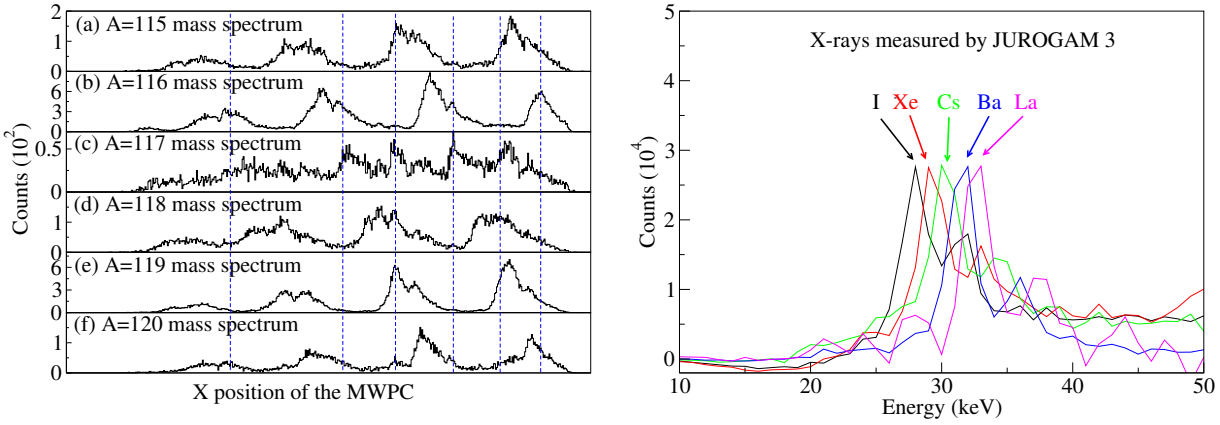

Figure 7.3: (left) Mass spectra for different A measured by the MWPC, obtained by tagging on selected γ rays detected by JUROGAM 3, which belong to nuclei with different mass. (right) Zoom on the low-energy region of the spectra for different nuclei showing the X-rays in coincidence with bands of different nuclei populated in the reaction.

The level scheme of ^{118}Cs divided in two parts is shown in Fig. 7.1, where the band labels are placed above the bands. The complete experimental information on the γ-ray transitions of ^{118}Cs is reported in Table 7.1. Double-gated spectra obtained from prompt $\gamma\gamma\gamma$ coincidences showing the transitions of the newly identified bands reported in the present work are given in Figs. 7.4, 7.6 and 7.8. Spectra for Bands 1, 6 and 7 obtained from prompt-delayed coincidences of γ-rays detected by JUROGAM 3 and the detectors at the MARA focal plane are shown in Figs. 7.5 and 7.7.

The assignment of the bands to ^{118}Cs is based on the coincidence of the prompt $\gamma\gamma$ coincidences with recoiling evaporation residues with mass 118 detected at the MARA focal plane, and with the 31 keV K_α X rays of cesium nuclides detected in prompt coincidence with the in-band transitions by JUROGAM 3 array at the target position. The mass spectra and the peaks of X-rays for different nuclei shown in Fig. 7.3.

For ^{118}Cs, the GM coupling rule [166] play an important role in assigning the configuration of the bands. The coupling rules are as follows [166]:

$$I = \Omega_p + \Omega_n \qquad if \quad \Omega_p = \Lambda_p \pm \frac{1}{2} \quad and \quad \Omega_n = \Lambda_n \pm \frac{1}{2}, \tag{7.1}$$

$$I = |\Omega_p - \Omega_n| \qquad if \quad \Omega_p = \Lambda_p \pm \frac{1}{2} \quad and \quad \Omega_n = \Lambda_n \mp \frac{1}{2}. \tag{7.2}$$

High-spin states in ^{118}Cs can arise from one proton in the $\pi h_{11/2}[541]3/2^-$, $\pi g_{9/2}[404]9/2^+$, $\pi d_{5/2}[420]1/2^+$, or $\pi g_{7/2}[422]3/2^+$ orbitals which were observed at 110, 86, 112, and 0 keV in ^{119}Cs, and from a neutron in the $\nu h_{11/2}[532]5/2^-$, $\nu d_{5/2}[413]5/2^+$, or $\nu h_{11/2}[411]3/2^+$ orbitals observed at 66, 53, and 0 keV in ^{119}Ba, respectively.

7.2.1 Bands γ, 1, 2, 3, 4 and 5

Band 1, first reported in Ref. [127], is the most strongly populated band structure. The spectrum of Band 1 is shown in Fig. 7.4 (a). It is confirmed, except for the highest 1346- and 1408-keV transitions in the two signature partners of the band, which are not observed. The cascade of transitions feeding the state depopulated by the 1076-keV transition is also confirmed. Nine weak transitions feeding the low-lying states of Band 1, and one transition of 620 keV connecting two of them, have been also identified and grouped under the label Band γ.

The band-head spin and parity of Band 1 were first assigned as $I^\pi = 10^+$ in Ref. [127]. However, from the systematics of the $\pi h_{11/2} \otimes \nu h_{11/2}$ bands in odd-odd Cs nuclei published in Ref. [168], it results that the band-head spin of Band 1 should be 8^+. We therefore adopt spin-parity $I^\pi = 8^+$ for the state populated by the 200-keV transition. We identified a new 69-keV transition which depopulates the 8^+ state, which has an intensity ≈ 30 times lower than that of the feeding 200-keV transition. The transition being weak, we could not extract its electromagnetic character. As the electron conversion coefficients for the possible $E2$, $M1$ or $E1$ electromagnetic characters of

the 69-keV transition are 7.0, 2.6 and 0.6, respectively, which cannot account for the missing intensity below the 8^+ state, one conclude that the 8^+ state is isomer, with a half-life in the nanosecond range. Unfortunately, we could not measure the half-life of this short-lived isomer, because in the present thin-target experiment the residual nuclei fly away from the focus of the Compton-suppressed γ-ray detectors of the JUROGAM 3 array. The isomeric character of the 8^+ band head is similar to that observed for the band head of the $\pi h_{11/2} \otimes \nu h_{11/2}$ band in ^{120}Cs, in which the depopulating 183-keV transition measured in a thick-target experiment, presented stopped and Doppler-shifted components, indicating an isomeric character with a half-life in the sub-nanosecond range [125], in which the depopulating 183-keV transition measured in a thick-target experiment, presented stopped and Doppler-shifted components, indicating an isomeric character with a half-life in the sub-nanosecond range.

Based on the Weisskopf estimates of the transition probability for the 69-keV transition, one can safely exclude the $E1$ and $M2$ characters which lead to long half-lives of 0.85 μs (assuming a hindrance factor of 10^{-6}) and 824 μs, respectively. The half-lives for $M1$ and $E2$ transitions being $T_{1/2} = 0.06$ ns and $T_{1/2} = 9.8$ μs, respectively, we tentatively assign a mixed $M1/E2$ character, predominantly $M1$, to the 69-keV transition, leading to a state with $I^\pi = 7^+$. No other transitions in prompt coincidence with the 69-keV transitions have been observed below the 7^+ state.

We then searched for delayed transitions detected at the MARA focal plane in coincidence with the prompt transitions of Band 1 measured at the target position. One can see in Fig. 7.5 that five delayed transitions have been identified, with energies of 46, 61, 65, 79 and 126 keV, which, based on the prompt coincidence relationships between the clover detectors mounted around the MARA focal plane, were placed in three parallel cascades, 46-79, 61-65 and 126 keV, just below the 7^+ state populated by the 69-keV transition. The observation of these delayed γ-ray cascades lead to a state located 126 keV below the 7^+ isomer, to which we tentatively assigned spins and parities based on the analysis of the isomer decay, as described in the following. No other transitions have been observed at the MARA focal plane in coincidence with the delayed transitions depopulating the 7^+ isomer, indicating that the three γ-ray branches populate one of the two known long-lived isomers, which can only be the $I = (6, 7, 8)$, $T_{1/2}$= 17(3) s isomer [164], since the observed delayed transitions depopulate the high-spin 7^+ state and cannot have the high multipolarity required to populate the $I = 2$ isomer [163]. A half-life $T_{1/2} = 0.55(6)$ μs has been extracted from the fit of the time spectrum obtained by summing the time spectra of the 79- and 126-keV depopulating transitions of the 7^+ isomer, as shown in the right panel of Fig. 7.5. As we could not perform an angular correlation analysis of the events measured at the MARA focal plane, the electromagnetic characters of these transitions are not established experimentally. The half-life of the 7^+ isomer can be accounted for by assuming $E1$, $E2$ or $M2$ electromagnetic characters of the 126-keV transition, which lead to spins and parities between 5^+ and 8^- for the state fed by the 126-keV transition. Taking also into account the prompt coincidence between the 46- and 79-keV transitions, and between the 61- and 65-keV transitions, only states with spins and parities 6^- and 7^- for the final state can lead to an isomer half-life in the microsecond range.

Based on the GM coupling rule [166], high-spin isomers in ^{118}Cs can arise from one proton in the $\pi g_{9/2}[404]9/2^+$ orbital which was observed at 86 keV in ^{119}Cs, and from a neutron in the $\nu h_{11/2}[532]5/2^-$ or $\nu h_{11/2}[411]3/2^+$ orbitals observed at 53 and 66 keV in ^{119}Ba, with spins 7^- and 6^+, respectively. As will be discussed in the following, we assigned spin-parity 7^- to Band 3, and therefore we identified the long-lived isomeric state populated by the 126-keV transition with the 7^- band head of Band 3.

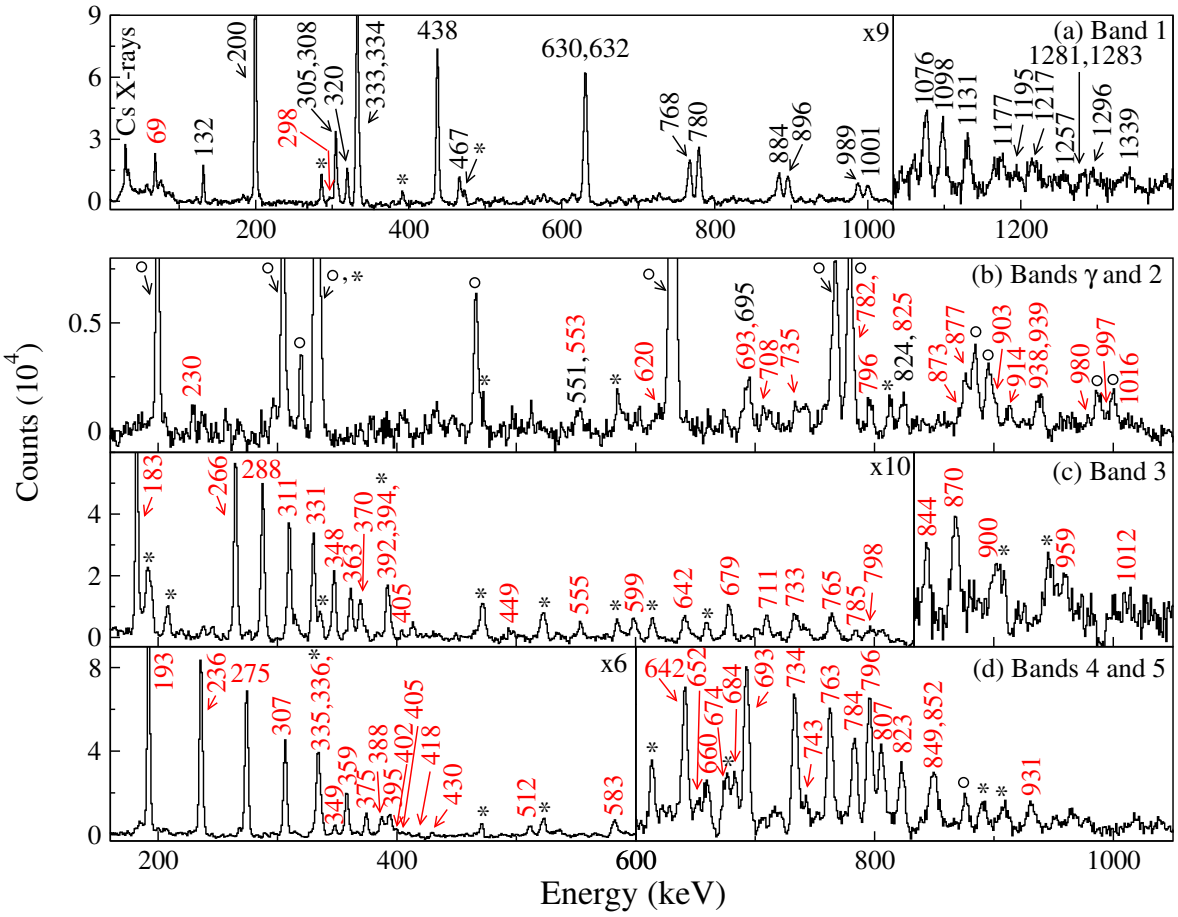

Figure 7.4: Double-gated spectra for Bands 1, γ, 2, 3, 4 and 5 of ^{118}Cs. Peak energies for the newly identified are written with red color. Transitions from ^{116}Xe, ^{118}Xe, ^{119}Cs are indicated with an asterisk, while those from Band 1 present in the spectrum of Band 2 ^{118}Cs are indicated with a circle. The lists of gating transitions for each spectrum are the following: for Band 1 132, 200, 305, 438, 467, 632, 768, 780, 884, 896, 988, 1001, 1076, 1098, 1176, 1340 keV; for Bands 2 and γ 132, 200, 305, 305, 438, 467 keV; for Band 3 183, 266, 288, 311, 331, 348, 363, 555, 599, 642, 679 keV; for Bands 4 and 5 193, 236, 275, 307, 388, 512, 583, 642, 693, 734, 763 keV.

The order of the transitions in the two 46-79 keV and 61-65 keV cascades, as well as the spins and parities of the intermediate levels in these cascades, could not be established, because many combinations of spins and parities lead to half-lives of the order of a microsecond for the 7^+ isomer. Therefore, the intermediate levels in these cascades have spins 5 or 6, and their excitation energies and parities are not fixed in Fig. 7.1.

Band 2 is newly identified, and its spectrum is shown in Fig. 7.4 (b). It is very weakly populated and is composed of two cascades of $E2$ transitions feeding states of Band 1 up to spins 17^+. The odd-spin cascade of Band 2 up

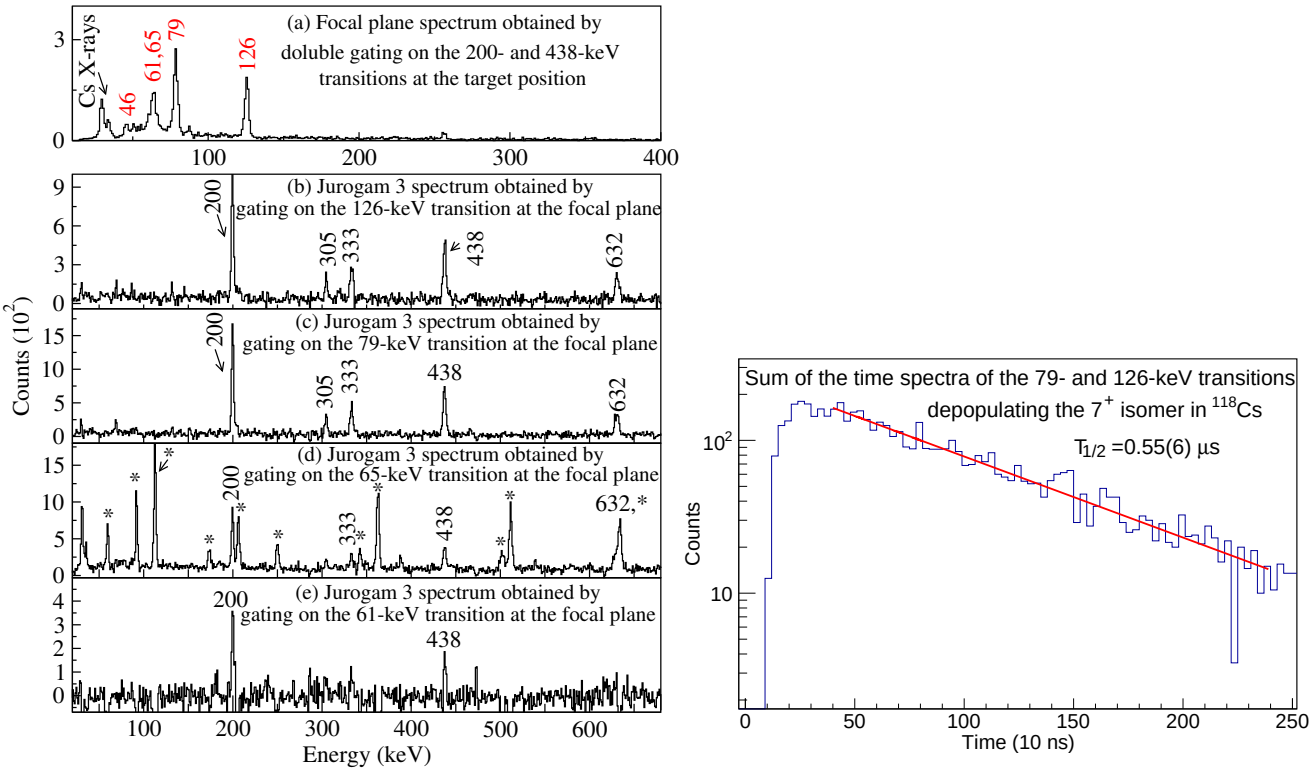

Figure 7.5: (left) Prompt-delayed coincidence spectra for Band 1. Peak energies for the newly identified transitions are in red. The asterisks in panel (d) indicate transitions of Band 1 in ^{119}Ba. (right) Fit of the time spectrum obtained by summing the time spectra of the 79- and 126-keV transitions depopulating the 126-keV 7^+ isomer of ^{118}Cs, produced by gating on the 200-keV transition detected with JUROGAM 3 at the target position.

to spin 19 and its connecting transitions to Band 1 have been previously reported in Ref. [127], but were wrongly placed to feed states of the odd-spin cascade of Band 1. No transitions between the odd- and even-spin cascades are observed. The coincidence relationships of the present work clearly show that the 668-keV transition, the two 230- and 782-keV transitions, and the weak 844-keV transition directly populate the even-spin states 10^+, 12^+ and 14^+ of Band 1, respectively.

Band 3 is newly identified, and its spectrum is shown in Fig. 7.4 (c). It is populated with an intensity $\approx$ 50% of that of Band 1, and is composed of two long cascades of $E2$ transitions, interconnected by strong $M1/E2$ transitions up to spin 23. We tentatively assign a spin-parity 7^- to the band-head, based on the intensity of the band, on systematics and on the PNC-CSM calculations. No other prompt transitions depopulating the 7^- band-head at the target position, neither delayed transitions detected at the MARA focal plane in coincidence with in-band transitions detected at the target position, have been observed. This indicates the isomeric character of the 7^- band-head, with a half-life of at least several microseconds. We identify the band-head of Band 3 with the $T_{1/2}$= 17(3) s isomer for which a spin $I = (6, 7, 8)$ has been suggested [164], selecting thus $I = 7$ among the three possible spins values, and we assign it negative parity, leading therefore to spin-parity $I^\pi = 7^-$ for the $T_{1/2}$= 17(3) s isomer. As will be discussed in the following, we assigned spin-parity 7^- to Band 3, and therefore we identified the long-lived isomeric

state populated by the 126-keV transition with the 7^- band-head of Band 3.

Band 4 is newly identified, and its spectrum is shown in Fig. 7.4 (d). It is populated with an intensity $\approx$ 50% of that of Band 1. It is composed of two cascades of $E2$ transitions, interconnected by strong $M1/E2$ transitions up to spin 19. Even if Band 4 has properties similar to those of Band 3, no transitions have been observed between the two bands, suggesting opposite parities or very different spins and/or excitation energies. However, as the intensities of Bands 3 and 4 are not very different and their pattern are very similar, most probably their excitation energies are very different. We can tentatively assign $I^\pi = 6^+$ for the band-head, which is in agreement with the $\pi[404]9/2^+ \otimes \nu[411]3/2^+$ favored configuration predicted by the GM rule. An alternative configuration can be $\pi[404]9/2^+ \otimes \nu[413]5/2^+$, which leads to $I^\pi = 4^+$ for the band-head. No other transitions have been observed at the target position in prompt coincidence with in-band transitions, indicating an isomeric character of the band-head with a half-life at least several microseconds, as in the case of Band 3. A weakly populated band, labeled Band 5, feeding the states of Band 4 with spins between 8^+ and 12^+ has been also identified.

7.2.2 Bands 6 and 7

Band 6 is newly identified, and its spectrum is shown in Fig. 7.6 (a). It has an intensity similar to that of Band 3, which is $\approx$ 15% of that of Band 1. It is composed of strong $M1/E2$ transitions, and weak $E2$ crossover transitions. No other prompt transitions detected at the target position were observed in coincidence with in-band transitions, but a delayed 66-keV transition has been observed at the MARA focal plane in coincidence with the in-band transitions observed at the target position. The prompt-delayed coincidence spectra for Band 6 is shown in Fig. 7.7 (a). As the 66-keV transition is also observed in coincidence with the in-band transitions of Band 7, we placed it on top of the ground state to which we assigned spin-parity $I^\pi = 2^-$. Based on the PNC-CSM calculations which suggest a $\pi[541]3/2^- \otimes \nu[411]3/2^+$ configuration for Band 6, we tentatively assign $I^\pi = 3^-$ to its band-head. With this assignment, the isomeric character of the $I^\pi = 3^-$ band-head of Band 6 at an excitation energy of 66 keV is induced by a hindrance due to the very different configuration than the $\pi[404]9/2^+ \otimes \nu[532]5/2^-$ configuration assigned to the ground state (see Section 7.3). Due to insufficient statistics, the half-life of the 66-keV isomeric state could not be measured from the delayed spectra collected at the MARA focal plane.

Band 7 is newly identified, and its spectrum is shown in Fig. 7.6 (b). It is populated with an intensity of $\approx$ 10% of that of Band 1, and is composed of levels connected by strong $M1/E2$ transitions and a few weak $E2$ crossover transitions. No other prompt transitions detected at the target position were observed in coincidence with in-band transitions, but, as in the case of Band 6, a delayed 66-keV transition has been observed at the MARA focal plane in coincidence with the in-band transitions observed at the target position. The prompt-delayed coincidence spectra for Band 7 is shown in Fig. 7.7 (b). We assumed that this delayed transition is the same as that observed in delayed coincidence with Band 6, and we placed the lowest prompt 79-keV transition on top of the

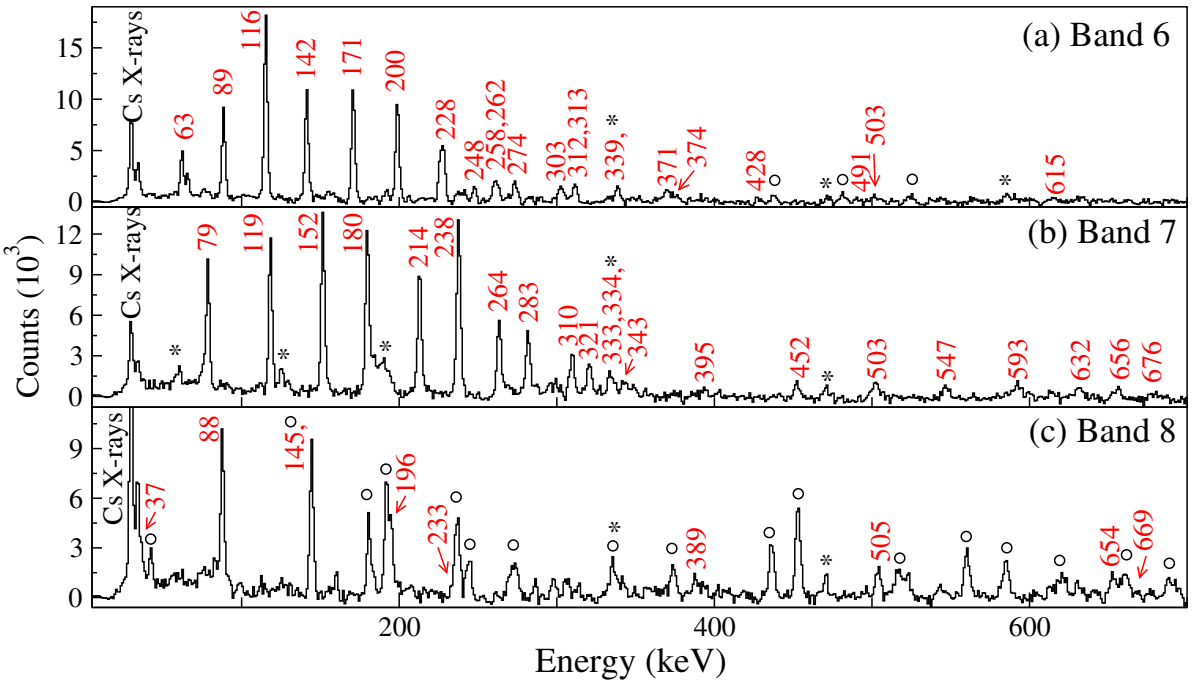

Figure 7.6: Double-gated spectra for Bands 6, 7 and 8 of ^{118}Cs. Peak energies for the newly identified are written with red color. Transitions from ^{118}Xe are indicated with an asterisk, while those from other bands in ^{118}Cs are indicated with a circle. The lists of gating transitions for each spectrum are the following: for Band 6 89, 142, 171, 200, 228 keV; for Band 7 79, 119, 152, 180, 214, 264 keV; for Band 8 88, 145, 193, 389, 505, 654 keV.

66-keV state, which leads to spin-parity 4^- for the band-head of Band 7. The assigned $\pi[422]3/2^+ \otimes \nu[532]5/2^-$ configuration being very different from that assigned to Band 6 explain the missing connecting transitions between the two bands. The isomeric character can be explained by the occupation of a different neutron orbital than in the $\pi[404]9/2^+ \otimes \nu[532]5/2^-$ configuration assigned to the 2^- ground state.

7.2.3 Bands 8, 9 and 10

Five cascades of $E2$ transitions interconnected by many $M1/E2$ and three $E2$ transitions, which were grouped in three bands with labels 8, 9 and 10, are newly identified, being populated with intensities of 45%, 60% and 15% of that of Band 1, respectively. The interconnecting transitions lead to identical parity of all five $E2$ cascades, which we assign as negative. The lowest state of these negative-parity bands is that populated by the 43-keV transition from Band 10. Based on the systematics of the spins and parities of the low-lying bands in the neighboring nuclei, and on the existence of a long-lived $T_{1/2}$= 14(2) s, $I = 2$ isomer [164], which we assign it as the band-head of Band 8 and adopt as the ground state of ^{118}Cs. The spectrum of Band 8 is shown in Fig. 7.6 (c).

Band 9 is composed of two long cascades of $E2$ transitions developing up to spin 28^-, interconnected by $M1/E2$ transitions up to spin 11^-. Its spectra are shown in Fig. 7.8 (a) and (b) with signatures α = 1 and 0, respectively. Five connecting transitions have been identified between Band 8 and Band 9. The odd-spin cascade of Band 9 is connected by the 408- and 384-keV E2 transitions to Band 10, indicating that both bands have the same parity,

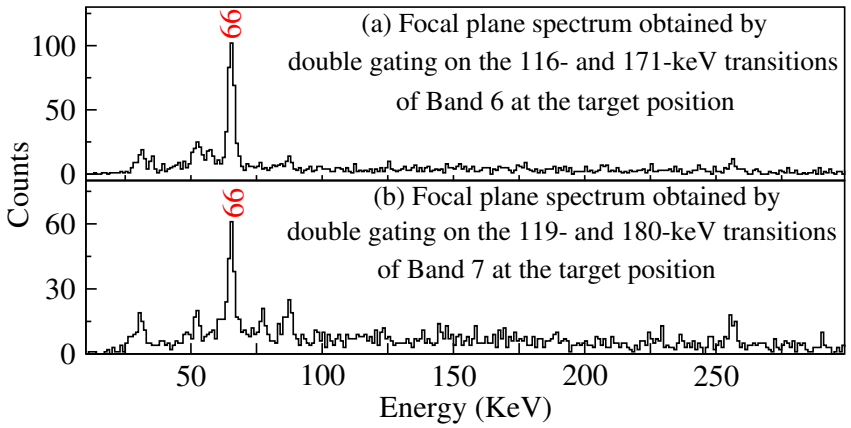

Figure 7.7: Prompt-delayed coincidence spectra for Bands 6 and 7. Peak energies for the newly identified transitions are in red.

which we assigned as negative parity. The 8^- state of Band 10 mainly decays to Band 8, while the two 198- and 298-keV transitions interconnect the odd- and even-spin states of the band. The spectra of Band 10 are shown in Fig. 7.6 (c) and (d) with signatures α =1 and 0, respectively.

7.3 Discussion

7.3.1 General considerations

The structure of the odd-odd nucleus ^{118}Cs is more complex than that of the odd-even neighboring nuclei ^{119}Cs and ^{119}Ba, on which detailed experimental information and theoretical interpretations have been discussed in Chapters 5 and 6. In the case of ^{118}Cs we should start from the two known long-lived isomers, one with half-life $T_{1/2} = 14(2)s$ and low spin $I = 2$, and one with half-life $T_{1/2} = 17(3)s$ and high spin $I = (6, 7, 8)$, which, however, have not experimentally established excitation energies and parities [164, 128]. The last NNDC evaluation of ^{118}Cs has been released long time ago, in 1995 [124], and consists of only one band, which was in fact wrongly assigned to ^{118}Cs [169]. This wrong assignment of a band in ^{118}I to ^{118}Cs has been already mentioned in Ref. [127], but not yet corrected on the ENSDF website.

As the excitation energies of the observed bands in ^{119}Cs and ^{119}Ba are comprised within 200 keV, the expected excitation energies of the bands in ^{118}Cs are also expected to be low, comprised within a few hundreds of keV. This expectation is also supported by the theoretical predictions of Ref. [4], in which the energies of the four low-lying isomers are calculated between 0 and 161 keV. However, as discussed above, not all bands observed in ^{118}Cs could be interconnected by γ rays, and therefore their relative excitation energies could not be established. This uncertainty also induces an inherent difficulty in the assignment of spins and parities to the observed bands. In following discussion we will only tentatively assign spins-parities and excitation energies to the observed bands.

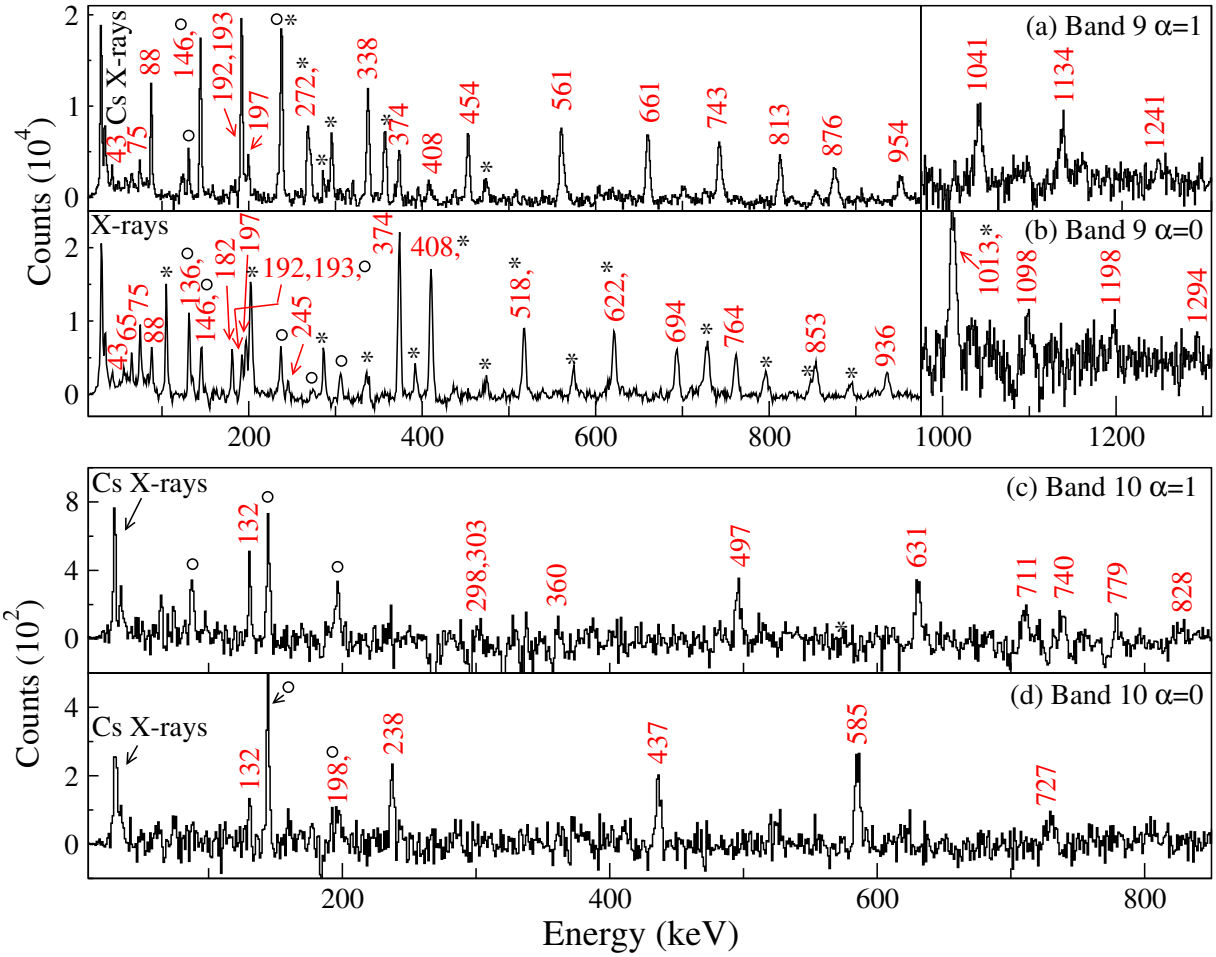

Figure 7.8: Double-gated spectra for Bands 6, 7 and 8 of ^{118}Cs. Peak energies for the newly identified are written with red color. Transitions from ^{118}Xe are indicated with an asterisk, while those from other bands in ^{118}Cs are indicated with a circle. The lists of gating transitions for each spectrum are the following: for Band 6 89, 142, 171, 200, 228 keV; for Band 7 79, 119, 152, 180, 214, 264 keV; for Band 8 88, 145, 193, 389, 505, 654 keV.

The present complex level scheme of ^{118}Cs can be viewed as consisting of several groups of bands. The first group consists of the strongly populated positive-parity Band 1, the weakly populated bands, and states decaying to it. It is built on top of the high-spin 7^+ isomer with a half-life $T_{1/2} = 0.55(6)$ μs, which we assume to decay through several transitions to the long-lived 7^-, $T_{1/2}$= 17(3) s isomer, assigned as band-head of Band 3. The second group consists of the well populated strongly-coupled Bands 3 and 4 composed of long cascades of strong dipole and crossover $E2$ transitions, and the weakly populated Band 5 which decays to Band 4. As no delayed transitions have been observed despite the strong population of these bands, one conclude that they are built on long-lived isomers, which can occur if the bands have low excitation energies, and/or have spin-parity that hinder their decay to low-spin states. To account for the missing interconnecting transitions between Bands 3 and 4, we assigned them opposite parities, negative to Band 3 and positive to Band 4, and band-head spin-parity 7^- and $(6^+, 4^+)$, respectively. The third group consists of Bands 6 and 7, which are composed of shorter sequences of dipole transitions than Bands 3 and 4, and weak crossover transitions. They decay via the delayed 66-keV transition that we placed above the

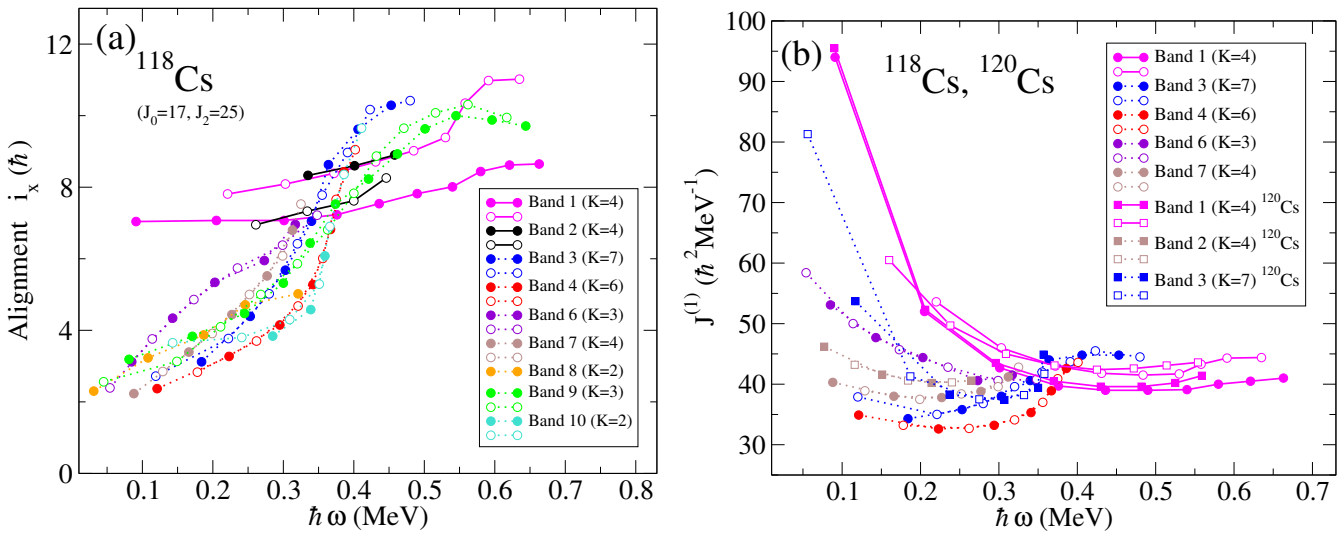

Figure 7.9: (a) Single-particle angular momenta i_x of all bands of ^{118}Cs. The Harris parameters are $J_0 = 17\ \hbar^2\text{MeV}^{-1}$ and $J_1 = 25\ \hbar^4\text{MeV}^{-3}$. The K values corresponding to the adopted band-heads of each band are also indicated. (b) Moments of inertia $J^{(1)}$ of all bands of ^{118}Cs and of ^{120}Cs [125]. For all figures, the positive-parity and negative-parity bands are drawn with continuous and dotted lines, respectively. The states with signature $\alpha = +1/2$ and $\alpha = -1/2$ are drawn with filled and open symbols, respectively.

assigned 2^- ground state, leading to spins and parities 3^- and 4^- for the band-heads of Bands 6 and 7, respectively. The fourth group consists of Bands 8, 9 and 10, which are interconnected by many transitions, and we place on top of the 2^- ground state. Therefore, these three bands have all tentatively assigned negative parity.

The spin assignment to the 8^+ band-head of the $\pi h_{11/2} \otimes \nu h_{11/2}$ band, which in ^{118}Cs is Band 1, was done based on systematics [168]. An alternative 10^+ assignment can result from the comparison with the reported level scheme of the neighboring ^{120}Cs nucleus [170]. However, this alternative assignment is not supported by the present results, which show the existence below the band-head of Band 1 of a $M1$ 69-keV transition in cascade with a delayed $E1$ 126-keV transition, leading to a long-lived isomer with excitation energy 195 keV lower than that of the band-head, to which we assign spin-parity 7^-. A 10^+ assignment to the band-head of Band 1 would lead to a $I^\pi = 9^-$ isomer, which does not correspond to any low-lying two-quasiparticle configuration, and also was not observed in any neighboring nucleus. We therefore give credit to the $I^\pi = 7^-$ assignment to the state populated by the 126-keV transition, which we identify with the $T_{1/2}$= 17(3) s isomer and we assign to the band-head of Band 3. This assignment gives therefore support to the $I = 8^+$ spin-parity for the band-head of Band 1.

The spins and parities of the other bands are based on the following alignment analysis and PNC-CSM calculations, and are therefore tentative.

7.3.2 Alignment analysis and configuration assignments

Single-particle angular momenta i_x as a function of the rotational frequency $\hbar\omega$ are shown in Fig. 7.9 (a). One can see that all bands except for Bands 1 and 2 exhibit i_x values below $\approx 3.5\ \hbar$ at low rotational frequencies, and alignment gains at rotational frequencies of $\hbar\omega \leq 0.35$ MeV. It results that in all bands except for Bands 1 and 2, at most one proton or one neutron occupies a $h_{11/2}$ orbital, leaving thus unblocked the $h_{11/2}$ alignment of one proton, of one neutron, or of both of them. The first alignment gains at $\hbar\omega \approx 0.4$ MeV can be induced by either $h_{11/2}$ protons or $h_{11/2}$ neutrons, depending on the deformation: for $\varepsilon_2 \approx 0.3$ the $h_{11/2}$ protons align first at $\hbar\omega \approx 0.35$ MeV, followed by $h_{11/2}$ neutrons which align at $\hbar\omega \approx 0.45$ MeV, whereas for a smaller deformation of $\varepsilon_2 \approx 0.25$ the opposite occurs, that is the $h_{11/2}$ neutrons align before the $h_{11/2}$ protons.

The alignment exhibited in Band 1 is around 7 $\hbar$, in agreement with the $\pi[541]3/2^- \otimes \nu[532]5/2^-$ configuration previously assigned in Ref. [127]. It does not show any alignment gain up to a rotational frequency of $\hbar\omega \approx 0.5$ MeV, indicating the blocking of both the $h_{11/2}$ proton and neutron alignments, and therefore indicating a configuration with the unpaired proton and unpaired neutron placed in $h_{11/2}$ orbitals. The alignment increases gradually up to $\hbar\omega \approx 0.5$ MeV, where gains of $\approx 2\hbar$ and $\approx 1\hbar$ in the $\alpha = 1$ and $\alpha = 0$ signature partners, respectively, are exhibited. These alignment gains have been attributed to $h_{11/2}$ neutrons in Ref. [127], but as discussed in the following section, the present calculations suggest that should be attributed to $h_{11/2}$ protons (see Fig. 7.10 (a)).

The alignments exhibited by the two signature partners of Band 2 are very similar to those of Band 1, suggesting a configuration similar to that of Band 1, that is $\pi[541]3/2^- \otimes \nu[532]5/2^-$.

The alignment of Band 3 is around 2.5 $\hbar$ at low frequency, exhibits an alignment gain of $\approx 8\ \hbar$ at $\hbar\omega \approx 0.35$ MeV, and saturates at $i_x \approx 10\ \hbar$ at high frequency. This alignment pattern indicates the blocking of a second $h_{11/2}$ alignment, and therefore excludes a configuration involving two positive-parity orbitals. It is very similar to that of Band 8 of ^{119}Cs, which has an excitation energy of 86 keV and $\pi g_{9/2}[404]9/2^+$ configuration, suggesting therefore the presence of the $\pi g_{9/2}[404]9/2^+$ proton orbital in its configuration, and keeping thus free the $\pi h_{11/2}$ proton orbital which induces the observed alignment gain. The unpaired neutron should be placed in the lowest negative-parity orbital $\nu h_{11/2}[532]5/2^-$, which generates Band 1 in the neighboring odd-even ^{119}Ba nucleus at an excitation energy of 66 keV. The coupling of these two orbitals leads to the $\pi g_{9/2}[404]9/2^+ \otimes \nu h_{11/2}[532]5/2^-$ configuration, which is expected to have a low excitation energy and we therefore assign to Band 3. The small alignment at low frequency of $i_x \approx 2.5\ \hbar$ is in agreement with the assigned configuration, since only the $\nu h_{11/2}[532]5/2^-$ neutron in the $h_{11/2}$ mid-shell orbital contributes to the alignment, the strongly coupled $\pi g_{9/2}[404]9/2^+$ proton having negligible alignment. As the $\nu[532]5/2^-$ orbital is occupied, the $h_{11/2}$ neutron alignment is blocked, and the alignment observed at $\hbar\omega \approx 0.3$ MeV is therefore due to a pair of $h_{11/2}$ protons.

The alignment exhibited by Band 4 is similar to that of Band 3, but occurs at a slightly higher frequency of $\hbar\omega \approx 0.35$ MeV. Despite the very similar alignment patterns, Bands 3 and 4 are not connected by any transition,

indicating very different configurations or transitions which are hindered due to high spin difference between the states of the two bands. This can occur if the unpaired proton is in the same high-Ω positive-parity $\pi g_{9/2}[404]9/2^+$ orbital as in Band 3, while the neutron is instead in a positive-parity orbital, leading to positive parity for Band 4, therefore opposite to that of Band 3, and leading to $E1$ or $M2$ connecting transitions that are hindered. The best agreement of the moment of inertia is obtained by involving the $\nu g_{7/2}[411]3/2^+$ orbital. The configuration of Band 4 can therefore be $\pi g_{9/2}[404]9/2^+ \otimes \nu g_{7/2}[411]3/2^+$, leading to a band-head spin 6^+. With this assignment both the $h_{11/2}$ proton and $h_{11/2}$ neutron alignments are unblocked. It is in agreement with the observed alignment which is sharper and does not show a saturation at high frequency like in the case of Band 3. An alternative configuration can be $\pi g_{9/2}[422]3/2^+ \otimes \nu d_{5/2}[413]5/2^+$, which leads to band-head spin 4^+. This alternative configuration has both the proton and neutron orbitals different from those of Band 3, can also account for the missing connecting transitions between Bands 3 and 4.

Bands 6 and 7 exhibit smooth up-bands with stepper slopes than in the other bands, are composed of degenerate signature partners, and are not connected by any transition. The near degeneracy of the signature partners in both bands strongly suggest the occupation of high-Ω orbitals. Possible configurations have been investigated, and the best agreements have been obtained for the $\pi[541]3/2^- \otimes \nu[411]3/2^+$ for Band 6 leading to band-head spin-parity 3^-, and $\pi[422]3/2^+ \otimes \nu[532]5/2^-$ for Band 7 leading to band-head spin-parity 4^-.

Bands 8, 9 and 10 are interconnected by several transitions, leading to the same parity for all three bands, which we assigned as negative. The alignment exhibited by Bands 8 and 9 are similar, but more gradual than those of Bands 3 and 4. An alignment gain of $\approx 7\ \hbar$ at $\hbar\omega \approx 0.35$ MeV is exhibited, which saturates at high frequency at $i_x \approx 10\hbar$, like in Band 3, and therefore should be due to the alignment of $h_{11/2}$ protons. There are two positive-parity proton orbitals, $\pi[420]1/2^+$ and $\pi[422]3/2^+$, that can be coupled with a neutron in the $\nu[532]5/2^-$ for Bands 8, 9 and 10, which are $\pi[420]1/2^+ \otimes \nu[532]5/2^-$ and $\pi[422]3/2^+ \otimes \nu[532]5/2^-$, with favored (unfavored) band-head spins given by GM rule as 3^- (2^-) and 1^- (4^-), respectively.

Bands 8 and 9 being connected by strong transitions and having a similar alignment, can be based on the GM partners of the same $\pi[420]1/2^+ \otimes \nu[532]5/2^-$ configuration, with $K = 2$ and $K = 3$, respectively. Band 10 can have the same $\pi[422]3/2^+ \otimes \nu[532]5/2^-$ configuration as Band 7, but built on $K = 1$ GM partner, which is in agreement with its lower alignment than that of Band 7.

7.3.3 PNC-CSM calculations

In order to investigate the possible configurations of the observed bands we performed PNC-CSM calculations. However, we do not discuss the γ band which cannot be described by the PNC-CSM calculations, and the very weakly populated Band 5 which has tentative spins and parity assignments. Single-particle Routhian diagrams as function of rotational frequency for prolate deformation are shown in Fig. 5.16 (a). They were used to guide the

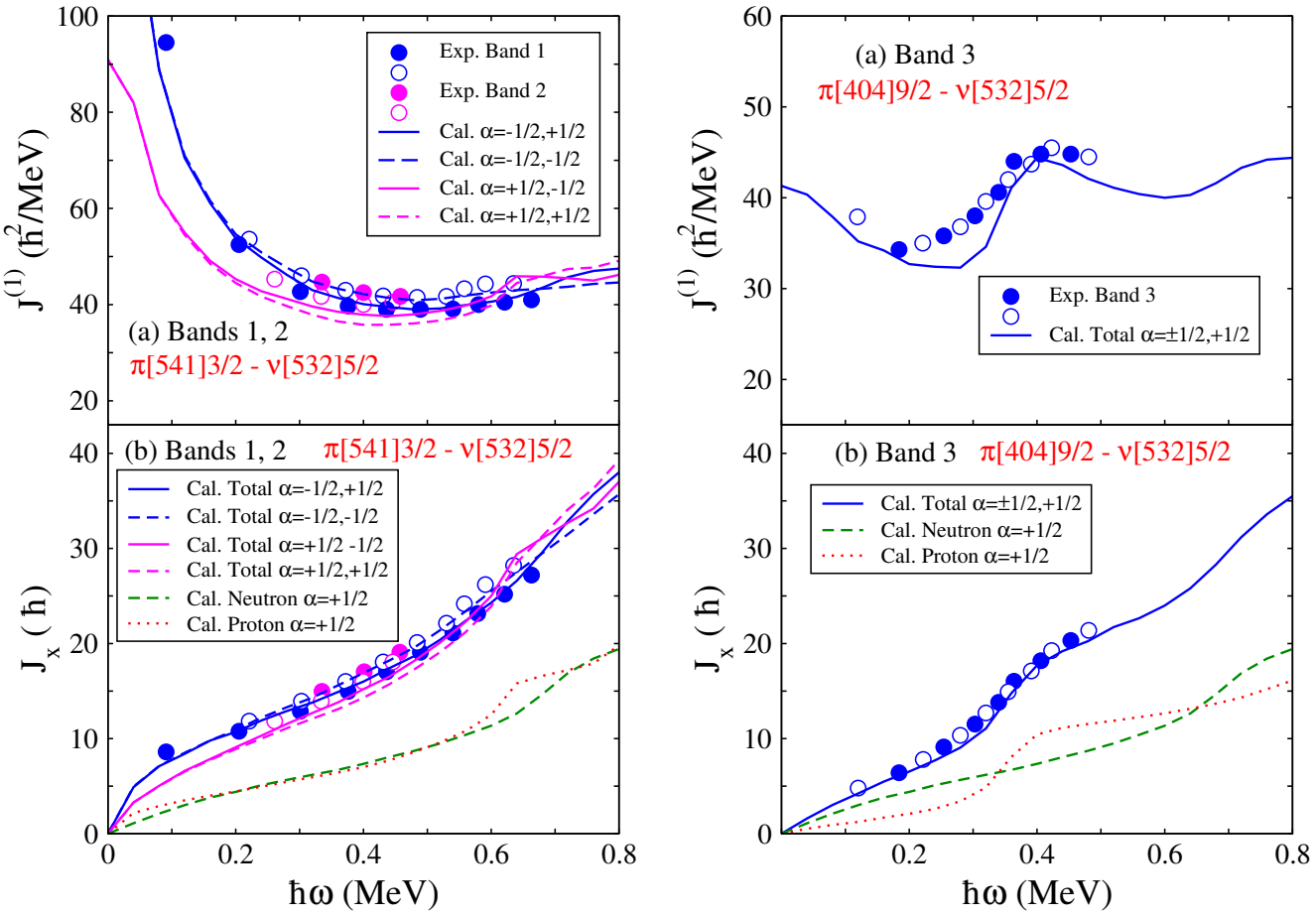

Figure 7.10: (a) Moment of inertia $J^{(1)}$, (b) projection of the angular momentum on the cranking axis J_x for the $\pi[541]3/2^-(\alpha = -1/2) \otimes \nu[532]5/2^-$ configuration assigned to Bands 1 and 2 of ^{118}Cs based on the PNC-CSM calculations for a deformation of $\varepsilon_2 = 0.32$. (c) Moment of inertia $J^{(1)}$, (d) projection of the angular momentum on the cranking axis J_x for the Band 3 assigned the configuration $\pi[404]9/2^+ \otimes \nu[532]5/2^-$. The states with signature $\alpha = +1/2$ and $\alpha = -1/2$ are drawn with filled and open symbols, respectively. The signatures of the proton and neutron orbitals involved in each configuration are also indicated.

search of the closest quasiparticle orbitals to the proton and neutron Fermi surfaces.

The moments of inertia for similar bands observed in ^{118}Cs and ^{120}Cs [125] are shown for comparison in Fig. 7.9 (b). Bands with very similar pattern in both nuclei, which indicate similar configurations. In ^{118}Cs we identified two more bands than in ^{120}Cs, which are Bands 4 and 6.

We performed PNC-CSM calculations for all configurations involving proton and neutron orbitals close to the Fermi surfaces. In the configuration assignment process we took into account the alignment properties discussed in the preceding section, the relative intensities and decay properties of the bands, as well as the systematics of both odd-even and odd-odd nuclei in the region. We adopted an axial deformation with $\varepsilon_2 = 0.32$, similar to that used for ^{119}Cs and ^{119}Ba. The results are presented in Figs. 7.10 -7.12.

One can see in Fig. 7.10 (a) that Bands 1 and 2 are well reproduced by the same $\pi[541]3/2^- \otimes \nu[532]5/2^-$ configuration, involving the $\alpha = -1/2$ and $\alpha = +1/2$ signature partners of the $\pi[541]3/2^-$ orbital in Band 1 and

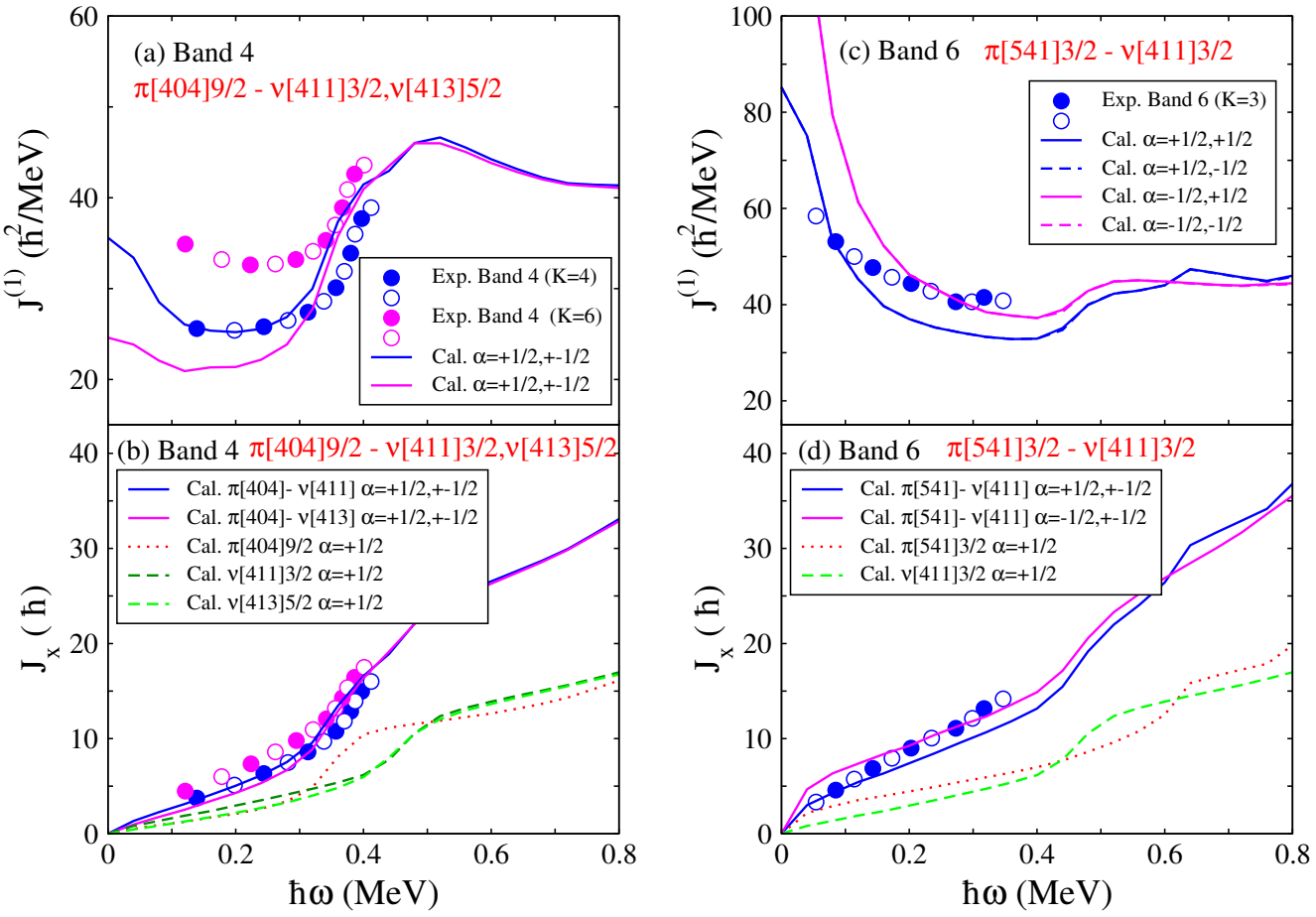

Figure 7.11: (a) Moment of inertia $J^{(1)}$, (b) projection of the angular momentum on the cranking axis J_x for the $\pi[404]9/2^+ \otimes \nu[411]3/2^+$ and $\pi[404]9/2^+ \otimes \nu[413]5/2^+$ configuration assigned to Band 4 of ^{118}Cs based on the PNC-CSM calculations for a deformation of $\varepsilon_2 = 0.32$. (c) Moment of inertia $J^{(1)}$, (d) projection of the angular momentum nn the cranking axis J_x for the Band 6 assigned the configuration $\pi[541]3/2^- \otimes \nu[411]3/2^+$. The states with signature $\alpha = +1/2$ and $\alpha = -1/2$ are drawn with filled and open symbols, respectively. The signatures of the proton and neutron orbitals involved in each configuration are also indicated.

Band 2, respectively. The first proton and neutron $h_{11/2}$ alignments being blocked, the calculated J_x increases smoothly up to high frequencies of $\hbar\omega \approx 0.6$ MeV, where the second proton and second neutron alignments occur. The calculated spin aligned along the rotation axis J_x for Band 2 is slightly lower than that of Band 1, which is in disagreement with the experiment, pointing to a slightly smaller deformation of Band 2, like in the case of Band 2 of ^{119}Cs which is built on the $\pi[541]3/2^-(\alpha = -1/2)$ orbital.

The configurations assigned to Bands 3 and 4 are based on their alignment pattern, which is similar to that of the Band 8 of ^{119}Cs which is built on the $\pi[404]9/2^+$ orbital (see Figs. 7.10, 7.11). It is well reproduced over the entire observed frequency range, while the increase of the moment of inertia at $\hbar\omega \approx 0.35$ MeV is calculated a bit more rapid than the observed one. The configuration assigned to Band 4 involves the same $\pi[404]9/2^+$ proton orbital as in Band 3, which can be coupled to either the $\nu[411]3/2^+$ or $\nu[413]5/2^+$ positive-parity neutron orbitals to obtain the observed increase of the moment of inertia at $\hbar\omega \approx 0.35$ MeV. The alignment gain is equally well reproduced by the

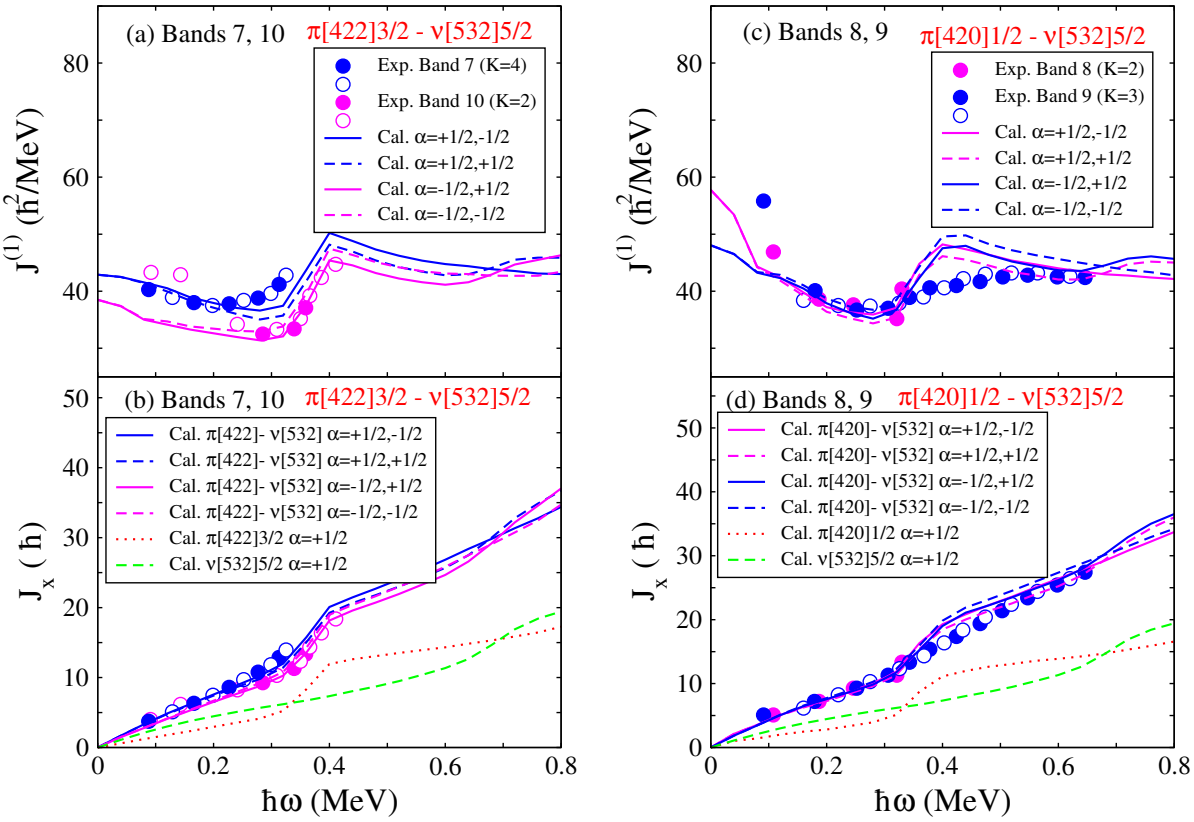

Figure 7.12: (a) Moment of inertia $J^{(1)}$, (b) projection of the angular momentum on the cranking axis J_x for the $\pi[422]3/2^+ \otimes \nu[532]5/2^-$ configuration assigned to Bands 7 and 10 of ^{118}Cs based on the PNC-CSM calculations for a deformation of $\varepsilon_2 = 0.32$. (c) Moment of inertia $J^{(1)}$, (d) projection of the angular momentum nn the cranking axis J_x for the Bands 8 and 9 assigned the configuration $\pi[420]1/2^+ \otimes \nu[532]5/2^-$. The states with signature $\alpha = +1/2$ and $\alpha = -1/2$ are drawn with filled and open symbols, respectively. The signatures of the proton and neutron orbitals involved in each configuration are also indicated.

two alternative configurations, being induced by $h_{11/2}$ protons. The coupling with the $\nu[413]5/2^+$ orbital reproduce better the observed pattern. However, we prefer to assign the $\pi[404]9/2^+ \otimes \nu[411]3/2^+$ configuration to Band 4, because the present PNC-CSM calculations cannot well reproduce the moments of inertia of the positive-parity neutron orbitals, as in the case of ^{119}Ba.

Bands 6 and 7 have a behavior which is quite different from that of Bands 3 and 4, presenting weaker crossover transitions, starting and ending at lower frequencies, and being in delayed coincidence with the 66-keV transition which can be placed above the ground state to which we assigned spin-parity $I^\pi = 2^-$. It is therefore natural to assume lower band-head spins than Bands 3 and 4. In addition, Band 6 has a moment of inertia which decreases with increasing rotational frequency, like Band 1, suggesting the occupation of the $\pi[541]3/2^-$ orbital (see Fig. 7.11). In fact, only configurations involving the $\pi[541]3/2^-$ orbital have calculated moments of inertia in qualitative agreement with Band 6, and the best agreement is obtained by involving the $\alpha = -1/2$ signature partner. We therefore assign the $\pi[541]3/2^-(\alpha = -1/2) \otimes \nu[411]3/2^+$ configuration to Band 6. The missing connecting transitions

between Band 6 and 7, as well as their delayed coincidence with the 66-keV transition, suggest opposite parities and similar band-head spins. A qualitative good agreement for Band 7 is obtained for the $\pi[422]3/2^+ \otimes \nu[532]5/2^-$ configuration (see Fig. 7.12).

Bands 8, 9 and 10 are interconnected by several transitions, which fix the relative energies, the spins, the same parity, and also indicate significant mixing. The bands exhibit alignments which saturates at values around $i_x \approx 10$ $\hbar$, indicating the alignment of only one pair of $h_{11/2}$ nucleons. As the behavior of the moments of inertia is very different for configurations involving $h_{11/2}$ protons like those of Bands 1 and 6, and are similar to those involving $h_{11/2}$ neutrons like in Band 3 and 7, we are induced to choose configurations involving the negative-parity $\nu[532]5/2^-$ neutron orbital. As one can see in Fig. 7.12 (a), Band 10 is very well reproduced by the $\pi[422]3/2^+ \otimes \nu[532]5/2^-$ configuration, which is is similar to that assigned to Band 7, but involves the $\pi[422]3/2^+(\alpha = +1/2)$ orbital with opposite signature. Bands 7 and 10 can therefore be GM partners with $K = 4$ and $K = 1$, respectively. The assigned configurations to Bands 7 to 10 involve $\pi[422]3/2^+$ and $\nu[532]5/2^-$ orbitals, which have non-degenerate signature partners, while the experimental signature splitting in the two bands is very small. This can be due to axial asymmetry and/or significant interaction between the bands, which are not taken into $\nu[532]5/2^-$ account in the present calculations. In addition, it is supposed that other potentials, like Wood-Saxon, can reproduce better the properties of the bands.

Bands 8 and 9 can involve the $\pi[420]1/2^+$ orbital, for which the agreement is not as good as for the other bands, but qualitatively acceptable, see Fig. 7.12 (c). The coupling with the $\nu[532]5/2^-$ orbital leads to the $\pi[420]1/2^+ \otimes \nu[532]5/2^-$ configuration, with GM partners with $K = 2$ and $K = 3$, which are in agreement with the band heads of Bands 8 and 9, respectively. The presence of the low-Ω $\pi[420]1/2^+$ orbital leads to significant Coriolis mixing between the two bands, and can explain the strong interconnecting transitions. However, as one can see in Fig. 7.12 (c), the present calculations cannot reproduce the smooth up-bending in Band 9. This may be due to a stronger interaction between the two- quasiparticle band and the four-quasiparticle band than in other bands in the backbending regine, and should be further inverstigated in the future.

7.4 Conclusion

The present work reports one of the most complete level schemes from low to high spin in odd-odd proton-rich cesium nuclei. Ten new bands have been identified in the odd-odd ^{118}Cs nucleus. Four new isomers have also been identified, with very different half-lives, one in the nanosecond range, two in the microsecond range, and one with much longer half-life. The analysis of the alignment properties combined with the results of extensive PNC-CSM calculations, led to a global good understanding of the bands structures. The present results constitute a unique set of spectroscopic information which can be used to test state-of-the-art theoretical models aiming to describe strongly-deformed proton-rich lanthanide nuclei.

Table 7.1: Experimental information including the γ-ray energies E_γ, energies of the initial levels E_i, relative intensities I_γ, anisotropies R_{DCO} and/or R_{ac}, parameter a_2, parameter a_4, polarization asymmetries A, mixing ratios δ, multipolarities, and the spin-parity assignments to the observed states in ^{118}Cs. The transitions listed with increasing energy are grouped in bands.

E_γ (keV)[a]	E_i (keV)	I_γ^b	R_{DCO}^c	R_{ac}^d	a_2	a_4	A	δ	Mult.	$J_i^\pi \rightarrow J_f^\pi$
Band 1										
132.3	x+833.3	35(8)	0.5(2)[e]						$M1/E2$	$(12^+) \rightarrow (11^+)$
200.1	x+395.1	1000	0.87(9)[e]				0.14(3)		$E2$	$(10^+) \rightarrow (8^+)$
298.3	x+1465.4	6(4)							$(M1/E2)$	$(14^+) \rightarrow (13^+)$
305.2	x+700.3	210(25)	0.43(7)[e]		-0.70(10)	0.22(18)	-0.08(4)		$M1/E2$	$(11^+) \rightarrow (10^+)$
308.2	x+3449.9	13(4)							$(M1/E2)$	$(19^+) \rightarrow (18^+)$
320.3	x+2565.6	28(5)		0.9(3)					$M1/E2$	$(17^+) \rightarrow (16^+)$
333.3	x+1797.7	150(35)		0.67(8)			-0.05(1)		$M1/E2$	$(15^+) \rightarrow (14^+)$
334.2	x+1167.4	240(65)		0.67(8)					$M1/E2$	$(13^+) \rightarrow (12^+)$
438.2	x+833.3	780(25)	1.11(6)[e]				0.10(1)		$E2$	$(12^+) \rightarrow (10^+)$
467.0	x+1167.4	100(15)	1.1(3)[e]						$E2$	$(13^+) \rightarrow (11^+)$
629.5	x+1797.7	170(45)	1.0(2)[e]						$E2$	$(15^+) \rightarrow (13^+)$
632.1	x+1465.4	380(45)	1.0(2)[e]				0.08(3)		$E2$	$(14^+) \rightarrow (12^+)$
767.9	x+2565.6	130(20)	1.0(3)[e]						$E2$	$(17^+) \rightarrow (15^+)$
780.0	x+2245.4	190(40)	1.0(3)[e]	1.4(2)					$E2$	$(16^+) \rightarrow (14^+)$
884.5	x+3449.9	80(16)		1.3(2)					$E2$	$(19^+) \rightarrow (17^+)$
896.0	x+3141.4	80(16)	1.1(4)[e]						$E2$	$(18^+) \rightarrow (16^+)$
987.8	x+4437.7	90(20)		1.3(2)					$E2$	$(21^+) \rightarrow (19^+)$
1001.0	x+4142.5	50(10)		1.5(3)					$E2$	$(20^+) \rightarrow (18^+)$
1076.4	x+5514.1	36(10)		1.3(4)					$E2$	$(23^+) \rightarrow (21^+)$
1098.4	x+5240.9	22(6)		1.5(7)					$E2$	$(22^+) \rightarrow (20^+)$
1131.0	x+6645.1	21(9)		1.5(5)					$E2$	$(25^+) \rightarrow (23^+)$
1177.1	x+6418.0	6(3)							$(E2)$	$(24^+) \rightarrow (22^+)$
1195.3	x+7840.4	3(2)							$(E2)$	$(27^+) \rightarrow (25^+)$
1220.7	x+8015.8	3(2)							$(E2)$	$(27^+) \rightarrow (25^+)$
1257.2	x+7675.2	2(1)							$(E2)$	$(26^+) \rightarrow (24^+)$
1281.0	x+6795.1	5(4)							$(E2)$	$(25^+) \rightarrow (23^+)$
1283.0	x+9123.4	2(1)							$(E2)$	$(29^+) \rightarrow (27^+)$
1296.0	x+9311.8	1(1)							$(E2)$	$(29^+) \rightarrow (27^+)$
1338.9	x+9014.1	1(1)							$(E2)$	$(28^+) \rightarrow (26^+)$
Transitions depopulating the isomeric states (8^+) **and** (7^+)										
69.3	x+195	33(9)							$(M1/E2)$	$(8^+) \rightarrow (7^+)$
46.3	x+125.7									$(7^+) \rightarrow$
61.4	x+61.4									$(7^+) \rightarrow$
64.7	x+125.7									$\rightarrow (7^-)$
79.0	x+79.0									$\rightarrow (7^-)$
126.0	x+125.7								$(E1)$	$(7^+) \rightarrow (7^-)$
Band γ										
620.2	x+1873.8	10(5)								
Band $\gamma \rightarrow$ **Band 1**										
553.3	x+1253.6	18(8)								$\rightarrow (11^+)$
708.0	x+1875.4	11(6)								$\rightarrow (13^+)$
735.4	x+1568.7	17(8)								$\rightarrow (12^+)$
796.2	x+1963.6	11(6)								$\rightarrow (13^+)$
872.8	x+1706.1	17(9)								$\rightarrow (12^+)$
902.5	x+2069.9	5(2)								$\rightarrow (13^+)$
980.3	x+1680.6	6(2)								$\rightarrow (11^+)$
1016.2	x+1849.5	10(5)								$\rightarrow (12^+)$
1108.0	x+1808.0	6(3)								$\rightarrow (11^+)$
Band 2										
550.8	x+1614.5	3(2)							$(E2)$	$(13^+) \rightarrow (11^+)$
693.3	x+2737.3	10(3)							$(E2)$	$(16^+) \rightarrow (14^+)$
695.0	x+2309.5	4(2)							$(E2)$	$(15^+) \rightarrow (13^+)$
824.0	x+3133.5	8(6)							$(E2)$	$(17^+) \rightarrow (15^+)$
824.8	x+3562.3	19(7)							$(E2)$	$(18^+) \rightarrow (16^+)$
913.5	x+4047.0	5(4)							$(E2)$	$(19^+) \rightarrow (17^+)$
937.8	x+4500.1	10(5)							$(E2)$	$(20^+) \rightarrow (18^+)$
Band 2 $\rightarrow$ **Band 1**										
229.5	x+1062.8	6(2)							$(M1/E2)$	$(11^+) \rightarrow (12^+)$
667.6	x+1062.8	7(3)							$(M1/E2)$	$(11^+) \rightarrow (10^+)$
781.5	x+1614.5	12(4)							$(M1/E2)$	$(13^+) \rightarrow (12^+)$
844.1	x+2309.5	12(9)							$(M1/E2)$	$(15^+) \rightarrow (14^+)$
877.3	x+2044.7	34(9)							$(M1/E2)$	$(14^+) \rightarrow (13^+)$
939.3	x+2737.3	22(15)							$(M1/E2)$	$(16^+) \rightarrow (15^+)$

Table 7.1 (*Continued.*)

E_γ (keV)[a]	E_i (keV)	I_γ^b	R_{DCO}^c	R_{ac}^d	a_2	a_4	A	δ	Mult.	$J_i^\pi \rightarrow J_f^\pi$
997.0	x+3562.3	13(4)							$(M1/E2)$	$(18^+) \rightarrow (17^+)$
Band 3										
182.9	x+182.9	450(70)	1.2(2)[f]	0.91(5)	-0.15(9)	0.31(17)	-0.03(2)	0.10(35)	$M1/E2$	$(8^-) \rightarrow (7^-)$
265.5	x+448.4	280(50)	1.0(2)[f]	0.9(1)	-0.18(2)	0.10(2)	-0.2(1)	0.00(20)	$M1/E2$	$(9^-) \rightarrow (8^-)$
288.3	x+736.7	150(26)	1.0(2)[f]	0.74(8)	-0.00(30)	0.11(57)	-0.3(2)	0.10(20)	$M1/E2$	$(10^-) \rightarrow (9^-)$
310.5	x+1047.3	90(18)	0.9(1)[f]	1.0(2)					$M1/E2$	$(11^-) \rightarrow (10^-)$
330.8	x+1378.5	68(14)	1.1(2)[f]	1.0(2)					$M1/E2$	$(12^-) \rightarrow (11^-)$
347.9	x+1726.4	45(9)		0.7(2)					$M1/E2$	$(13^-) \rightarrow (12^-)$
362.6	x+2089.1	27(6)		0.9(3)					$M1/E2$	$(14^-) \rightarrow (13^-)$
370.0	x+2459.2	11(3)		1.0(4)					$M1/E2$	$(15^-) \rightarrow (14^-)$
392.4	x+3245.6	10(3)							$(M1/E2)$	$(17^-) \rightarrow (16^-)$
394.2	x+2853.7	7(2)							$(M1/E2)$	$(16^-) \rightarrow (15^-)$
405.1	x+3651.4	3(2)							$(M1/E2)$	$(18^-) \rightarrow (17^-)$
448.6	x+448.4	16(5)							$(E2)$	$(9^-) \rightarrow (7^-)$
554.5	x+736.7	27(7)		1.3(5)					$E2$	$(10^-) \rightarrow (8^-)$
599.2	x+1047.3	46(9)		1.5(4)					$E2$	$(11^-) \rightarrow (9^-)$
642.4	x+1378.5	45(9)		1.2(3)					$E2$	$(12^-) \rightarrow (10^-)$
679.1	x+1726.4	50(10)	1.6(5)[f]	1.2(3)					$E2$	$(13^-) \rightarrow (11^-)$
710.6	x+2089.1	36(7)		1.3(3)					$E2$	$(14^-) \rightarrow (12^-)$
732.8	x+2459.2	25(5)		1.4(3)					$E2$	$(15^-) \rightarrow (13^-)$
764.6	x+2853.7	19(9)		1.6(8)					$E2$	$(16^-) \rightarrow (14^-)$
785.3	x+3245.6	5(4)							$(E2)$	$(17^-) \rightarrow (15^-)$
797.7	x+3651.4	7(2)							$(E2)$	$(18^-) \rightarrow (16^-)$
844.3	x+4088.8	8(3)							$(E2)$	$(19^-) \rightarrow (17^-)$
869.9	x+4521.3	7(3)							$(E2)$	$(20^-) \rightarrow (18^-)$
899.6	x+4988.4	3(2)							$(E2)$	$(21^-) \rightarrow (19^-)$
959.4	x+5480.7	2(1)							$(E2)$	$(22^-) \rightarrow (20^-)$
1011.9	x+6000.3	1(1)							$(E2)$	$(23^-) \rightarrow (21^-)$
Band 4										
192.6	y+192.6	550(150)	0.93(7)[f]	0.86(4)	-0.22(7)	0.14(12)		0.00(20)	$M1/E2$	$(7^+) \rightarrow (6^+)$
236.4	y+429.1	525(100)	1.11(7)[f]	0.82(3)	-0.22(5)	0.08(10)	-0.02(1)	0.00(15)	$M1/E2$	$(8^+) \rightarrow (7^+)$
274.6	y+703.8	300(50)	1.11(9)[f]	0.85(4)	-0.11(18)	0.06(34)	-0.07(2)	0.10(10)	$M1/E2$	$(9^+) \rightarrow (8^+)$
307.0	y+1011.1	250(50)	0.97(9)[f]	0.89(5)	-0.12(6)	0.23(11)	-0.02(1)	0.10(25)	$M1/E2$	$(10^+) \rightarrow (9^+)$
335.3	y+1346.1	180(35)	1.0(2)[f]	0.87(5)	-0.38(6)	-0.00(10)		-0.10(15)	$M1/E2$	$(11^+) \rightarrow (10^+)$
358.5	y+1704.5	70(14)	1.1(1)[f]	0.9(3)					$M1/E2$	$(12^+) \rightarrow (11^+)$
374.9	y+2079.8	32(9)		0.8(2)					$M1/E2$	$(13^+) \rightarrow (12^+)$
387.9	y+2467.6	22(6)		1.0(3)					$M1/E2$	$(14^+) \rightarrow (13^+)$
395.1	y+2863.2	21(5)		0.9(4)					$M1/E2$	$(15^+) \rightarrow (14^+)$
401.8	y+3263.9	8(2)		0.9(5)					$M1/E2$	$(16^+) \rightarrow (15^+)$
405.3	y+3669.9	6(2)							$(M1/E2)$	$(17^+) \rightarrow (16^+)$
418.4	y+4087.1	4(2)							$(M1/E2)$	$(18^+) \rightarrow (17^+)$
430.0	y+4518.8	5(3)							$(M1/E2)$	$(19^+) \rightarrow (18^+)$
430.0	y+429.1	60(20)	1.7(8)[f]						$E2$	$(8^+) \rightarrow (6^+)$
511.7	y+703.8	60(10)	2.0(5)[f]				0.12(6)		$E2$	$(9^+) \rightarrow (7^+)$
582.7	y+1011.1	110(20)	1.6(5)[f]	1.35(8)					$E2$	$(10^+) \rightarrow (8^+)$
641.8	y+1346.1	100(20)	2.0(4)[f]				0.05(3)		$E2$	$(11^+) \rightarrow (9^+)$
693.3	y+1704.5	110(30)	1.2(4)[e]				0.07(2)		$E2$	$(12^+) \rightarrow (10^+)$
733.8	y+2079.8	83(17)	0.8(2)[e]	1.4(1)					$E2$	$(13^+) \rightarrow (11^+)$
763.1	y+2467.6	90(20)	1.1(5)[e]	1.4(2)					$E2$	$(14^+) \rightarrow (12^+)$
783.6	y+2863.2	56(11)		1.4(2)					$E2$	$(15^+) \rightarrow (13^+)$
796.3	y+3263.9	53(12)	1.3(5)[e]	1.4(2)					$E2$	$(16^+) \rightarrow (14^+)$
806.7	y+3669.9	42(10)		1.3(2)					$E2$	$(17^+) \rightarrow (15^+)$
823.2	y+4087.1	30(8)		1.5(3)					$E2$	$(18^+) \rightarrow (16^+)$
848.9	y+4518.8	28(7)		1.2(3)					$E2$	$(19^+) \rightarrow (17^+)$
Band 5										
113.5	y+1671.5	5(3)							$(M1/E2)$	$(11^+) \rightarrow (10^+)$
336.0	y+2355.8	5(3)							$(M1/E2)$	$(13^+) \rightarrow (12^+)$
348.8	y+2020.1	9(4)							$(M1/E2)$	$(12^+) \rightarrow (11^+)$
640.9	y+2661.0	9(5)							$(E2)$	$(14^+) \rightarrow (12^+)$
684.3	y+2355.8	26(10)		1.4(5)					$E2$	$(13^+) \rightarrow (11^+)$
743.2	y+3099.0	10(6)							$(E2)$	$(15^+) \rightarrow (13^+)$
814.0	y+3913.0	5(4)							$(E2)$	$(17^+) \rightarrow (15^+)$
Band 5→ Band 4										
651.6	y+2355.8	12(5)							$(M1/E2)$	$(13^+) \rightarrow (12^+)$
660.4	y+1671.5	34(13)		0.9(3)					$M1/E2$	$(11^+) \rightarrow (10^+)$
674.0	y+2020.1	16(7)							$(M1/E2)$	$(12^+) \rightarrow (11^+)$
852.3	y+1556.1	10(6)							$(M1/E2)$	$(10^+) \rightarrow (9^+)$
931.2	y+1360.3	17(5)							$(M1/E2)$	$(9^+) \rightarrow (8^+)$
Band 6										
62.6	128.8	20(10)		0.9(5)					$M1/E2$	$(4^-) \rightarrow (3^-)$

Table 7.1 (*Continued.*)

E_γ (keV)[a]	E_i (keV)	I_γ^b	R_{DCO}^c	R_{ac}^d	a_2	a_4	A	δ	Mult.	$J_i^\pi \rightarrow J_f^\pi$
89.1	217.9	60(20)		0.63(9)	-0.93(4)	0.32(6)		-1.6(3) or -0.4(3)	$M1/E2$	$(5^-) \rightarrow (4^-)$
115.9	333.8	80(20)	0.9(4)[f]	0.91(5)	-0.52(19)	0.31(7)		-3.6(13) or -0.1(5)	$M1/E2$	$(6^-) \rightarrow (5^-)$
141.8	475.7	80(20)		0.63(9)	-0.49(10)	0.29(17)		-4.0(16) or -0.1(4)	$M1/E2$	$(7^-) \rightarrow (6^-)$
171.4	647.1	50(20)	0.8(4)[f]	0.91(5)					$M1/E2$	$(8^-) \rightarrow (7^-)$
199.5	846.6	45(15)		0.73(9)					$M1/E2$	$(9^-) \rightarrow (8^-)$
227.8	1074.4	30(10)	0.8(4)[f]	0.7(2)					$M1/E2$	$(10^-) \rightarrow (9^-)$
258.3	475.7	10(5)							$(E2)$	$(7^-) \rightarrow (5^-)$
261.7	1336.4	8(3)							$(M1/E2)$	$(11^-) \rightarrow (10^-)$
303.2	1639.6	7(3)							$(M1/E2)$	$(12^-) \rightarrow (11^-)$
311.6	1951.3	5(3)							$(M1/E2)$	$(13^-) \rightarrow (12^-)$
312.8	647.1	4(3)							$(E2)$	$(8^-) \rightarrow (6^-)$
339.0	2290.3	4(3)							$(M1/E2)$	$(14^-) \rightarrow (13^-)$
370.8	846.6	6(4)							$(E2)$	$(9^-) \rightarrow (7^-)$
374.0	2664.3	3(2)							$(M1/E2)$	$(15^-) \rightarrow (14^-)$
427.8	1074.4	3(2)							$(E2)$	$(10^-) \rightarrow (8^-)$
490.7	1336.4	3(2)							$(E2)$	$(11^-) \rightarrow (9^-)$
615.3	1951.3	2(1)							$(E2)$	$(13^-) \rightarrow (11^-)$
Transition depopulating the isomeric band-head 3^- of Band 6										
65.9	65.9								$(E1)$	$(3^-) \rightarrow (2^-)$
Levels populating the 9^-, 10^- and 11^- states of Band 6										
248.3	1094.9	5(4)								$\rightarrow (9^-)$
254.5	1348.7	3(2)								$\rightarrow (10^-)$
274.0	1348.7	14(6)								$\rightarrow (10^-)$
502.5	1348.7	9(5)								$\rightarrow (9^-)$
Band 7										
118.8	263.7	60(23)		0.7(1)					$M1/E2$	$(5^-) \rightarrow (4^-)$
152.0	415.7	50(20)	1.3(5)[f]	0.80(9)					$M1/E2$	$(6^-) \rightarrow (5^-)$
180.4	596.1	45(14)		0.74(8)					$M1/E2$	$(7^-) \rightarrow (6^-)$
213.5	809.6	30(10)		0.9(1)					$M1/E2$	$(8^-) \rightarrow (7^-)$
238.3	1047.9	25(9)		0.9(2)					$M1/E2$	$(9^-) \rightarrow (8^-)$
263.9	1311.8	17(7)		0.8(3)					$M1/E2$	$(10^-) \rightarrow (9^-)$
282.7	1594.5	9(3)							$(M1/E2)$	$(11^-) \rightarrow (10^-)$
310.2	1904.7	4(2)							$(M1/E2)$	$(12^-) \rightarrow (11^-)$
320.8	2225.9	2(1)							$(M1/E2)$	$(13^-) \rightarrow (12^-)$
333.0	596.1	10(6)							$(E2)$	$(7^-) \rightarrow (5^-)$
334.1	2560.3	1(1)							$(M1/E2)$	$(14^-) \rightarrow (13^-)$
342.5	2902.4	1(1)							$(M1/E2)$	$(15^-) \rightarrow (14^-)$
394.9	809.6	3(2)							$(E2)$	$(8^-) \rightarrow (6^-)$
452.3	1047.9	5(3)							$(E2)$	$(9^-) \rightarrow (7^-)$
502.8	1311.8	6(3)							$(E2)$	$(10^-) \rightarrow (8^-)$
547.3	1594.5	2(1)							$(E2)$	$(11^-) \rightarrow (9^-)$
592.8	1904.7	2(1)							$(E2)$	$(12^-) \rightarrow (10^-)$
631.8	2225.9	2(1)							$(E2)$	$(13^-) \rightarrow (11^-)$
655.9	2560.3	1(1)							$(E2)$	$(14^-) \rightarrow (12^-)$
676.0	2902.4	1(1)							$(E2)$	$(15^-) \rightarrow (13^-)$
Band 7 $\rightarrow$ Band 6										
79.0	144.9	30(20)		0.79(8)					$M1/E2$	$(4^-) \rightarrow (3^-)$
Band 8										
233.3	312.6	30(10)							$(E2)$	$(6^-) \rightarrow (4^-)$
388.9	701.3	6(3)							$(E2)$	$(8^-) \rightarrow (6^-)$
504.5	1205.8	5(3)							$(E2)$	$(10^-) \rightarrow (8^-)$
653.9	1859.7	4(3)							$(E2)$	$(12^-) \rightarrow (10^-)$
669.0	2528.7	2(2)							$(E2)$	$(14^-) \rightarrow (12^-)$
Band 8 $\rightarrow$ Band 9										
36.7	79.4	30(20)							$(M1/E2)$	$(4^-) \rightarrow (3^-)$
145.0	312.6	90(30)		0.8(2)					$M1/E2$	$(6^-) \rightarrow (5^-)$
195.8	701.3	5(4)							$(M1/E2)$	$(8^-) \rightarrow (7^-)$
Band 9										
74.8	117.3	80(40)		0.5(2)					$M1/E2$	$(4^-) \rightarrow (3^-)$
125.0	167.6	10(5)							$(E2)$	$(5^-) \rightarrow (3^-)$
145.7	313.8	40(10)		0.7(2)					$M1/E2$	$(6^-) \rightarrow (5^-)$
182.3	687.6	24(8)							$(M1/E2)$	$(8^-) \rightarrow (7^-)$
191.7	505.4	20(10)							$(M1/E2)$	$(7^-) \rightarrow (6^-)$
197.0	313.8	75(20)		1.4(5)					$E2$	$(6^-) \rightarrow (4^-)$
245.4	1205.5	11(20)							$(M1/E2)$	$(10^-) \rightarrow (9^-)$
272.1	959.2	32(15)							$(M1/E2)$	$(9^-) \rightarrow (8^-)$
315.2	1520.3	19(9)							$(M1/E2)$	$(11^-) \rightarrow (10^-)$
338.1	505.4	40(15)		1.3(4)					$E2$	$(7^-) \rightarrow (5^-)$
373.8	687.6	160(70)	0.9(3)[e]	1.2(2)					$E2$	$(8^-) \rightarrow (6^-)$
453.6	959.2	100(40)	1.9(4)[f]	1.3(3)					$E2$	$(9^-) \rightarrow (7^-)$
518.0	1205.5	110(40)		1.3(2)					$E2$	$(10^-) \rightarrow (8^-)$
561.0	1520.3	80(30)		1.6(3)					$E2$	$(11^-) \rightarrow (9^-)$

Table 7.1 $(Continued.)$

E_γ (keV)[a]	E_i (keV)	I_γ^b	R_{DCO}^c	R_{ac}^d	a_2	a_4	A	δ	Mult.	$J_i^\pi \rightarrow J_f^\pi$
621.7	1827.2	70(20)		1.2(3)					$E2$	$(12^-) \rightarrow (10^-)$
660.5	2180.8	70(20)		1.4(3)					$E2$	$(13^-) \rightarrow (11^-)$
693.6	2520.8	50(20)		1.3(3)					$E2$	$(14^-) \rightarrow (12^-)$
743.4	2924.2	34(11)		1.6(5)					$E2$	$(15^-) \rightarrow (13^-)$
763.9	3284.7	35(14)		1.6(6)					$E2$	$(16^-) \rightarrow (14^-)$
813.2	3737.4	13(4)		1.4(5)					$E2$	$(17^-) \rightarrow (15^-)$
853.1	4137.8	11(3)							$(E2)$	$(18^-) \rightarrow (16^-)$
876.4	4613.8	11(3)							$(E2)$	$(19^-) \rightarrow (17^-)$
935.9	5073.7	14(4)							$(E2)$	$(20^-) \rightarrow (18^-)$
953.8	5567.6	9(3)							$(E2)$	$(21^-) \rightarrow (19^-)$
1013.1	6086.8	13(4)							$(E2)$	$(22^-) \rightarrow (20^-)$
1041.1	6608.7	8(3)							$(E2)$	$(23^-) \rightarrow (21^-)$
1097.9	7184.7	3(1)							$(E2)$	$(24^-) \rightarrow (22^-)$
1133.3	7742.0	6(3)							$(E2)$	$(25^-) \rightarrow (23^-)$
1197.8	8382.5	2(1)							$(E2)$	$(26^-) \rightarrow (24^-)$
1241.2	8983.2	2(1)							$(E2)$	$(27^-) \rightarrow (25^-)$
1294.4	9676.9	1(1)							$(E2)$	$(28^-) \rightarrow (26^-)$
Band 9 $\rightarrow$ Band 8										
42.7	42.7	40(20)							$(M1/E2)$	$(3^-) \rightarrow (2^-)$
37.3	117.3	17(10)							$(M1/E2)$	$(4^-) \rightarrow (4^-)$
88.2	167.6	66(30)	1.0(2)[f]	0.6(2)					$M1/E2$	$(5^-) \rightarrow (4^-)$
192.8	505.4	20(10)							$(M1/E2)$	$(7^-) \rightarrow (6^-)$
Band 9 $\rightarrow$ Band 10										
64.9	313.8	30(20)		0.5(2)					$M1/E2$	$(6^-) \rightarrow (5^-)$
135.8	687.6	9(4)							$(M1/E2)$	$(8^-) \rightarrow (7^-)$
407.5	959.2	18(9)							$(E2)$	$(9^-) \rightarrow (7^-)$
Band 10										
198.1	750.7	5(4)							$(M1/E2)$	$(8^-) \rightarrow (7^-)$
298.1	1048.2	4(3)							$(M1/E2)$	$(9^-) \rightarrow (8^-)$
303.3	551.6	16(8)							$(E2)$	$(7^-) \rightarrow (5^-)$
496.6	1048.2	19(10)		1.3(3)					$E2$	$(9^-) \rightarrow (7^-)$
585.4	1336.1	30(15)		1.3(2)					$E2$	$(10^-) \rightarrow (8^-)$
631.4	1679.6	18(10)							$(E2)$	$(11^-) \rightarrow (9^-)$
688.5	2024.6	20(10)		1.3(4)					$E2$	$(12^-) \rightarrow (10^-)$
711.1	2390.7	16(9)							$(E2)$	$(13^-) \rightarrow (11^-)$
726.8	2751.4	4(3)							$(E2)$	$(14^-) \rightarrow (12^-)$
739.5	3130.2	11(7)							$(E2)$	$(15^-) \rightarrow (13^-)$
779.4	3909.6	7(4)							$(E2)$	$(17^-) \rightarrow (15^-)$
828.0	4737.6	4(2)							$(E2)$	$(19^-) \rightarrow (17^-)$
Band 10 $\rightarrow$ Band 8										
436.9	750.7	40(20)		1.3(2)					$E2$	$(8^-) \rightarrow (6^-)$
Band 10 $\rightarrow$ Band 9										
131.5	248.8	100(50)		0.8(2)					$M1/E2$	$(5^-) \rightarrow (4^-)$
237.8	551.6	70(30)	1.0(3)[f]	0.7(1)					$M1/E2$	$(7^-) \rightarrow (6^-)$
360.3	1048.2	6(4)							$(M1/E2)$	$(9^-) \rightarrow (8^-)$
384.0	551.6	7(4)							$(E2)$	$(7^-) \rightarrow (5^-)$

[a]The error on the transition energies is 0.3 keV for transitions below 500 keV, 0.7 keV for transitions between 500 and 1000 keV, and 1.0 keV for transitions above 1000 keV. The error on the transition transition energies is 1.0 keV for the transition inthesities less 10.
[b]Relative intensities corrected for efficiency, normalized to the intensity of the 200.1 keV ($10^+ \rightarrow 8^+$ of Band 1) transition [126]. The transition intensities were obtained from a combination of total projection and gated spectra.
[c]R_{DCO} has been deduced from an asymmetric $\gamma - \gamma$ coincidence matrix sorted with the detectors at 157.6° on one axis, and detectors at $\approx$ 90° on the other axis. The tentative spin-parity of the states are given in parentheses.
[d]R_{ac} has been deduced from two asymmetric $\gamma - \gamma$ coincidence matrices sorted with the detectors at 133.6° and 157.6° on one axis, and detectors at $\approx$ 90° on the other axis. The tentative spin-parity of the states are given in parentheses.
[e] DCO ratio from spectrum gated on stretched quadrupole transition.
[f] DCO ratio from spectrum gated on stretched dipole transition.

Chapter 8

Conclusion and future work

8.1 Conclusion

The very neutron-deficient strongly-deformed ^{119}Cs, ^{119}Ba, and ^{118}Cs nuclei have been studied with the JUROGAM 3 γ-ray detector array coupled to the MARA recoil-mass separator setup. Two most complete level schemes from low to high spin in the odd-even and odd-odd proton-rich cesium nuclei, ^{119}Cs and ^{118}Cs, were observed. One new rotational band and several low-lying states were newly identified in ^{119}Ba. The configurations of the observed bands were assigned based on the analysis of the alignment properties of the bands, on systematics and on particle number conserving cranked shell model (PNC-CSM) calculations.

We have identified low-lying isomers, with half-lives of $T_{1/2} = 0.36(2)$ μs and $T_{1/2} = 55(5)$ μs, for the $5/2^-$ and $11/2^-$ band heads of the bands based on neutron and proton $h_{11/2}$ orbitals in ^{119}Ba and ^{119}Cs, respectively. In ^{118}Cs, the 8^+ band-head of the $\pi h_{11/2} \otimes \nu h_{11/2}$ band is a short-lived isomer with a half-life in the nanosecond range which cannot be measured, while the 7^+ state below it is a long-lived isomer for which a half-life of $T_{1/2} = 0.55(6)$ μs has been measured.

Prolate-oblate shape coexistence close to the ground state in the strongly-deformed proton-rich nucleus ^{119}Cs was observed for the first time. Band 3 built on a $11/2^-$ state at 670 keV, has properties which unequivocally indicate the strongly-coupled $\pi h_{11/2}[505]11/2^-$ configuration associated with oblate shape. Together with Band 1, the decoupled $\pi h_{11/2}[541]3/2^-$ band built on the a $11/2^-$ prolate state at 110 keV, it provides evidence of shape coexistence at low spin in proton-rich strongly deformed cesium.

The chiral bands built on a configuration with only protons in the transient backbending regime was also observed for the first time in ^{119}Cs. Band 9 which is nearly degenerate to the strongly-coupled $\pi g_{9/2}$[404]9/2$^+$ band of ^{119}Cs was identified. It exhibits a backbending similar to that of Band 8, at nearly constant rotation frequency. Tilted axis cranking covariant density functional theory with pairing correlations and PNC-CSM calculations show that the backbending is induced by the rotational alignment of two $h_{11/2}$ protons, whose angular momenta reorient from

the short to the intermediate axis, in a plane orthogonal to the angular momentum of the strongly-coupled $g_{9/2}$ proton which keeps aligned along the long axis. The total spin points in 3D, inducing the breaking of the chiral symmetry and giving rise to nearly degenerate doublet bands. We can conclude that the chirality in nuclei is a general phenomenon, being robust and present not only in a two-component quantum many-body system, but also in a one-component quantum many-body system as well.

8.2 Future work

We observed several isomeric states with a half-life in the nanosecond range, e.g., the 8^+ state of Band 1 in ^{118}Cs and the $11/2^-$ state of Band 3 in ^{119}Cs, which can not be measured by using the recoil mass separators. Thus, it would be interesting to measure these lifetimes by proposing a dedicated experiment, in which we should use a thick target instead of the thin target, resulting in the residual nuclei stopped and decaying at the target position. Meanwhile such an experiment would increase the statistics of the data, which would allow to identify some weak connecting transitions between the floating rotational bands of ^{118}Cs.

Appendix A

JUROGAM 3 detector angles

Table A.1: The information of JUROGAM 3 detector angles.

Dectector ID[a]	θ^b	ϕ^c
T01	157.6	0
T02	157.6	72
T03	157.6	144
T04	157.6	216
T05	157.6	288
T06	133.6	18
T07	133.6	54
T08	133.6	90
T09	133.6	126
T10	133.6	162
T11	133.6	198
T12	133.6	234
T13	133.6	270
T14	133.6	306
T15	133.6	342
Q01	104.5	15
Q02	104.5	45
Q03	104.5	75
Q04	104.5	105
Q05	104.5	135
Q06	104.5	165
Q07	104.5	195
Q08	104.5	225
Q09	104.5	255
Q10	104.5	285
Q11	104.5	315
Q12	104.5	345
Q13	75.5	15
Q14	75.5	45
Q15	75.5	75
Q16	75.5	105
Q17	75.5	135
Q18	75.5	165
Q19	75.5	195
Q20	75.5	225
Q21	75.5	255
Q22	75.5	285
Q23	75.5	315
Q24	75.5	345

[a] T is tapered detector, Q is clover detector.
[b] The θ is defined with respect to the beam direction.
[b] The $\phi = 0^\circ$ is defined as vertically upwards, increases in a clockwise direction when the array is viewed from a position upstream.

Appendix B

Synthèse en français

Le présent travail est consacré à la spectroscopie des noyaux extrêmement riches en protons dans la région de masse $\approx$ 120, en particulier ^{119}Cs, ^{118}Cs et ^{119}Ba. L'étude des noyaux dans cette région de masse est intéressante car ils offrent l'opportunité d'étudier plusieurs phénomènes, comme l'interaction proton-neutron, l'évolution de la déformation nucléaire vers le milieu des couches majeures $N, Z = 52 - 82$, l'émission de particules chargées directe et après la décroissance beta. En plus, nous pouvons également étudier les propriétés des bandes de rotation collectives de bas à très haut spin, ainsi que l'existence d'états isomériques multiples comme prédit dans la Réf. [4]. Cependant, l'étude des noyaux de baryum et de césium les plus légers est confrontée à la difficulté croissante de peupler les états de spin élevé en utilisant des réactions de fusion-évaporation, en raison du choix limité de combinaisons projectile-cible et des petites sections transversales pour l'évaporation des neutrons près de la ligne de goutte du proton.

L'expérience a été réalisée au JYFL à l'aide du dispositif JUROGAM 3 + MARA [95, 97, 100]. Le noyau composé ^{122}Ce a été produit en utilisant le faisceau d'ions ^{64}Zn avec une énergie finale de 255 MeV, et il a été bombardé sur une cible autoportante de ^{58}Ni enrichi avec une épaisseur de 0.75 mg/cm^2. L'intensité du faisceau était d'environ 2-3 pnA. La durée de la manipulation était d'environ 3 jours. Les noyaux excités de ^{119}Cs, ^{119}Ba et ^{118}Cs ont été peuplés par les canaux de réaction 3p, 2p1n et 3p1n avec des sections efficaces calculées à l'aide de HIVAP de 150 mb, 20 mb et 40 mb, respectivement.

Un total de 4×10^{10} événements de coïncidence rapide de rayons γ avec multiplicité $\geq$ 3 ont été collectés par le JUROGAM 3. Les spectres à double grille obtenus à partir des coïncidences rapides γ montrent les transitions des bandes nouvellement identifiées. Les identifications des spins et des parités d'états sont basées sur les valeurs extraites de R$_{ac}$, R$_{dco}$, et la polarisation linéaire. L'attribution des nouvelles bandes à différents noyaux est basée sur la coïncidence de γ prompt avec les résidus rapides $\gamma\gamma$ avec les résidus d'évaporation en recul de masse différente détectés au niveau du plan focal MARA, et avec les rayons X K_α de différents nucléides détectés en coïncidence prompt avec les transitions dans la bande par le réseau JUROGAM 3 à la position de la cible.

Toutes les bandes du ^{119}Cs sont interconnectées par des transitions multiples, fixant ainsi leurs énergies relatives. Les spins et les parités sont déterminés pour la plupart des bandes observées. Les énergies d'excitation de toutes les bandes observées sont déterminées et les configurations des bandes observées sont attribuées. Les plusieurs nouvelles bandes observées dans ^{119}Cs conduisent à l'un des schémas de niveaux les plus complets des noyaux de Cs riches en protons. Dans le cas de ^{118}Cs, nous avons obtenu dix nouvelles bandes, ainsi que d'autres états, ce qui conduit au plus grand ensemble d'excitations proton-neutron des noyaux de lanthanides impairs près de la limite de stabilité proton. Une nouvelle bande de rotation et plusieurs états de bas énergie ont été identifiés dans ^{119}Ba. Les configurations des bandes observées ont été attribuées sur la base de l'analyse des propriétés d'alignement des bandes, de la systématique et des calculs du modèle en couches inclinée conservant le nombre de particules (PNC-CSM).

Nous avons identifié des isomères de faible durée de vie, avec des demi-vies de $T_{1/2} = 0,36(2)$ μs et $T_{1/2} = 55(5)$ μs, pour les têtes de bande $5/2^-$ et $11/2^-$ des bandes basées sur les orbitales de neutrons et de protons $h_{11/2}$ dans ^{119}Ba et ^{119}Cs, respectivement. Dans le ^{118}Cs, deux autres isomères à longue durée de vie ont été identifiés : une transition de 66 keV détectée au plan focal de MARA, indiquant une demi-vie de l'ordre de la microseconde, alors qu'aucune transition dépeuplante n'a été identifiée pour l'autre, indiquant une demi-vie beaucoup plus longue. Pour les états isomères dans la bande $\pi h_{11/2} \otimes \nu h_{11/2}$, la tête de bande 8^+ est un isomère à courte durée de vie avec une demi-vie de l'ordre de la nanoseconde, tandis que l'état 7^+ en dessous est un isomère à longue durée de vie avec une demi-vie de $T_{1/2} = 0,55(6)$ μs.

Les formes oblate peuvent être induites par de grands écarts d'énergie, comme ceux à $Z = 56$ et $N = 60$ au-dessus des couches principales $Z, N = 50$, et favorisées par la présence près des surfaces de Fermi d'orbitales de Nilsson à haute valeur Ω qui ont une forte force motrice vers la forme oblate. Les noyaux de lanthanides riches en protons sont parmi les meilleurs cas d'états fondamentaux oblate, principalement en raison de l'orbitale $\pi[505]11/2^-$, qui présente la pente la plus raide en fonction de la déformation quadripolaire : lorsqu'elle est couplée à un noyau oblate, elle donne naissance à des bandes fortement couplées composées de partenaires de signature dégénérés qui peuvent se développer sur des plages de spins étendues, permettant ainsi l'étude de leurs propriétés.

Dans cette expérience, nous rapportons la première observation d'une bande de parité négative oblate dans le noyau fortement déformé ^{119}Cs riche en protons. La configuration de la bande 3 ne peut être basée seulement sur l'orbitale $\pi h_{11/2}[505]11/2^-$ qui est proche de la surface de Fermi pour une déformation oblate, donnant ainsi confiance dans la parité négative attribuée. La décroissance de la bande 3 uniquement vers les trois états $5/2^+$, $7/2^+$ et $9/2^+$ sous la tête de bande, et l'absence de transitions de connexion entre ces états et les autres états de parité positive, suggère fortement que ces états sont également basés sur des formes oblates, associées à l'occupation des orbitales $\pi[413]5/2^+$ et/ou $\pi[402]5/2^+$ proches de la surface de Fermi pour la déformation oblate. La bande de parité négative 3 supposée avoir une forme oblate ne se décompose pas en d'autres bandes de parité négative, qui sont toutes interprétées de manière cohérente comme construites sur une forme prolate. Cela peut

s'expliquer par l'existence d'une différence entre les minima oblate et prolate, qui peut atteindre 5 MeV [39, 40, 41], mais aussi par une orientation très différente du spin du proton impair par rapport au noyau qui peut conduire à des transitions interdites ΔK. En plus, il ne se désintègre pas vers les états vers les états bas peuplés par les transitions des bandes 4 et 5, qui sont également basées sur des formes prolates. On peut donc spéculer que la désintégration de la bande 3 se fait vers des états construits sur la même forme oblate, avec des configurations construites sur des orbitales $\pi[413]5/2^+$ et $\pi[402]5/2^+$ proches de la surface de Fermi pour une déformation oblate de $\varepsilon_2 \approx -0.2$. L'absence d'orbitales élevées de type Ω près de la surface de Fermi de $Z = 55$ pour une déformation allongée de $\varepsilon_2 \approx 0.3$, qui peut expliquer la décroissance observée de la Bande 3, est un autre argument en faveur des formes oblates attribuées à la Bande 3 et aux états de parité positive vers lesquels elle décro2̂t. Ces états oblats coexistent à bas spins avec plusieurs états prolates associés aux orbitales à faible valeur de Ω $\pi[422]3/2^+$, $\pi[420]1/2^+$, et $\pi[541]3/2^-$, et à l'orbitale à forte valeur de Ω $\pi[404]9/2^+$, qui sont toutes proches de la surface de Fermi pour $\varepsilon_2 \approx 0.3$. L'observation expérimentale d'états oblats bas coexistant avec des états prolates à l'intérieur de quelques dizaines de keV est favorisée par le grand écart au-dessus de la surface de Fermi du proton $Z = 55$ pour la déformation oblate, induite par les orbitales fortement inclinées vers le bas et à haut degré d'oméga.

En résumé, la coexistence d'une forme prolate-oblate proche de l'état fondamental dans le noyau riche en protons fortement déformé ^{119}Cs a été observée pour la première fois. La bande 3 construite sur un état $11/2^-$ à 670 keV, a des propriétés qui indiquent la configuration fortement couplée $\pi h_{11/2}[505]11/2^-$ associée à la forme oblate. Avec la bande 1, la bande découplée $\pi h_{11/2}[541]3/2^-$ construite sur l'état prolate $11/2^-$ à 110 keV, elle fournit des preuves de la coexistence de formes à faible spin dans les lanthanides fortement déformés riches en protons.

Dans le ^{119}Cs, les bandes 8 et 9 sont presque dégénérées et ont des moments d'inertie similaires. Les moments angulaires alignés des particules uniques (Fig. 5.25) montrent les configurations similaires des bandes 8 et 9, qui présentent des croisements avec des configurations à trois quasi-particules à des fréquences de rotation de 0,32 et 0,37 MeV, respectivement. Le gain de moment angulaire est de $\approx\ 8\ \hbar$, ce qui indique l'alignement d'une paire de particules $h_{11/2}$, et la contribution négligeable de l'orbitale du proton fortement couplée $[404]9/2^+$. La bande 10 présente une configuration complètement différente, avec un moment angulaire aligné inférieur de $\approx\ 6\ \hbar$, qui augmente régulièrement jusqu'à $\approx\ 9\ \hbar$ sur la gamme de fréquences observée, tandis que le MoI diminue de $\approx\ 53$ $\hbar^2$MeV^{-1} à basse fréquence à $\approx\ 40\ \hbar^2$MeV^{-1} au sommet de la bande. Cela indique clairement une configuration différente de la bande 10 par rapport à celle des bandes 8 et 9. Sur la base des accords entre les résultats expérimentaux et les calculs effectués à l'aide du PNC-CSM, l'alignement du moment angulaire calculé J_x pour la configuration $\pi[404]9/2^+$ de la bande 8, et sa décomposition en contributions du proton et du neutron, indiquent que le pliage arrière est due à l'alignement d'une paire de protons $h_{11/2}$ à une fréquence de ≈ 0.35 MeV/$\hbar$, suivi par l'alignement plus graduel d'une paire de neutrons à ≈ 0.5 MeV/$\hbar$. Les orbitales de la couche $N = 4$ ne fournissent qu'une augmentation graduelle des moments angulaires. Quant à la contribution de l'orbitale $\pi[404]9/2^+$, elle reste

presque constante avec la fréquence de rotation, ce qui signifie que cette orbitale reste alignée le long de l'axe long. La bande 10 a un moment d'inertie (MoI) similaire à celui de la bande découplée construite sur l'état $11/2^-$ [126], qui est basé sur l'orbitale $\pi[541]3/2^+$. Sa parité positive et la quasi-dégénérescence de leurs partenaires de signature indiquent la présence de deux nucléons dans des orbitales de parité opposée de haute valeur Ω, qui induisent un alignement en accord avec l'expérience uniquement pour les neutrons. Nous attribuons donc la configuration de trois quasi-particules $\pi[541]3/2(\alpha = +1/2) \otimes \nu^2[413]5/2[523]5/2$ à la bande 10.

Les modèles d'alignement similaires et les rapports $B(M1)/B(E2)$ des probabilités de transition réduites des bandes 8 et 9 suggèrent des configurations de particules uniques identiques (voir les figures 5.24 et 5.26). L'alignement de la particule unique de la bande 9 est plus élevé d'environ 2 $\hbar$ que celui de la bande 8 juste au-dessus de la tête de la bande, ce qui suggère une interprétation en tant que bande γ. Les fréquences de rotation légèrement différentes des backbends observées dans les bandes 8 et 9 peuvent être dues à des MoIs légèrement différents induits par des directions différentes des axes de rotation dans les deux bandes. Les propriétés de la bande 9 sont en accord avec une interprétation chirale de la bande γ construite sur la configuration $\pi[404]9/2^+ \otimes \pi h^2_{11/2}$. Cependant, pour adopter cette interprétation, il faut exclure d'autres configurations possibles. La fréquence de croisement plus faible dans la bande 9 que dans la bande 8 peut également être attribuée à une éventuelle déformation plus faible de la bande 9. Une telle hypothèse a été proposée pour une bande aux propriétés similaires observée dans le noyau pair-pair ^{118}Xe [150], qui peut être considéré comme le noyau du ^{119}Cs. La bande dans le noyau ^{118}Xe a été interprétée comme la bande γ qui évolue à haut spin par l'alignement d'une paire de neutrons, qui, étant située au milieu de la couche $h_{11/2}$, aurait une force motrice vers une déformation plus petite et pourrait réduire la fréquence de croisement. Nous avons vérifié ce scénario alternatif par des calculs PNC-CSM qui sont montrés dans la Fig. 5.30, où l'on peut voir que pour des déformations plus petites que celle de la bande 8 ($\varepsilon_2 \approx 0.32$), le moment d'inertie expérimental n'est pas bien reproduit : pour $\varepsilon_2 \approx 0.28$ l'alignement des neutrons est significativement retardé par rapport à celui des protons et donne lieu à un saut non observé à $\hbar\omega \approx 0.40$ MeV, tandis que pour des déformations plus faibles $J^{(1)}$ est largement surestimé. Nous pouvons donc écarter la plus petite déformation et l'alignement des neutrons correspondant pour la Bande 9. Une autre configuration possible de la bande 9 peut être $\pi[422]3/2^+$, qui est proche de la surface de Fermi et peut donner lieu à une bande avec des partenaires de signature presque dégénérés. Cependant, trois arguments importants s'opposent à cette interprétation: i) la bande 9 ne se désintègre seulement en bande 8 et non en une autre bande construite sur l'orbitale proche $[420]1/2^+$, avec laquelle la $[422]3/2^+$ est fortement mélangée; ii) les deux signatures observées de la bande 9 sont dégénérées au bas de la bande, ce qui est en contradiction avec les calculs; iii) le mélange de la configuration [404]9/2$^+$ à haut degré de liberté avec d'autres états proches à faible degré de liberté comme [420]1/2$^+$ et [422]3/2$^+$ devrait être faible. On peut donc en conclure que la bande 9 est construite sur la même configuration à trois protons que la bande 8 dans la région de flexion arrière, un dans l'orbitale [404]9/2$^+$ à haut degré de liberté et deux dans les orbitales $h_{11/2}$ à faible degré de liberté. La géométrie presque orthogonale des moments angulaires des orbitales impliquées de

haute et de basse valeur, les modèles d'alignement similaires et les rapports $B(M1)/B(E2)$ des probabilités de transition réduites, suggèrent fortement la nature chirale des bandes 8 et 9.

Le mouvement collectif qui donne naissance aux bandes 8 et 9 dans le ^{119}Cs peut donc être une rotation 3D et avoir un caractère chiral. Pour un noyau impair-pair ^{119}Cs, l'observation pour la première fois de bandes chirales dans ce noyau révèle un nouveau type de chiralité, que nous pouvons appeler "chiralité électrique", qui est basée sur une configuration impliquant uniquement des protons, l'un dans l'orbitale fortement couplée $\pi g_{9/2}[404]9/2^+$, et les deux autres dans les orbitales $\pi h_{11/2}$. On connaÎt des bandes fortement couplées basées sur des orbitales de Nilsson à haute valeur de Ω dans des noyaux avec un nombre impair de protons (Rh, Ag, Sb) ou un nombre impair de neutrons (Nd, Sm, Gd, Dy) [124], mais elles ont toutes été observées en dessous de la région de flexion arrière, où la configuration n'implique qu'une seule quasiparticule, et où la géométrie chirale 3D ne peut pas être réalisée parce qu'il manque l'une des trois jambes du moment angulaire. Les nouvelles bandes chirales dans le ^{119}Cs sont au contraire observées dans la région de flexion induite par l'alignement de deux protons $h_{11/2}$, ayant ainsi une configuration à trois protons. Le moment angulaire total des bandes résulte de deux protons $h_{11/2}$ tournant de l'axe court à l'axe intermédiaire du noyau triaxial, et d'un proton $g_{9/2}$ fortement couplé collé le long de l'axe long. La direction du moment angulaire total se déplace en 3D, ce qui donne lieu à des bandes chirales que l'on peut appeler des bandes $R\chi D$ (*Revolving Chiral Doublet*).

Une figure schématique montrant la géométrie des moments angulaires est donnée à la Fig. 5.31. Les deux protons de $h_{11/2}$ placés sur des orbitales de bas niveau à la base de la couche $h_{11/2}$ ont les moments angulaires alignés le long de l'axe court à la base de la bande. Lorsque le spin augmente, leurs moments angulaires passent de l'axe court à l'axe intermédiaire. Le spin total I tourne en 3D du plan court-long $(s-l)$ au bas de la bande au plan intermédiaire-long $(i-l)$ au sommet de la bande. Le régime chiral s'étend sur un large changement de spin, et se termine lorsque les moments angulaires des deux protons $h_{11/2}$ sont presque complètement alignés le long de l'axe intermédiaire de rotation collective. En raison de la triaxialité du noyau, la symétrie chirale brisée induit deux bandes de doublets dégénérés avec des moments angulaires totaux qui sont des images miroir l'un de l'autre dans le plan $s-l$.

La bande 9 qui est presque dégénérée par rapport à la bande fortement couplée $\pi g_{9/2}$[404]9/2$^+$ de ^{119}Cs a été identifiée. Elle présente une contre-flexion similaire à celle de la bande 8, à une fréquence de rotation presque constante. Des calculs de théorie fonctionnelle de la densité covariante avec corrélations d'appariement et de PNC-CSM montrent que le backbending est induit par l'alignement rotationnel de deux protons $h_{11/2}$, dont les moments angulaires se réorientent de l'axe court vers l'axe intermédiaire, dans un plan orthogonal au moment angulaire du proton $g_{9/2}$ fortement couplé qui reste aligné le long de l'axe long. Le spin total pointe en 3D, induisant la rupture de la symétrie chirale et donnant lieu à des bandes de doublets presque dégénérés. Nous pouvons conclure que la chiralité dans les noyaux est un phénomène général, robuste et présent non seulement dans un système quantique à corps multiples à deux composants, mais aussi dans un système quantique à corps multiples à un composant.

List of Figures

List of Tables

Bibliography

[1] P. Ring, and P. Schuck. *The nuclear many-body problem*. Springer Science & Business Media, 2004.

[2] R. Bengtsson, and J.D. Garrett. The cranking model - theoretical and experimental bases. *World Scientific Publishing Co Pte Ltd*. 1984.

[3] W. R. Leo. Techniques for nuclear and particle physics experiments. *Springer Science & Business Media*, 2012.

[4] H. L. Liu, F. R. Xu, S. W. Xu, R. Wyss, and P. M. Walker. High-spin isomeric structures in exotic odd-odd nuclei: Exploration of the proton drip line and beyond. *Physical Review C*, 76, 034313, 2007.

[5] B. K. Thomson, B. Kelvin, and W. Thomson. Baltimore lectures on molecular dynamics and the wave theory of light. *Cambridge University Press*, 2010.

[6] G. H. Wagnière. On chirality and the universal asymmetry: reflections on image and mirror image. *John Wiley & Sons*, 2007.

[7] P. Y. Bruice. Organic chemistry 4th edition. *Pearson Education (US)*, 2000.

[8] S. Frauendorf, and J. Meng. Tilted rotation of triaxial nuclei. *Nuclear Physics A*, 617, 131, 1997.

[9] P. W. Zhao. Multiple chirality in nuclear rotation: A microscopic view. *Physics Letters B*, 773, 1, 2017.

[10] J. Meng and S. Q. Zhang. Open problems in understanding the nuclear chirality. *Journal of Physics G: Nuclear and Particle Physics*, 37, 064025, 2010.

[11] A. N. Bohr and B. R. Mottelson. Nuclear Structure (In 2 Volumes). *World Scientific Publishing Company*, 1998.

[12] C. M. Petrache, D. Bazzacco, S. Lunardi, C. Rossi Alvarez, G. D. Angelis, M. D. Poli, D. Bucurescu, C. A. Ur, P. B. Semmes, and R. Wyss. Rotational bands in the doubly odd nucleus ^{134}Pr. *Nuclear Physics A*, 597, 106, 1996.

[13] K. Starosta, T. Koike, C. J. Chiara, D. B. Fossan, D. R. LaFosse, A. A. Hecht, C. W. Beausang, M. A. Caprio, J. R. Cooper, R. Krücken, et al. Chiral doublet structures in odd-odd $N = 75$ isotones: Chiral vibrations. *Physical Review Letters*, 86, 971, 2001.

[14] B. W. Xiong, and Y. Y. Wang. Nuclear chiral doublet bands data tables. *Atomic Data and Nuclear Data Tables*, 125, 193, 2019.

[15] R. Guo, W. J. Sun, J. Li, D. Yang, Y. H. Liu, C. K. Ru, and J. H. Chi. Systematic investigations of positive-parity doublet bands with three-quasiparticle configurations in ^{125,127,129,131}Cs. *Physical Review C*, 100, 034328, 2019.

[16] A. A. Raduta. Specific features and symmetries for magnetic and chiral bands in nuclei. *Progress in Particle and Nuclear Physics*, 90, 241, 2016.

[17] K. Starosta, T. Koike, C. J. Chiara, D. B. Fossan, and D. R. LaFosse. Chirality in odd-odd triaxial nuclei. *Nuclear Physics A*, 682, 375, 2001.

[18] B. Qi, S. Q. Zhang, S. Y. Wang, J. M. Yao, and J. Meng. Examining B(M1) staggering as a fingerprint for chiral doublet bands. *Physical Review C*, 79, 041302, 2009.

[19] S. Q. Zhang, B. Qi, S. Y. Wang, and J. Meng. Chiral bands for a quasi-proton and quasi-neutron coupled with a triaxial rotor. *Physical Review C*, 75, 044307, 2007.

[20] I. Hamamoto. Possible presence and properties of multi-chiral-pair bands in odd-odd nuclei with the same intrinsic configuration. *Physical Review C*, 88, 024327, 2013.

[21] S. Frauendorf. Spontaneous symmetry breaking in rotating nuclei. *Reviews of Modern Physics*, 73, 463, 2001.

[22] S. Guo, C. M. Petrache, D. Mengoni, Y. H. Qiang, Y. P. Wang, Y. Y. Wang, J. Meng, Y. K. Wang, S. Q. Zhang, P. W. Zhao, et al. Evidence for pseudospin-chiral quartet bands in the presence of octupole correlations. *Physics Letters B*, 807, 135572, 2020.

[23] B. F. Lv, C. M. Petrache, Q. B. Chen, J. Meng, A. Astier, E. Dupont, P. Greenlees, H. Badran, T. Calverley, D. M. Cox, et al Chirality of ^{135}Nd reexamined: Evidence for multiple chiral doublet bands. *Physical Review C*, 100, 024314, 2019.

[24] C. M. Petrache, B. F. Lv, Q. B. Chen, J. Meng, A. Astier, E. Dupont, K. K. Zheng, P. T. Greenlees, H. Badran, T. Calverley, et al. Multiple chiral bands in ^{137}Nd. *The European Physical Journal A*, 56, 1, 2020.

[25] C. M. Petrache, B. F. Lv, A. Astier, E. Dupont, Y. K. Wang, S. Q. Zhang, P. W. Zhao, Z. X. Ren, J. Meng, P. T. Greenlees, et al. Evidence of chiral bands in even-even nuclei. *Physical Review C*, 97, 041304, 2018.

[26] K. Heyde, and J. L. Wood. Shape coexistence in atomic nuclei. *Reviews of Modern Physics*, 83, 1467, 2011.

[27] H. Morinaga. Interpretation of some of the excited states of 4n self-conjugate nuclei. *Physical Review*, 101, 254, 1956.

[28] A. N. Andreyev, M. Huyse, P. V. Duppen, L. Weissman, D. Ackermann, J. Gerl, F. P. Hessberger, S. Hofmann, A. Kleinböhl, G. Münzenberg, et al. A triplet of differently shaped spin-zero states in the atomic nucleus ^{186}Pb. *Nature*, 405, 430, 2000.

[29] J. Pakarinen, I. G. Darby, S. Eeckhaudt, T. Enqvist, T. Grahn, P. T. Greenlees, V. Hellemans, K. Heyde, F. Johnston-Theasby, P. Jones, et al. Evidence for oblate structure in ^{186}Pb. *Physical Review C*, 72, 011304, 2005.

[30] H. Hübel, A. P. Byrne, S. Ogaza, A. E. Stuchbery, G. D. Dracoulis, and M. Guttormsen. High-spin structure of $^{190-194}$Hg and the cranked shell model. *Nuclear Physics A*, 453, 316, 1986.

[31] D. Ye, R. V. F. Janssens, M. P. Carpenter, E. F. Moore, I. Ahmad, K. B. Beard, Ph. Benet, M. W. Drigert, U. Garg, Z. W. Grabowski, et al. Nucleon alignment in ^{191}Hg. A competing mechanism at moderate spins. *Physics Letters B*, 236, 7, 1990.

[32] S. M. Fischer, D. P. Balamuth, P. A. Hausladen, C. J. Lister, M. P. Carpenter, D. Seweryniak, and J. Schwartz. Evidence for collective oblate rotation in $N = Z$ ^{68}Se. *Physical Review Letters*, 84, 4064, 2000.

[33] E. Clément, A. Görgen, W. Korten, E. Bouchez, A. Chatillon, J. -P. Delaroche, M. Girod, H. Goutte, A. Hürstel, Y. Le Coz, et al. Shape coexistence in neutron-deficient krypton isotopes. *Physical Review C*, 75, 054313, 2007.

[34] E. S. Paul, C. W. Beausang, D. B. Fossan, R. Ma, W. F. Piel. Jr. , N. Xu, L. Hildingsson, and G. A. Leander. Collective oblate band in ^{131}La due to the rotational alignment of $h_{11/2}$ neutrons. *Physical Review Letters*, 58, 984, 1987.

[35] E. S. Paul, P. J. Twin, A. O. Evans, A. Pipidis, M. A. Riley, J. Simpson, D. E. Appelbe, D. B. Campbell, P. T. W. Choy, R. M. Clark, et al. Return of Collective Rotation in ^{157}Er and ^{158}Er at Ultrahigh Spin. *Physical Review Letters*, 98, 012501, 2007.

[36] U. S. Tandel, S. K. Tandel, P. Chowdhury, D. Cline, C. Y. Wu, M. P. Carpenter, R. V. F. Janssens, T. L. Khoo, T. Lauritsen, C. J. Lister, et al. Collective Oblate Rotation at High Spins in Neutron-Rich ^{180}Hf. *Physical Review Letters*, 101, 182503, 2008.

[37] C. M. Petrache, S. Frauendorf, B. F. Lv, A. Astier, E. Dupont, S. Guo, M. L. Liu, X. H. Zhou, K. L. Wang, P. T. Greenlees, et al. Collective rotation of an oblate nucleus at very high spin. *Physical Review C*, 99, 041301, 2019.

[38] P. Möller, R. Bengtsson, B. G. Carlsson, P. Olivius, T. Ichikawa, H. Sagawa, and A. Iwamoto. Axial and reflection asymmetry of the nuclear ground state. *Atomic Data and Nuclear Data Tables*, 94, 758, 2008.

[39] L. M. Robledo, R. R. Rodríguez-Guzmán, and P. Sarriguren. Evolution of nuclear shapes in medium mass isotopes from a microscopic perspective. *Physical Review C*, 78, 034314, 2008.

[40] H. L. Wang, J. Yang, M. L. Liu, and F. R. Xu. Evolution of ground-state quadrupole and octupole stiffnesses in even-even barium isotopes. *Physical Review C*, 92, 024303, 2015.

[41] M.Girod, and S.Hilaire. Hartree-fock-bogliubov results based on the gogny force. `http://www-phynu.cea.fr/science_en_ligne/carte_potentiels_microscopiques/carte_potentiel_nucleaire_eng.htm.`, 2006.

[42] G. A. Lalazissis, D. Vretenar, and P. Ring. Ground-state properties of deformed proton emitters in the relativistic Hartree-Bogoliubov model. *Nuclear Physics A*, 650, 133, 1999.

[43] M. Aggarwal. Coexisting shapes with rapid transitions in odd-Z rare-earth proton emitters. *Physical Review C*, 89, 024325, 2014.

[44] J. Srebrny, T. Czosnyka, Ch. Droste, S. G. Rohoziński, L. Próchniak, K. Zajac, K. Pomorski, D. Cline, C. Y. Wu, A. Bäcklin, et al. Experimental and theoretical investigations of quadrupole collective degrees of freedom in ^{104}Ru. *Nuclear Physics A*, 766, 25, 2006.

[45] L. E. Svensson, C. Fahlander, L. Hasselgren, A. Bäcklin, L. Westerberg, D. Cline, T. Czosnyka, C. Y. Wu, R. M. Diamond, and H. Kluge. Multiphonon vibrational states in ^{106,108}Pd. *Nuclear Physics A*, 584, 547, 1995.

[46] C. Y. Wu, H. Hua, D. Cline, A. B. Hayes, R. Teng, R. M. Clark, P. Fallon, A. Goergen, A. O. Macchiavelli, and K. Vetter. Multifaceted yrast structure and the onset of deformation in ^{96,97}Sr and ^{98,99}Zr. *Physical Review C*, 70, 064312, 2004.

[47] G. S. Simpson, J. A. Pinston, D. Balabanski, J. Genevey, G. Georgiev, J. Jolie, D. S. Judson, R. Orlandi, A. Scherillo, I. Tsekhanovich, et al. High-spin μs isomer in ^{98}Zr. *Physical Review C*, 74, 064308, 2006.

[48] T. Kibedi and R. H. Spear. Electric monopole transitions between 0^+ states for nuclei throughout the periodic table. *Atomic Data and Nuclear Data Tables*, 89, 77, 2005.

[49] J. L. Wood, E. F. Zganjar, C. De Coster, and K. Heyde. Electric monopole transitions from low energy excitations in nuclei. *Nuclear Physics A*, 651, 323, 1999.

[50] T. Klug, A. Dewald, V. Werner, P von Brentano, and R. F. Casten. The B(E2: $4_2^+ \rightarrow 2_2^+$) value in ^{152}Sm and β-softness in phase coexisting structures. *Physics Letters B*, 495, 55, 2000.

[51] D. Tonev, A. Dewald, T. Klug, P. Petkov, J. Jolie, A. Fitzler, O. Möller, S. Heinze, P von Brentano, and R. F. Casten. Transition probabilities in ^{154}Gd: Evidence for X(5) critical point symmetry. *Physical Review C*, 69, 034334, 2004.

[52] O. Möller, A. Dewald, P. Petkov, B. Saha, A. Fitzler, K. Jessen, D. Tonev, T. Klug, S. Heinze, J. Jolie, et al. Electromagnetic transition strengths in ^{156}Dy. *Physical Review C*, 74, 024313, 2006.

[53] M. G. Mayer and J. H. D. Jensen. Elementary theory of nuclear shell structure. *Wiley*, 1955.

[54] I. Ragnarsson, and S. G. Nilsson. Shapes and shells in nuclear structure. *Cambridge University press*, 2005.

[55] G. Gamow. Mass defect curve and nuclear constitution. *Proceedings of the Royal Society of London. Series A, Containing Papers of a Mathematical and Physical Character*, 126, 632, 1930.

[56] N. Bohr. Neutron capture and nuclear constitution *Nature* 137, 344, 1936.

[57] N. Bohr and F. Kalckar. On the transmutation of atomic nuclei by impact of material particles. *Levin & Munksgaard*, 1937.

[58] H. A. Bethe and R. F. Bacher. Nuclear physics a. stationary states of nuclei. *Reviews of Modern Physics*, 8, 82, 1936.

[59] C. F. v. Weizsäcker. Zur theorie der kernmassen. *Zeitschrift für Physik*, 96, 431, 1935.

[60] A. H. Wapstra. Atomic masses of nuclides. *Springer Berlin Heidelberg*, 1958.

[61] N. Bohr, and J. A. Wheeler. The mechanism of nuclear fission. *Physical Review*, 56, 426, 1939.

[62] E. Feenberg, and K. C. Hammack. Nuclear shell structure. *Physical Review*, 75, 1877, 1949.

[63] M. G. Mayer. On closed shells in nuclei. ii. *Physical Review*, 75, 1969, 1949.

[64] O. Haxel, J. H. D. Jensen, and H. E. Suess. On the ”magic numbers” in nuclear structure. *Physical Review*, 75, 1766, 1949.

[65] R. D. Woods and D. S. Saxon. Diffuse surface optical model for nucleon-nuclei scattering. *Physical Review*, 95, 577, 1954.

[66] E. Feenberg and B. T. Feld. Shell theory of the nucleus. *Physics Today*, 8, 22, 1955.

[67] A, Raccanelli, D, Bertacca, O, Doré, and R, Maartens. Large-scale 3D galaxy correlation function. *arXiv preprint arXiv:1306.6646*.

[68] D. L. Hill and J. A. Wheeler. Nuclear constitution and the interpretation of fission phenomena. *Physical Review*, 89, 1102, 1953.

[69] S. G. Nilsson. Binding states of individual nucleons in strongly deformed nuclei. *Dan. Mat. Fys. Medd.*, 29, 1, 1955.

[70] A. V. Afanasjev, D. B. Fossan, G. J. Lane, and I. Ragnarsson. Termination of rotational bands: disappearance of quantum many-body collectivity. *Physics Reports*, 322, 1, 1999.

[71] A. V. Afanasjev and I. Ragnarsson. Gradual loss of collectivity in rotational bands in the A $\sim$ 110 (Z $\geq$ 50, N $\sim$ 60) mass region. *Nuclear Physics A*, 591, 387, 1995.

[72] T. Bengtsson and I. Ragnarsson. Rotational bands and particle-hole excitations at very high spin. *Nuclear Physics A*, 436, 14, 1985.

[73] D. R. Inglis. Particle derivation of nuclear rotation properties associated with a surface wave. *Physical Review*, 96, 1059, 1954.

[74] D. R. Inglis. Nuclear moments of inertia due to nucleon motion in a rotating well. *Physical Review*, 103, 1786, 1956.

[75] R. Bengtsson and S. Frauendorf. An interpretation of backbending in terms of the crossing of the ground state band with an aligned two-quasiparticle band. *Nuclear Physics A*, 314, 27, 1979.

[76] R. Bengtsson and S. Frauendorf. Quasiparticle spectra near the yrast line. *Nuclear Physics A*, 327, 139, 1979.

[77] T. Miyazima, and Y Wada. Nuclear Moments of Inertia. *Progress of Theoretical Physics*, 21, 269, 1959.

[78] R. D. Lawson. Theory of the nuclear shell model, volume 9. *Clarendon Press Oxford*, 1980.

[79] R. Nave. Calculation of coulomb barrier. `http://hyperphysics.phy-astr.gsu.edu/hbase/NucEne/coubar.html`, 2000.

[80] J. K. Bitok, F. G. Kanyeki, W. O. Obonyo, J. K. Tanui, D. K. Kandie, and K. M. Khanna. Calculation of fusion reaction cross-section and angular momentum window of ^{6}Li, ^{16}O, ^{56}Fe and ^{86}Kr on Fusion with ^{208}Pb at ELAB= 500MeV. *International Journal of Physics and Mathematical Sciences*, 2, 72, 2012.

[81] LISE++ group. Exotic beam production with fragment separators. `http://lise.nscl.msu.edu/introduction.html`, 2021.

[82] G. F. Knoll. Radiation detection and measurement. *John Wiley & Sons*, 2010.

[83] C. C. Chang. Auger electron spectroscopy. *Surface Science*, 25, 53, 1971.

[84] R. D. Evans. Compton effect. *Springer Berlin Heidelberg*, pages 218–298, 1958.

[85] S. Weinberg. The quantum theory of fields, volume 2. *Cambridge university press*, 1995.

[86] E. M. Pell. Ion drift in an n-p Junction. *Journal of Applied Physics*, 31, 291, 1960.

[87] D. V Freck and J. Wakefield. Gamma-Ray Spectrum obtained with a Lithium-drifted $p-i-n$ Junction in Germanium. *Nature*, 193, 669, 1962.

[88] G. Duchêne, F. A Beck, P. J. Twin, G. De France, D. Curien, L. Han, C. W. Beausang, M. A. Bentley, P. J. Nolan, and J. Simpson. The Clover: a new generation of composite Ge detectors. *Nuclear Instruments and Methods in Physics Research Section A: Accelerators, Spectrometers, Detectors and Associated Equipment*, 432, 90, 1999.

[89] N. Fourches, A. Huck, and G. Walter. The role of secondary defects in the loss of energy resolution of fast-neutron-irradiated hpge gamma-ray detectors. *IEEE transactions on nuclear science*, 38, 1728, 1991.

[90] U. Fano. On the theory of ionization yield of radiations in different substances. *Physical Review*, 70, 44, 1946.

[91] U. Fano. Ionization yield of radiations. ii. the fluctuations of the number of ions. *Physical Review*, 72, 26, 1947.

[92] F, A, Beck, Th. Byrski, D. Durien, G. Duchene, G. de France, B. Kharraja, L. Wei, P. Butler, G. Jones, P. Jones, et al. The clover detector. 1992.

[93] J. Simpson. The EUROBALL spectrometer. *Zeitschrift für Physik A Hadrons and Nuclei*, 358, 139, 1997.

[94] I. Y. Lee. The gammasphere. *Progress in Particle and Nuclear Physics*, 28, 473, 1992.

[95] J. Pakarinen, J. Ojala, P. Ruotsalainen, H. Tann, H. Badran, T. Calverley, J. Hilton, T. Grahn, P. T. Greenlees, M. Hytönen, et al. The JUROGAM 3 spectrometer. *The European Physical Journal A*, 56, 1, 2020.

[96] C. W. Beausang, S. A. Forbes, P. Fallon, P. J. Nolan, P. J. Twin, J. N. Mo, J. C. Lisle, M. A. Bentley, J. Simpson, F. A. Beck, et al. Measurements on prototype Ge and BGO detectors for the Eurogam array. *Nuclear Instruments and Methods in Physics Research Section A: Accelerators, Spectrometers, Detectors and Associated Equipment*, 313, 37, 1992.

[97] J. Saren, J. Uusitalo, M. Leino, P.T. Greenlees, U. Jakobsson, P. Jones, R. Julin, S. Juutinen, S. Ketelhut, M. Nyman, et al. The new vacuum-mode recoil separator MARA at JYFL. *Nuclear Instruments and Methods in Physics Research Section B: Beam Interactions with Materials and Atoms*, 266, 4196, 2008.

[98] J. Sarén. The ion-optical design of the MARA recoil separator and absolute transmission measurements of the RITU gas-filled recoil separator. *Research report/Department of Physics, University of Jyväskylä*, 2011.

[99] A. Ghiorso, S. Yashita, M. E. Leino, L. Frank, J. Kalnins, P. Armbruster, J. -P. Dufour, and P. K. Lemmertz. Sassy, a gas-filled magnetic separator for the study of fusion reaction products. *Nuclear Instruments and Methods in Physics Research Section A: Accelerators, Spectrometers, Detectors and Associated Equipment*, 269, 192, 1988.

[100] J. Uusitalo, J. Sarén, J. Partanen, and J. Hilton. Mass Analyzing Recoil Apparatus, MARA. *Acta Physica Polonica B*, 50(3), 2019.

[101] R. D. Page, A. N. Andreyev, D. E. Appelbe, P. A. Butler, S. J. Freeman, P. T. Greenlees, R. -D. Herzberg, D. G. Jenkins, G. D. Jones, P. Jones, et al. The GREAT spectrometer. *Nuclear Instruments and Methods in Physics Research Section B: Beam Interactions with Materials and Atoms*, 204, 634, 2003.

[102] J. Hilton, J. Uusitalo, J. Sarén, R. D. Page, D. T. Joss, M. A. M. AlAqeel, H. Badran, A. D. Briscoe, T. Calverley, D. M. Cox, et al. α-spectroscopy studies of the new nuclides ^{165}Pt and ^{170}Hg. *Physical Review C*, 100, 014305, 2019.

[103] E. S. Paul, P. J. Woods, T. Davinson, R. D. Page, P. J. Sellin, C. W. Beausang, R. M. Clark, R. A. Cunningham, S. A. Forbes, D. B. Fossan, et al. In-beam γ-ray spectroscopy above ^{100}Sn using the new technique of recoil decay tagging. *Physical Review C*, 51, 78, 1995.

[104] I. Lazarus, E. E. Appelbe, P. A. Butler, P. J. Coleman-Smith, J. R. Cresswell, S. J. Freeman, R. D. Herzberg, I. Hibbert, D. T. Joss, S. C. Letts, et al. The GREAT triggerless total data readout method. *IEEE Transactions on Nuclear Science*, 48, 567, 2001.

[105] A. Jokinen. The Jyväskylä Accelerator Laboratory. *Nuclear Physics News*, 24, 4, 2014.

[106] P. Rahkila. Grain - a java data analysis system for total data readout. *Nuclear Instruments and Methods in Physics Research Section A: Accelerators, Spectrometers, Detectors and Associated Equipment*, 595, 637, 2008.

[107] D. C. Radford. ESCL8R and LEVIT8R: Software for interactive graphical analysis of HPGe coincidence data sets. *Nuclear Instruments and Methods in Physics Research Section A: Accelerators, Spectrometers, Detectors and Associated Equipment*, 361, 297, 1995.

[108] D. C. Radford. Background subtraction from in-beam HPGe coincidence data sets. *Nuclear Instruments and Methods in Physics Research Section A: Accelerators, Spectrometers, Detectors and Associated Equipment*, 361, 306, 1995.

[109] T. Tachibana H. Koura, J. Katakura and F. Minato. Chart of the Nuclides 2014. *Japanese Nuclear Data Commitee and Nuclear Data Center Japan Atomic Energy Agency*, 2014.

[110] P. Doornenbal. In-beam gamma-ray spectroscopy at the RIBF. *Progress of Theoretical and Experimental Physics*, 2012, 03C004, 2012.

[111] R. Kshetri. Modeling of clover detector in addback mode. *Journal of Instrumentation*, 7, P07008, 2012.

[112] A. Krämer-Flecken, T. Morek, R. M. Lieder, W. Gast, G. Hebbinghaus, H. M. Jäger, and W. Urban. Use of DCO ratios for spin determination in γ-γ coincidence measurements. *Nuclear Instruments and Methods in Physics Research Section A: Accelerators, Spectrometers, Detectors and Associated Equipment*, 275, 333, 1989.

[113] C. J. Chiara, M. Devlin, E. Ideguchi, D. R. LaFosse, F. Lerma, W. Reviol, S. K. Ryu, D. G. Sarantites, O. L. Pechenaya, C. Baktash, et al. Probing $sd - fp$ cross-shell interactions via terminating configurations in ^{42,43}Sc. *Physical Review C*, 75, 054305, 2007.

[114] K. Starosta, T. Morek, Ch. Droste, S. G. Rohoziński, J. Srebrny, A. Wierzchucka, M. Bergström, B. Herskind, E. Melby, T. Czosnyka, et al. Experimental test of the polarization direction correlation method (PDCO). *Nuclear Instruments and Methods in Physics Research Section A: Accelerators, Spectrometers, Detectors and Associated Equipment*, 423, 16, 1999.

[115] K.S. Krane, R. M. Steffen, and R. M. Wheeler. Directional correlations of gamma radiations emitted from nuclear states oriented by nuclear reactions or cryogenic methods. *Atomic Data and Nuclear Data Tables*, 11, 351, 1973.

[116] C. Bargholtz and P. -E. Tegnér. Gamma-gamma directional correlations: Simplifications at high spin. *Nuclear Instruments and Methods in Physics Research Section A: Accelerators, Spectrometers, Detectors and Associated Equipment*, 256, 513, 1987.

[117] L. P. Ekström and A. Nordlund. Gamma-gamma correlations with detector arrays. *Nuclear Instruments and Methods in Physics Research Section A: Accelerators, Spectrometers, Detectors and Associated Equipment*, 313, 421, 1992.

[118] A. Herzáň, S. Juutinen, K. Auranen, T. Grahn, P. T. Greenlees, K. Hauschild, U. Jakobsson, P. Jones, R. Julin, S. Ketelhut, et al. Detailed spectroscopy of ^{193}Bi. *Physical Review C*, 92, 044310, 2015.

[119] W. D. Hamilton. The Electromagnetic Interaction in Nuclear Spectroscopy. *IOP Publishing*, 1976.

[120] L. W. Fagg and S. S. Hanna. Polarization measurements on nuclear gamma rays. *Reviews of Modern Physics*, 31, 711, 1959.

[121] D. L. Falkoff. Polarization correlation of successive gamma-ray quanta. *Physical Review*, 73, 518, 1948.

[122] D. R. Hamilton. Polarization and Direction of Propagation of Successive Quanta. *Physical Review*, 74, 782, 1948.

[123] G. J. Schmid, A. O. Macchiavelli, S. J. Asztalos, R. M. Clark, M. A. Deleplanque, R. M. Diamond, P. Fallon, R. Kruecken, I. Y. Lee, R. W. MacLeod, et al. Gamma-ray polarization sensitivity of the Gammasphere segmented germanium detectors. *Nuclear Instruments and Methods in Physics Research Section A: Accelerators, Spectrometers, Detectors and Associated Equipment*, 417, 95, 1998.

[124] E.A. McCutchan. NNDC Online Data Service. `http://www.nndc.bnl.gov/ensdf/`, 2021.

[125] B. Cederwall, F. Lidén, A. Johnson, L. Hildingsson, R. Wyss, B. Fant, S. Juutinen, P. Ahonen, S. Mitarai, J. Mukai, et al. Signature inversion in ^{120}Cs: Evidence for a residual pn interaction. *Nuclear Physics A*, 542, 454, 1992.

[126] F. Liden, B. Caderwall, P. Ahonen, D. W. Banes, B. Fant, J. Gascon, L. Hildingsson, A. Johnson, S. Juutinen, A. Kirwan, et al. Alignment processes in ^{119}Cs, ^{121}Cs and ^{123}Cs. *Nuclear Physics A*, 550, 365, 1992.

[127] J. F. Smith, C. J. Chiara, D. B. Fossan, G. R. Gluckman, G. J. Lane, J. M. Sears, I. Thorslund, H. Amro, C. N. Davids, R. V. F. Janssens, et al. First observation of excited states in ^{118}Cs: signature inversion in the $\pi(h_{11/2}) \otimes \nu(h_{11/2})$ band. *Physics Letters B*, 406, 7, 1997.

[128] C. Thibault, F. Touchard, S. Büttgenbach, R. Klapisch, M. D. S. Simon, H. T. Duong, P. Jacquinot, P. Juncar, S. Liberman, P. Pillet, et al. Hyperfine structure and isotope shift of the D2 line of $^{118-145}$Cs and some of their isomers. *Nuclear Physics A*, 367, 1, 1981.

[129] K. E. G. Loebner, M. Vetter, and V. Hönig. Nuclear intrinsic quadrupole moments and deformation parameters. *Nuclear Data Tables A*, 7, 495, 1970.

[130] D. M. Symochko, E. Browne, and J. K. Tuli. Nuclear data sheets for $A = 119$. *Nuclear Data Sheets*, 110, 2945, 2009.

[131] J. Y. Zeng, T. H. Jin, and Z. J. Zhao. Reduction of nuclear moment of inertia due to pairing interaction. *Physical Review C*, 50, 1388, 1994.

[132] Z. H. Zhang, M. Huang, A. V. Afanasjev, et al. Rotational excitations in rare-earth nuclei: A comparative study within three cranking models with different mean fields and treatments of pairing correlations. *Physical Review C*, 101, 054303, 2020.

[133] K. K. Zheng, C. M. Petrache, et al. Candidate revolving chiral doublet bands in ^{119}Cs, Submitted to EPJA.

[134] N. J. Stone. Table of nuclear magnetic dipole and electric quadrupole moments. *Atomic Data and Nuclear Data Tables*, 90, 75, 2005.

[135] P. W. Zhao, S. Q. Zhang, J. Peng, H. Z. Liang, P. Ring, and J. Meng. Novel structure for magnetic rotation bands in ^{60}Ni. *Physics Letters B*, 699, 181, 2011.

[136] J. Meng, J. Peng, S. Q. Zhang, and P. W. Zhao. Progress on tilted axis cranking covariant density functional theory for nuclear magnetic and antimagnetic rotation. *Frontiers of Physics*, 8, 55, 2013.

[137] Y. K. Wang. Yrast band of ^{109}Ag described by tilted axis cranking covariant density functional theory with a separable pairing force. *Physical Review C*, 96, 054324, 2017.

[138] P. W. Zhao, Z. P. Li, J. M. Yao, J. Meng, et al. New parametrization for the nuclear covariant energy density functional with a point-coupling interaction. *Physical Review C*, 82, 054319, 2010.

[139] K. Q. Lu, Z. X. Li, Z. P. Li, J. M. Yao, and J. Meng. Global study of beyond-mean-field correlation energies in covariant energy density functional theory using a collective hamiltonian method. *Physical Review C*, 91, 027304, 2015.

[140] P. W. Zhao, L. S. Song, B. Sun, H. Geissel, J. Meng, et al. Crucial test for covariant density functional theory with new and accurate mass measurements from Sn to Pa. *Physical Review C*, 86, 064324, 2012.

[141] Y. L. Yang and Y. K. Wang. Nuclear chart in covariant density functional theory with dynamic correlations: From oxygen to tin. *Chinese Physics C*, 44, 034102, 2020.

[142] P. W. Zhao, S. Q. Zhang, J. Meng, et al. Explanation of the simplicity of the quadrupole moments recently observed in Cd isotopes from covariant density functional theory. *Physical Review C*, 89, 011301, 2014.

[143] P. W. Zhao, J. Peng, H. Z. Liang, P. Ring, J. Meng, et al. Antimagnetic rotation band in nuclei: A microscopic description. *Physical Review Letters*, 107, 122501, 2011.

[144] P. W. Zhao, J. Peng, H. Z. Liang, P. Ring, J. Meng, et al. Covariant density functional theory for antimagnetic rotation. *Physical Review C*, 85, 054310, 2012.

[145] L. F. Yu, P. W. Zhao, S.Q. Zhang, P. Ring, J. Meng, et al. Magnetic rotations in ^{198}Pb and ^{199}Pb within covariant density functional theory. *Physical Review C*, 85, 024318, 2012.

[146] Y. Tian, Z. Y. Ma, and P. Ring. A finite range pairing force for density functional theory in superfluid nuclei. *Physics Letters B*, 676, 44, 2009.

[147] T. Nikšić, Z. P. Li, D. Vretenar, L. Próchniak, J. Meng, and P. Ring. Beyond the relativistic mean-field approximation. iii. Collective Hamiltonian in five dimensions. *Physical Review C*, 79, 034303, 2009.

[148] Z. P. Li, T. Nikšić, D. Vretenar, J. Meng, G. A. Lalazissis, and P. Ring. Microscopic analysis of nuclear quantum phase transitions in the N $\approx$ 90 region. *Physical Review C*, 79, 054301, 2009.

[149] P. W. Zhao, S. Q. Zhang, J. Meng, et al. Impact of pairing correlations on the orientation of the nuclear spin. *Physical Review C*, 92, 034319, 2015.

[150] J. M. Sears, D. B. Fossan, G. R. Gluckman, J. F. Smith, I. Thorslund, E. S. Paul, I. M. Hibbert, and R. Wadsworth. Collectivity in even $^{116}_{54}$Xe and $^{118}_{54}$Xe isotopes. *Physical Review C*, 57, 2991, 1998.

[151] B. Ding, Z. Liu, D. Seweryniak, P. J. Woods, H. L. Wang, J. Yang, H. L. Liu, C. N. Davids, M. P. Carpenter, T. Davinson, et al. First identification of excited states in ^{117}Ba using the recoil-β-delayed proton tagging technique. *Physical Review C*, 95, 024301, 2017.

[152] R. Ma, Y. Liang, E. S. Paul, N. Xu, D.B. Fossan, L. Hildingsson, and R. A. Wyss. Competing proton and neutron rotational alignments: Band structures in ^{131}Ba. *Physical Review C*, 41, 1990.

[153] J. F. Smith, C. J. Chiara, D. B. Fossan, G. J. Lane, J. M. Sears, I. Thorslund, I. M. Hibbert, R. Wadsworth, I. Y. Lee, and A. O. Macchiavelli. Multiple shape-driving $\nu(h11/2)^2$ and $\pi(h11/2)^2$ alignments in ^{120}Ba. *Physics Letters B*, 483, 7–14, 2000.

[154] A. P. Byrne, K. Schiffer, G. D. Dracoulis, B. Fabricius, T. Kibédi, A. E. Stuchbery, and K. P. Lieb. High-spin bandcrossing in ^{129}Ba. *Nuclear Physics A*, 548, 131, 1992.

[155] A. Al-Khatib, A. K. Singh, H. Hübel, P. Bringel, A. Bürger, J. Domscheit, A. Neußer-Neffgen, G. Schönwaßer, G. B. Hagemann, C. Ronn Hansen, et al. Competition between collective and noncollective excitation modes at high spin in ^{124}Ba. *Physical Review C*, 74, 014305, 2006.

[156] J. F. Smith, C. J. Chiara, D. B. Fossan, G. J. Lane, J. M. Sears, I. Thorslund, H. Amro, C. N. Davids, R. V. F. Janssens, D. Seweryniak, et al. Identification of excited states in ^{119}Ba. *Physical Review C*, 61, 044329, 2000.

[157] C. N. Davids, and J. D. Larson. The argonne fragment mass analyzer. *Nuclear Instruments and Methods in Physics Research Section B: Beam Interactions with Materials and Atoms*, 40, 1224, 1989.

[158] B. Cederwall, A. Johnson, R. Wyss, C. G. Lindén, S. Mitarai, J. Mukai, B. Fant, S. Juutinen, P. Ahonen, and J. Nyberg. High-spin states in ^{121}Ba and deformation-dependent alignments. *Nuclear Physics A*, 529, 410, 1991.

[159] S. A. Wells, D. E. Evans, J. A. R. Griffith, D. A. Eastham, J. Groves, J. R. H. Smith, D. W. L. Tolfree, D. D. Warner, J. Billowes, I. S. Grant, et al. Fluorescent atom coincidence spectroscopy of extremely neutron-deficient barium isotopes. *Physics Letters B*, 211, 272, 1988.

[160] A. C. Mueller, F. Buchinger, W. Klempt, E. W. Otten, R. Neugart, C. Ekström, and J. Heinemeier. Spins, moments and charge radii of barium isotopes in the range $^{122-146}$Ba determined by collinear fast-beam laser spectroscopy. *Nuclear Physics A*, 403, 234, 1983.

[161] J. M. Blatt, and V. F. Weisskopf. Theoretical nuclear physics. *Courier Corporation*, 1991.

[162] Bricc v2.3s conversion coefficient calculator. `http://bricc.anu.edu.au/`, 2018.

[163] F. Ames, G. Audi, D. Beck, G. Bollen, M. D. S. Simon, R. Jertz, H. J. Kluge, A. Kohl, M. König, D. Lunney, et al. High-accuracy mass determination of unstable cesium and barium isotopes. *Nuclear Physics A*, 651, 3, 1999.

[164] J. Genevey-Rivier, A. Charvet, G. Marguier, C. Richard-Serre, J. d'Auria, A. Huck, G. Klotz, A. Knipper, G. Walter, I. Collaboration, et al. Level structure of light even xenon nuclei populated in the decays of isomeric and ground states of ^{118,120,122}Cs. *Nuclear Physics A*, 283, 45, 1977.

[165] F. R. Xu, P. M. Walker, J. A. Sheikh, and R. Wyss. Multi-quasiparticle potential-energy surfaces. *Physics Letters B*, 435, 257, 1998.

[166] C. J. Gallagher Jr and S. A. Moszkowski. Coupling of angular momenta in odd-odd nuclei. *Physical Review*, 111, 1282, 1958.

[167] A. K. Jain, B. Maheshwari, S. Garg, M. Patial, and B. Singh. Atlas of nuclear isomers. *Nuclear Data Sheets*, 128, 1, 2015.

[168] Y. Z. Liu, J. B. Lu, Y. J. Ma, G. Y. Zhao, H. Zheng, and S. G. Zhou. Spin assignments of yrast bands in odd-odd isotopes $^{118-132}$Cs. *Physical Review C*, 58, 1849, 1998.

[169] P. Bednarczyk, G. D. Angelis, P. Spolaore, D. Ackermann, J. Rico, D. Bazzacco, S. Lunardi, L. Müller, C. R. Alvarez, F. Scarlassara, et al. First observation of the excited states in the doubly odd nucleus ^{118}Cs identified throughγ-recoil coincidences. *Zeitschrift für Physik A Hadrons and Nuclei*, 346, 325, 1993.

[170] C. B. Moon, S. J. Chae, J. H. Ha, T. Komatsubara, Y. Sasaki, T. Jumatsu, K. Yamada, K. Satou, and K. Furuno. Level structure of ^{120}Cs. *Nuclear Physics A*, 696, 45, 2001.

université PARIS-SACLAY

ÉCOLE DOCTORALE
Particules, hadrons, énergie et noyau : instrumentation, imagerie, cosmos et simulation (PHENIICS)

Titre: Phénomènes de collectivité et de formes dans les noyaux ^{119}Cs, ^{119}Ba, et ^{118}Cs extrêmement déficients en neutrons étudiés avec le dispositif JUROGAM 3 + MARA

Mots clés: Spectroscopie nucléaire, états de hauts spins, isomères, triaxialité, coexistence de formes, chiralité

Résumé: Deux schémas de niveaux très complets ont été établis jusqu'à très hauts spins dans les noyaux de lanthanides riches en protons, ^{119}Cs (impair-pair) et ^{118}Cs (impair-impair). Ces nouveaux résultats, ainsi qu'une bande de rotation nouvellement identifiée et plusieurs états de basse énergie d'excitation mis en évidence dans ^{119}Ba, contribuent de manière significative à la compréhension de l'évolution de la collectivité et de la triaxialité en direction de la drip-line proton dans cette région de noyaux. Deux états isomériques situés à basse énergie d'excitation, avec des demi-vies de $T_{1/2} = 0.36(2)$ μs et $T_{1/2} = 55(5)$ μs, ont été identifiés comme les têtes de bande $5/2^-$ et $11/2^-$ des bandes basées sur les orbitales neutron $h_{11/2}$ dans ^{119}Ba, et proton $h_{11/2}$ dans ^{119}Cs. Un état isomérique a été mesuré avec une demi-vie de $T_{1/2} = 0.55(6)$ μs pour l'état 7^+ en dessous de la tête de bande 8^+ appartenant à la bande $\pi h_{11/2} \otimes \nu h_{11/2}$ dans ^{118}Cs. Les structures des bandes observées ont été discutées sur la base des propriétés d'alignement des bandes, de la systématique, et des calculs de modèle en couches tournant conservant le nombre de particules.

Une coexistence de formes prolate-oblate proche de l'état fondamental dans le noyau riche en protons fortement déformé ^{119}Cs a été observée pour la première fois. Ces résultats ouvrent la voie à d'autres investigations expérimentales et théoriques sur les noyaux de lanthanides très riches en protons, pour lesquels des formes aplaties dans l'état fondamental sont prédites. Des bandes chirales construites sur une configuration impliquant uniquement des protons dans le régime de backbending transitoire ont également été observées pour la première fois dans ^{119}Cs, montrant que la chiralité est un phénomène général dans les noyaux, étant robuste et présent non seulement dans des systèmes quantiques à plusieurs corps avec deux composantes, protons et neutrons, mais aussi dans les systèmes quantiques à une composante, seulement protons. Les calculs utilisant le modèle en couches tournant conservant le nombre de particules et le modèle TAC-2D avec fonctionnelle de densité covariante reproduisent bien la coexistence oblate-prolate ainsi que les bandes chirales observées dans le noyau ^{119}Cs.

Title: Collectivity and shape phenomena in extremely neutron deficient ^{119}Cs, ^{119}Ba, and ^{118}Cs studied with the JUROGAM 3 + MARA setup

Keywords: Nuclear spectroscopy, high-spin states, isomers, triaxiality, shape coexistence, chirality

Abstract: Two most complete level schemes from low to high spin in the odd-even and odd-odd proton-rich lanthanide nuclei, ^{119}Cs and ^{118}Cs, have been established. Together with one newly identified rotational band and several low-lying states in ^{119}Ba, they significantly contribute to the understanding of the evolution of collectivety and triaxiality on the way towards the proton drip-line. Two low-lying isomeric states, with half-lives of $T_{1/2} = 0.36(2)$ μs and $T_{1/2} = 55(5)$ μs, for the $5/2^-$ and $11/2^-$ band heads of the bands based on neutron and proton $h_{11/2}$ orbitals in ^{119}Ba and ^{119}Cs, respectively, have been identified. One isomeric state with a half-life of $T_{1/2} = 0.55(6)$ μs, for the 7^+ state below the 8^+ band-head of the $\pi h_{11/2} \otimes \nu h_{11/2}$ band in ^{118}Cs, has been measured. The structures of the observed bands has been discussed based on the alignment properties of the bands, on systematics and on particle number conserving cranked shell model calculations.

Prolate-oblate shape coexistence close to the ground state in the strongly-deformed proton-rich nucleus ^{119}Cs was observed for the first time. The results open the way to further experimental and theoretical investigations of lanthanide nuclei close to the proton drip line, for which ground-state oblate shapes are predicted. Chiral bands built on a configuration with only protons in the transient backbending regime was also observed for the first time in ^{119}Cs, showing that the chirality in nuclei is a general phenomenon, being robust and present not only in a two-component quantum many-body system, but also in a one-component quantum many-body system as well. Calculations using the particle-number conserving cranked shell model and two dimensional tilted axis cranking covariant density functional theory, well reproduce the observed oblate-prolate coexistence and chiral bands in ^{119}Cs.